UNIVERSITY OF SOUTHAMPTON

Peculiar Optical Transients in the Dark Energy Survey

by

Miika Aleksi Pursiainen

A thesis submitted in partial fulfillment for the
degree of Doctor of Philosophy

in the
Faculty of Engineering and Physical Sciences
Department of Physics and Astronomy

December 2020

UNIVERSITY OF SOUTHAMPTON

Abstract

Department of Physics and Astronomy

Doctor of Philosophy

Peculiar Optical Transients in the Dark Energy Survey

by Miika Aleksi Pursiainen

This thesis investigates the properties of peculiar optical transients discovered by the Dark Energy Survey (DES). DES was an optical sky survey designed to study the nature of dark energy using type Ia supernovae (SNe) as cosmic standardisable candles. The DES supernova programme (DES-SN) detected transient events in 2013 – 2018 by observing ten fields of 3 deg^2 each with a weekly cadence for $\sim$ 5 months a year. As a result $\sim$ 29000 optical transients were identified by DES-SN.

I performed two archival searches to identify rapidly evolving transients (RETs) in DES-SN data. In the first one, $\sim$ 1600 Single-Season Transients (SSTs) that exhibited fast light curve evolution as estimated by Gaussian fits, were inspected resulting in discovery of 92 RETs. The RETs were characterised by short rise times ($t_{\rm rise} \lesssim 10$ d) and blue peak colours ($g - r \lesssim 0.6$) distinguishing them from other known transient classes in DES-SN, especially with interpolated Gaussian Process light curves. Thus in the second search, all SSTs with similar rise times and peak colours as the RETs were inspected, once type Ia SNe and transients exhibiting multi-season variability or long decline timescales were excluded. 14 additional RETs were discovered, resulting in the final sample of 106 including 52 with known redshifts.

The RETs were found on a range of redshifts (0.05 – 1.56) and peak luminosities ($-15.8 \gtrsim M \gtrsim -22.6$) and they were characterised by light curve evolution with time above half maximum brightness, $t_{\rm half} \lesssim 12$ d, distinguishing them from standard SNe. Their photometric data was well fitted with a blackbody model, mostly revealing hot ($\sim$ 8000 – 30000 K) and large ($\sim 10^{14}$ – 10^{15} cm) photospheres that were cooling and expanding in time. Furthermore, three RETs were found to exhibit receding photospheres.

The host galaxy analysis revealed that the RETs appear to occur in star-forming galaxies, indicating an origin in massive stars. However, the nickel decay cannot explain the peak luminosities with the quick rises, but due to the lack of spectroscopic data the powering mechanism could not be identified. Thus the physical nature of RETs remains unknown.

I also investigated two peculiar double-peaked DES-SN transients. Their light curves were nearly identical despite 2.5 mag difference in brightness, but no transients with a similar evolution were found in the literature. While the spectra revealed blueshifted calcium absorption in one event, classification could not be secured for either. The events occurred in very different host environments: one near the nucleus of a spiral galaxy and the other at the outskirts of a passive one. While the nearly identical, but highly atypical light curves could imply a similar origin, the differences in the luminosities and host environments might also indicate that they are physically different.

"Look again at that dot.
That's here.
That's home.
That's us.

On it everyone you love,
everyone you know,
everyone you ever heard of,
every human being who ever was,
lived out their lives.

The aggregate of our joy and suffering,
thousands of confident religions, ideologies, and economic doctrines,
every hunter and forager,
every hero and coward,
every creator and destroyer of civilisation,
every king and peasant,
every young couple in love,
every mother and father, hopeful child, inventor and explorer,
every teacher of morals, every corrupt politician,
every superstar, every supreme leader,
every saint and sinner in the history of our species lived there

on a mote of dust suspended in a sunbeam."

—Carl Sagan: "the Pale Blue Dot"

Contents

List of Figures

List of Tables

Abbreviations

2dF	**T**wo-**d**egree **F**ield system
AAT	**A**nglo-**A**ustralian **T**elescope
ACES	**A**rizona **C**DFS **E**nvironment **S**urvey
AGN	**A**ctive **G**alactic **N**uclei
ATLAS	**A**steroid **T**errestrial-impact **L**ast **A**lert **S**ystem
BAO	**B**aryon **A**coustic **O**scillations
BCS	**B**lue **C**hannel **S**pectograph
BH	**B**lack **H**ole
BSG	**B**lue **S**uper **G**iant
CaST	**Ca**lcium **S**trong **T**ransient
CCD(s)	**C**harge-**C**oupled **D**evice**s**
CCSN(e)	**C**ore **C**ollapse **S**uper**N**ova**e**
CDFS	**C**handra **D**eep **F**ield **S**outh
CRTS	**C**atalina **R**eal-time **T**ransient **S**urvey
CSM	**C**ircum**S**tellar **M**aterial
CTIO	**C**erro **T**ololo **I**nter-American **O**bservatory
Dec.	**Dec**lination
DECam	**D**ark **E**nergy **Cam**era
DEIMOS	**DE**ep **I**maging **M**ulti-**O**bject **S**pectrograph
DES	**D**ark **E**nergy **S**urvey
DESDM	**D**ark **E**nergy **S**urvey **D**ata **M**anagement
DES-SN	**D**ark **E**nergy **S**urvey **S**uper**N**ova Programme
DLR	**D**irectional **L**ight **R**adius
EC	**E**lectron **C**apture
ELAIS-S1	**E**uropean **L**arge-**A**rea **I**nfrared **S**pace observatory **S1** survey

ESSENCE	**E**quation of **S**tate: **S**up**E**r**N**ovae trace **C**osmic **E**xpansion
FBOT	**F**ast-rising **B**lue, **O**ptical **T**ransient
FELT	**F**ast **E**volving, **L**uminous **T**ransient
FIR	**F**ar-**I**nfra**R**ed
FWHM	**F**ull **W**idth at **H**alf **M**aximum
GALEX	**GAL**axy evolution **EX**plorer
GAMA	**GA**laxy and **M**ass **A**ssembly survey
GMOS	**G**emini **M**ulti-**O**bject **S**pectrograph
GP	**G**aussian **P**rocess
GTC	**G**ran **T**elescopio **C**anarias
GW	**G**ravitational **W**ave
HSC	**H**yper **S**uprime-**C**am
HSC-SSP	**H**yper **S**uprime-**C**am **S**ubaru **S**trategic **P**rogram transient survey
Ic-BL	Type **Ic** **B**road-**L**ine
IMACS	**I**namori-**M**agellan **A**real **C**amera and **S**pectrograph
INTEGRAL	the **INTE**rnational **G**amma-**R**ay **A**strophysics **L**aboratory
(i)PTF	(**i**ntermediate) **P**alomar **T**ransient **F**actory
KN(e)	**K**ilo**N**ova**e**
LADUMA	**L**ooking **A**t the **D**istant **U**niverse with the **M**eerKAT **A**rray
LBNL	**L**awrence **B**erkeley **N**ational **L**aboratory
LBV	**L**uminous **B**lue **V**ariable
LDSS-3	**L**ow **D**ispersion **S**urvey **S**pectrograph **3**
LGRB	**L**ong duration **G**amma-**R**ay **B**urst
LIGO	**L**aser **I**nterferometer **G**ravitational-wave **O**bservatory
LOSS	**L**ick **O**bservatory **S**upernova **S**earch
LRIS	**L**ow **R**esolution **I**maging **S**pectrometer
LRN(e)	**L**uminous **R**ed **N**ova**e**
LSST	**L**egacy **S**urvey of **S**pace and **T**ime
MIR	**M**id-**I**nfra**R**ed
NCSA	**N**ational **C**enter for **S**upercomputing **A**pplications
NIR	**N**ear-**I**nfra**R**ed
NOAO	**N**ational **O**ptical **A**stronomy **O**bservatory
NS	**N**eutron **S**tar

OSIRIS	**O**ptical **S**ystem for **I**maging and low-intermediate-**R**esolution **S**pectroscopy
Pan-STARRS	**Pan**aoramic **S**urvey **T**elescope and **R**apid **R**esponse **S**ystem
PS1-MDS	**P**AN-**S**TARRS1 **M**edium **D**eep **S**urvey
PRIMUS	**PRI**sm **MU**lti-object **S**urvey
R.A.	**R**ight **A**scension
RET	**R**apidly **E**volving **T**ransient
RLOF	**R**oche-**L**obe **O**ver**F**low
RNe	**R**ed **N**ova**e**
RSG	**R**ed **S**uper **G**iant
RSS	**R**obert **S**tobie **S**pectrograph
SALT	**S**outh **A**frican **L**arge **T**elescope
SDSS	**S**loan **D**igital **S**ky **S**urvey
SED	**S**pectral **E**nergy **D**istribution
SFH	**S**tar **F**ormation **H**istory
(s)SFR	(**s**pecific) **S**tar **F**ormation **R**ate
SLSN(e)	**S**uper**L**uminous **S**uper**N**ova**e**
SMBH	**S**uper**M**assive **B**lack **H**ole
SN(e)	**S**uper**N**ova**e**
SNLS	**S**uper**N**ova **L**egacy **S**urvey
SST	**S**ingle **S**eason **T**ransient
SV	**S**cience **V**erification
SWIRE	**S**pitzer **W**ide-area **I**nfra**R**ed **E**xtragalactic survey
TDE)	**T**idal **D**isruption **E**vent
UV	**U**ltra**V**iolet
WD	**W**hite **D**warf
VIDEO	**V**ISTA **D**eep **E**xtragalactic **O**bservations **S**urvey
VISTA	**V**isible and **I**nfrared **S**urvey **T**elescope for **A**stronomy
VLT	**V**ery **L**arge **T**elescope
WR	**W**olf-**R**ayet
XMM-Newton	**X**-ray **M**ulti-Mirror **M**ission **Newton**
XMM-LSS	**XMM**-Newton **L**arge **S**cale **S**tructure legacy field
YSG	**Y**ellow **S**uper **G**iant
ZAMS	**Z**ero **A**ge **M**ain **S**equence

ZTF	**Z**wicky **T**ransient **F**acility

Declaration of Authorship

I, Miika Aleksi Pursiainen, declare that this thesis titled, 'Peculiar Optical Transients in the Dark Energy Survey' and the work presented in it are my own. I confirm that:

- This work was done wholly or mainly while in candidature for a research degree at this University.
- Where any part of this thesis has previously been submitted for a degree or any other qualification at this University or any other institution, this has been clearly stated.
- Where I have consulted the published work of others, this is always clearly attributed.
- Where I have quoted from the work of others, the source is always given. With the exception of such quotations, this thesis is entirely my own work.
- I have acknowledged all main sources of help.
- Where the thesis is based on work done by myself jointly with others, I have made clear exactly what was done by others and what I have contributed myself.
- Parts of this thesis are presented in Pursiainen et al. (2018), Pursiainen et al. (2020) and Wiseman et al. (2020a)

Signed:

Date:

Acknowledgements

To the Southampton Supernova Group. To Charlotte, Chris, Claudia, Cosimo, Georgios, Lisa, Mark, Mat, Matt, Mike, Phil, Regis, Rob and Tomás, and to the Portsmouth constituents Ben, Lizi and Maria. Thank you for all the inspiring science chats and discussions; for all the help and support. It has been a pleasure to know all of you and I hope we get a chance to work together in the years to come.

To my peers in the office 4057. To Sam, Georgios, Sadie, Maxi, Chris, Vicky, Noel, Alex, Aru, Mayukh, Claire, Brian, Jakub, Santiago and Arianna. Thank you for all the coffees and sweets we shared; for all the chances to ignore work and procrastinate.

To my Mayflower colleagues. To Andy, Dave, Bella, Alex, Claire and Maria. For all those countless moments of politely discussing the joys of undergraduate teaching.

To all PhD students and Post-docs in the Southampton Astronomy Group. To my friends and colleagues. Thank you for all the laughs and stories we shared together. For all the words of support. For all the trips to pub, whether it was a Thursday crawl or a gloomy Friday. For all the pints of beer and cider and all the shots of vodka, be it Fisherman's Friend, Salmiakki or even Arctic Blueberry.

To my dear Tegan. Thank you for everything. For the times climbing up a mountain; for the rainy days spent with puzzles and tea. For the times watching the stars come out at Pitts Deep. And to Mark and Ruth; thank you for a place to stay during the truly unfortunate times.

To my friends abroad. To Eero and Susanna in Finland; thank you for all those countless days spent trekking up and down the mountainside. To Ina in Japan; for all the pasta we have cooked together over the years. To Bogi in Denmark; for all the trips to Budapest with sör and pálinka. Csak az ETO!

And last but not least, to my family in Finland. To Ritva in Joensuu, and to Jouni and Päivi in Oulu. Thank you for all the visits and support over the years. To Tuukka; for all those times tickling for trout and grayling at evening twilight or the crack of dawn. To Reetta; for all the lazy days spent cooking and playing board games. I wouldn't be here if it hadn't been for all of you.

To whom it may concern...

Chapter 1

Introduction

Supernovae (SNe) are cataclysmic explosions at the end of stars lives that can be bright enough to outshine their respective host galaxies. They are rare (a few per century in a Milky Way-like galaxy; Li et al. 2011b) and thus their study is very strongly focused on SNe outside the Milky Way. The first extragalactic SN, S Andromedae (also known as SN1885), was discovered in late 19th century in Andromeda galaxy by E. Hartwig in Dorpat (current Tartu), Estonia (Hartwig et al. 1885), but it was not recognised as one at the time. Over the next few decades the number of discovered SNe increased slowly as the discoveries were made by sheer luck. Finally, in early 1930s enough objects with similar observable features were discovered that these bright extragalactic transients were given a name *Super-Novae* by Walter Baade and Fritz Zwicky (Baade & Zwicky 1934). Zwicky was also the first to put in place a dedicated search for SNe using telescopes on Mount Wilson finding around five new SNe per year with a demanding effort of comparing photographic plates to find new, bright sources of light (Zwicky 1938). The number of discovered SNe per year from 1880 to Autumn 2019 is shown in Figure 1.1.

As technology evolved rapidly over the next few decades the number of found SNe increased drastically. The first robotic SNe searches in 1960s and 1970s allowed seamless reacquiring of target galaxies and resulted in discovery of few tens of SNe per year. In 1980s searches using CCD cameras mounted on larger telescopes discovered the first SNe on cosmological distances. The discovery of distant SNe sparked a discussion of using a particular bright class of SNe, called type Ia SNe, to test cosmological models by using them as standard candles. While such an idea had been postulated since the discovery of SNe (Baade 1938), it was not possible to put it in use until large samples of homogeneous

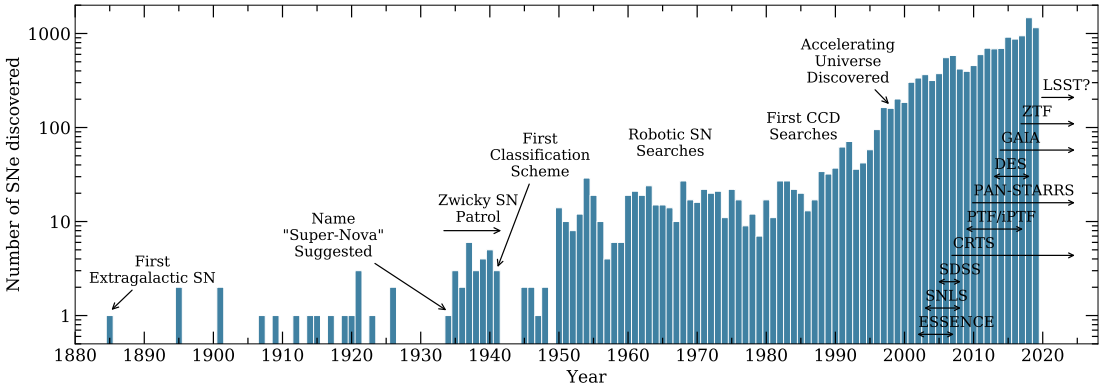

FIGURE 1.1: Histogram of discovered supernovae since 1880 with some highlighted key events. Some influential past, on-going and future surveys have been noted on the right. The mentioned surveys are Equation of State: SupErNovae trace Cosmic Expansion (ESSENCE, 2002-2007; Miknaitis et al. 2007), Supernova Legacy Survey (SNLS, 2003-2008; Pritchet & SNLS Collaboration 2005) The Sloan Digital Sky Survey-II (SDSS-II) Supernova Survey (2005-2008; Frieman et al. 2008; Sako et al. 2008), The Catalina Real-Time Transient Survey (CRTS, 2007 to present; Djorgovski et al. 2011), Palomar Transient Factory (PTF) followed by intermediate PTF (iPTF, 2009-2017; Rau et al. 2009), The Panoramic Survey Telescope and Rapid Response System (PAN-STARRS) Medium Deep Survey (PS1-MDS, 2010 to present; Chambers et al. 2016), Dark Energy Survey (DES) Supernova Program (DES-SN, 2013-2018; Flaugher 2005), Gaia space mission (2014 to present; Perryman et al. 2001), Zwicky Transient Facility (ZTF, successor of PTF/iPTF, 2017 to present; Bellm et al. 2019) and the Legacy Survey of Space and Time (LSST, Scheduled to start 2020; LSST Science Collaboration et al. 2009; Ivezić et al. 2019). The diagram has been created based on list of SNe compiled by Isaac Shivvers[1]. The data is collected from International Astronomical Union's official list[2], the Transient Name Server[3] and the list maintained by David Bishop at the Rochester Academy of Sciences[4].

SNe were discovered.

In the late 1990s two groups, High-Z Supernova Search Team and Supernova Cosmology Project, used type Ia SNe to independently prove that expansion of the Universe is accelerating (Riess et al. 1998; Perlmutter et al. 1999). The result was later awarded the Nobel Price of Physics in 2011 as a testimony of its significance to the field of physics. With this immense discovery the interest in discovering new SNe increased strongly in the early 21st century. Several dedicated SN surveys were founded and some of the most influential ones have been highlighted in Figure 1.1. Quickly more than a thousand new SNe per yer were discovered. While the primary motive for many of these surveys was to collect well observed samples type Ia SNe for to their cosmological importance, used untargeted, wide-field approach resulted in discovery of all kinds of SNe and other extragalactic transients including new, peculiar ones that had never been seen before.

[1] http://www.ishivvers.com/maps/sne
[2] https://wis-tns.weizmann.ac.il/
[3] http://www.cbat.eps.harvard.edu/lists/Supernovae
[4] http://www.rochesterastronomy.org/snimages/sndateall

In this thesis I will focus on one particular class of extragalactic events whose discovery was made possible by the decades of work resulting in deep, high-cadence SN surveys — the enigmatic rapidly evolving transients. However, before introducing their peculiar properties the stage has to be set. In the following I will give a overview of the traditional SN classification scheme with its recent complex additions and describe the most important physical processes powering their light curves. From there I embark on a mission to characterise other families of recently discovered extragalactic transient phenomena and finally conclude the Chapter by introducing the rapidly evolving transients and discussing their relation to SNe.

1.1 Supernova Family

Since the discovery of the first extragalactic SN, S Andromedae, it took half a century until the first spectroscopic sample of 14 SNe was brought forth by Minkowski (1941), outlying the first classification scheme between two types of SNe. Nine spectroscopically nearly homogeneous events were classified as type I SNe due to their spectral similarity. The remaining five SNe were quite diverse in their properties, but all of them showed hydrogen emission in their spectra unlike the type I SNe. Thus, they were given the classification of type II SNe using the presence/absence of hydrogen as the first classification criterion. Representative near-peak spectra of different H-poor and H-rich types of SNe are presented in Figure 1.2, where the main line features and the responsible elements are highlighted.

1.1.1 Standard Supernova Types

While the original criterion is still the foundation of the modern classification scheme, the spectral diversity of both of classes of SNe has increased significantly. In 1985 Wheeler & Levreault discovered the first example of a peculiar type I SN which was spectroscopically distinct from the dominant population with a key difference being the lack of blueshifted Si II λ6355 absorption feature. Later the same year Elias et al. coined the terms type Ia SN for the dominant population and type Ib SN for the newly discovered subclass. Furthermore, Harkness et al. (1987) identified several He I absorption lines in the peak spectra of SNe Ib giving rise to clear classification criterion for this class (evidence of helium but no hydrogen). Only a few years later Wheeler & Harkness (1990) introduced a subtype Ic SNe for those events that were spectroscopically similar to Ib SNe, but lacked the helium lines. Types Ib and Ic are often referred to as Ibc SNe as they are often difficult to distinguish from each due to the weakness of the helium lines.

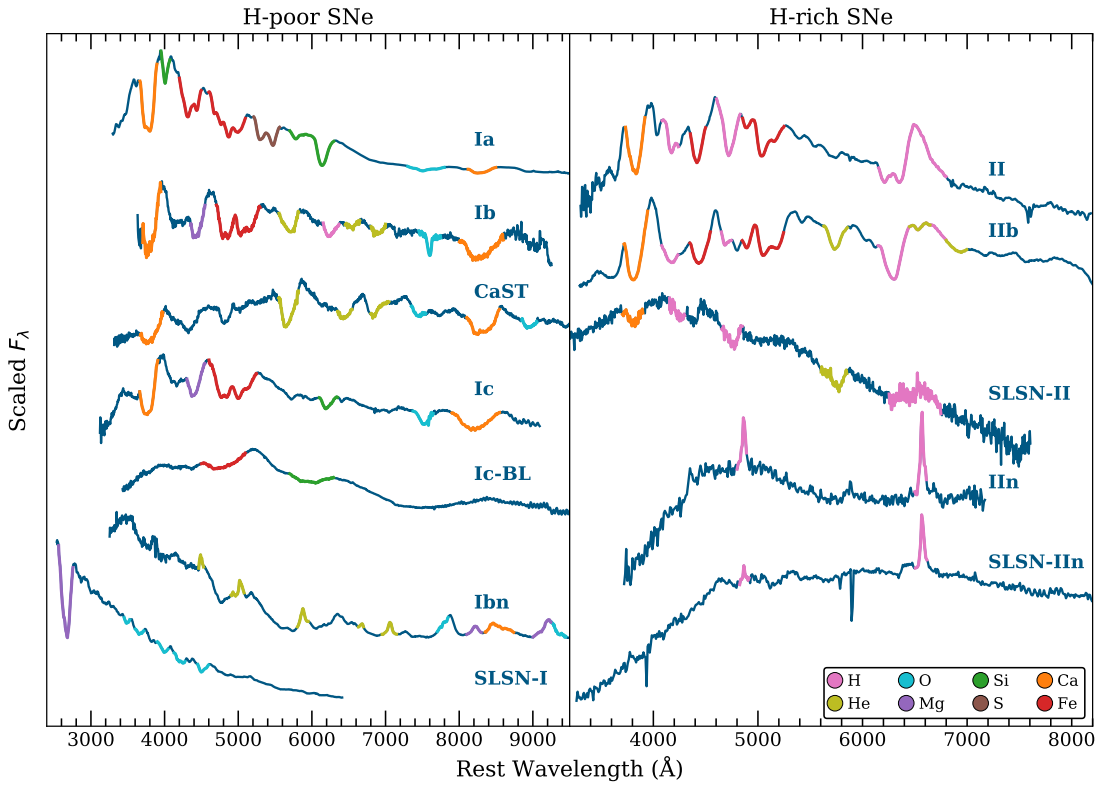

FIGURE 1.2: Representative near-peak spectra for different SN types with some significant line features and the responsible elements highlighted. The spectra are collected from the Open Supernova Catalog (Guillochon et al. 2016) and first presented in the following papers. Type Ia SN2011fe (Pereira et al. 2013), type Ib iPTF13bvn (Srivastav et al. 2014), CaST PTF11kmb (Foley 2015), type Ic SN2007gr (Valenti et al. 2008), type Ic-BL SN1998bw (Patat et al. 2001), type Ibn SN2006jc (Foley et al. 2007), SLSN-I PTF09cnd (Quimby et al. 2018), type II SN2013ej (Yuan et al. 2016), type IIb SN2011dh (Ergon et al. 2014), SLSN-II (Faran et al. 2014), type IIn SN2005kj (Taddia et al. 2013) and SLSN-IIn SN2006gy (Smith et al. 2007). Note that some of the spectra are uncalibrated.

Type II SNe have also gone through a dramatic increase of subtypes. In 1979, Barbon et al. classified type II SNe based on their light curve evolution. The SNe that exhibited a plateau after the peak brightness were named type IIP and those that did not type IIL for their linear decline. Despite the photometric differences the spectra of both types show characteristic broad, Balmer emission lines with P Cygni line profiles (Oke & Searle 1974). In this thesis both of these types will be refereed to as normal type II SNe. Later on two additional types of SNe II were introduced. Type IIb SNe undergo a transition from a hydrogen rich early phases into having a Ib-like helium dominated spectra around the peak brightness (Filippenko 1988). Type IIn SNe, on the other hand, exhibit strong, narrow hydrogen emission lines (Schlegel 1990), distinctly different from the broad emission seen in normal type II SNe.

Li et al. (2011c) estimated the population fractions for the three main types of SNe (types Ia, Ibc and II) derived based on 175 SNe within 60 Mpc observed by the Lick

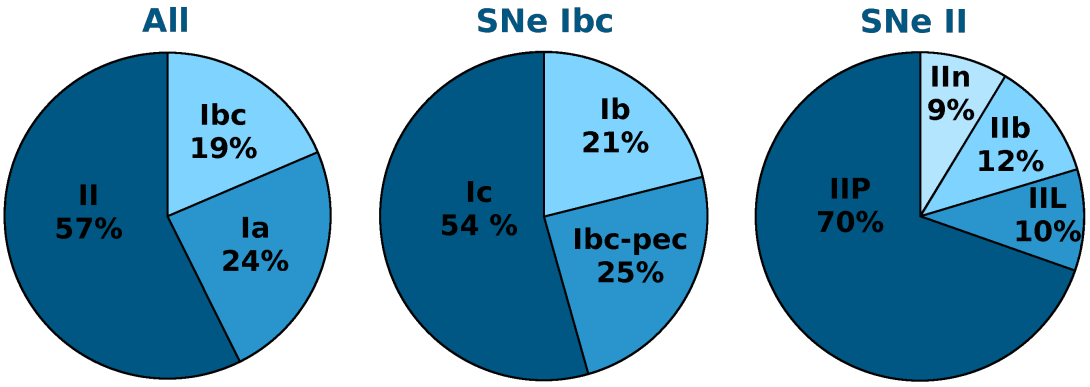

FIGURE 1.3: Population fractions of SN types (adapted from Figure 9. in Li et al. 2011c).

Observatory Supernova Search (LOSS). The resulting fractions are presented in Figure 1.3. While type Ia SNe dominated the numbers of observed SNe (79%; Li et al. 2011c), in actual population fractions they only constitute a quarter. The large difference is caused by the higher peak luminosity of type Ia SNe: as they are brighter than most type II and type Ibc SNe they can be discovered further away. The same LOSS sample was recently re-analysed by Shivvers et al. (2017) and in their study they showed that, while the fractions between the main types are not affected, some type Ib SNe may have been misclassified as Ic SNe making them actually more numerous than their He-poor cousins.

Apart from the spectral differences, the peak luminosities of different SNe types also differ considerably from each other. The spread is perfectly demonstrated by the study of Richardson et al. (2014), where the authors collected data of as many SN they could find — mostly from Asiago Supernova Catalog (Barbon et al. 1989) — and constructed histograms of the volume limited absolute peak magnitudes in B band for the common SN subtypes. The work is summarised in Table 1.1, where the average values of M_{B} are presented with the standard deviation and approximate range of the spread. Type Ia SNe are clearly the brightest class of the standard SNe, but they also demonstrate the smallest spread.

1.1.2 Newer Supernova Types

The classification scheme is not set in stone and to reflect the diversity of new SNe, it is constantly evolving. As the number of discovered SNe has increased over the years, so has the discovery rate of events that either show individual peculiar observables or are just distinctly different from the aforementioned classes. As a result, further observational

TABLE 1.1: The average absolute B band magnitudes at peak for different SN types as provided by Richardson et al. (2014).

SN Type	$\overline{M}_B$[a]	σ[b]	Range[c]	N[b]
Type Ia	-19.26 ± 0.20	0.51	-18.0 – -20.0	171
Type Ib	-17.54 ± 0.33	0.94	-16.0 – -19.0	18
Type Ic	-17.67 ± 0.40	1.04	-15.0 – -19.0	36
Type IIb	-17.03 ± 0.45	0.93	-15.5 – -18.5	15
Type IIL	-17.98 ± 0.34	0.90	-16.5 – -20.0	17
Type IIP	-16.80 ± 0.37	0.97	-14.5 – -19.0	74
Type IIn	-18.62 ± 0.32	1.48	-17.0 – -20.0	21

[a] Mean of the distribution.
[b] Statistical standard deviation from the mean.
[c] Approximate range of the distribution.
[d] Number of SNe in each class.

classes of SNe have been created. For a review of the recent development of the SNe classification scheme see e.g. Gal-Yam (2017).

In 1998, Galama et al. presented SN1998bw, a SN showed spectral similarity to type Ic SNe but with significantly broadened line features. Few years later, a similar SN, SN2002ap (Mazzali et al. 2002; Gal-Yam et al. 2002; Foley et al. 2003), was discovered and the subtype was named the type Ic Broad-Line (Ic-BL). Furthermore, the diversity of Ib SNe was increased with the discovery of SN2006jc. The SN exhibited helium lines but in a from of narrow emission rather than broad absorption as is the case for Ib SNe (Foley et al. 2007; Pastorello et al. 2007). As more such events were discovered, they were quickly named as type Ibn SNe in an analogue of type IIn SNe (Pastorello et al. 2008).

Similarly, the discovery of SN2005ap (Quimby et al. 2007) and SN2006gy (Ofek et al. 2007; Smith et al. 2007) forced a creation of a new subtype. While the SNe were spectroscopically different in that the latter showed narrow Balmer emission lines and the former not, they were both significantly brighter than any SNe known before. In 2011, Quimby et al. brought forth a sample of six SNe, that included SN2005ap and previously published SCP 06F6 (Barbary et al. 2009), that were spectroscopically similar to SN2005ap showing O II, Mg II, Si III and CII absorption but were also equally luminous. Furthermore, this observational class of bright SNe became even more diverse with the discovery of SN2008es (Miller et al. 2009; Gezari et al. 2009). Its spectra showed hydrogen but now in a form of broad P Cygni emission typical for normal type II SNe. Given that the light curve was also rather quick with a linear decline, the SN was tentatively classified as type IIL SN. While the three types of bright SNe were spectroscopically different from each other, they were quickly put under an umbrella term of superluminous SNe (SLSNe) due

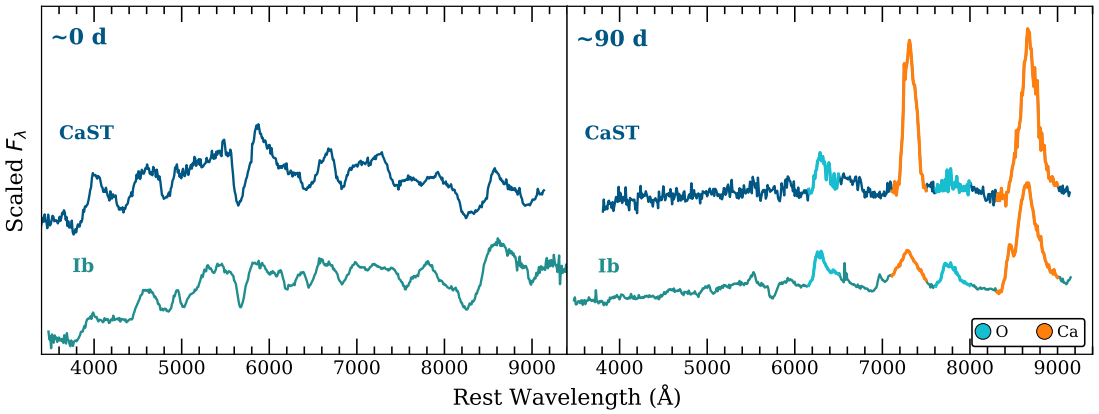

FIGURE 1.4: Comparison of near-peak and nebular spectra of a CaST and a type Ib SN. The spectra are collected from the Open Supernova Catalog (Guillochon et al. 2016) and first presented in the following papers: CaST PTF11kmb (Foley et al. 2015) and type Ib SN2008D (Modjaz et al. 2009; Shivvers et al. 2019).

to their extreme brightnesses of $M \lesssim -21$ (Gal-Yam 2012). Following the conventional classification scheme those SLSNe that show hydrogen emission are type II and the ones that do not are type I. In this thesis those SLSNe-II that show only narrow hydrogen emission are called SLSNe-IIn following the naming convention of Gal-Yam (2019).

The last exotic type of SNe to mention are the calcium strong transients (CaSTs; Shen et al. 2019), also known as Ca-rich SNe (Perets et al. 2010) and Ca-rich gap transients (Kasliwal et al. 2012), first discovered with the prototype SN2005E (Perets et al. 2010). Their spectra shows prominent He absorption features and thus they appear to be similar to type Ib SNe around peak brightness. However, they develop very strong calcium emission features in the nebular phase at least when compared to oxygen emission which typically observed abundantly in type Ib SNe (see e.g. Kasliwal et al. 2012). Near-peak and nebular spectra of a CaST and a SN Ib are shown in Figure 1.4 for comparison. While the number of discovered CaSTs is only a few tens (Shen et al. 2019), they are actually estimated to be very common with a volumetric rate of $\gtrsim 30\%$ of the type Ia SNe (Frohmaier et al. 2018). However, as their light curves are characteristically faint and fast and stay within 50% of their peak brightness of $-15 \gtrsim M \gtrsim -16.5$ only for 10 – 15 d (see e.g. Shen et al. 2019, and references therein), they are very difficult to discover and thus their total number has remained small.

1.2 Physical Interpretation of Supernovae

While the classification scheme of SNe is straightforward in its spectroscopic essence, it has evolved into a complicated system applying cuts also based on the photometric data (i.e. the shape of the decline or the peak brightness). The diversifying scheme

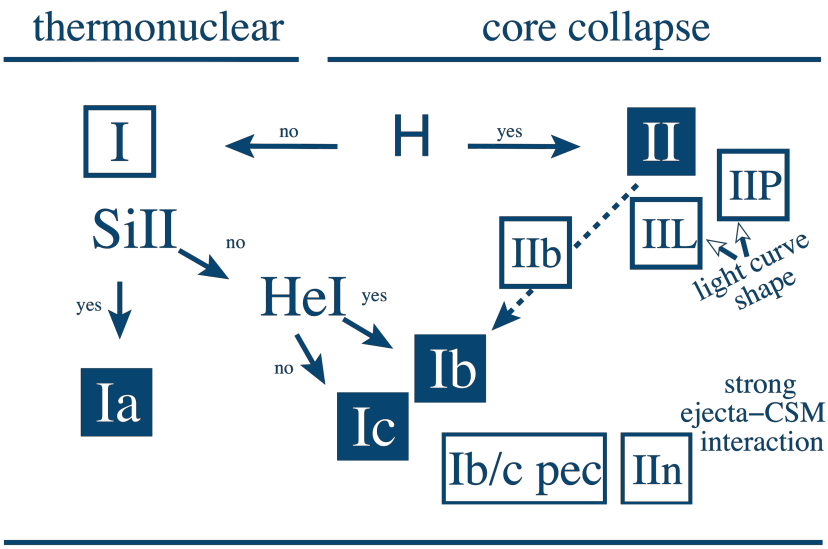

FIGURE 1.5: Simplified classification scheme for SNe (adapted from Figure 1. in Turatto 2003).

perfectly demonstrates that SNe are in fact observed to be on a spectrum of observable properties and no SN inside a subtype is identical to the next one. The variations of the observables (i.e. the spectra and the light curves) both inside a subtype and between different subtypes are caused by the physical diversity in the population of the progenitors. As some physical configurations are likelier than the others, the majority of SNe originating from the same type of progenitors are similar to each other and thus belong to the "dominant" population, while the unlikelier configurations produce outliers that show only some features of the dominant population. Not only does this give rise to all peculiar SNe inside each subtype, but it can also explain how different subtypes are related to each other. Therefore, it is up to physical interpretation of the SNe to understand which types of SNe are physically linked and actually originate from similar progenitors. Simplified classification scheme summarising the physical connection of different types of SNe has been presented in Figure 1.5.

In terms of actual physical scenarios, SNe are assumed to originate from two main channels that were first proposed in 1960 by Hoyle & Fowler. In the first scenario, the explosion is caused by a thermonuclear runaway reaction triggered inside an electron degenerate white dwarf (WD), while in the second one the powering engine is a collapsing core of a massive star ($\gtrsim 8\ M_\odot$). The exact details on how either of these physical scenarios actually lead to an explosion are not very well understood, but in the case of many subtypes there is strong direct evidence promoting a certain type of progenitor system for the SNe of that type. In the following I will give a brief overview of the explosion mechanisms based on the current consensus, but I will also discuss how the said scenarios are related to different SNe subtypes.

1.2.1 Thermonuclear Supernovae

Thermonuclear SNe are explosions where the progenitor is a WD supported by electron degeneracy pressure. Under a simplified scenario such an explosion occurs when a WD, accreting matter from a binary companion, eventually approaches the limiting Chandrasekhar mass of $M_{\rm Ch} \sim 1.4\ M_{\odot}$. At this point the core of the WD is fully degenerate and it can no longer support the increasing mass. Exothermic thermonuclear runaway reaction is triggered inside the WD in conditions of both high temperature and pressure. The released immense amount of energy unbinds the WD leading to a bright and powerful cosmic explosion (Hillebrandt & Niemeyer 2000).

1.2.1.1 Type Ia Supernovae

Type Ia SNe are the most common class of thermonuclear SNe. The scenario has been speculated and commonly agreed on to explain type Ia SNe since the 1960s (see e.g. Hoyle & Fowler 1960). As virtually all type Ia SNe show remarkable similarity in both photometric and spectroscopic properties, the physical scenario had to be such that it produces the same observable properties with only small variations and only thermonuclear explosion of a carbon-oxygen WD (CO WD) was considered capable of achieving that (Woosley et al. 1986). However, despite the strong theoretical groundwork, the observational evidence to prove the scenario waited until 2011 to be discovered.

Finally, in August 2011, a near-by type Ia SN2011fe exploded in the spiral galaxy M101 at a distance of 6.4 Mpc (Shappee & Stanek 2011), providing a very extensive data-set starting from only $\sim$ 11 h after the explosion (Nugent et al. 2011; Bloom et al. 2012). Not only was the size of the progenitor was constrained to be $R < 0.1\ R_{\odot}$ based on the early photometric data, but the early spectra also showed unburned high-velocity carbon and oxygen features seen only $\sim$ 1 d after the explosion (Nugent et al. 2011). Based on these findings it was concluded that SN2011fe occurred when a CO WD approached the Chandrasekhar mass and exploded as a type Ia SN. While the exact type of the companion star of the primary WD could not be determined, it was constrained to be a subgiant, a main-sequence star or a secondary WD (Li et al. 2011a).

The light curve of a type Ia SN is not powered directly by the explosion itself, but rather by radioactive decay of elements synthesised by the explosion. In the SN process, ^{12}C and ^{16}O of the primary WD are ignited and transmuted in to higher order elements such as ^{28}Si and ^{56}Ni. Out of the resulting elements ^{56}Ni is the most important in understanding the SN physics. The isotope is unstable and it is produced in large quantities in type Ia SNe ($\sim 0.4 - 1.2\ M_{\odot}$; Childress et al. 2015) and thus it directly provides the energy

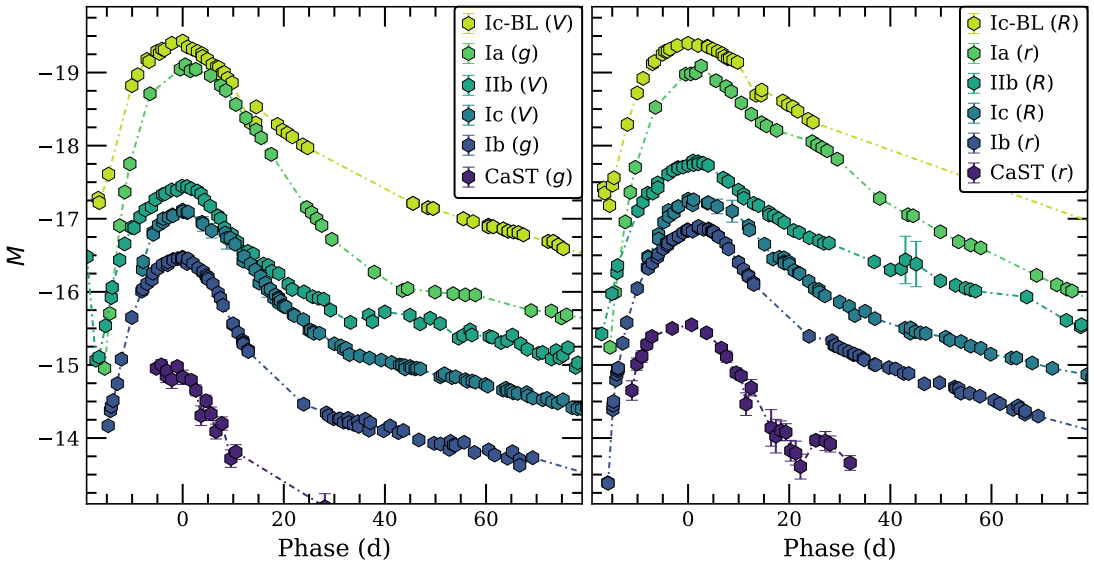

FIGURE 1.6: Example g/V (left) and r/R (right) light curves of a type Ia SN, a CaST and SESNe shown since the observed peak in g/V. The light curves are collected from the Open Supernova Catalog (Guillochon et al. 2016) and first presented in the following papers: type Ic-BL SN1998bw (Galama et al. 1998; McKenzie & Schaefer 1999; Sollerman et al. 2000), type Ia SN2011fe (Richmond & Smith 2012; Tsvetkov et al. 2013; Munari et al. 2013), type IIb SN2011dh (Sahu et al. 2013), type Ic SN2007gr (Bianco et al. 2014), type Ib iPTF13bvn (Fremling et al. 2016), CaST PTF11kmb (Lunnan et al. 2017).

for the SN emission. In the process, ^{56}Ni decays via inverse β decay (β^+) with half-life of $t_{1/2} = 6.08$ d into ^{56}Co, which further decays in ^{56}Fe through both electron capture (EC) and β^+ decay with $t_{1/2} = 77.2$ d (Colgate & McKee 1969). The decay chain of ^{56}Ni is also presented in Equation 1.1, where the average emitted energy per nucleus for each decay process is given (Nadyozhin 1994).

$$^{56}\text{Ni} \xrightarrow[E_\gamma \sim 1.75 \text{ MeV}]{t_{1/2} = 6.08 \text{ d}} {}^{56}\text{Co} \xrightarrow[E_\gamma \sim 3.73 \text{ MeV}]{t_{1/2} = 77.2 \text{ d}} {}^{56}\text{Fe}. \tag{1.1}$$

As a result, the bolometric luminosity at the peak brightness of a type Ia SN is directly related to the mass of ^{56}Ni synthesised in the explosion. The relation is known as Arnett's Rule (Arnett 1982) and it can be used to approximately estimate the amount of ^{56}Ni in a SN (see e.g. Stritzinger & Leibundgut 2005) — for type Ia SNe it has been found to be accurate to 20% (e.g. Blondin et al. 2013), but for type Ibc SNe it deviates up to 50% (Dessart et al. 2015, 2016). Example optical light curves of type Ia SN2011fe are presented in Figure 1.6, with light curves of a example CaST and different types of SESNe.

1.2.1.2 Calcium-Strong Transients

Another likely type of thermonuclear supernovae are the recently discovered CaSTs. As a faint and elusive class of transients, no direct evidence of their explosion mechanism has been seen. However, indirect findings have lead to a common consensus that these transients are likely not a result of a core-collapse of a massive star, despite their spectroscopic resemblance to Ib SNe, but are rather thermonuclear in origin. The most important individual piece of evidence implying such a conclusion are the explosion locations of CaSTs. They are always found on the outskirts of their respectable host galaxies with an average offset measured in few tens of kiloparsecs (see e.g. Shen et al. 2019, and reference therein). Furthermore, they appear to occur preferentially in non-star-forming galaxies in cluster environments (Kasliwal et al. 2012; Foley 2015; Lunnan et al. 2017). Massive, short-lived stars are not expected to be found in such locations and thus any scenario requiring them is disfavoured.

The remaining scenarios are then related to thermonuclear runaway explosions involving a WD (or two) of some kind, but no agreement has been found on what the exact mechanism is. Several scenarios have been suggested and many of them are found to explain at least some of the observed peculiarities. For instance, in one proposed scenario a merger of He WDs with CO or O-Ne WDs can explain the faint and fast evolving light curves (García-Berro et al. 2017). Another similar model of a detonated He layer on a low-mass CO WD ($M \lesssim 0.6\ M_{\odot}$ can produce the inferred chemical composition without disrupting the WD and causing it to explode as type Ia SNe (Shen et al. 2010; Waldman et al. 2011). However, none of these models can explain why CaSTs would only be found in remote locations and thus their origin remains unknown. Great overviews of the peculiar physical characteristics and the invoked theoretical scenarios of CaSTs can be found in Taubenberger (2017) and Shen et al. (2019).

1.2.2 Core-Collapse Supernovae

Core-Collapse SNe (CCSNe) include both H-rich type II SNe and H-poor Ibc and they are more common than the previously discussed thermonuclear SNe as shown in Figure 1.3. As a rule, the progenitor of a CCSN is a massive star with zero age main sequence (ZAMS) mass of $M \gtrsim 8\ M_{\odot}$. Such a star can produce sufficient conditions (i.e. temperature and pressure) in its core to ignite the carbon reservoir created during earlier phases of H and He fusion, while a star with a smaller original mass will eventually shrink into a CO WD. A series of subsequent exothermic fusion reactions of C, Ne, O and Si leads to production of Fe in the core. As the fusion of iron nuclei is an endothermic process and would require energy to occur, the fusion never starts.

The core has thus lost its radiative pressure and is now supported temporarily by the pressure of degenerate electrons. However, the core keeps gaining mass due to Si burning occurring on a layer outside the Fe core. Once the mass of the core approaches the Chandrasekhar limit $M_{\rm Ch}$, the core starts to collapse on itself under the tremendous force of gravity. The contraction leads to a rapidly increasing temperature and thus creation of high energy γ-rays that break down the Fe nuclei first to α-particles and then to protons and neutrons via photodisintegration. Under the high pressure the protons join with free electrons via EC process producing even more neutron-rich material. The EC reactions also create an unthinkable amount of neutrinos, effectively trapped inside the contracting core. Further neutrinos are also created via neutrino pair-production under very high temperature of the core.

Upon reaching nuclear densities the collapse of the core finally decelerates and "bounces" giving a rise to spherical shock wave propagating outwards. However, the shock wave stagnates having lost its energy to dissociation of heavy nuclei in the outer core and thus is not enough to unbind the star. From here on the exact details on how the explosion occurs are uncertain. However, the common consensus is that explosion is related to the large number of produced neutrinos. In fact, the significant majority ($\sim$ 99%) of the potential energy released in the contraction of the star is carried away in the form neutrinos, and only a fraction goes to the emission and the kinetic energy of the SN. Thus, it is assumed that the escaping neutrinos deposit a fraction of their energy via some uncertain physical mechanism to the supernova ejecta reviving the stalled shock and thus exploding the star. Excellent overviews of the CCSN explosion theory are presented in e.g. Bethe (1990); Woosley & Weaver (1986); Janka et al. (2007); Janka (2017) and on the observational properties of CCSN progenitors in Smartt (2009).

1.2.2.1 Hydrogen-Rich Core-Collapse Supernovae

Hydrogen-Rich CCSNe were one of the first types of SNe ever detected and following the original classification criteria of Minkowski (1941) they are classified as type II SNe due to the prominent hydrogen features visible in their spectra. The most famous example of a type II is SN1987A, a close by SN that exploded in Tarantula Nebulae in the Large Magellanic Cloud, making it the closest SN that has been observed with modern technology. Due to its very nearby location, it was possible to quickly verify SN1987A as a CCSN. The electromagnetic emission was accompanied by a coincident detection of 25 neutrinos, 12 by Kamiokande II (Hirata et al. 1987), 8 by the Irvine-Michigan-Brookhaven detector (Bionta et al. 1987) and 5 by Baksan neutrino observatory (Alekseev et al. 1988), as expected from a core-collapse of a massive star. Furthermore, its disappeared progenitor star, Sk-69°202, was quickly identified in pre-explosion images by White & Malin

(1987), providing additional evidence in favour of the core-collapse scenario. Later on the progenitor was classified as a Blue Super Giant (BSG) star with $T_{\rm eff} \sim 17500$ K by Walborn et al. (1989), with an inferred radius of $\sim 50\ R_{\odot}$.

Type IIP SNe are the most common out of all type II SNe (see Figure 1.3). They originate from core-collapse of Red Super Giant (RSG) stars with several progenitor stars in a mass range of $M \sim 10 - 17\ M_{\odot}$ discovered (see e.g. Smartt 2009, for review). These stars are very extended with thick hydrogen envelopes found at radii of $R \sim 500 - 1500\ R_{\odot}$ giving a natural rise to plateaus in their light curves with a scenario first suggested by Chevalier (1976). After the core-collapse, the resulting shock ejects the star causing the explosion but the shock also ionises the hydrogen in the envelope. The expanding ejecta cools from outside in and eventually the temperature of the outermost layer of the ejected envelope has cooled sufficiently for the hydrogen to recombine. Neutral hydrogen is transparent so outside this "recombination front" the emission no longer needs to scatter, unlike inside the opaque ejecta underneath the front. Thus the front is also the photosphere of the SN. As the emission is physically created at the outer layer of the ejecta, type IIP SNe rise faster than for instance SNe Ia for which the emission from ^{56}Ni decay has to scatter through the surrounding ejecta. After being formed, the recombination front then moves inwards with the cooling temperature while the envelope further expands. The two motion roughly balance each other out and the front stays at approximately constant radius. As the temperature and radius stay the same so must the luminosity as well, and thus the plateau of the type IIP light curve is created. Once the recombination front has gone through the whole envelope, the luminosity suddenly drops. The vast reservoir of energy deposited in the hydrogen envelope by the shock has been depleted and afterwards the dominant power source of emission is ^{56}Co decay chain as a result of the nominal amount of nickel synthesised in the explosion ($M_{\rm Ni} \lesssim 0.1\ M_{\odot}$; Müller et al. 2017). Example light curves of a type IIP SN are shown in Figure 1.7 with light curves of a type IIL SNe and SN1987A.

Progenitors of type IIL SNe have proven to be more elusive than those of type IIP SNe and no progenitors have been directly observed. However, it has been recently proposed that IIL SNe may in fact be similar to IIPs, but with an additional power source (see e.g. Arcavi et al. 2017b). The evidence supporting such a scenario are related to differences between IIP and IIL light curves. As discussed earlier IIL SNe do not exhibit a plateau in their light curves and instead decline linearly from the peak. However, their light curves show a sudden drop at similar epochs as the plateaus of IIP SNe end (Anderson et al. 2014; Valenti et al. 2015). Furthermore, they are also brighter than type IIP SNe (Patat et al. 1994; Li et al. 2011b; Anderson et al. 2014). Both of these features could be explained with an additional power source that declines in time and thus would mostly affect during the early light curve evolution. The source could for instance be interaction

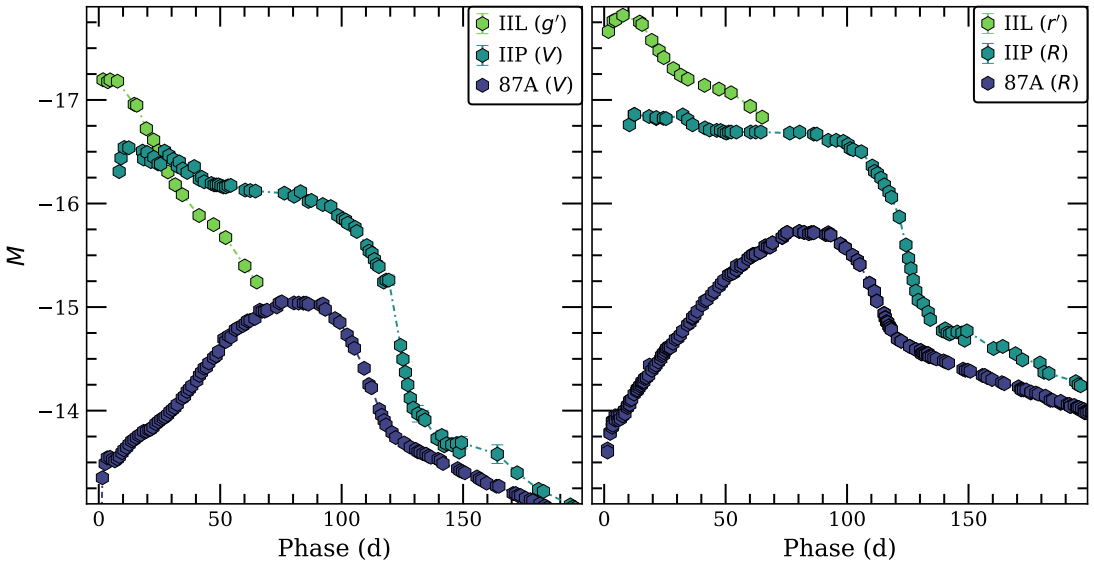

FIGURE 1.7: Example g'/V and r'/R light curves of type II SNe shown since the first detection. The light curves are collected from the Open Supernova Catalog (Guillochon et al. 2016) and first presented in the following papers: type IIL SN2008fq (Taddia et al. 2013), type IIP SN2017eaw (Tsvetkov et al. 2018), SN1987A (Menzies et al. 1987; Catchpole et al. 1987, 1988; Whitelock et al. 1988; Suntzeff et al. 1988)

with massive circumstellar material (CSM) or energy injected by a magnetar formed in the aftermath of the SN (Arcavi 2017), but for now the origin of IIL SNe and their relation to IIPs remain a subject of debate.

On the other hand, the emission mechanisms of type IIb and IIn SNe are well understood. The progenitor a of type IIb SN is assumed to be Yellow Super Giant (YSG) that has lost some or most of its hydrogen envelope due to stripping by a binary companion. Few such progenitors have been seen and in the case of SN1993J a remaining companion super giant was identified a decade after the explosion (Van Dyk et al. 2002; Maund et al. 2004). Without a thick hydrogen envelope a type IIb cannot produce a light curve plateau seen in IIP SNe and its light curve is powered by ^{56}Ni decay chain similarly to type Ia SNe (see Equation 1.1). In some IIb SNe it is also possible to observe a short precursory bump before the main peak credited to a rapid shock-cooling of the remaining extended low-mass ($R \sim 500\ R_\odot$, $M \sim 0.2\ M_\odot$) envelope surrounding the star (e.g. SN1993J; Nomoto et al. 1993; Podsiadlowski et al. 1993; Woosley et al. 1994).

A progenitor of one type IIn SN has been detected and identified as a Luminous Blue Variable (LBV) star (SN2005gl; Gal-Yam et al. 2007). LBVs are evolved massive ($\gtrsim$ 40 $M_\odot$) and due to their consequent high luminosity, they are known to experience strong outbursts during their evolution (see e.g. Maeder & Conti 1994, for review). The most famous example of a LBV is the galactic η Carinae that is enshrouded in nebula of its own making. The nebula is hydrogen rich (e.g. Davidson et al. 1986) and

thus and explosion occurring inside it would create narrow hydrogen emission lines due to interaction between ejecta and the CSM (e.g. Chevalier & Fransson 1994; Chugai & Danziger 1994; Fransson et al. 2002). Under such scenario, the light curve is powered by an external process of CSM interaction outside the photosphere of the SN. Therefore, the light curve shape is solely dictated by the amount and the structure of the CSM surrounding the progenitor star, explaining the photometric diversity of SNe IIn (see e.g. Taddia et al. 2013). For an excellent overview of interacting SNe refer to Smith (2017)

In this context, it is very ironic that the most local type II SN to date is SN1987A. It was definitely a peculiar SN as its progenitor was identified to be a BSG rather than any of the progenitors discussed above. In fact 87A-like SNe are now known to be the most uncommon type of SNe II discovered as Smartt et al. (2009) estimated that only 3% of all CCSNe explode in a similar fashion. In 87A-like SNe a significant portion of the explosion energy goes into expanding the compact progenitor star adiabatically rather than heating and ionising the hydrogen in the envelope. Therefore, the light curve is powered namely by ^{56}Ni decay chain rather than hydrogen recombination. The luminosity increases slowly as the emission has to diffuse through the ejecta and the light curve turns to decline only when more radiative energy escape than is created in ^{56}Ni and ^{56}Co decays (see Figure 1.7). After the peak the light curves follow the ^{56}Co decay similarly to type IIP SNe. An excellent overview of SN1987A and the emission mechanism is given in Arnett et al. (1989).

1.2.2.2 Hydrogen-Poor Core-Collapse Supernovae

Hydrogen-Poor CCSNe consists of two classes, Ib and Ic SNe and their subtypes, with the characteristic feature being complete absence of any hydrogen features in the spectra (see Figure 1.2). Their progenitors are known to be massive stars since the serendipitous discovery of an X-ray flash at the beginning of type Ib SN2008D light curve (Soderberg et al. 2008). Such a feature has long been theorised to occur when the shock wave, triggered by the collapsing core, finally reaches the outer layers of the doomed progenitor star causing a powerful ultraviolet (UV) and X-ray flash lasting only for few minutes to few hours (Colgate 1974; Klein & Chevalier 1978). However, while the discovery verifies that the progenitor of SN2008D was a massive star, it does not explain how the star lost its thick hydrogen envelope.

Under historical terms, two scenarios have been suggested to answer this question. In the first proposed scenario the progenitor is a massive lone Wolf-Rayet star (WR; Begelman & Sarazin 1986; Gaskell et al. 1986). The stars of this class are evolved and are known to shed most or all of their hydrogen envelopes during their evolution. The second

scenario, on the other hand, relies on binary interaction and consequent stripping of the progenitor star either via Roche-Lobe Overflow (RLOF) or common envelop evolution (see e.g. Podsiadlowski et al. 1992; Nomoto et al. 1995, and reference therein). While it is still debated which of these scenarios is the dominant process, the binary scenario has accumulated more direct observational evidence with the recent discovery of a Ib SN iPTF13bvn. The progenitor star of this SN is visible in the pre-explosion images and its photometry was tentatively found to be compatible with a WR star of $M \sim 11\ M_{\odot}$ at the time of explosion (Cao et al. 2013). However, hydrodynamical modelling showed that the quickly evolving light curve could only be explained by a progenitor with $M \sim 3.5\ M_{\odot}$ and ejecta mass of $M_{\rm ej} \sim 1.9\ M_{\odot}$ (Bersten et al. 2014; Fremling et al. 2014) inconsistent with the prediction of the single star scenario of $M_{\rm ej} \sim 8\ M_{\odot}$ (Groh et al. 2013). Thus, the binary model was invoked to explain iPTF13bvn (Bersten et al. 2014; Fremling et al. 2014).

While the progenitors of a type Ic SNe have been elusive so far it is possible to discuss their likely properties by comparing the SNe of types Ib and Ic with each other. It is commonly assumed that these SNe are physically very similar as strongly supported by both spectroscopic (see Figure 1.2) and photometric similarities (see e.g. Lyman et al. 2016). In fact, apart from minor differences (i.e. presence/absence of He features in spectra) the bulk properties of the two subtypes are effectively indistinguishable from each other. Therefore, it is reasonable to further assume that the progenitors of the two types are similar to each other, different only in the level of stripping they have experienced. Type Ic SNe come from massive stars that have shed also their helium envelopes and not only their hydrogen ones. Under the unifying assumption, the transitional type IIb SNe are also assumed to have a similar origin, but now with less stripping so that the progenitor star retains some of its hydrogen. The type IIb, Ib and Ic SNe are thus commonly known as stripped envelope SNe (SESNe).

In the absence of a thick hydrogen envelope, the light curves of SESNe are powered by the ^{56}Ni decay chain as is the case for type Ia SNe. However, the amount of synthesised ^{56}Ni is typically significantly smaller than for Ias ($\overline{M}_{\rm Ni} \lesssim 0.2\ M_{\odot}$; Lyman et al. 2016; Prentice et al. 2016) and thus the light curves are normally fainter ($-15 \gtrsim M \gtrsim -19$ Richardson et al. 2014). However, type Ic-BL SNe, also assumed to be SESNe, are found to be more energetic and their peak luminosities often rival or exceed those of Ia SNe (see e.g. Cano 2013; Taddia et al. 2015; Lyman et al. 2016; Prentice et al. 2016; Taddia et al. 2018, 2019). Example SESNe light curves of types IIb, Ib, Ic and Ic-BL are presented in Figure 1.6, with light curves of a type I SNe and a CaST.

Type Ibn SNe are one of the rarest types out of all H-poor CCSNe with only $\lesssim 30$ transients discovered (Pastorello et al. 2016; Hosseinzadeh et al. 2017), but despite the

small number there is already a good understanding on what their progenitors are. The narrow He emission lines must be created in shock interaction with a He-rich CSM surrounding the progenitor similarly to narrow H lines seen in type IIn SNe. Furthermore, the CSM has to be H-poor in at least the most cases, as while some discovered type Ibn SNe exhibit also narrow H lines (Pastorello et al. 2008), it is not a feature of the of the whole population. Therefore, the progenitors SNe Ibn have been assumed to be massive CO WR stars embedded in thick He envelope since the discovery of the prototype SN2006jc (Foley et al. 2007; Pastorello et al. 2007). The scenario is further supported by a coincidental giant stellar outburst that was detected at the location of the SN two year prior to the explosion (Foley et al. 2007; Pastorello et al. 2007).

1.2.3 Superluminous Supernovae

Since their discovery the SLSNe have been raising confusion on what kind of power source can produce such bright and long lasting light curves. While the topic has been studied for more than a decade, the nature of SLSNe remains as a topic of debate. In this Section, I will give a brief overview on the current understanding of SLSNe. For further reading, excellent reviews on the topic are presented in Howell (2017) and Gal-Yam (2019).

The nature of the progenitor stars of SLSNe-I is reasonably well constrained, even if no progenitors have been discovered. The light curves of SLSNe-I appear to be similar to the bulk population of type Ic SNe, but with increased brightness and duration (Nicholl et al. 2015a). Similarly, the spectra of SLSNe-I taken a few weeks after the peak brightness resemble the peak spectra of SNe Ic (e.g. Pastorello et al. 2010; Nicholl et al. 2015a). Thus it is reasonable to assume that SLSNe-I originate from massive, stripped stars. The hypothesis is further supported by the host galaxy properties: SLSNe-I are found in small galaxies with high specific star formation (i.e. amount of stars formed weighted by the stellar mass of the galaxy) and thus have an overpopulation of massive stars (e.g. Neill et al. 2011).

However, even if the progenitors of SLSNe-I are assumed to be massive stars, the physical mechanism powering the emission is still poorly understood. It is universally agreed that ^{56}Ni and ^{56}Co decay, powering type Ic SNe, cannot explain the light curves of the superluminous ones (see e.g. Pastorello et al. 2010; Chomiuk et al. 2011; Quimby et al. 2011; Howell et al. 2013; Nicholl et al. 2015a, for discussion) and alternative scenarios has been sought for. The most commonly applied scenario uses energy released in rotational decay of a newly born, rapidly spinning magnetar as an internal power source. Such a scenario was first invoked for a peculiar type Ib SN2005bf (Maeda et al. 2007), but it was soon developed further and applied to SLSNe (Woosley 2010; Kasen & Bildsten 2010).

Overall, such a model describes the photometric evolution of SLSNe-I well with some exception (see e.g. Nicholl et al. 2015a; Angus et al. 2019; De Cia et al. 2018). However, the model is simplistic with only three parameters (ejecta mass $M_{\rm ej}$, initial magnetic field B and initial spin period P; Inserra et al. 2013) making it very flexible. Thus the model might be a proxy and behave as an undescribed deposit of energy inside the SN. Other central engine scenarios, such as late accretion onto a formed black hole (BH; Dexter & Kasen 2013) might be able to perform as well. Furthermore, it is also likely that the light curves are in fact powered by some kind of a hybrid scenario. For instance, even if the ^{56}Ni decay cannot alone explain the light curves, it is still expected to contribute to the total energy budget as it is known to be the dominant power source in some other stellar explosion. For now, in the lack of direct observational evidence supporting the popular magnetar scenario, the power source remains unknown.

As there are only a few known members of SLSNe-II — e.g SN2008es (Miller et al. 2009; Gezari et al. 2009), CSS121015 (Benetti et al. 2014), SN2013hx and PS15br (Inserra et al. 2018b) — constraining their progenitor and explosion mechanisms is difficult. However, their photometric and spectroscopic evolution appears to be similar type IIL SNe apart from the fact that the SLSNe are brighter and evolve slower. The situation is comparable to the differences between the samples SLSNe-I and type Ic SNe, indirectly implying that the progenitors of SLSNe-II are also massive starts but now with hydrogen envelopes. While, Inserra et al. (2018b) suggested that SLSNe-II could be powered with a magnetar spin-down or some other central engine model, the source of energy is still poorly understood.

The nature of the second class of hydrogen-rich of SLSNe, SLSNe-IIn, is better understood. Due to their spectral similarity with the normal type IIn SNe (see Figure 1.2), they are assumed to originate from similar progenitors. As the type IIn SNe are powered by interaction between CSM and SN ejecta their photometric properties including the peak luminosities are very diverse and many type IIn SNe have been detected up to brightnesses of $M \sim -20$ (e.g. Richardson et al. 2014) being nearly as luminous as the SLSNe with the traditional cut off at $M = -21$ (Gal-Yam 2012). As such it seems reasonable to assume that the SLSNe-IIn are more luminous cousins of the type IIn SNe.

1.3 Other Extragalactic Optical Transients

As discussed above the influx of new, peculiar SNe has sparked an interest in following the sky more widely and regularly than before. However, the marvel of extragalactic transients is not that of SNe alone and the modern untargeted, wide-field approach has unravelled other populations of transient events not related to explosions of stars known

as SNe. Here, I will give a brief overview to some of the most common such transients, and discuss how they are characterised.

1.3.1 Tidal Disruption Events

Supermassive black holes (SMBH) in the cores of galaxies are capable of producing very bright transient events by swallowing wandering stars. Theoretically such events were predicated already in 1970s (see e.g. Hills 1975; Frank & Rees 1976; Lidskii & Ozernoi 1979; Rees 1988) and in the last decade they have finally been discovered with few tens of candidate objects (see Komossa 2015, for review). In the process, the star's path takes it too close to the SMBH and it gets tidally disrupted when the enormous tidal forces exceed the self-gravity of the star. Significant portion of the disrupted star accretes on the SMBH, creating bright flare known as a Tidal Disruption Event (TDE).

While there is no classification scheme to distinguish TDEs, some observable features are characteristic for them and can thus help in the identification. Since TDEs occur around SMBHs, they are always found in a nuclear region of a galaxy. Furthermore, their spectra are typically prominent with broad hydrogen and/or helium emission lines (depending on the composition of the disrupted star) that are symmetric unlike the ones seen in SNe (Gezari et al. 2012; Arcavi et al. 2014). While it is possible to use these lines to identify a TDE early on, the lines do not always appear before the time of the peak brightness. For example, for ASASSN-18pg the lines were visible in the first spectrum taken ~ 2 weeks after the first detection, 26 days before the peak (Holoien et al. 2020), but for PS18kh they only appeared around the peak brightness roughly a month after the first detection (Holoien et al. 2019).

The final characteristic feature of TDEs is related to their light curve evolution. TDEs are known to be slow evolving with rise times of about a month following the increase of the mass-accretion rate. The rise is typically followed by a slow decline with a theoretical decline rate of $t^{-5/3}$ (Rees 1988; Phinney 1989). Based on these features it is possible to identify a TDE.

1.3.2 Supernova Impostors

SN impostors are non-terminal eruptions of massive LBV stars that can reach peak luminosities similar to CCSNe (Van Dyk et al. 2000; Maund et al. 2006). In fact they are often misclassified as type IIn SNe as, due to the similar progenitors, the exhibit very similar spectra with narrow hydrogen emission lines. The key difference to distinguish an impostor from a SN is that its progenitor start should remain intact after the outburst.

However, determining if the star actually survived might not be an easy task to perform as can be demonstrated with the example of SN2009ip.

The "SN" exhibited a faint impostor outburst in 2009 and was given a SN designation. Soon after it was discovered that the transient was in fact caused by an outburst of a massive ($M \sim 50{-}60\ M_{\odot}$) star rather than a real SN (Smith et al. 2010; Foley et al. 2011). However, in 2012 the star became again violently active first reaching a peak brightness $M \approx -15.5$ before further brightening up to $M \approx -18$ three weeks later (see e.g. Fraser et al. 2013; Mauerhan et al. 2013; Pastorello et al. 2013). The transient has since been studied extensively, but it is still debated if it actually exploded as a SN in 2012, or if this was just another outburst of the LBV star. Therefore, securely distinguishing an impostor from a SN might be nearly impossible task in case of some transient events. A brief review summarising characteristics of SN impostors and SN2009ip can be found in Pastorello & Fraser (2019).

1.3.3 Luminous Red Novae

Another class of odd transients reaching luminosities of faint CCSNe ($-13 \gtrsim M \gtrsim -15$) is the Luminous Red Novae (LRNe; see e.g. Mauerhan et al. 2015; Kankare et al. 2015; Smith et al. 2016b; Blagorodnova et al. 2017). Their photometric and spectroscopic properties are very inhomogeneous and claiming a secure classification is at times difficult. However, Pastorello et al. (2019) collected a sample of LRNe and found certain similarities in their observables — characteristic for the population of events. While, the light curves of LRNe are heterogeneous and do not look alike, they typically show double-peaked shape. Furthermore, the first peak appears to be bluer and shorter while the second is redder and lasts a longer time. The spectra of the LRNe evolve during the evolution as well. In the beginning of the light curve, narrow P Cygni hydrogen emission lines are superposed on a blue continuum, while during the second peak the hydrogen lines have nearly faded away and narrow metal absorption lines emerge instead.

To explain the diverse observable properties, LRNe have been suggested to be caused by outbursts occurring during stellar mergers (Smith et al. 2016b; Mauerhan et al. 2018) and the merger scenario is strongly supported by studies done on galactic Red Novae (RNe). RNe are thought to be effectively the same, but scaled down versions of LRNe due to photometric and spectroscopic similarities (see Pastorello et al. 2019, for comparison and discussion). In the case of one RN, V1309 Scorpii, a stellar merger was unequivocally proven as the physical scenario. Its progenitor system was observed to show oscillations of brightness with decreasing period until an outburst, caused by the merger, occurred and the oscillation ceased to exists (Tylenda et al. 2011). However, while the merger

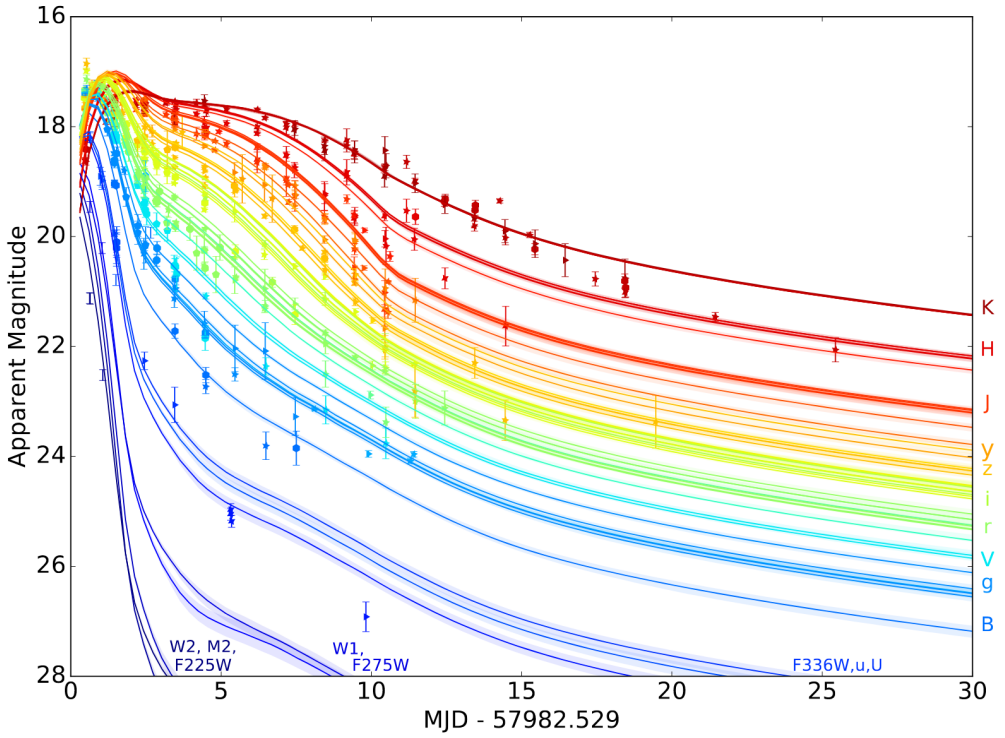

FIGURE 1.8: Multi-band UV, optical and NIR light curves of the KN AT2017gfo. The figure has been taken from Villar et al. (2017) and the has been collected from Andreoni et al. (2017); Arcavi et al. (2017b); Coulter et al. (2017); Cowperthwaite et al. (2017); Díaz et al. (2017); Drout et al. (2017); Evans et al. (2017); Hu et al. (2017); Kasliwal et al. (2017); Lipunov et al. (2017); Pian et al. (2017); Pozanenko et al. (2018); Shappee et al. (2017); Smartt et al. (2017); Tanvir et al. (2017); Troja et al. (2017); Tanaka et al. (2017); Valenti et al. (2017)

scenario is thus supported for LRNe as well, a scenario invoking an outburst in a lone, massive star has not been ruled out conclusively (Pastorello et al. 2019).

1.3.4 Kilonovae

Kilonovae (KNe) are transient events occurring as a result of double NS or NS-BH binary merger (Metzger et al. 2010). Even though the KNe were first introduced under theoretical terms in 1998 by Li & Paczyński, in the last few years the study of KNe has focused on one particular NS binary merger discovered as an electromagnetic counterpart of a Gravitational Wave (GW) signal, GW170817, detected by Laser Interferometer Gravitational-Wave Observatory (LIGO; Abbott et al. 2017). The KN in question is SSS17a (see e.g. Coulter et al. 2017; Drout et al. 2017; Kilpatrick et al. 2017) also known as AT2017gfo (see e.g. Alexander et al. 2017; Blanchard et al. 2017; Chornock et al. 2017; Cowperthwaite et al. 2017; Fong et al. 2017; Margutti et al. 2017; Nicholl et al. 2017; Smartt et al. 2017; Soares-Santos et al. 2017; Valenti et al. 2017). The event was not detected during a standard survey monitoring like virtually all transients discussed

above, but as a triggered follow-up of many collaborations hoping to catch the fleeting light of something extraordinary in the localisation contours of the LIGO detection and coincident gamma-ray detections from the Fermi gamma-ray space telescope and the International Gamma-Ray Astrophysics Laboratory (INTEGRAL). Details on the efforts to discover the transient and the resulting multi-messenger follow-up campaign performed on AT2017gfo can be found in (LIGO Scientific Collaboration et al. 2017).

Multi-band UV, optical and near-infrared (NIR) light curves of AT2017gfo has been presented in Figure 1.8. The KN was very quickly evolving and its optical light curve was already declining at the epoch of discovery ~ 0.5 d after the merger and continued to decline until the transient had faded out of view in ~ 10 d later (Drout et al. 2017; Soares-Santos et al. 2017; Valenti et al. 2017). AT2017gfo was in fact one of the fastest extragalactic transient ever detected in optical as it declined $\sim 4-6$ mag in less than a week. Its spectra was well described by blackbody emission for the first few days, but later on it started to show some complex features different from anything observed before. The spectra shows for instance evidence of strontium (Watson et al. 2019) created via rapid neutron-capture process (r-process; Pian et al. 2017).

In the r-process, heavy seed nuclei are bombarded by a large quantity of free neutrons. In such conditions, they capture the neutrons faster than the resulting nuclei decay, leading to an increasing neutron number. These heavy, neutron-rich nuclei will then eventually decay into products that cannot be produced via any other process. The created nuclei are very common and it has been estimated since late 1950s that approximately half of the elements heavier than iron in the Universe must be synthesised via the r-process (Burbidge et al. 1957; Cameron 1957). Thus there must be some common astrophysical site that produces a high neutron flux, but what that site actually is has been debated for decades. Among other scenarios, binary NS mergers were suggested to be a possible source for the heavy nuclei Symbalisty & Schramm (1982); Freiburghaus et al. (1999), but before the discovery of the KN AT2017gfo no direct evidence on where the r-process occurs had been seen (see e.g. Cowan et al. 2019, for review).

1.4 Rapidly Evolving Transients

Now that the all classes of extragalactic optical transients discussed in this thesis are introduced, it is time to turn the attention towards the main topic: the rapidly evolving transients (RETs) also known under the names fast evolving, luminous transients (FELTs; Rest et al. 2018) and fast-rising blue optical transients (FBOTs; Margutti et al. 2019) in the literature. These transients are not spectroscopically classified as a uniform type of events like the classical SNe, but they are rather described by peculiar photometric

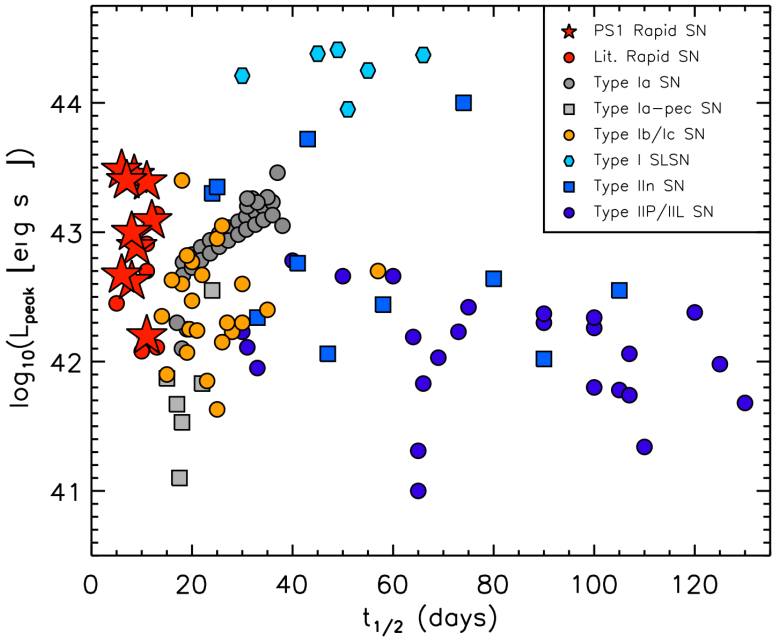

FIGURE 1.9: Peak bolometric luminosity against the time above half-maximum brightness of PS1-MDS RETs and literature transients. The figure has been taken from Drout et al. (2014) and the data collected from Matheson et al. (2000); Nugent et al. (2002); Hamuy (2003); Campana et al. (2006); Taubenberger et al. (2006, 2008); Valenti et al. (2008); Botticella et al. (2009); Cobb et al. (2010); Kasliwal et al. (2010); Ofek et al. (2010); Perets et al. (2010); Poznanski et al. (2010); Andrews et al. (2011); Chomiuk et al. (2011); Drout et al. (2011); Quimby et al. (2011); Arcavi et al. (2012); Bersten et al. (2012); Kasliwal et al. (2012); Kiewe et al. (2012); Scalzo et al. (2012); Valenti et al. (2012); Drout et al. (2013); Foley et al. (2013); Lunnan et al. (2013); Margutti et al. (2014)

properties. The RETs are characterised by rapid photometric evolution with rise times of $t_{\rm rise} \lesssim 10$ d and nearly as fast decline timescales making them faster than is expected of the standard SNe populations.

The fast evolution of RETs has actually been the reason why their characterisation has been difficult in the past. SN surveys are often designed to discover and follow type Ia SNe for cosmology, for which high cadence of a few days is not necessarily required. Therefore, it has been possible to detected rapid events but it has difficult to characterise them early enough for follow-up observations. As a result the number of discovered RETs remained small as only individual events were discovered including peculiar SNe such as type Ibn SN 1999cq (Matheson et al. 2000), type Ib SN2002bj (Poznanski et al. 2010), type Ic SN2005ek (Drout et al. 2013) and type IIn PTF09uj (Ofek et al. 2010).

However, within the last decade the landscape of fast transients has started to change with the increasing number of discoveries from deep, high cadence surveys. The first dedicated search for events with fast light curve evolution was performed by Drout et al. (2014) in the archival data set of Pan-STARRS1 Medium Deep Survey (PS1-MDS) and it

resulted in s discovery of 14 transients, 10 of which had a spectroscopic redshift. The discovered RETs clearly occurred on faster timescales than literature SNe as demonstrated by the spread of the time above half-maximum brightness $t_{1/2}$ presented in Figure 1.9 (Figure 7. in Drout et al. 2014). While the RETs have similar peak luminosities with type Ia SNe, their timescales of $t_{1/2} < 12$ d are clearly faster than what any SN types exhibit.

The PS1-MDS sample also provided the first direct evidence that these fast events are actually fairly common. While the discovered sample of 14 events was not particularly large, their volumetric rate was estimated to be 4800 – 8000 yr^{-1} Gpc^{-3}. The value corresponds to 4% – 7% of the CCSN rate estimated by Botticella et al. (2008) and to 19% – 31% of the SESNe rate estimated by Li et al. (2011b). While the presented values are uncertain they do clearly demonstrate that the RETs are indeed very common.

Since the discovery of the PS1-MDS sample searching for these undescribed events has become one of the focuses of transient astrophysics and in the years to follow several new, exciting RETs were discovered. This includes events such as KSN2015K with a superb high-cadence Kepler light curve (Rest et al. 2018), extremely rapidly declining SN2018kzr (McBrien et al. 2019) and a equally fast SN2019bkc classified as a CaST (Prentice et al. 2020). The key properties of the most noteworthy literature RETs are summarised in Table 1.2, with the reported classifications.

Based on the variety of different spectroscopic classifications the fast transients appear to be very heterogeneous class of events that are only similar in apparent photometric properties. Several different scenarios have been considered to explain the peculiarities of individual events including the explosion of a stripped massive star (e.g. Drout et al. 2013; Tauris et al. 2013; Kleiser & Kasen 2014; Kleiser et al. 2018), shock breakout either in CSM (Ofek et al. 2010; Rest et al. 2018; Ho et al. 2019a) or an extended low-mass stellar envelope (Drout et al. 2014), accretion-induced collapse of a WD or a WD–NS merger (McBrien et al. 2019), CSM interaction (Arcavi et al. 2016) and magnetar spin-down (Arcavi et al. 2016). While some models have been disfavoured by the data (e.g. magnetar spin-down; Arcavi et al. 2016), a number of models could still viably explain the observed properties of individual RETs. Furthermore, given the diversity of the seen properties it is actually very likely that not all events can be explained with the same scenario and it is entirely possible that several progenitor channels can produce fast evolving light curves.

The best observed transient listed in Table 1.2 is likely AT2018cow at $z = 0.014$. Even if it is not the brightest or the fastest RET in the list, it might very well be the most extraordinary one. Its discovery in the Asteroid Terrestrial-impact Last Alert System (ATLAS; Tonry et al. 2018) o band image resulted in a multi-wavelength follow-up

TABLE 1.2: List of example RETs from the literature. Only events for which redshift dependant quantities could be measured are listed.

Event	**Type**	**No.**	$M_{R/r}$ (mag)	t_{rise} (d)	$t_{1/2}$ [a] (d)	Δm_{15} [b] (mag)	**Ref.**
Samples of RETs							
PS1-MDS[c]	-	10	-17 – -20	$\lesssim 7$	$\lesssim 12.0$	0.5 – 2.1	[1]
HSC SSP[d]	-	5	-17 – -20	$\lesssim 10$	$\lesssim 18.5$	-	[2]
Individual RETs							
SN1999cq	Ibn	-	-19.6	~ 4	-	~ 2	[3]
SN2002bj	Ib	-	$\sim$ -18.5	< 7	-	~ 2	[4]
SNLS04D4ec	-	-	$\sim$ -20.0	< 10	-	~ 1	[5]
SN2005ek	Ic	-	-17.3	$\lesssim 9$	-	2.9	[6]
PTF09uj	IIn	-	$\sim$ -19.0	~ 6	-	~ 2	[7]
SN2010X	-	-	-17.0	-	-	~ 2.5	[8]
LSQ13ddu	SESN	-	-19.7	4.8	-	2.2	[9]
KSN2015K	-	-	$\sim$ -19.0	2.2	6.8	-	[10]
SN2015U	Ibn	-	$\sim$ -19.5	$\lesssim 10$	~ 12	~ 2	[11,12,13]
iPTF15ul	Ibn	-	-20.5	~ 4	-	$\gtrsim 2.5$[e]	[14]
iPTF16asu	Ic-BL	-	$\sim$ -20.0	4.0	-	~ 1	[15]
HSC17dbpf	-	-	$\sim$ -21.0	$\lesssim 5$	-	-	[16]
AT2018cow	-	-	-19.9	~ 2.5	~ 4.5	~ 3	[17,18]
SN2018gep	Ic-BL	-	$\sim$ -19.5	3.0	-	~ 1	[19]
SN2018kzr	-	-	$\sim$ -18.0	< 3	-	~ 5	[20]
ZTF18abvkwla	Ic-BL	-	$\sim$ -21.0	1.8	-	$\gtrsim 1.5$[e]	[21]
SN2019bkc	CaST	-	-17.3	5 – 6	-	~ 5	[22,23]

[a] Time above half-maximum brightness.
[b] Number of magnitudes decline in first 15 days post-peak.
[c] Pan-STARRS1 Medium Deep Survey (PS1-MDS).
[d] Hyper Suprime-Cam Subaru Strategic Program (HSC SSP) transient survey.
[e] Transient not observed for 15 d post-peak.
References: [1] Drout et al. (2014), [2] Tampo et al. (2020), [3] Matheson et al. (2000), [4] Poznanski et al. (2010), [5] Arcavi et al. (2016), [6] Drout et al. (2013), [7] Ofek et al. (2010), [8] Kasliwal et al. (2010), [9] Clark et al. (2020), [10] Rest et al. (2018), [11] Tsvetkov et al. (2015), [12] Pastorello et al. (2015), [13] Shivvers et al. (2016), [14] Hosseinzadeh et al. (2017), [15] Whitesides et al. (2017), [16] Moriya et al. (2019), [17] Prentice et al. (2018), [18] Perley et al. (2019), [19] Ho et al. (2019a), [20] McBrien et al. (2019), [21] Ho et al. (2020), [22] Chen et al. (2020), [23] Prentice et al. (2020)

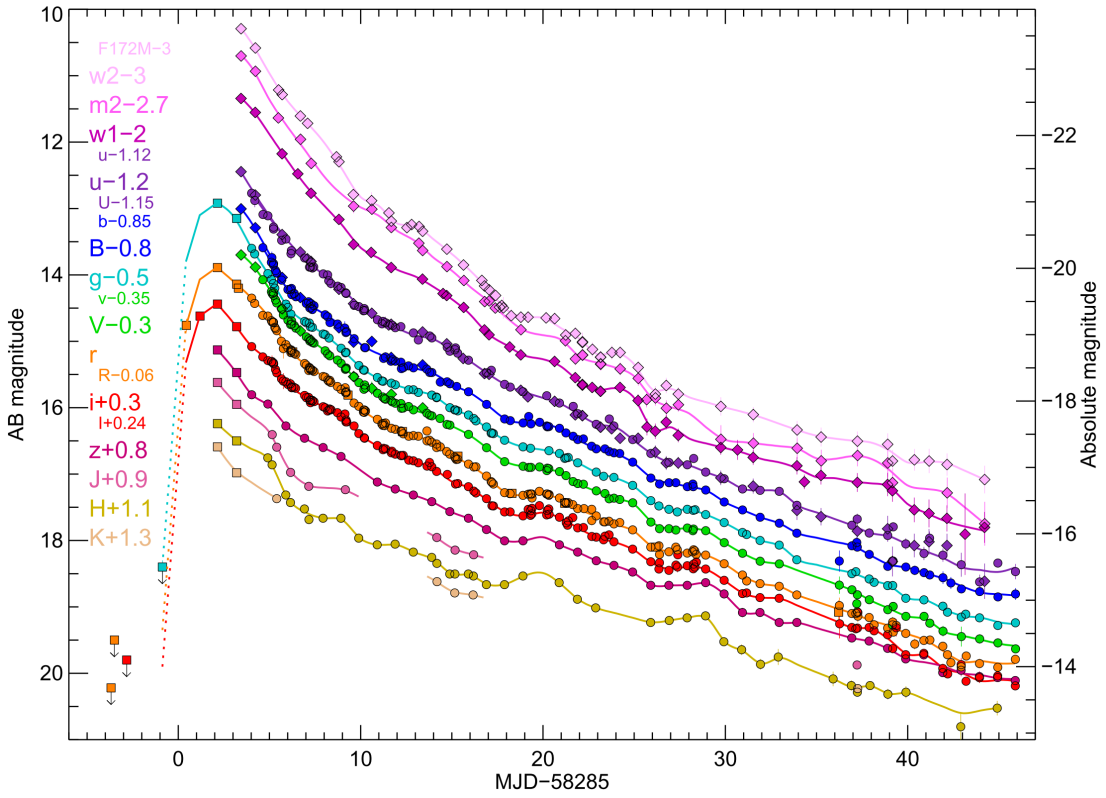

FIGURE 1.10: NIR, optical and UV light curves of AT2018cow. The Figure has been taken from Perley et al. (2019).

campaign spanning from radio and millimetre waves (Margutti et al. 2019; Ho et al. 2019b; Huang et al. 2019) to NIR, optical and UV observations (Prentice et al. 2018; Margutti et al. 2019; Perley et al. 2019) ans all the way to X-ray emission as well (Ho et al. 2019b; Margutti et al. 2019; Kuin et al. 2019).

As can be seen in Figure 1.10, the light curve of AT2018cow rose to peak brightness of $M \sim -20$ in ~ 2.5 d in optical and was already declining at the time follow-up observation were triggered (Prentice et al. 2018; Perley et al. 2019). The large data set clearly indicated that AT2018cow was unique in comparison to any known literature transient. As a result, many physical scenarios have been suggested in literature, including a TDE of a main sequence star (Perley et al. 2019) or of a WD (Kuin et al. 2019) by an intermediate mass BH, electron capture collapse of merged WDs (Lyutikov & Toonen 2019), common envelope jets SN (Soker et al. 2019), magnetar (Mohan et al. 2020) and a wind-driven transient (Uno & Maeda 2020), but a common consensus has not yet been met on what the powering mechanism was.

The strongest constraint for the physical model comes from the multi-wavelength data of AT2018cow and two additional transients that have been reported to show similar observable properties. ZTF18abvkwla exhibited similar radio and optical light curves as AT2018cow (Ho et al. 2020) and CSS161010 demonstrated further similarity in X-ray

properties as well (Coppejans et al. 2020). The radio and X-ray data imply the presence of a high-velocity outflows in all three of the transients with $v \sim 0.1c$ for AT2018cow (Margutti et al. 2019), $v \gtrsim 0.5c$ for ZTF18abvkwla (Ho et al. 2020) and $v \gtrsim 0.55c$ for CSS161010 (Coppejans et al. 2020). In order to explain the extreme outflows along with the peculiar observable properties, a central engine (i.e a NS or a BH) scenario has been proposed (Margutti et al. 2019; Ho et al. 2020; Coppejans et al. 2020). Under such a scenario, an internal "engine" would provide a transient with large reservoir of energy after an initial explosion. For example, such an engine could be an newly-born accreting BH inside a SN ejecta, formed by a core-collapse of a massive star, but other engine-driven scenarios have not been ruled out.

1.5 Thesis outline

In this thesis, I use the excellent data set of the Dark Energy Survey Supernova Programme to discover and analyse peculiar optical transients. THe majority of the thesis focuses on different aspects of the enigmatic rapidly evolving transients, from designing a search to discover them in the archival data to discussion of the potential physical mechanisms behind them. Furthermore, I also discuss the properties of two peculiar double-peaked transients, one of which was discovered during a live selection of RETs. An outline of this work is as follows.

In Chapter 2, I introduce the Dark Energy Survey and its dedicated SN programme. I describe how DES-SN discovers SNe and other transient phenomena in its observation and how machine learning is applied to determine whether they are real or artifact sources, but I will also introduce the follow-up resources of DES-SN. Furthermore, I also describe the properties of a library of interpolate DES-SN light curves used later in this thesis to search for RETs.

In Chapter 3, I describe how the two searches to discover RETs in DES-SN data were created, what the assumptions and the selection criteria were and how well they performed on a set of sample transients and on the full DES-SN data set. I also give an overview of the discovered sample 106 RETs, including the redshift and absolute magnitude distributions.

In Chapter 4, I discuss the observable characteristics of the sample RETs. This includes analysis of both photometric and spectroscopic data in comparison to other extragalactic transients.

In Chapter 5, I turn the focus on the host galaxies of the RETs. Their spectroscopic and photometric properties analysed, in order to determine what galaxy types seem the

host the enigmatic RETs. Furthermore, the implications of the host properties on the progenitors of RETs are also discussed.

In Chapter 6, I provide discussion on physical interpretation of the RETs based on the analysis done in the previous chapters. I also provide direct comparison of individual RETs to best observed rapid events in the literature.

In Chapter 7, I introduce two additional peculiar transient one of which was discovered during the search for RETs. Their highly atypical double-peaked light curve evolution is nearly identical to each other, but no similar transients has been reported before. In the chapter I describe how the transients were discovered and provide their main observable characteristics. I also discuss their host galaxy properties and describe how the transients differ from reported literature events.

In Chapter 8, I provide a summary of my work and discuss its implications for the future studies of RETs and other peculiar transients.

Chapter 2

The Dark Energy Survey

The discovery of accelerating Universe made based on cosmological type Ia SNe (Riess et al. 1998; Perlmutter et al. 1999) has revolutionised the study of cosmology in the last few decades. The accelerating expansion can only be explained with a previously unknown cosmological component — appropriately named as "dark energy" for its elusive essence — that must have dominated the expansion of the Universe for the last few billion years. Despite its importance the nature of the component is not understood and one of the key problems in modern physics is to understand its properties and origin.

Luckily, the dark energy can be investigated as it leaves signs of its presence in cosmological observations typically divided into two "flavours". First, the dark energy affects the geometry of the Universe by expanding it with an evolving rate — an effect which can be directly measured by using cosmological standard candles (i.e. type Ia SNe) or rulers. The other visible effect is embedded in the largest structures of the Universe — galaxy clusters, filaments and voids. The growth of such structures is suppressed as the gravity has less time to pull matter towards the over-dense regions. Such feature can be addressed by observing the distribution of the large scale structure. However, quantifying the effect of the dark energy is not an easy task. The analysis requires the usage of several cosmological probes investigating both of the two flavours to constrain its influence on the Universe. A survey that observes a large fractions of the sky with a high precision, to both discover SNe and map the cosmic structure, is needed.

The story of the Dark Energy Survey (DES) starts in July 2004 when the DES collaboration was founded in response to a call from the National Optical Astronomy Observatory (NOAO) to design a new astronomical instrument to be mounted on the 4-meter Victor M. Blanco telescope at Cerro Tololo Inter-American Observatory (CTIO) near La Serena, Chile. In exchange the winning collaboration would be awarded up to 30% of the

observing time on the telescope during the first five years after the completion of the instrument. The DES collaboration entered the competition with a design for an advanced wide-field camera with a goal to carry out a survey to investigate the nature of the ambiguous dark energy. The review panel found the scientific plan exciting and awarded the DES collaboration 525 nights in exchange for the Dark Energy Camera (DECam). The five year survey operated from August to February each year starting in Autumn 2013 and has thus already ceased observing operations. Following the submitted plan, the survey time was split between a wide field survey of ~ 5000 deg^2 and a dedicated SN programme (DES-SN) of 10 SN fields of 2.7 deg^2 each — the size of single DECam pointing.

Because the observations have only recently finished, the significant majority of the key cosmological analysis of DES is still underway and the final cosmological results are expected within next few years. However, the DES collaboration has already published several proof-of-concept papers based on analysis on fractions of the final data-set (see e.g. DES Collaboration et al. 2019b, and reference therein). Furthermore, while the cosmological insight is the key interest of the survey, several DES papers have also been written on the secondary science goals including the transient astrophysics. For example, Angus et al. (2019) published 21 SLSNe-1 and 1 SLSN-II discovered by DES-SN providing the largest homogeneously-selected sample of SLSNe at high redshifts to date. The work presented in this thesis focuses on peculiar transients I discovered in the DES-SN data.

In this Chapter I will discuss the Dark Energy Survey operations including the Dark Energy Camera and both the wide-field survey and the SN programme. I will give an overview of the data processing and of the procedure to discover transients in the data stream. Furthermore, I will describe the key features of the most important follow-up facilities DES-SN has used during its operations. The data from these facilities is crucial for the analysis presented later in this thesis.

2.1 The Dark Energy Camera

DECam was designed and built by the DES collaboration to meet the requirements of a state-of-the-art cosmological survey with needs for both wide-field imaging and accurate photometry of faint sources. The camera has a wide field of view of 3 deg^2 (2.2 deg in diameter) covered by 62 4096×2048 px charge-coupled devices (CCDs or "chips") for imaging and further 12 2048×2048 px CCDs used for guiding and focus purposes. Thus, the actual imaging area of single pointing is 2.7 deg^2 corresponding to approximately 15 times the size of full moon. The CCDs also have a high resolution with a pixel scale of 15×15 μm corresponding to a plate scale of $0.263''$/px. As the DES target

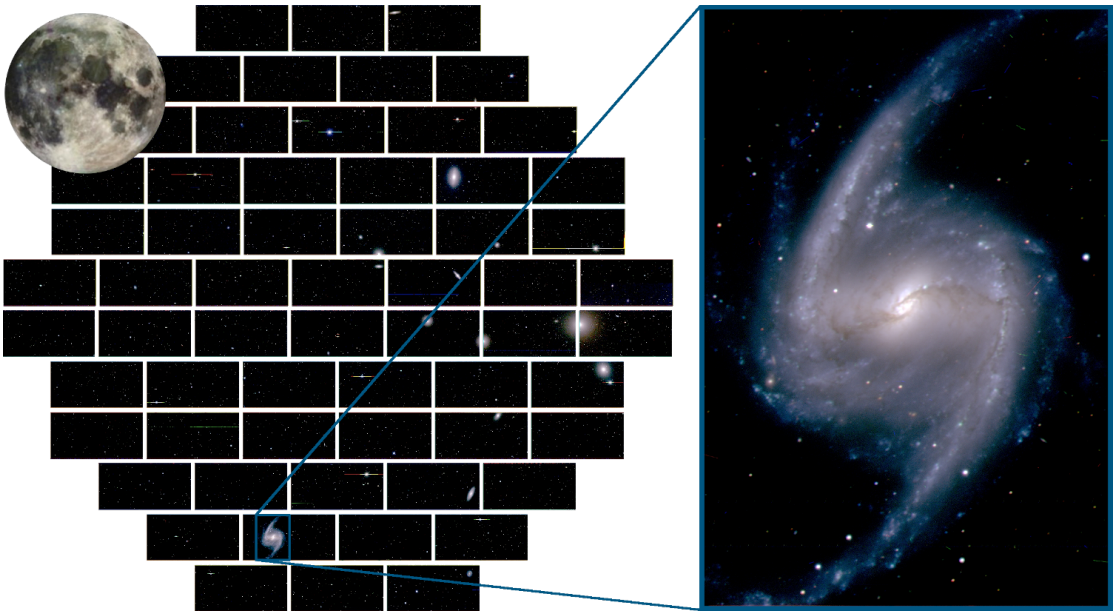

FIGURE 2.1: Multi-colour DECam image of the Fornax Cluster. The image is composed of several "first light" images taken on 12th of September 2012. In addition a zoom-in on the spiral galaxy NGC 1365 visible in one of the chips is presented. The full moon is shown in scale and would it fit $\sim$ 15 times in the DECam field of view. The figure has been adapted from Flaugher et al. (2015).

sources are at cosmological distances (i.e. high redshift), the emission is heavily shifted towards the redder wavelengths. Therefore, all 74 CCDs of the instrument are especially red-sensitive using a CCD design developed by Lawrence Berkeley National Laboratory (LBNL; Holland et al. 2003, 2007).

DECam obtained its official first light on the night of September 12, 2012 by targeting the Fornax cluster. The multi-colour composition of images taken on that night is shown in Figure 2.1, with a zoom-in on the spiral galaxy NGC 1365 visible in one of the chips. The figure also demonstrated the hexagonal CCD layout of the instrument, with the characteristic gaps between the CCDs. While the instrument has a wide field of view, as demonstrated with the full moon, it also reaches amazing precision in each individual chip. While the figure shows all 62 science chips, 2.5 of these are no longer operational (Morganson et al. 2018).

In its original design DECam was only equipped with optical *griz* filters similar to those used by the Sloan Digital Sky Survey (SDSS; York et al. 2000). However, after the design was finalised DES decided to add Y filter in infrared (IR) to identify high redshift quasars in the wide-field survey. These five filters form the core wavelength bands DES operates with: the wide-field survey uses all five filters while the SN search utilises only the original four. The transmission functions of the DES *grizY* bands are shown in Figure 2.2. Later on CTIO has bought two additional filters, u and VR, and installed them on DECam for the usage of astronomical community, but they are not used by

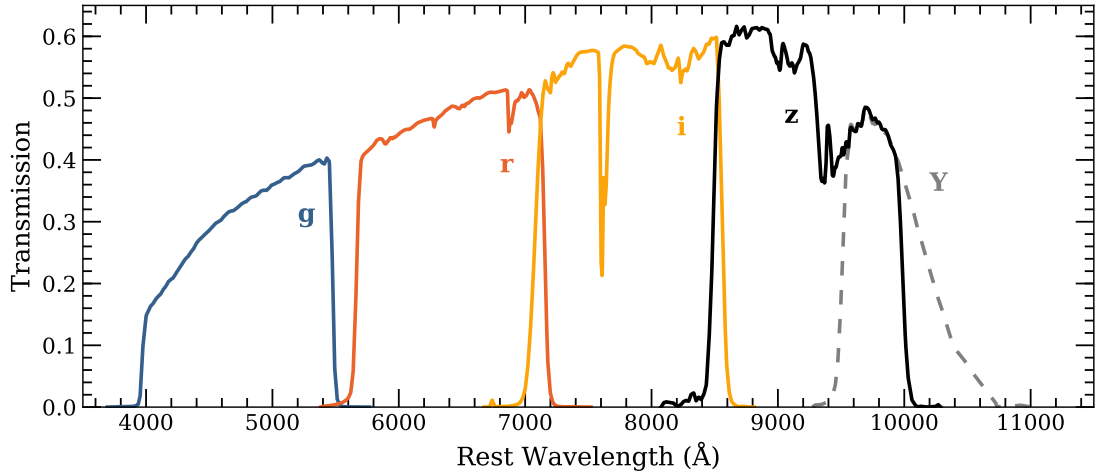

FIGURE 2.2: The transmission functions for the DES filters. DES-SN uses *griz* and *Y* band is only used in the wide-field survey.

DES. For excellent review on DECam and its technical characteristics see Flaugher et al. (2015).

2.2 The Wide-Field Survey

The DES wide-field survey covers a total of ~ 5000 deg^2 corresponding to approximately 1/8 of the sky. When the analysis of the final data set is completed, the wide field survey will have characterised 300 million galaxies and tens of thousands of galaxy clusters with the five broadband filters (*grizY*). Following the DES observing strategy, the individual DECam pointings are exposed for 90 s in *griz* and 45 s in *Y*. Consecutive exposures in the same field are offset by roughly half the focal plane on average, so that the targets are observed by different chips in each pointing. The dithering of the exposures is done in order to minimise the inhomogeneities due to chip gaps, malfunctioning chips and problematic regions close to the chip edges. The overlaying exposures are then stacked together in order to increase the total exposure time. Individual sub-pointing fragments in the wide-field survey area are not exposed as long and the number of the stacked images varies between 1 and ~ 10. This is demonstrated in Figure 2.3 where the footprint of the DES wide-field survey is shown with a heat map of the stacked *r* band exposure times. In the figure the locations of the SN fields are also shown. For an excellent overview of the DES wide-survey observations see DES Collaboration et al. (2018b), where the details of the first DES data release are given.

The DES wide-field survey is used primarily to study the nature of dark energy with three complementary probes: large-scale angular clustering of galaxies, weak gravitational lensing and galaxy cluster counts. Angular clustering of galaxies gives insight to

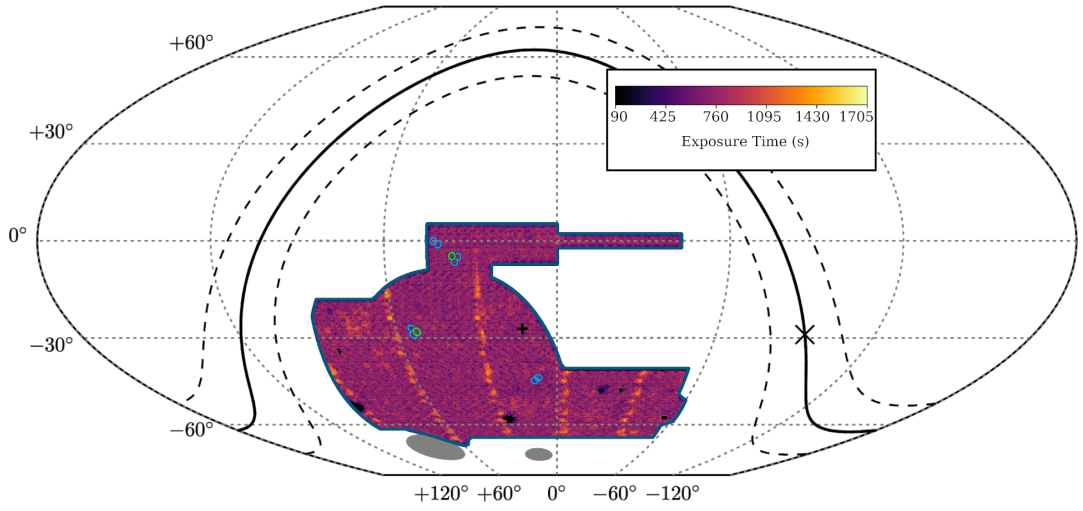

FIGURE 2.3: The footprint of Dark Energy Survey operations in celestial coordinates. The effective exposure times in r band (in seconds) are shown as a heat map for the $\sim$ 5000 deg^2 wide-field survey. The eight "shallow" SN fields are marked with blue circles and and the two "deep" fields with green circles. The figure has been adapted from Figure 2. in DES Collaboration et al. (2018b) by adding the heat map (courtesy of Adriano Pieres).

Baryon Acoustic Oscillations (BAO) that can be used as "standard rulers" in cosmology (Eisenstein 2005) and can thus directly measure the changing geometry of the Universe. BAO are fluctuations in the large scale structure distribution. They are caused by the acoustic waves in the primordial photon-baryon plasma at the epoch of recombination in the early Universe. At that epoch the hydrogen — created in the aftermath of the Big Bang — recombined in significant numbers due to the cooling temperature of the Universe, "freezing" the density waves in the plasma in place. The perturbation has since expanded with the evolution of the Universe and it can be used to measure cosmic lengths at different epochs. For details on how the BAO analysis is done see DES Collaboration et al. (2019a), where the results based on the first year of DES are given.

The weak gravitational lensing and the number of galaxy clusters, on the other hand, provide evidence of the suppressed growth in the large scale structure. With weak lensing DES looks at subtle changes in the shapes of background galaxies due to gravitational lensing caused by foreground matter. By measuring such distortions the distribution of the foreground matter can be inferred. In this case the foreground matter consists mostly of "dark matter", the mysterious matter component that interacts with the visible Universe only via gravitation. Jointly with the dark matter distribution DES also searches for galaxies in clusters at different redshift and thus DES is mapping the distribution of all matter on the large scale. Galaxy clusters are large potential wells occupying huge volumes in space and thus their spacial distribution and evolution in time are affected by how the Universe was evolving at different epochs. While DES does not have

TABLE 2.1: Locations of the DES-SN fields. The associated legacy fields are also given.

Legacy Field	**DES Field**	**R.A. (J2000)**	**Dec.**
CDFS	C1	03h 37m 05.83s	-27:06:41.8
	C2	03h 37m 05.83s	-29:05:18.2
	C3	03h 30m 35.62s	-28:06:00.0
ELAIS-S1	E1	00h 31m 29.86s	-43:00:34.6
	E2	00h 38m 00.00s	-43:59:52.8
SDSS Stripe 82	S1	02h 51m 16.80s	00:00:00.0
	S2	02h 44m 46.66s	-00:59:18.2
XMM-LSS	X1	02h 17m 54.17s	-04:55:46.2
	X2	02h 22m 39.48s	-06:24:43.6
	X3	02h 25m 48.00s	-04:36:00.0

spectroscopic facilities to measure the exact redshifts to large numbers of galaxies, the photometric redshifts inferred from the *grizY* data provide a good approximation that can be used for cosmological parameters. Testing the predictions from different cosmological models against the distribution of the known matter can then give very stringent constraints for the cosmology. The details how the the joint weak lensing and galaxy cluster analysis is done in DES are shown in DES Collaboration et al. (2018a).

2.3 The Supernova Programme

The Dark Energy Survey Supernova Programme is the largest SN survey for type Ia SN cosmology to date. It has recently finished the cosmological analysis on 207 spectroscopically classified type Ia SNe from the first three years of the survey and work on the final five year sample of a few thousand photometrically classified SNe (i.e. based on fits to *griz* light curve evolution) is currently underway (see DES Collaboration et al. 2019b, and references therein). The final sample will be the largest compilation of type Ia SNe used in a cosmological analysis, with the second largest being the Pantheon sample of $\sim$ 1000 SNe compiled from various smaller samples (Scolnic et al. 2018). In the following I will give a brief overview to DES-SN observations. For more in depth discussion of the observing strategy see D'Andrea et al. (2018).

TABLE 2.2: Exposure times of the DES-SN single epoch observations in *griz* bands (Adapted from Table 2. in D'Andrea et al. 2018).

Filter	Central λ (Å)	Shallow Fields			Deep Fields		
		t_{exp} [a]	N_{exp} [b]	Depth [c]	t_{exp} [a]	N_{exp} [b]	Depth [c]
g	4830	175	1	23.7	600	3	24.6
r	6430	150	1	23.6	1200	3	24.8
i	7830	200	1	23.5	1800	5	24.7
z	9180	400	2	23.3	3630	11	24.4

[a] Total combined exposure of one epoch in seconds.
[b] Number of exposures per epoch.
[c] Median limiting single-epoch magnitude over the first three DES observing seasons as defined in (Kessler et al. 2015).

2.3.1 The Supernova Fields

Prior to the start of DES, Bernstein et al. (2012) simulated outcomes of various different SNe survey strategies to find the optimised strategy for the needs of type Ia cosmology. They discovered that a 10-field hybrid plan with 2 deep fields and 8 shallow fields with *griz* photometry serves the goal the best. The field location were then selected by giving special attention to coincident legacy survey data and to overlap with the deep NIR Visible and Infrared Survey Telescope for Astronomy (VISTA) Deep Extragalactic Observations (VIDEO; Jarvis et al. 2013) survey and the mid-infrared (MIR) Spitzer Wide-area Infrared Extragalactic (SWIRE; Lonsdale et al. 2003) survey regions. The amount of Milky Way extinction was also considered an important factor. The selected fields are located in four groupings on the sky, with each of them containing two shallow fields and two of them a single deep field (see Figure 2.3). The fields are given prefixes based on the coincident legacy field — "C" fields are clustered around the Chandra Deep Field South (CDFS), "E" fields partially overlap with European Large-Area Infrared Space Observatory S1 (ELAIS-S1) survey, "S" fields are found in the SDSS Stripe 82 footprint and "X" fields in the X-ray Multi-Mirror Mission Newton (XMM-Newton) Large-Scale Structure (XMM-LSS) legacy field. The coordinates of each 10 SN fields are given in Table 2.1. Note that suffixes 1 and 2 refer to shallow fields and 3 to deep fields.

2.3.2 DES-SN Observations and Observing Strategy

The exposure times of a single epoch observations of DES-SN fields (over all *griz* bands) were split so that the 8 shallow fields were exposed in total as long as a single deep field. While this does make the shallow fields significantly shallower than the deep ones, they still reach limiting magnitude of ~ 23.5 in all bands (D'Andrea et al. 2018). The exposure times of single *griz* epochs are shown in Table 2.2. Note that some of the longer

FIGURE 2.4: Multi-colour image of chip 37 in the shallow DES-SN field X1 (left) and multi-colour image of chip 44 in the deep DES-SN field X3 (right). The images have been composed using the five year DES-SN deep-stack images of *gri* bands (Wiseman et al. 2020b).

exposures are split into a number of shorter ones and coadded together. Throughout this thesis I will refer to a set of such observations taken in one field and one band during one night as a filter-epoch. The difference between the shallow and deep fields is further demonstrated in Figure 2.4, where multi-colour single chip images in X1 and X3 fields are shown. In the deep field X3 significantly more distant (i.e. faint and red) sources are visible as a consequence of the longer exposure time. In Table 2.2, I also provide the median depths in each band over the first three years of DES. The single exposure depths were measured by inserting "fake" type Ia SNe — simulated with `SNANA` program (Kessler et al. 2009) — into the images and finding the magnitude when less than half of the inserted SNe were recovered in the image processing pipeline described in Section 2.4.1.

Instead of a human decisions, DES used an algorithmic scheduler `ObsTac` (Neilsen & Annis 2014) to decide what observation sequence would be observed next. The decision was always made based on the current conditions at the telescope, how complete the wide-field survey was and on the duration, $\Delta t_{\rm seq}$, since each accepted SN sequence was last taken. Here "sequence" refers to a set of observations that once started have to be finished, regardless of possibly worsened conditions. In case of the shallow fields, *griz* bands consist a total of one observing sequence, while in the deep fields each band was its own sequence. A SN sequence was triggered when $\Delta t_{\rm seq} \geq 4$ d and the seeing in zenith was $\geq 1.1''$ in i band or alternatively when $\Delta t_{\rm seq} \geq 7$ d. The SN fields were observed during high seeing by design as the better observing conditions were required by the weak lensing studies under the wide-field survey. In case several SN fields met the criteria, the field with highest $\Delta t_{\rm seq}$ was given the priority. Additionally, further criteria were imposed based on the conditions on the SN fields themselves. First, the seeing measured in the fields had to be $\leq 1.3''$ (deep) or $\leq 1.8''$ (shallow). Furthermore, the estimated sky brightness (in mag/arcsec^2 above dark sky) was also limited to be ≤ 3 for gr and ≤ 2 for iz bands, but if $\Delta t_{\rm seq} \geq 7$ d for a shallow field the constraint was relaxed to 5 for g, 4 for r and 3 to iz. Finally, `ObsTac` also required the airmass of a sequence to be < 1.5 at the start of an observation sequence.

A DES-SN sequence was considered accepted if it passed a number of quality criteria. An image had to have a measured point spread function (PSF) width (measured as full width at half maximum or "FWHM") at zenith $\leq 2''$, estimated by correcting the seeing in the exposure for airmass and wavelength. Additionally, the quality was also estimated with constant 20th mag fake sources that were injected into the search exposures similarly to the SNe Ia fakes mentioned earlier. The average signal to noise ratio of such a fake had to be ≥ 20 in the shallow fields or ≥ 80 in deep fields. In case at least a single exposure in an observing sequence failed to meet the criteria, the $\Delta t_{\rm seq}$ of the sequence did not reset and the sequence was observed with high priority during the following nights. This was done even if the other exposures in the sequence were good quality and were accepted for analysis.

As a consequence of the DES scheduling, the DES-SN fields were observed with a roughly weekly cadence for the duration of the DES observing operations with the significant majority (91%) of consecutive, accepted filter-epochs taken 4 – 14 d apart from each other (D'Andrea et al. 2018). The dates of every accepted observations in *griz* bands for all 10 fields over the first three years of DES are shown in Figure 2.5, demonstrating the spread of observations. In the figure the different observing seasons, or "years", Year 1, Year 2 and Year 3 are denoted as Y1, Y2, Y3 and the abbreviation will be used throughout this thesis. The figure perfectly demonstrated that in the shallow fields all four *griz* bands were observed during the same night, apart from the few incidences

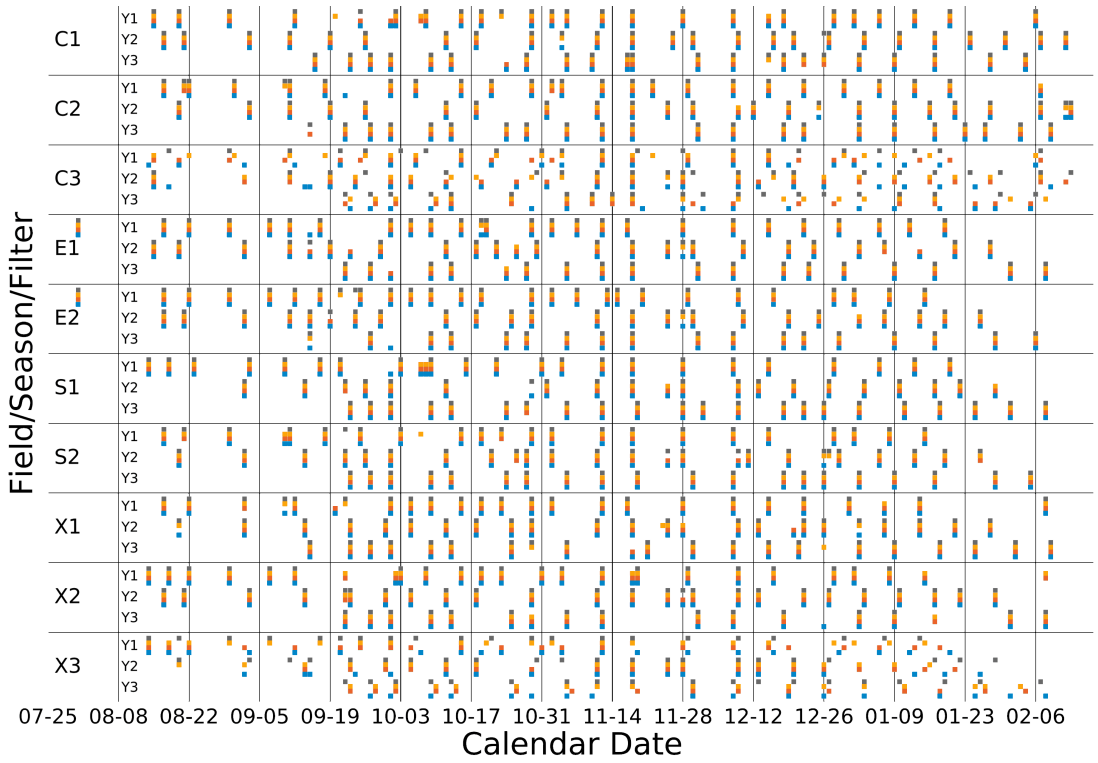

FIGURE 2.5: All accepted *griz* observation during the first three years of DES-SN denoted with blue, red, yellow and grey, respectively. The different observing seasons are denoted as Y1, Y2 and Y3. The figure has been adapted from Figure 2. in D'Andrea et al. (2018).

where at least one band failed resulting in repetition of the sequence. However, in the deep fields the bands are often observed on different nights due to their significantly longer exposure times. The different observing strategy between the fields has an impact on some of the science results discussed later in this thesis.

The DES-SN observations were mostly taken in good conditions during dark time. However, CTIO also scheduled some grey and bright time for DES in order to provide the community access to DECam during various astronomical conditions. The impact on the DES-SN observations is small but it can be clearly seen in Figure 2.6, where the limiting depth histograms of DES-SN filter-epochs in Y1 – Y3 are shown. While the limiting depths mostly cluster around the median values in both shallow and deep fields, the distributions extend to much shallower depths due to observations done in poorer conditions. Furthermore, the bluer the band in question is, the more strongly it is affected by observing across various levels of sky brightness. Thus the histograms of the bluer bands are more strongly broadened.

While most of the discussion on the DES-SN observing strategy presented here is done based on the first three observing seasons, the discussion is representative of the whole survey. The DES observing strategy stayed the same during years four and five and no

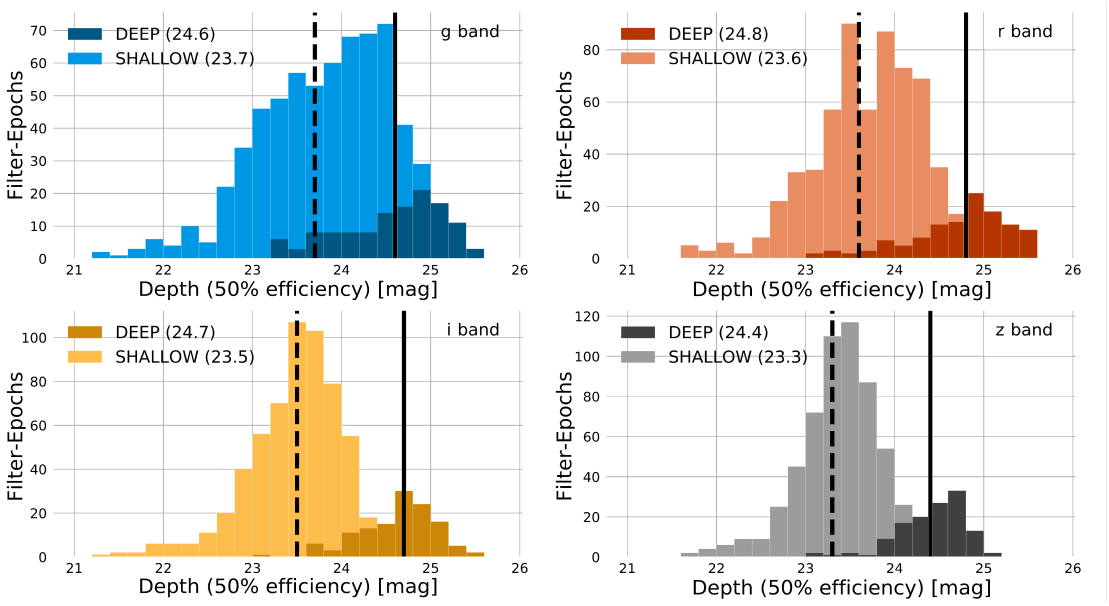

FIGURE 2.6: Depth histograms of DES-SN filter-epochs over the first three observing seasons (adapted from Figure 5. in D'Andrea et al. 2018). Median depths in shallow and deep fields are shown dashed and solid lines.

significant changes to the range of observations occurred. Thus the first three years give a representative view of the full 5-year DES supernova programme as well.

2.4 Data Processing of DES-SN observations

After each DES exposure is taken the resulting images are sent to NOAO for archiving and to the National Center for Supercomputing Applications (NCSA) at the University of Illinois at Urbana-Champaign for processing within a few minutes. At NCSA, the DES data management team (DESDM) performs all the needed standard procedures prior to scientific analysis, including correction for instrument crosstalk, bias subtraction, masking known bad pixels, correction for nonlinear pixel response and flat fielding. Furthermore, saturated stars and their associated "bleed trails" (charge overflow in the CCD) are masked, as are the cosmic rays and satellites visible in the images. These pre-processing steps are virtually the same for both the wide-field survey and the SN fields. For a full technical overview of the DES data processing see Morganson et al. (2018). Once the corrections are performed, the DES-SN images are passed forward to the difference imaging pipeline to search for new transient phenomena in the SN fields. All DES-SN data processing steps discussed below are performed by the DES-SN team and the steps were formalised before I joined the DES collaboration.

2.4.1 Difference Imaging

New transient events were discovered in the DES-SN images with the difference imaging pipeline `DiffImg` (Kessler et al. 2015) that uses several public `TERAPIX`/`AstrOmatic`[1] codes (Bertin et al. 2002). The detection of transients requires a precise subtraction of a template image from the coadded search exposures. The used templates are of superior quality compared to the single search images as they are formed by coadding on average 8.4 filter-epochs taken under good condition during the past DES observing seasons (Morganson et al. 2018). Years three, four and five use templates based on Y2 and Y2 based on Y1. Y1, however, used originally templates based on data observed during the preliminary Science Verification (SV; Bonnett et al. 2016; Rykoff et al. 2016) prior to the start of DES observations, before being reprocessed using the Y2 templates (Morganson et al. 2018).

For the subtractions to be successful, each template and search image has to be well calibrated. For this purpose, DES observed three distinct standard star fields at different airmasses on nightly basis. The fields are mostly in SDSS Stripe 82 or at Dec. $\approx -45°$ (see Appendix A in Drlica-Wagner et al. 2018). The observation were taken first during the evening twilight and then repeated during the morning one as well (Tucker et al. 2007). The stars in these fields have had their magnitudes converted into a "natural" system used by DES, where the corresponding colour terms are close to zero. These stars — known as the "secondary standard stars" — were used to determine the nightly zero points, atmospheric extinction coefficients and the colour terms, needed to convert the DECam exposures into the DES natural system. Further "tertiary standard stars" within each SN field were then used to perform the photometric calibration of the DES-SN exposures. The tertiary stars were observed in photometric conditions during the SV period and their magnitudes and colours are thus measured better than the nightly standards. Under good observing conditions there are 100 – 200 such stars in each of the 62 chips in the SN fields (Morganson et al. 2018). The tertiary stars were also used calibrate the template images. The calibrations of the DES-SN exposures have been measured to be excellent as both relative and absolute calibrations have been confirmed to be correct at 2% level in the `DiffImg` pipeline (Kessler et al. 2015).

In the `DiffImg` pipeline each individual chip of each SN field was processed independently. First, the `SCAMP` program (Bertin 2006) was used to find a joint astrometric solution for the template and science image pair. The stars used to find the solution were from the Fourth US Naval Observatory CCD Astrograph Catalog (UCAC-4; Zacharias et al. 2013) for Y1, but from Y2 onward more accurate B catalog from the United States Naval Observatory (USNO-B; Monet et al. 2003) was used. Once the solution was found, two

[1] `www.astromatic.net`

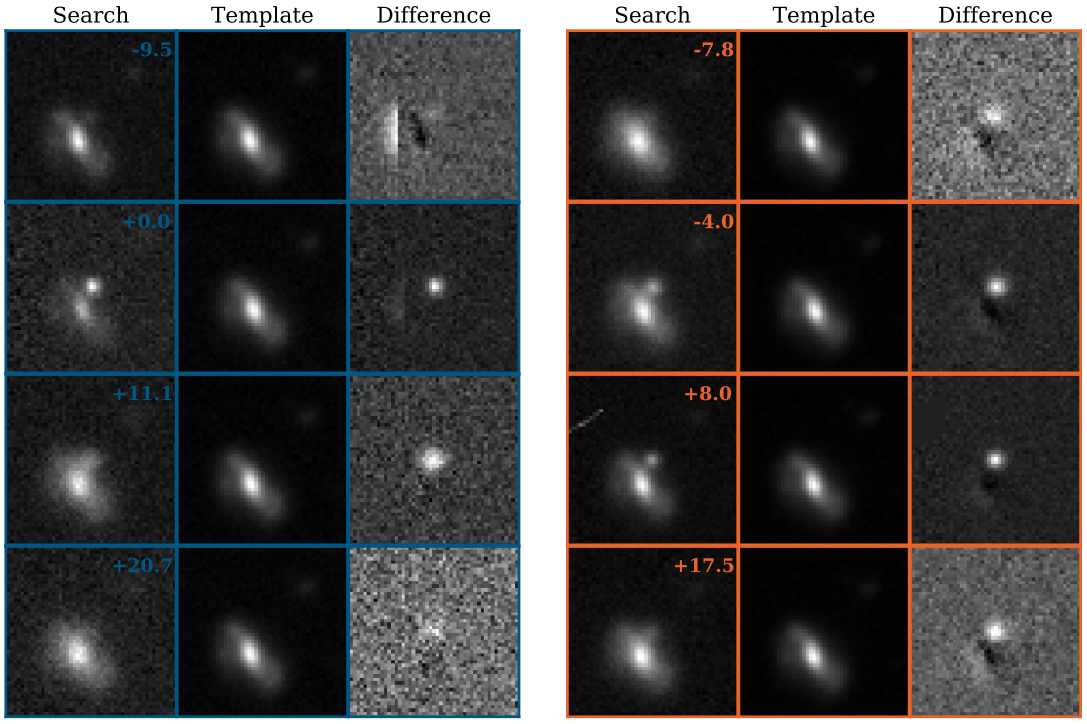

FIGURE 2.7: Example results of the `DiffImg` pipeline. Search, template and difference images are shown for DES16X3ega in both g (left) and r (right) bands for four selected epochs each. Shown stamps are 51×51 px in size corresponding to $\sim 14''$ at a side and the transient source is in the middle of each search and difference image.

types of fake sources were injected into the search exposures for data quality evaluation purposes. The first type was the constant, randomly placed 20th mag sources used to determine if an exposure reached the required signal-to-noise (see Section 2.3.2) and the second type was the type Ia SNe light curves simulated with `SNANA` used to estimate the depth of an exposure. The SNe were distributed within the redshift range 0.0 – 1.4 and they were placed around random galaxies with an exact location chosen by using a probability that was proportional to the surface brightness density of the selected galaxy. Approximately 20 fake SNe were found on each chip per epoch, but given that the light curves were evolving in time, only 1/3 were bright enough to be detected (Kessler et al. 2015). The flux of the inserted fakes was determined by using the tertiary standard stars measured in each SN field and the spread of the point-like fakes over the surrounding pixels was estimated with `PSFEx` program (Bertin 2011) to match the observing conditions.

Applying the found astrometric solution, the `SWARP` software (Bertin et al. 2002) was used to match the template to the search exposures and the alignment was achieved on a roughly 0.1 px level (Morganson et al. 2018). At this stage, `SWARP` was also used to coadd the search exposures for all multi-exposure observations (*griz* in deep fields and z in shallow fields) thus creating the final search images for these filter-epochs.

The astrometrically aligned images were then aligned photometrically using `HOTPANTS` (Becker 2015) modified to improve its performance (see Kessler et al. 2015, for details). `HOTPANTS` divided the template and science images into 10×20 px "stamps". In each pair of one template and one science stamp it searched for the optimal kernel to convolve the PSFs of a point source visible in both stamps. Once the optimised solution was found for each stamp, the template image could be convolved to match the science one under both astrometrical and photometrical terms. As a final product `HOTPANTS` provided the difference image, created by subtracting the aligned template from the search image. The candidate transient events were then discovered in the difference image with `SExtractor` software (Bertin & Arnouts 1996). Example search, template and difference images for DES16X3ega in four *gr* epochs are presented 2.7.

While in an ideal situation only the newly emerged transients would be detected with `SExtractor`, in reality various kinds of contamination passed the pipeline as well. Thus, the candidate sources had to fulfil certain criteria before they were accepted as "detections". The most important ones were the following: the object had to be brighter than 30th mag; it had a signal-to-noise ratio greater than 3.5; and its PSF was consistent with a point source. Other cuts were related to confirming that the subtraction was successful and that the transient was not coincident with a known bright source. For the full details on the criteria see Kessler et al. (2015). However, even after the described cuts $\sim$ 1.6 million "objects" passed the pipeline in every DES-SN season (D'Andrea et al. 2018) — far more than was realistically produced by extragalactic transients. As the number is also too large for a human inspection, a machine learning approach was implemented in order to identify the real transients.

2.4.2 Transient identification and forced photometry

The objects that passed the `DiffImg` pipeline were inspected to verify whether they were truly real or not. Traditionally the inspection would have been performed visually, possibly implementing a human bias on the selection. To avoid this, DES-SN developed a supervised machine learning algorithm `autoScan` based on the random forest technique (Goldstein et al. 2015). The algorithm was trained on $\sim$ 900000 `DiffImg` detections, half of which were flagged as non-real subtraction "artifacts" by human scanners and the other half were detections of fake type Ia SNe (created with `SNANA`; Kessler et al. 2009) injected into a set of search images. `autoScan` takes 51×51 px stamps centred on the detections as input and gives each stamp a score from 0 to 1, with 0 corresponding to a clear non-real artifact detection and 1 high quality source detection. While several features contribute to the scores the key features were the ratio of the detection brightness against the template brightness at the detection location, brightness difference between the detection

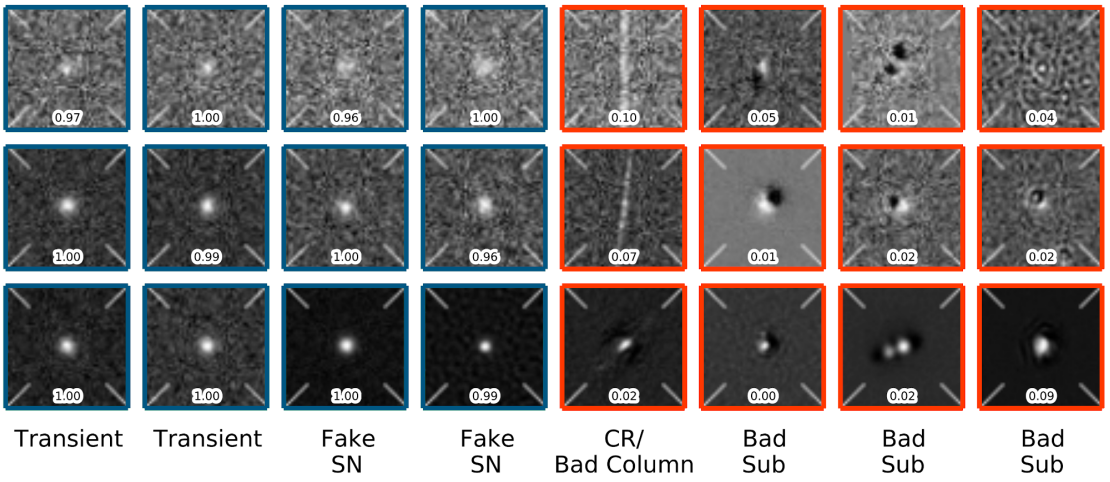

FIGURE 2.8: Difference image stamps with an `autoScan` score for legitimate detection of both real astronomical transients and injected fake SNe (left in blue boxes) and spurious artifacts (right in red boxes). Various signal to noise levels are presented on different rows: S/N $\leq$10 (top), 10 $<$ S/N $\leq$ 30 (middle) and 30 $<$ S/N $\leq$ 100 (bottom). "CR/Bad Column" refer to either a cosmic ray (middle and bottow row) missed in pre-processing or to a bad column on the chip (top). Columns with poor image subtractions, or "Bad Sub", can be a result of problematic astrometric solution, too shallow template images or poor observing conditions. The figure has been adapted from Figure 1 in Goldstein et al. (2015).

and a nearest catalog source and how point-source like the PSF was. Example stamps of both accepted and rejected candidates with the corresponding `autoScan` scores are presented in Figure 2.8. While Goldstein et al. (2015) discovered that `autoScan` score 0.5 is an optimal cutoff for the detections providing a minimal chance of a false detection, only objects with scores less than 0.3 were discarded at this stage.

In case there were two spatially coincident detections (within 1″) the event was designated a supernova identification number (SNID) if it met the following criteria. The detections had to be from different nights, but no more than 30 d apart and the `autoScan` score of both detections had to be $\geq$ 0.3. The detections could have been in the same, different or even multiple bands. In case the `autoScan` score was $\geq$ 0.5 for both detections, the transient event was given a DES-SN name, marking the year of the first detection and the DES-SN field with an alphabetical three letter suffix (e.g. DES16X3ega). A "forced photometry" light curve was produced for every candidate transient with a SNID number by finding the PSF-fitted flux at the detection location in all past search images. The transient location was determined to be the weighted mean of the detection locations and it was updated after every new detection. Thus the light curves were also re-created after every new accepted filter-epoch. An example 5-year light curve of a DES-SN transients DES16X3ega is presented in Figure 2.9. All DES-SN transient light curves presented in this thesis are either the forced photometry light curves or created based on them.

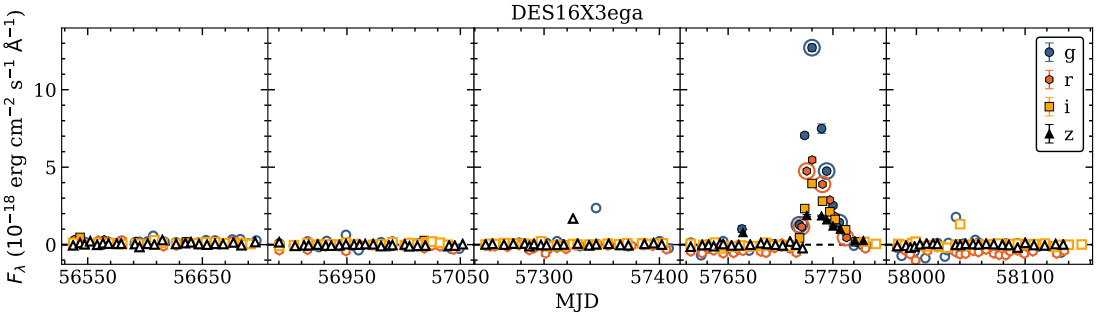

FIGURE 2.9: Example 5-year, 4-band forced photometry light curve of DES-SN transient DES16X3ega. 3σ detections are plotted with filled markers and non detections with open ones. The circled detections correspond to the `DiffImg` search and template stamps of DES16X3ega presented in Figure 2.7. Note that for clarity the errors are shown only for detections.

Following the described procedure, DES-SN gave a SNID number to $\sim$ 31600 transients, of which $\sim$ 29200 were assigned a name. The *griz* peak magnitude histograms for all named transients, as measured in the discovery season, are presented in Figure 2.10. The histograms are created based on Gaussian Process light curves presented in Section 2.6. While the majority of these transients are real (i.e. SNe, AGN etc.) a significant portion are not, as can be seen based on the number of transients for which the peak magnitudes were successfully estimated for (approximately 18000 – 25000 per band out of $\sim$ 29200). Thus DES-SN developed a "transient status" flag to evaluate the quality of the transients and "flag" possible artifact sources. The used criteria took into account four different indicators typical for an artifact: pixel correlation (detections repeated on single pixel, or on a column/row of pixels); detections in a single band over multiple bands; large time delay between the detections; and a large number of poor subtractions. The criteria were evaluated for each transient and each season separately. In case a transient passed all criteria, it was given a positive flag and if the transient passed the criteria only in a single season it was labelled as single-season transient (SST). In DES-SN there are $\sim$ 20700 SSTs with a SNID number and $\sim$ 19200 of them are named. While some non-real artifact sources still exists in the SST sample, their number has been cut down significantly. The SST sample is used later on in the thesis to discover interesting transients.

The post-processing of candidate transients includes two additional steps. Once the light curves had been created, the candidate SNe were photometrically classified using `SNANA` program `PSNID` (Sako et al. 2011). The program compares each light curve to *griz* light curve templates of the types Ia, II and Ibc SNe returning a probability, "FITPROB", that a model describes the light curve and Bayesian probability "PBAYES" of the candidate source belonging to a certain subtype. The fit results were then used to help the process of selecting viable candidates for spectroscopic follow-up. Another step of post-processing

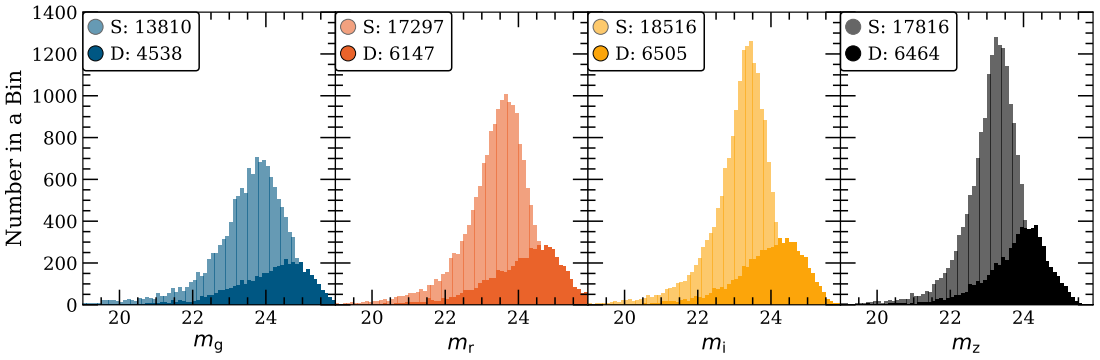

FIGURE 2.10: The *griz* peak magnitude histograms of all $\sim$ 29200 named DES-SN transients in the shallow fields (light shade) and deep fields (dark shade). Note that the histograms are created using the interpolated Gaussian Process light curves presented in Section 2.6. The peak of an individual transient was identified by selecting the highest flux with signal-to-noise ratio ≥ 3 in the discovery season. Note that in several cases no data point met the quality criteria.

the candidates was to match them with their likely host galaxies. For this purpose DES-SN used the Directional Light Radius method (DLR; Sullivan et al. 2006; Gupta et al. 2016; Sako et al. 2018). The unitless quantity $d_{\rm DLR}$, measured as the ratio of the distance between the candidate and the centre of a galaxy and the elliptical radius of the said galaxy (as measured by `SExtractor`) in the direction of the candidate, was estimated for all galaxies within 15″ of the candidate. The galaxy with smallest $d_{\rm DLR}$ was then assumed to be the host galaxy as long as the $d_{\rm DLR} < 4$. The same cutoff resulted in a high purity (97%) of finding the right host and a reasonable efficiency (80%) of finding any host for the SDSS-II SN survey sample (Sako et al. 2018). However, some host galaxies with a larger $d_{\rm DLR}$ have been selected in this thesis after visual inspection of the transient environment. Applying the DLR method increases the chances of finding the right host galaxy for small, faint hosts, but as a whole the difference is small as in the DES-SN sample in 98.8% of the cases the same host would have been found using the smallest angular separation from the candidate as the criterion (D'Andrea et al. 2018).

2.5 DES-SN Spectroscopic Follow-Up

The main goal of DES-SN was to obtain a large sample of a few thousand type Ia SNe for cosmological applications. Since the beginning of the survey, the plan has been to classify the majority of these SNe photometrically (Flaugher 2005), saving the survey from needing a tremendous amount of time and resources to spectroscopically classify distant, faint SNe live. As a result, DES-SN is by its very nature a photometric survey and as such it did not have spectroscopic capabilities to obtain complementary data for all discovered SNe. However, the spectroscopic follow-up data was still crucial as

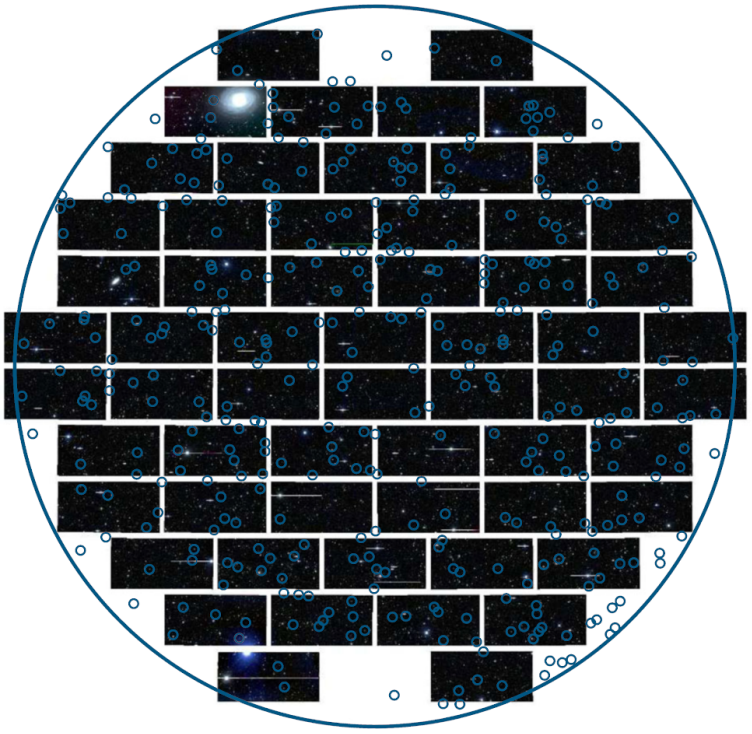

FIGURE 2.11: The field of view of 2df fibre positioner on AAT (large blue circle) over a DECam image. The two instruments are nearly identical in size and thus are 2df is a perfect spectroscopic follow-up instrument for DES-SN with its two 392 fibres. The shown small blue circles represents the fibre locations for one set of OzDES observations on AAT. The fibres are only 2″ in diameter and are too small to show against the 2.1° instrument. Figure has been adapted from Figure 1 in Yuan et al. (2015).

obtaining clear classifications for a sub-sample of SNe and spectroscopic redshifts of the host galaxies are needed to improve the cosmological analysis. Furthermore, as DES-SN was an exceptionally deep SN survey it provides a perfect facility for discovering other types of extragalactic transients, such as SLSNe, for which classification data is also needed. Thus, DES-SN had follow-up programmes on myriad telescopes and instruments around the globe for both live type Ia and live non-Ia SNe but also to obtain spectroscopic redshifts to the SN host galaxies. Here I will briefly introduce the most important spectroscopic follow-up programmes of DES-SN. For more in depth description of the obtained spectra and its importance to the survey see D'Andrea et al. (2018).

2.5.1 The Australian Dark Energy Survey OzDES

The largest individual spectroscopic programme for DES-SN is the 6-year, 100 night Australian Dark Energy Survey "OzDES" that operated with 3.9 m Anglo-Australian Telescope (AAT) in Australia. OzDES was an optimal partner for DES as the Two degree Field (2dF) robotic fibre positioner mounted on AAT (Lewis et al. 2002) has a nearly identical field-of-view per pointing as DECam as demonstrated in Figure 2.11.

With the AAOmega spectrograph (Smith et al. 2004), it can obtain up to 392 spectra per pointing with 2″ fibres providing DES-SN a large amount of spectroscopic data. The primary motives of the survey were to provide DES-SN with spectroscopic redshifts to the host galaxies of type Ia SNe, as well as to monitor AGN to measure their BH masses via reverberation mapping and to investigate if it is possible to use them as distance indicators at high redshifts. Detailed descriptions of the OzDES operations and the data quality can be found in Yuan et al. (2015), Childress et al. (2017) and Lidman et al. (2020).

During the first five years of the survey, OzDES was operational for 88 nights from August/September to December/January thus overlapping with DES-SN observations. During these season OzDES gave the highest priority to observations of live transients discovered by DES-SN. In Y1 and Y2 all transients with $m_{\rm r} \leq 22.5$ were added to the observing queue. In Y3 the criteria was extended to include all transients with $m_{\rm i} \leq 22.5$ regardless of r band brightness and all rising transients that were brighter than 23 mag in r or i band and rose at least 0.3 mag between detections. However, while the transients had a high priority only a fraction of the OzDES fibre time was used on them due to the relatively small number of bright candidates. Instead $\gtrsim 50\%$ of the OzDES time each year was used to observe AGN for the reverberation mapping study (King et al. 2015; Hoormann et al. 2019) and to obtain the spectroscopic redshifts to the host galaxies of previously discovered transients. All galaxies that were brighter than $m_{\rm r} \leq 24$ (within the 2″ aperture of a 2dF fibre) and were associated with a DES-SN transient that had a peak with signal-to-noise > 5 in at least two bands during a DES season were targeted. Host galaxy spectra were continuously stacked after each hour-long exposure; if a secure redshift was obtained, the host was removed from the queue and the fibre was reallocated to a new host. Objects without a secure redshift were continuously observed until a measurement was made, leading to some objects acquiring a total exposure times on the order of days. The final sixth year of OzDES was 12 nights in total and it was mostly used to observe SN hosts and AGN, due to the lack of live targets. Applications for further observation time are ongoing in the attempt to to secure as-yet unredshifted hosts. The OzDES survey had also a number of low priority target classes mainly related to host galaxies of SNe from other surveys or to certain specific types of galaxies or galaxy clusters. For details see Lidman et al. (2020).

The follow-up facilities of DES-SN with the number of transients targeted and the number spectra taken are listed in Table 2.3 highlighting the importance of OzDES observations. During the 6-year survey OzDES observed 2164 spectra of 1211 DES-SN transients with the AAT making it clearly the most important transients follow-up programme for DES-SN. Furthermore, OzDES also obtained redshifts to almost 38700 galaxies — including

TABLE 2.3: Spectroscopic follow-up programs for DES-SN.

Telescope	**Instrument**	**λ (Å)**	**Seasons**	**Transients[a]**	**Spectra[b]**
AAT	2dF/AAOmega	3800–8800	Y1–Y5	1211	2164
Magellan	LDSS-3	4250–10000	Y2–Y5	198	205
	IMACS	3900–10000			
VLT	X-Shooter	3000–24800	Y2–Y5	189	200
Gemini	GMOS	5200–9900	Y1,Y3–Y5	122	125
SALT	RSS	3850–8200	Y1–Y5	71	88
Keck	DEIMOS	4550–9600	Y1–Y3, Y5	42	47
	LRIS	3400–10250			
MMT	BCS	3300–8500	Y2–Y4	42	45
GTC	OSIRIS	4800–9200	Y1–Y5	36	37

[a] Number of transient sources targeted by the telescope.
[b] Number of spectra acquired for said transients.

$\sim$ 7000 SN hosts — in addition to compiling an extensive list of redshifts of galaxies found in literature (see Childress et al. 2017, for details).

2.5.2 Live Transient Programmes

DES-SN had three spectroscopic follow-up programmes for type Ia SNe in order to improve the cosmological analysis of the photometric sample. The first programme was to obtained a magnitude-limited sample of type Ia SNe due to its easily describable selection function. While the plan was to secure classification for all transients with $m_{\rm r} \leq 22$, a limiting magnitude of only 20.4 was reached (D'Andrea et al. 2018). As no other prior was used, this programme also observed other transients than type Ia SNe. The data for this programme was collected mostly by OzDES but it was supplemented by data taken with Robert Stobie Spectrograph (RSS; Smith et al. 2006) mounted on the 9.2 m South African Large Telescope (SALT) and Blue Channel Spectrograph (BCS; Angel et al. 1979) on the 6.5 m MMT (formerly known as Multiple Mirror Telescope). Some spectra observed under this programme are presented in this Thesis.

In the second programme, likely type Ia SNe in faint host galaxies were targeted. The cosmological analysis requires a spectroscopic redshift — most easily attained from the host galaxy — and thus virtually all photometrically classified SNe Ia in environments fainter than OzDES cut-off for host galaxy spectroscopy (24 mag) would be cut out creating a selection bias against increasing redshift and decreasing galaxy mass. The candidate SNe were selected based on their early-time light curves with the `PSNID` scores and they were prioritised based on the faintness of their respective hosts. The programme had dedicated time on X-shooter spectrograph (Vernet et al. 2011) on the 8.2 m Very Large

Telescope (VLT) *Kueyen* and on the Optical System for Imaging and low-intermediate-Resolution Integrated Spectroscopy (OSIRIS; Cepa et al. 2003) instrument on the 10.4 m Gran Telescopio Canarias (GTC). Further supplemental data was collected with the Low Dispersion Survey Spectrograph 3 (LDSS-3) and the Inamori-Magellan Areal Camera and Spectrograph (IMACS; Bigelow et al. 1998) instruments on the 6.5 m Magellan telescopes and on the Deep Imaging Multi-Object Spectrograph (DEIMOS; Faber et al. 2003) and the Low Resolution Imaging Spectrometer (LRIS; Oke et al. 1995) on the 10 m Keck telescopes.

The last SN Ia programme was designed to classify a representative sample of type Ia SNe in redshift space so that its redshift distribution would be similar to the final photometric sample. Such a sample is important as if any spectral dependency as a function of redshift is found in the representative sample it can be used to "correct" such a feature in the photometric sample. Furthermore, the sample has a vital role as a training set for the photometric classification of type Ia SNe. `PSNID` scores were used to select the targets for this programme. However, as the magnitude limited programme focused on the low-redshift SNe and the faint-host programme on SNe that could occur in faint high-redshift hosts, the representative sample program observed likely type Ia SNe in redshift range $0.3 - 0.7$. The programme collected data with dedicated proposals on the Magellan telescopes and on the two Gemini Multi-Object Spectrographs (GMOS; Hook et al. 2004) on the 8.1 m Gemini telescopes. Further data was observed on Keck and MMT.

The DES-SN collaboration also had several smaller non-Ia proposals on various telescopes. In particular two classes of transients had dedicated effort for spectroscopic follow up: SLSNe with VLT and type II SNe with Magellan and Gemini. Research using data taken under these programmes has already been presented in literature. For instance SLSNe DES13S2cmm (Papadopoulos et al. 2015), DES14X3taz (Smith et al. 2016a), DES15E2mlf (Pan et al. 2017), DES16C2nm (Smith et al. 2018) as well as the peculiar type II SN DES16C3cje (Gutiérrez et al. 2020) had spectra taken under these programmes as was some spectra presented later in this thesis.

2.6 Gaussian Process Light Curves

The forced photometry light curves described in the sections above form the majority of the photometric data used and analysed in this thesis. However, while the DES-SN light curves had a rough observing cadence of one week, the cadence varied a lot depending on the conditions on the telescope. The time between consecutive observations was measured to be in the range $4 - 14$ d for 91% of the cases and an thus even broader

range of temporal separations occurred (D'Andrea et al. 2018). The irregular cadence has no effect on the analysis of the data itself, but it can cause problems when parameters — such as rise time to the peak or the peak brightness — are measured and queried for without visual inspection of the light curves. Therefore, it is beneficial to interpolate the observed photometric data with a uniform cadence across the bands and in this thesis I use Gaussian Process (GP) regression to that end. I will refer to the resulting interpolated light curves as the GP light curves from now on. In the following I describe what Gaussian Processes are and what set-up was used to create the GP light curves.

Gaussian Processes are a generalised class of functions that can be used to model correlated noise in any series of data, such as time series. In general any two data points in a series can be joined together by an infinite number of different functions. In GP the distribution of those functions is described by a normal distribution and thus any finite subsample will also be a multivariate Gaussian. GP functions consist of two parameters: the mean function $\mu(x)$ and a "kernel" $k(x, x')$, which is a function that describes the covariance between data points x and x':

$$f(x) = GP(\mu(x), k(x, x')). \tag{2.1}$$

At each arbitrary point x, the distribution of function $f(x)$ is described by a Gaussian. While the exact value of the function $f(x)$ is thus unknown it must be within the distribution (Rasmussen & Williams 2006). Therefore, it is possible to estimate the mean $\mu(x)$ for the pool of possible functions. The shape of the distribution of $f(x)$ depends on how the close data points x and x' are considered to be related to each other. Their relation is described by the covariance function given by the chosen kernel. The covariance function itself depends on two hyper-parameters: the variance of the signal within the function and the characteristic scale length over which any significant variations of the signal can occur. In the case of time series data these hyper-parameters become the uncertainties of the flux measurements and a timescale in which significant variations in the level of flux occur. The continuous function $f(x)$ is then estimated for the given data and the assigned kernel. The GP light curves are created by estimating the mean value and the standard deviation of the function at certain points of time.

$$k(x^2) = exp\left(-\frac{x^2}{2}\right) \tag{2.2}$$

The functional form of the kernel may be selected to match the tendencies of the used data set. For the GP light curves presented in this thesis I have used a simple squared exponential model presented in Equation 2.2. While more complex models are capable

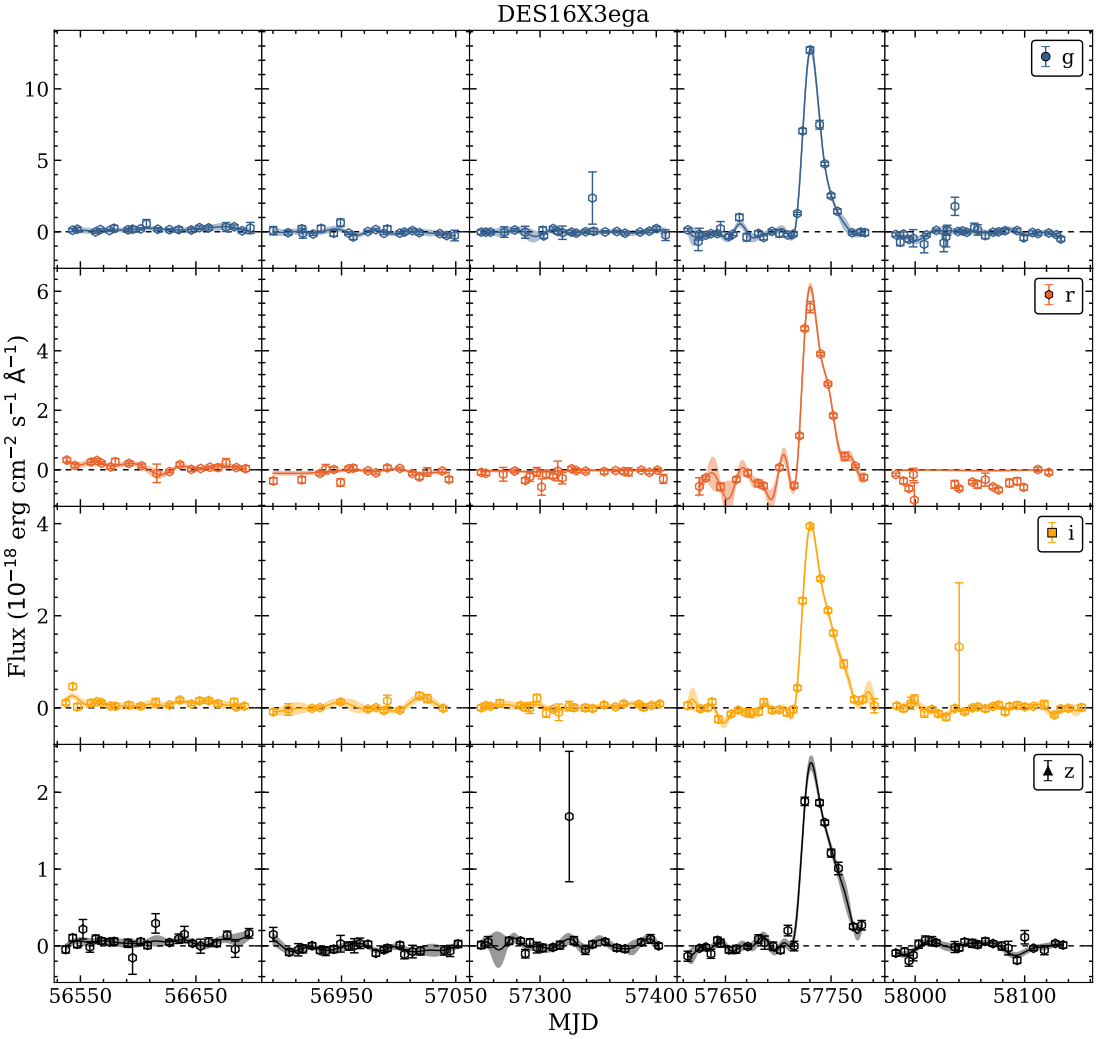

FIGURE 2.12: Example 5-year, 4-band GP *griz* light curves for DES-SN transient DES16X3ega. The original forced photometry light curves are shown with open markers. The mean function of a GP light curve described by a solid line and the standard deviation with a shaded regions around it. The GP light curves with $\Delta t_{\rm GP} = 5$ d were used to create the figure.

of fitting well described SN light curves beautifully (see e.g. Inserra et al. 2018a), they are also more prone to vary too strongly when fitting noise. As I use the GP light curves to describe the whole 5-year data, most of which is always noise due to short duration SNe in comparison, a simpler model is less likely to overfit the background variation.

The GP light curves can also be tuned further using the kernel hyper-parameters. While the errors of the data are what they are and they cannot be influenced, the choice of the characteristic timescale, $\Delta t_{\rm GP}$, has a strong effect on the resulting interpolation. If a chosen value is too small the resulting GP light curve would be as certain as the data, but it would also follow each data point exactly and if chosen too large all features in the observed light curve would be missed due to over-smooth interpolation. Thus, I created

interpolated GP light curves for several different values of $\Delta t_{\rm GP}$ and demonstrate below how they affect the interpolations.

The GP light curves were generated for all $\sim$ 29200 named DES-SN transients in all four *griz* bands with a Python package `George`[2] (Ambikasaran et al. 2016). The light curves have a constant 0.5 d cadence starting from the first accepted filter-epoch of the season regardless of the band so that for each GP epoch a flux value was estimated for all *griz* bands. However, GP data points are not created before/after the first/last observation of the year in a given band (i.e. the data is not extrapolated). In the process each DES-SN season and each *griz* band was treated independently so that the whole 5-year, 4-band set of light curves was created in 20 parts. An example of 5-year GP light curves in all *griz* bands created with $\Delta t_{\rm GP} = 5$ d is presented in Figure 2.12 for DES16X3ega. The observed forced photometry light curve is also shown to demonstrate the quality of the interpolation.

While the GP light curves presented in the figure seem to be performing well as a whole, there are a few individual features that catches the eye. First, the interpolation of r band seems to be following the variation of the non-detections very closely just before the onset of DES16X3ega causing the GP light curve to overfit. This is especially clear at MJD $\sim$ 57710, where the interpolation rises higher than the observed data point. While the feature is below 3σ, it demonstrates that choosing a small timescale might cause slight overfitting in the light curves. The second intriguing feature in the interpolations is that the peak in z band appears to rise higher than the observed values. In this case, the two real peak detections are observed 14 d apart and thus the interpolation has followed the trend of the observed light curve (i.e sharp rise and decline) causing the interpolation to rise higher.

In Figures 2.13 and 2.14 I demonstrate how the change of the characteristic timescale, $\Delta t_{\rm GP}$, affects the interpolated light curves for one example RET from the sample presented in this thesis and one type Ia SNe from DES-SN. In the figures I show the *griz* forced photometry light curves and the corresponding GP interpolations for $\Delta t_{\rm GP} = 4, 5, 6, 7$ d. Furthermore, I also provide the rise times in r band for each interpolation. The times were estimated from the first 3σ data point before the peak to the time of the peak flux. However do note that both g and r bands were required to have a 3σ data point at the peak epoch.

For the RET DES13X3nyg presented in Figure 2.13, the interpolation for $\Delta t_{\rm GP} = 5$ d appears to be the best at describing the data. For $\Delta t_{\rm GP} = 4$ d the light curves appear to be overfitting causing the interpolation to be very uncertain. However, for the timescales of 6 d and 7 d the interpolations underestimate the peak flux and appear to infer a longer

[2] https://george.readthedocs.io/

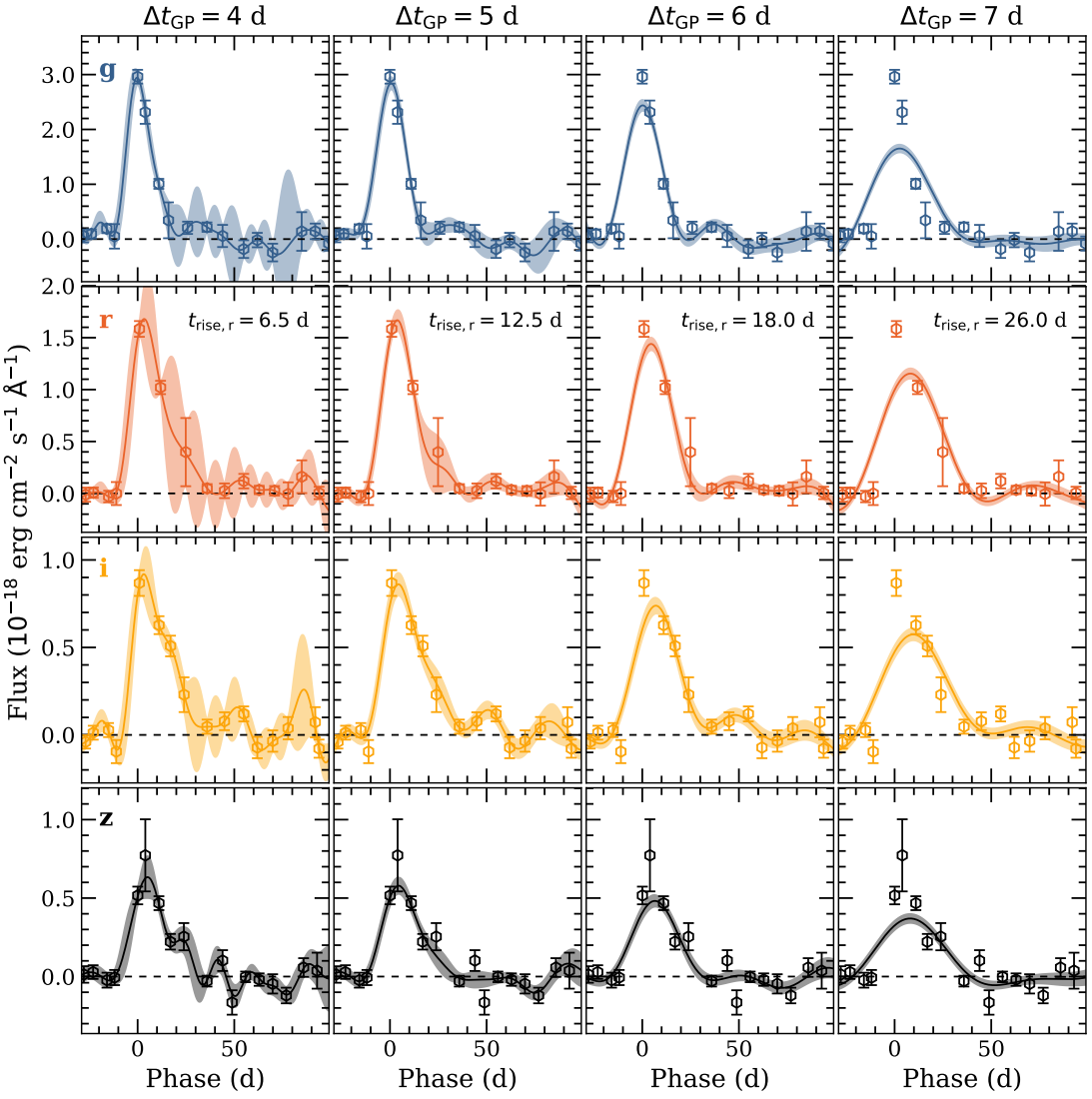

FIGURE 2.13: Interpolated observer frame GP light curves of RET DES13X3nyg for $\Delta t_{GP} = 4$, 5, 6, 7 d in the DES-SN *griz* bands. The forced photometry light curves are provided with open hexagons. The estimated rise times in r band are provided for each interpolation.

rise than in the forced photometry light curves. While the quality of the interpolations varies from RET to RET, these features appear to be generic for for the sample of RETs. Therefore, the timescale $\Delta t_{GP} = 5$ d appears to be the best at describing their light curve evolution as a whole.

For comparison, in Figure 2.14 I provide the GP light curves for an example type Ia SN from DES-SN. In this case the longer timescales of 6 d and 7 d appear to provide very realistic interpolations of the data in all bands. However, in the i and z bands the interpolation for 5 d seems to be reasonable as well, while in the r band the rise is very uncertain due to a gap in the observations. This has caused the estimated rise time of 7 d to be unrealistically small for a type Ia SN. Similar issue occurs on a fraction of SNe

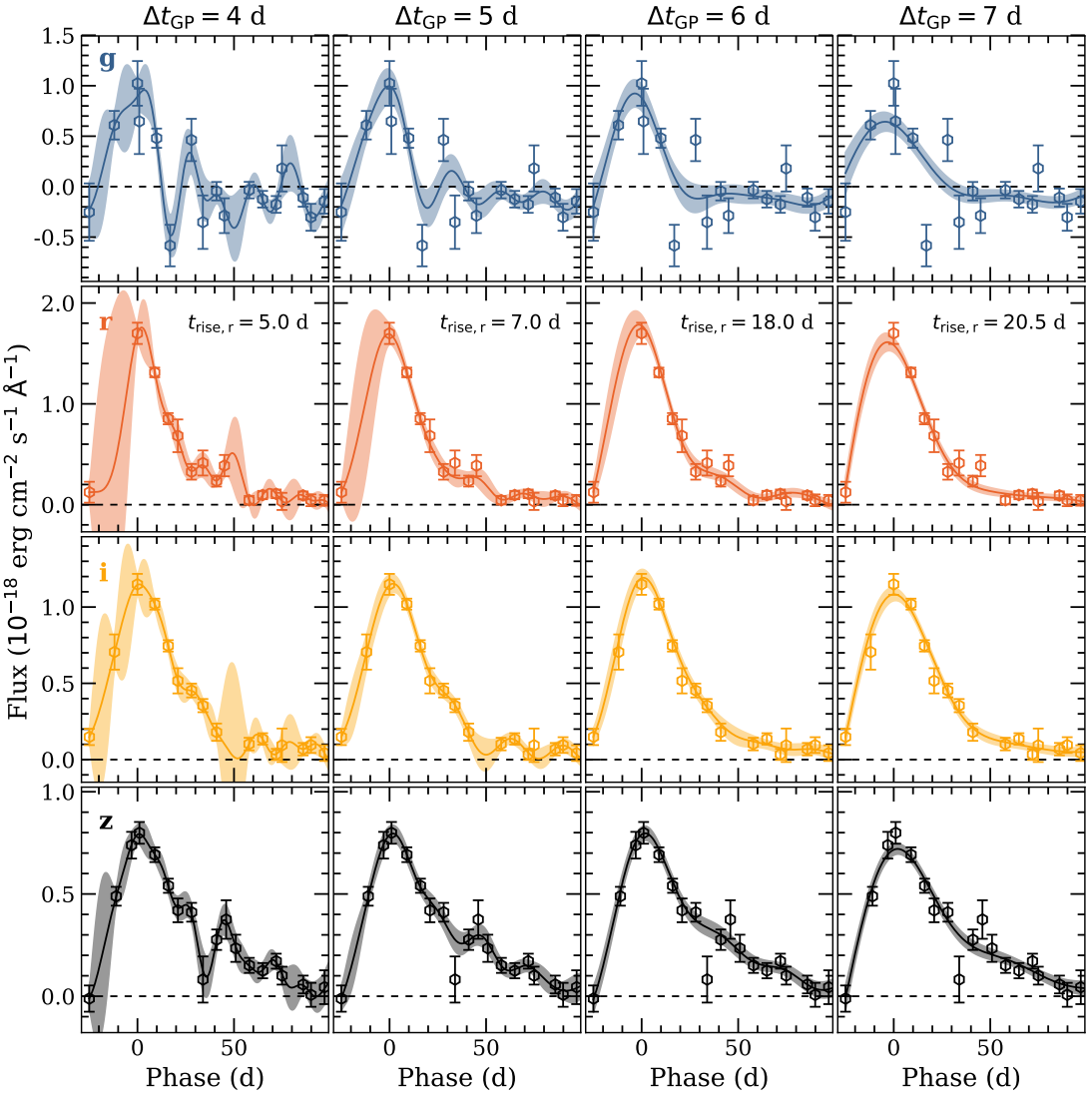

FIGURE 2.14: Interpolated observer frame GP light curves of type Ia SNe DES14X3ajv for $\Delta t_{\rm GP} = 4, 5, 6, 7$ d in the DES-SN *griz* bands. The forced photometry light curves are provided with open hexagons. The estimated rise times in r band are provided for each interpolation.

from DES-SN, but in general the light curve interpolations for $\Delta t_{\rm GP} = 5$ d are as good as for i and z shown in the Figure 2.14. Thus, the timescale $\Delta t_{\rm GP} = 5$ d appears to be the best at describing both RETs and SNe as a whole. It provides the best interpolations for the RETs and still seem to be providing good quality GP light curves for majority of the SNe as well. Therefore, I will use the GP light curves for $\Delta t_{\rm GP} = 5$ d in Section 3.2 to search for RETs.

Chapter 3

Rapidly Evolving Transients: Selection Criteria and Sample Overview

Now we can turn our attention towards the main topic of this thesis: the rapidly evolving transients. As discussed in Chapter 1, the fast evolving events are characterised by rapid photometric evolution — faster than is expected of the standard SNe populations. Thus, their discovery and analysis requires a high cadence optical survey probing a large volume on the sky. As such the Dark Energy Survey Supernova Programme provided an excellent opportunity to perform one of the first designated searches for RETs at the dawn of interest for the fast and luminous events.

In the next four Chapters I will be discussing the sample of 106 rapidly evolving transients I discovered in the DES-SN data. The later three Chapters will focus on observable properties and physical interpretation of the transients, but in this chapter I will start from the beginning and focus on the start of the project in early 2017, before the discovery of AT2017gfo and AT2018cow. I will discuss the aspects of how the sample of RETs was discovered in the data, but I will also provide an overview of the final sample. Significant portions of the work have already been published in Pursiainen et al. (2018), where I presented a sample of 72 transients discovered in the first four years of DES-SN.

3.1 First Search

In its five years of operation DES-SN detected $\sim$ 21000 events classified as SST (i.e. objects detected in image subtractions during one year but not the others). These objects

include different varieties of SNe and other transient phenomena, but also significant amounts of AGN and some spurious detections. In order to find peculiar transients, such as the rapidly evolving ones, it is important to cut down the number of viable candidates automatically before visual inspection of the light curves. Therefore, I devised a rudimentary photometric classification pipeline, `ClassPipe`, that used the DES-SN forced photometry light curves to determine if a transient phenomenon was truly single-season based on linear fits and further evaluated the duration of the transient based on Gaussian fits. The pipeline was developed during DES Y4, and thus it was applied first only to first four seasons of DES-SN data. Once Y5 had finished observations, the same search was performed on the data of the final season. All fitting presented in this thesis has been performed with `Python`[1] using the non-linear least-squares minimization and curve-fitting package `LMFIT` (Newville et al. 2014).

3.1.1 Automated classification of SN-like transients with `ClassPipe`

The pipeline first verified which of the classified SSTs occurred truly during a single DES-SN season. This was done by requiring that the light curve evolution of all transients had to be non-variable during all seasons outside of the event year (the year when event was formally discovered and named). Each of these seasons was split in half ($\sim$ 75 d each) and average slopes of each band in each interval were evaluated. In the second step the event year *griz* light curves of all transients were fit with Gaussian profiles in order to evaluate the duration and brightness of the events. The parameters of Gaussian fits used to characterise the events were the peak strength and MJD and FWHM.

Using the described criteria, a transient was classified as "SN-like" if it fulfilled the following conditions:

1. The second steepest mean slope of the linear fits (in absolute units) was smaller than 10^{-20} erg cm^{-2} s^{-1} Å^{-1} per day. The highest value was ignored as a means of outlier rejection. If less than two linear fits could be performed due to lack of data, the object was rejected. In such cases, subtracting the template from the search image was repeatedly unsuccessful. Possible reasons are failed subtraction of a bright galaxy or a transient location near a chip edge resulting in problematic subtractions.

2. The Gaussian fits peaked within 15 days from the mean peak MJD of the Gaussian fits in at least three bands.

[1] `www.python.org/`

3. The peak flux of the Gaussian fits were $> 10^{-19}$ erg cm^{-2} s^{-1} Å^{-1} in at least three bands or $> 5 \times 10^{-19}$ erg cm^{-2} s^{-1} Å^{-1} in at least one band. If the latter was true for only one band, the FWHM of that band also had to be in range 12 – 95 days, corresponding to a range where majority of tested DES SNe were found.

4. The mean observed flux of the event year over four bands was higher than the mean observed flux of any other season.

The limiting flux values in Cut 3. correspond to magnitudes of $m_{\mathrm{griz}} = 26.7, 26.0, 25.6, 25.3$ when the peak of Gaussian fit is brighter in at least three bands and $m_{\mathrm{griz}} = 25.0, 24.3, 23.9, 23.5$ in case of only one band. The typical average depths in DES-SN — as presented in Section 2.4 — are $m_{\mathrm{griz}} = 24.3, 24.6, 24.5, 24.3$ in the deep fields and $m_{\mathrm{griz}} = 23.6, 23.4, 23.2, 23.1$ in the shallow fields (Kessler et al. 2015). The cutoff limits are considerably lower to minimise the loss of interesting transients regardless how faint they were.

`ClassPipe` also looks for events that were either at the beginning or at the end of the season so that only the decline or the rise was observed. Such events were excluded as missing either pre- or post-peak evolution would make it difficult to asses the true duration of the transient causing them to be excluded regardless. A transients was determined to be on "decline" if at least one of the following were true:

- The peak flux was the first data point of the season and the second highest flux was one of the first three data points in at least two bands.
- The peak flux was the first data point in one band and the within first three data points in the other three bands. Additionally, the second highest fluxes were within the first three data points in every band.
- The peak MJD of a Gaussian fit was before the first observed data point in at least two bands.

As the rise of a SN light curve is typically much shorter in duration than the decline, the requirements for it were stricter. An event was determined to be on the "rise" if one of the following were true:

- The peak flux was the last data point of the year, and the second highest flux was within the last three data points in at least three bands.
- The peak MJD of a Gaussian fit was after the last data point year in at least two bands.

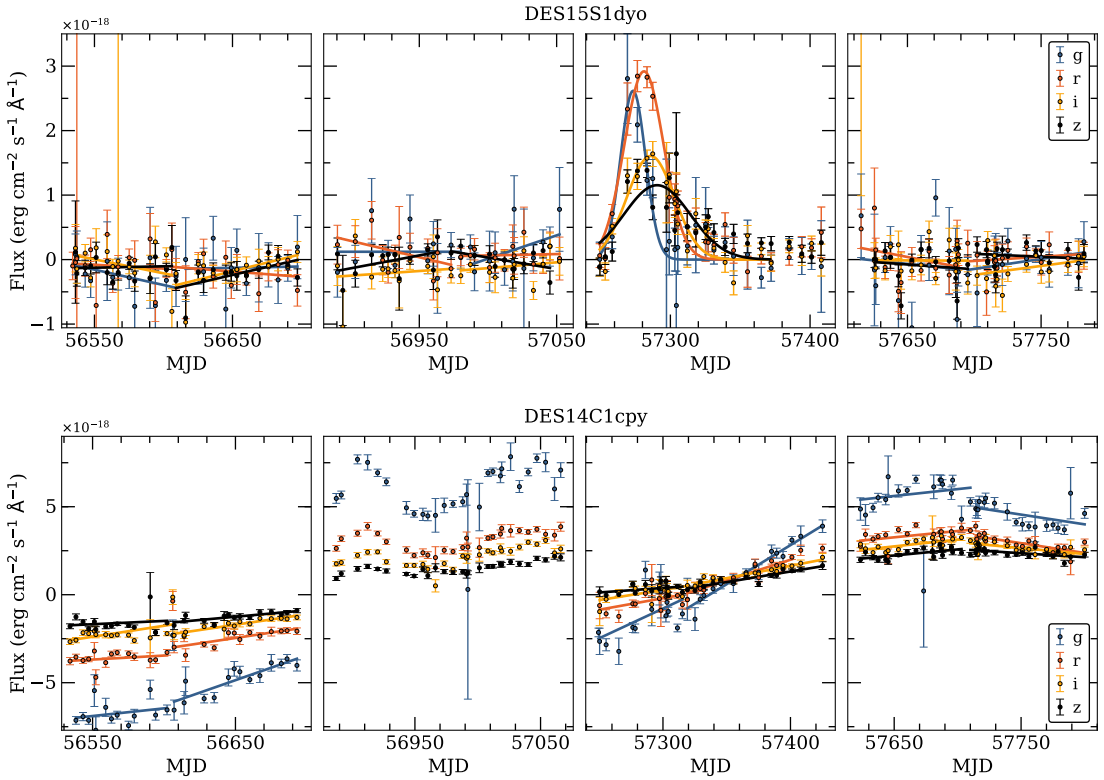

FIGURE 3.1: 4-year light curves of two example DES-SN transients showing the linear and Gaussian fits performed by the `ClassPipe` pipeline. Linear fits are used to characterise the background variability outside the event year and Gaussian fits the duration of the event itself. DES15S1dyo (top) is a likely type Ia SN that passed the pipeline and DES14X1cpy (bottom) is a likely AGN showing multi-year variability and thus it failed Cut 1.

To demonstrate how `ClassPipe` operates, two example 4-year light curves of DES-SN transients are presented in Figure 3.1. DES15S1dyo is a likely type Ia SN that passed the set of criteria, while DES14C1cpy is a likely AGN that showed multi-year variability and thus failed Cut 1.

The performance of `ClassPipe` was tested on spectroscopically confirmed SNe and AGN from the first three years of DES-SN with a several combinations of parameter values to optimise its performance before settling on the final cuts described above. The tests also verified that the pipeline did characterise transient phenomena correctly as demonstrated in Table 3.1. Significant majority of the SNe (262/294) passed the pipeline and more than half of the ones who did not pass were observed only in rise or decline (19/32) and were thus cut. The remaining few SNe that were cut by the pipeline have template subtraction issues at some point of the 4-year light curve causing them to be discarded either due to a large amount of variation outside the event season or insufficient amount of data for the linear fits. Only exception is one type II SN that was observed within two seasons and thus did not pass Cut 1. Furthermore, only 6/49 AGN passed the pipeline

TABLE 3.1: Results of `ClassPipe` on the spectroscopically classified SNe (Ia, II and Ibc) and AGN from first three years of DES-SN. The number of events discarded at each cut and the number of events that passed the pipeline are shown.

	SN Ia	**SN II**	**SN Ibc**	**AGN**
Total	251	34	9	49
Only Decline[a]	10	6	2	1
Only Rise[b]	0	1	0	0
Failed Cut 1.[c]	6	2	1	39
Failed Cut 2.[d]	0	1	0	3
Failed Cut 3.[e]	0	0	0	0
Failed Cut 4.[f]	3	0	0	0
Passed `ClassPipe`	232	24	6	6

[a] Observed only on decline.
[b] Observed only on rise.
[c] Cut based on the linear fits.
[d] Cut based peak MJD of the Gaussian fits.
[e] Cut based on peak flux of the Gaussian fits.
[f] Cut based on average flux outside the event year.

demonstrating that majority of the transient with multi-year variability were cut by the pipeline.

The pipeline was used to characterise the light curve behaviour of all unclassified DES-SN SSTs with a SNID number. The pipeline was first run on the first four years of DES-SN data, but once the observations of DES-SN Y5 were finished the pipeline was run on that data-set as well. The results of the pipeline on the five years of data are presented in Table 3.2 with the numbers of events cut at different phases of `ClassPipe`. Altogether roughly half of the of the transients passed `ClassPipe`, now having a crude measurement of the event duration in the form of FWHM. In order to include the information of all four bands in an easy manner the mean FWHM was used to search for transients with short light curve duration.

It is worth noting that the choice of using Gaussian fits to characterise the transient light curve widths may bias the results away from transient with rapidly rising but highly asymmetric light curves. However, later in this Chapter I present the results on parametrisation of the different populations of extragalactic transients and demonstrate that the rapidly evolving ones are discovered well with the assumption of a Gaussian profile.

3.1.2 Selection Criteria for Rapidly Evolving Transients

As discussed earlier, the RETs presented in the literature rise to peak brightness in $\lesssim 10$ d and stay above half of the peak brightness only for $\lesssim 12$ d and thus they evolve faster

TABLE 3.2: Results of `ClassPipe` on the full five years of DES-SN data. The rows are the same as in Table 3.1 apart from FWHM spread of the successful events.

	DESY1	**DESY2**	**DESY3**	**DESY4**	**DESY5**
Total	4280	4161	3618	4021	4686
Only Decline	302	235	242	252	140
Only Rise	77	101	49	64	51
Failed Cut 1.	409	389	135	176	137
Failed Cut 2.	774	808	862	1057	1547
Failed Cut 3.	521	507	559	670	833
Failed Cut 4.	174	76	127	80	70
Passed `ClassPipe`	2023	2045	1644	1722	1908
FWHM $>$ 30 d	1691	1783	1259	1359	1634
FWHM $<$ 30 d	332	262	385	363	274

than standard classes of SNe. Therefore, it is safe to assume that the fast events should have small values of FWHM as estimated by `ClassPipe`. The threshold for the visual inspection was chosen based on the FWHM distributions of spectroscopically confirmed type Ia, Ibc and II SNe from first three years of DES-SN shown in the top panel of Figure 3.2. The same set of SNe was used to test `ClassPipe` performance. As the Gaussian fits provide only a rough estimate of the light curve shape, the FWHM is not a particularly exact measurement of the light curve width. Thus, the cutoff limit FWHM = 30 d was selected so that it partially overlapped with the SN distributions in order not to lose interesting events at this stage. The selection focuses heavily on the fast end of all `ClassPipe` approved events as can be seen based on the mean FWHM distribution plotted in the bottom of Figure 3.2.

The sample of RETs was then unveiled by visually inspecting the light curves of all $\sim$ 1600 events with FWHM $<$ 30 d as was shown in Table 3.2. Most of these candidates were ultimately rejected as the small value of FWHM was driven by a single, possibly low signal-to-noise, data point above otherwise constant background level. However, close to FWHM = 30 d traditional types of SNe were also excluded based on their light curve evolution.

The visual inspection was performed in two phases. First, as the pipeline was finished prior to start of DES-SN Y5, it was done on the first four years of DES-SN resulting in a discovery of 72 transients. However, do note that one RET in the sample, DES16C1cbd, has FWHM = 30.9 d. The event was discovered during a visual inspection performed as a part of different analysis, but as it exhibited similar light curve evolution as the RETs it was included in the sample at this stage. Analysis based on the sample of the 72 RETs has been published in Pursiainen et al. (2018).

The sample of the discovered 72 RETs was used to create a rudimentary selection criteria to search for similar transients live during DES-SN Y5. One of the key features, in

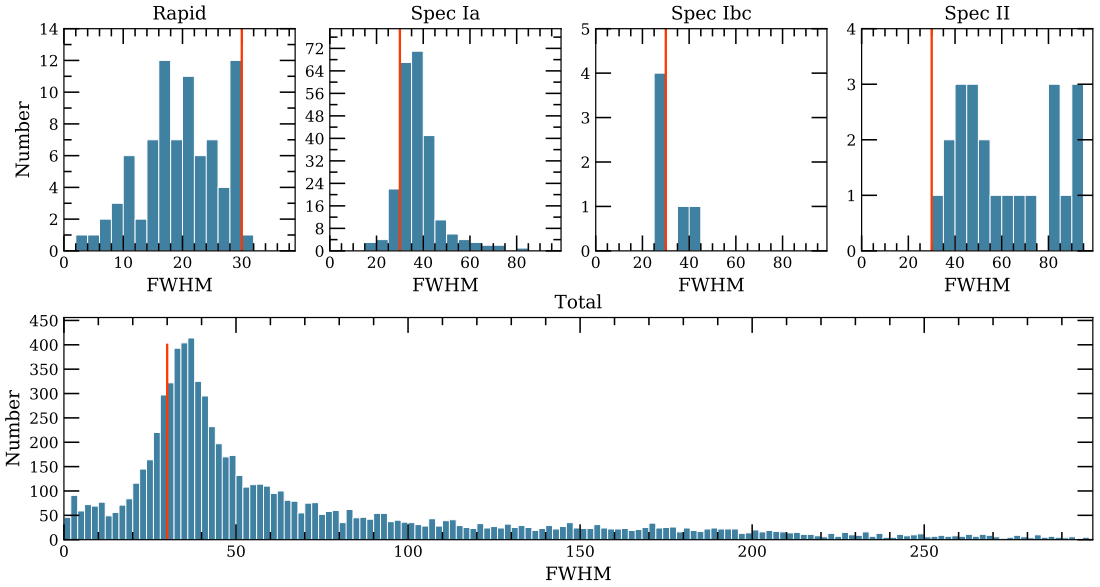

FIGURE 3.2: Mean FWHM distribution of the 82 RETs discovered with `ClassPipe` in comparison with spectroscopically confirmed samples of type Ia, Ibc and II SNe from the first three years of DES-SN in the top panel and FWHM distribution of all events that passed `ClassPipe` in the bottom panel (see Table 3.2). Red line refers to the cutoff limit of FWHM = 30 d for the RETs. Note that the one RET at FWHM > 30 d is DES16C1cbd identified as part of different analysis. All events found above FWHM = 300 d are ignored in the bottom panel.

addition to the fast light curve evolution, was their blue colours even in the observer frame. Thus, all new DES-SN events with relatively blue colours ($g - r < 0.2$) at first detection were visually inspected for possible spectroscopic follow-up. In total 10 events exhibiting similar light curve evolution as the RETs were discovered in such a way and added to the sample. While some of the brighter events were pushed to spectroscopic follow-up queue for VLT, due to the rapidly evolving nature of the targets had faded too much to obtain useful spectra. Once observations of Y5 had finished, `ClassPipe` was used for the second time to characterise the light curves of the final DES year and 10 RETs were discovered with the visual inspection bringing the sample up to 92 events. The FWHM distribution of the 82 RETs identified with `ClassPipe` (including DES16C1cbd) is presented in 3.2.

The search resulting in discovery of 92 RETs is referred to as the first search in this thesis. While majority of the sample was selected by inspecting transients with short light curve durations, 10 were identified during live selection in DES-SN Y5. Therefore, it is important to investigate if those 10 RETs would have been identified with the light curve inspection as well. Interestingly, while a few demonstrated small enough FWHM to be inspected, 7/10 did not. Some had slightly higher values of FWHM up to $\sim$ 45 d, but for two of the RETs the fits did not successfully describe the light curves at all and the values were found to be $\gtrsim$ 100 d. This, in addition to DES16C1cbd also found

at FWHM $>$ 30 d, clearly demonstrates that while the first search resulted in large number of discovered RETs, the search method and the applied cuts excluded some of the interesting transients. Thus, a more sophisticated search had to be created.

3.2 Enhanced Search with Light Curve Parametrisation

The first search for RETs in DES-SN was designed to be very rudimentary in its attempt to characterise the forced photometry light curves. The simplistic approach made it possible to look for exotic transients without knowing their observed characteristics (apart from the fast evolution) beforehand. The method was successful at its aim to discover RETs as it resulted in a large sample of photometrically selected fast transients. However, as the search relied heavily on visual inspection of the available data (e.g. images, light curves), it is difficult to be sure how complete the sample actually is, especially because some of the RETs were discovered outside the search criteria. Some transient could, for instance, be missed at high redshifts as the time dilation could cause the light curves to evolve too slowly in observer frame for the applied cuts. A new, more sophisticated approach to search for RETs was thus implemented in order to verify how complete the first search was, and it was built upon the sample of 92 RETs and the created GP light curves.

3.2.1 Peak $g - r$ Colour and Rise Time Parametrisation

As only a fraction of all $\sim$ 29200 transients in DES-SN have spectroscopic redshift from the host or the event, the search must be done in the observer frame. As discussed above, the key features of RETs that distinguishes them from most traditional SNe types are the fast light curve evolution and blue colour at peak brightness. Even though both of these quantities depend on the redshift of the transient, they still seem to distinguish the fast events from the traditional SN types. This is demonstrated in Figure 3.3, where the $g - r$ colour at the epoch of maximum observed brightness in the r band is shown against the r band rise time for the sample 92 RETs and spectroscopically confirmed type Ia, Ibc, II and SLSNe from DES-SN. Note that the spectroscopic samples are the 5-year ones and thus they are larger than the ones used during the original search. The quantities are based on the forced photometry light curves, and the colour was measured only for the transients with a 3σ g band detection within 2 days from the observed peak in r band and had an observed peak magnitude in both g and r bands brighter than 24 mag (shallow fields) or 25 mag (deep fields). The rise time is measured as the time between the maximum observed brightness and the last non-detection before it.

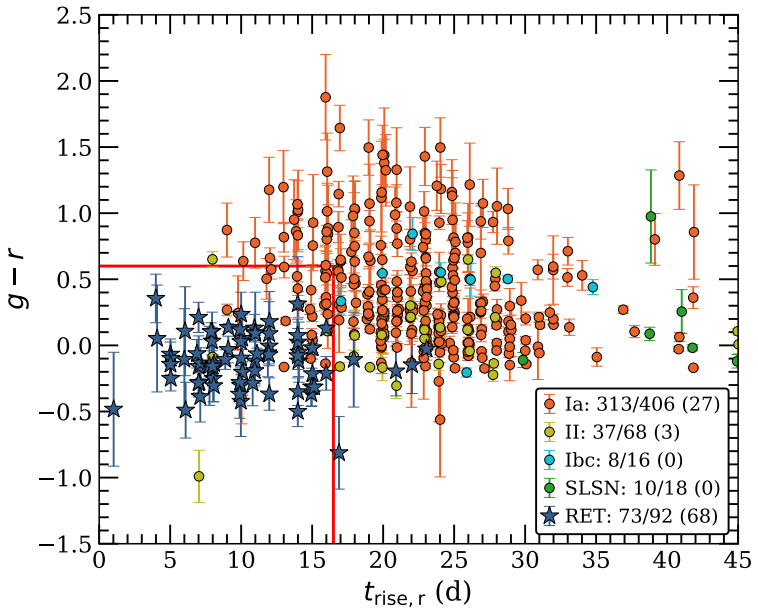

FIGURE 3.3: $g - r$ colour at the epoch of maximum observed brightness in r band against the rise time in r band. Both quantities are measured in the observer frame using the DES-SN forced photometry light curves. The given values for each transient class refer to how many transients could be plotted, how many transients there are in total and how many of the shown transients are inside the drawn red box.

Based on the figure the RETs cluster at shorter timescales and bluer colours than other SNe, even in observer frame. However, using the observed photometric data directly has several problems that can be improved. First measuring the peak colour of a transient is often problematic. DES-SN did not always observe g and r bands on the same or even consecutive nights, thus making it impossible to measure the peak colour in a number of cases. The numbers of transient that could be plotted in the figure highlights the issue — i.e. peak colour and rise time was measure only for 313/406 type Ia SNe. The rise time suffers from a similar issue. Measuring a rise time of $10 - 15$ days is difficult to perform with a one week cadence when it has to be done without fitting a light curve model and thus the rise time values in the figure are spread over a wide range. The issue is the clearest for type Ia SNe and the sample of RETs. As a result of the two, problems using the observed data directly results in reduced samples of transients spread over a wide range of rise times. Thus, even if the data clearly shows that the peak colour and rise time can be used to distinguish fast transients in the observer frame, the RET sample overlaps significantly with other transient populations.

3.2.2 Improved Parametrisation with GP Light Curves

To improve the estimation of the parameters the light curves will have to be interpolated. For this purpose I chose to use the GP light curves introduced in Section 2.6. The

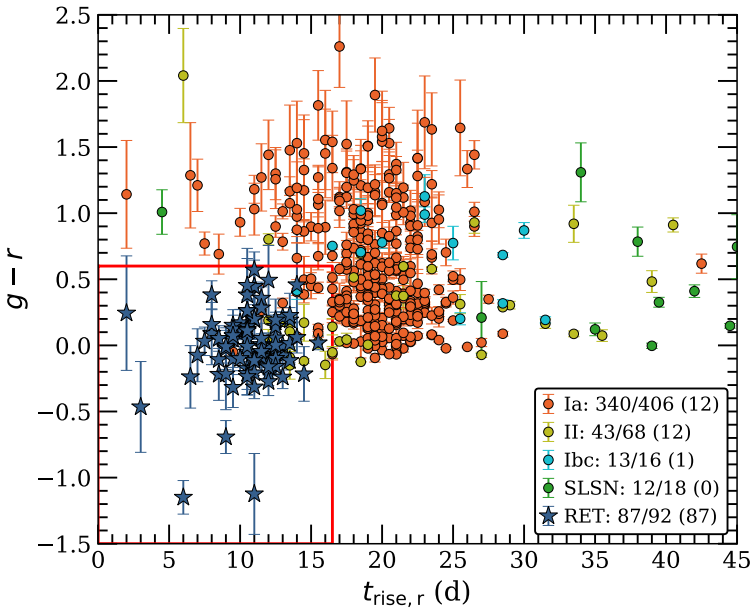

FIGURE 3.4: Same as Figure 3.3, but created with the GP light curves for timescale of 5 days. Note that the red box is drawn at $-1.5 < g - r < 0.6$ and $t_{\mathrm{rise,r}} < 16.5$ d in order to optimise the selection for RETs against other type of events. The given values for each transient class refer to how many transients could be plotted, how many transients there are in total and how many of the shown transients are inside the drawn red box.

interpolated light curves have 0.5 d cadence and each epoch has a flux value for every band and thus both rise time and peak colour should be easy to estimate. In Figure 3.4 a significantly improved version of the peak colour vs. rise time plot created using the GP light curves with $\Delta t_{\mathrm{GP}} = 5$ d is shown. The distributions of all transient classes are less spread out and now there is a clear division between the populations of RETs and type Ia SNe. All plotted RETs are contained within a region of $-1.5 < g - r < 0.6$ and $t_{\mathrm{rise,r}} < 16.5$ d (hereafter referred to as the RET region) which minimises the contamination from other classes of transients. For instance only 12/340 plotted type Ia SNe are found in the same region. In the figure, a small number of type Ia SNe appear to have uncharacteristically small rise times ($\lesssim 15$ d). This is caused by uncertain interpolations of the forced photometry light curves with gaps in the data. Example of a such situation has been shown in Figure 2.14.

For the presented GP version of the peak colour vs. rise time plot, the peak in r band is found by requiring both g and r band to have 3σ data points at that epoch, but the limits for peak magnitudes were the same as for Figure 3.3. In case no such epoch existed the event in question was excluded. The 5/92 RETs not plotted in the Figure 3.4 were excluded as their peak magnitudes of the GP light curves were fainter than the cut off limits. On the other hand, the excluded spectroscopically classified SNe were cut as they

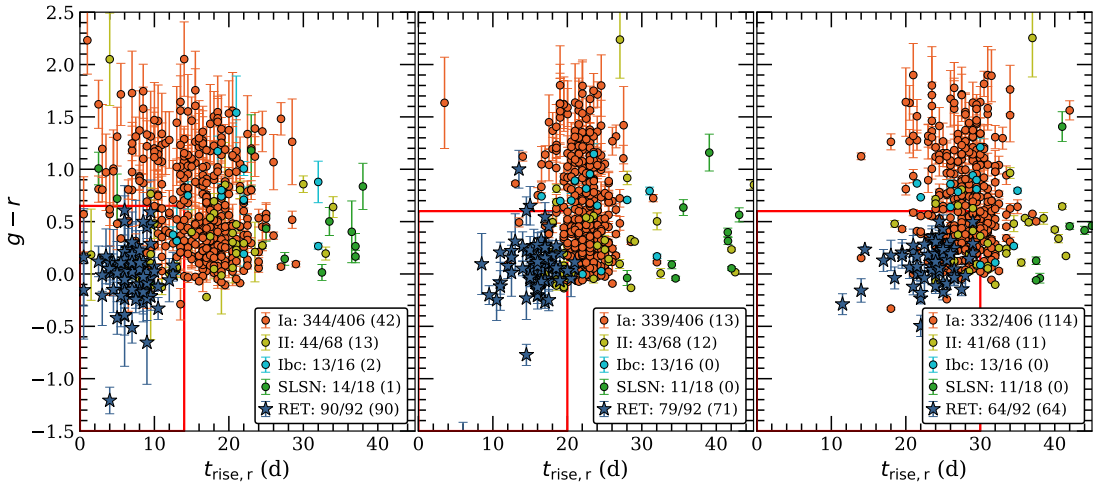

FIGURE 3.5: Same as Figure 3.3, but created with the GP light curves for $\Delta t_{\rm GP}$ of 4 days (left), 6 days (middle) and 7 days (right). Note that the red boxes are different and they are drawn to roughly optimise the selection of RETs against other type of events.

were either observed only on the decline or they were found at high redshifts and thus the g band emission had faded out.

As discussed in Section 2.6, the GP light curves created with $\Delta t_{\rm GP} = 5$ d appeared to be best at describing the forced photometry light curves of the RETs, but they also worked well for most of the type Ia SNe. In order to confirm that the timescale is a good choice for the selection, I created the same peak $g - r$ vs. rise time plot for the other sets of GP light curves created using $\Delta t_{\rm GP} = 4, 6, 7$ d for comparison. The resulting plots are shown in Figure 3.5, and it is clear that the timescale $\Delta t_{\rm GP} = 5$ d is the best out of the four examples. At higher timescales ($\Delta t_{\rm GP} = 5, 6$ d), fewer events pass the cuts to be plotted and the distributions of different classes are more blended together. However, for $\Delta t_{\rm GP} = 4$ d the distributions of SNe are visible broader than for $\Delta t_{\rm GP} = 5$ as the interpolation of the light curves now overestimating the real features while providing uncertain GP Light curves. Thus, while the RETs are still reasonably well described, the samples of SNe overlap with them more.

3.2.3 Selection of the Rapidly Evolving Transients

As a next step of this part of analysis, I used the created GP light curves (with $\Delta t_{\rm GP} = 5$ d) to estimate the peak $g-r$ colours and the rise times as describe above for all unclassified SSTs in DES-SN. The quantities could be estimated for 3164 transients, out of which 1212 are located in the RET region. The density distribution of these events is shown in Figure 3.6 (top left) visually showing three main components. First, there is a strong hot spot directly overlaying the bulk of RET population as presented in Figure 3.4. Furthermore,

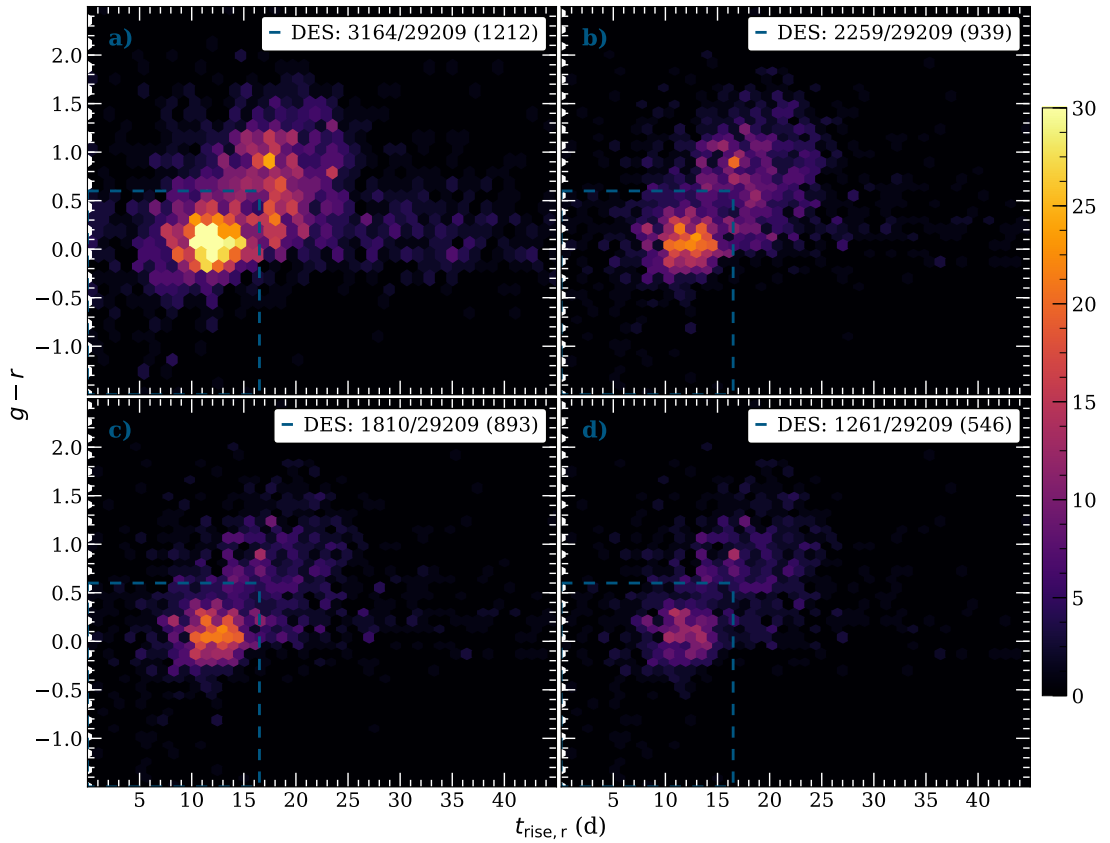

FIGURE 3.6: Peak $g-r$ vs. $t_{\mathrm{rise,r}}$ density plots for DES-SN transients after each used cut. a) All DES-SN transients for which peak colour and rise time could be estimated, b) remaining events after cuts for likely AGN, c) after `PSNID` cuts for likely type Ia SNe and d) after cuts for slowly declining transients. The given colour scale refers to the number of events in each hexagon. The RET selection region is shown with dashed blue lines. The given values for each subplot refer to how many transients could be plotted, how many transients there are in total and how many of the shown transients are inside the drawn blue box.

the Ia population from the same Figure is also clearly visible circling around the top-right corner of the RET region. The final visual feature is the faint "tail" at roughly $g-r \sim 0.0$ extending towards long rise times. While, the number of events in the selection region (1212) is still high for a visual inspection of the light curves, no known contaminants have yet been removed. In the following I present the three cuts used to improve the selection. The additional subplots in Figure 3.6 refer to events left after each of these cuts.

The most obvious classes of interfering transients are AGN, type Ia SNe and any fast rising but slowly declining transients. AGN often exhibit multi-season variability on different timescales and it is likely that at least some AGN would be found inside the RET region. It is also safe to assume that there are some contaminating type Ia SNe given that the 12/340 ($\sim$ 3.5%) of them are found in the same region in Figure 3.4. Furthermore, a significant portion of type II SNe are found to have a fast rise time

comparable to those of RETs (see e.g. Gall et al. 2015; González-Gaitán et al. 2015) and in Figure 3.4 12/43 are found inside the red box. Thus, it is reasonable to expect some of the 1212 events to be fast rising but slowly declining. Luckily all three classes have observable properties that differ from the RETs that can be used to remove them prior to visual inspection of the available data. Note that the purpose is not to reject all such events, but to remove as many as possible without removing any RETs.

The clearest observable feature that separates AGN from RETs is that most of them show some level of multi-season variability that RETs do not exhibit. Such a difference should be clearly visible in the light curves and thus it should be possible to use the difference to separate them from each other. For this purpose, I designed a Convolutional Neural Network (CNN) binary classifier to divide the remaining 3164 transients into two categories: "AGN" and "SN-like", using the full 5-year, 4-band GP light curves. The CNN architecture is presented in Appendix A, but in summary it was designed to look for features that occurred on short 2 d timescale in the 4-band GP light curves and search how those features evolved over intervals of $\sim$ 40 d to distinguish differences in AGN and transient light curve evolution.

The classifier was trained and tested using a sample of 572 transients that consisted of the spectroscopically classified SNe from 5 years of DES-SN and the discovered RETs and a sample 261 AGN either classified by DES-SN or monitored by OzDES. The final accuracy of the classifier was 0.992 for the test sample with 4/79 AGN classified as SN-like but more importantly no SN-like transient was classified as AGN in the test set of 390. The classifier was run on all 3164 events shown in 3.6. As a result 779/3164 events were classified as AGN using the neural network and a further 126 did not pass the simple light curve cut requiring that each band in each year should have more than 50 d worth of GP light curve. The resulting $g - r$ vs. rise time density plot is shown in Figure 3.6 (top right) for the remaining 2259 events. It is clearly visible that classified AGN were found in all regions of the parameter space as the number of events has decreased across the plot. Additionally, the "tail" has almost completely disappeared. However, despite the clear effect on the plot, only 273 events were rejected inside the selection region and 939 transients still remained.

As the CNN classifier was used to remove AGN based on their multi-season variability, it is interesting to investigate how it performed in comparison to the original simplistic cut using the linear fits for the same end, especially as the linear fits were performed on all 3164 events shown in Figure 3.6 allowing a direct comparison. Interestingly, while 2206 events were classified as SN-like in both, the classifiers agreed only on 89 AGN. Further investigation revealed that 690 events were classified as AGN by the CNN but not by the linear fits. While 186/690 were excluded by the further criteria during the

original search, this still leaves 504 events that were passed by the pipeline. Finally, 53 events were classified as AGN based on the linear fits, but not by the CNN. Note that the remaining 126 events were excluded by the CNN classifier due to their parse GP light curves.

Based on the numbers it is clear that the CNN classified more events as AGN than the original simple approach. I have visually inspected light curves of some of the transients that were classified differently and it seems like the CNN is also performing better. The 53 transients classified as AGN by the original search seem to be a mixed back of events. Majority appear to be classified as AGN due to subtractions issues in the light curves, causing the linear fits to be too steep. While most of these events seem to be completely artificial, a few obvious SN-like phenomena were classified as AGN as well. Furthermore, a few transients showing low-level multi-year variability were also identified. These events were mistakenly classified as SN-like by the CNN, but based on the results of the test sample it is expected that some AGN are misclassified as $\sim 5\%$ of the AGN (4/79) were labelled as SN-like. The inspection of few tens of the 690 events classified as AGN by the CNN did not reveal mistakes as all of the light curves showed at least some level of multi-season variability. While the CNN classifier certainly is not perfect, it seems to have performed better than the original selection done with linear fits as is supported by its performance on the test sets.

The next implemented cut was to remove some highly probable type Ia candidates. Type Ia light curve evolution is well understood and therefore light curve fitters — such as `PSNID` — are good at recognising them. Therefore for this cut I relied on the library of `PSNID` fits DES-SN performed on every transient. Using parameters `FITPROB` > 0.91 and `PBAYES` > 0.82 for Ia fits, highly likely type Ia SNe candidates were recognised and removed. No known RETs would have been cut with the selected threshold, but approximately half of the known type Ia SNe (220/406) would have been recognised. The cut resulted in 449 removed events in total but only 46 were inside the selection region. The resulting peak colour vs. rise time distribution is shown in Figure 3.6 (bottom left) and its clear that significant portion of the events have indeed been removed from the region type Ia SNe exhibit in Figure 3.4.

As the final cut I focused on the slowly declining events of any kind. RETs are rapidly evolving by nature so it is easy to design a cut that would reject any transients that decline more slowly. At this stage, all events that declined to half of their r band peak flux > 24 d were removed from the sample. Such a cut would remove 48/68 spectroscopically classified type II SNe, but only one RET. The RET in question (DES17X3bvf) had a 16 day gap in observations in r band during which the g band was observed three times characterising the peak. Thus, the peak is missed in the r and the remaining detection

are low signal-to-noise. The cut resulted in total 549 events being removed, 347 of which were in the RET selection region. The distribution of the remaining events is shown 3.6 (bottom right) and its clear that the cut was good at rejecting extra transients inside the selection region, while having only a small effect outside. As a result 1261 events remained in total with an acceptable number of only 546 in the RET region.

The 546 transients were then inspected visually. While the majority were rejected for being spurious detections, showing level of multi-season variability missed by the CNN, or exhibiting evidence for a slower decline timescale, 14 new RETs were discovered with the method. Eight were not inspected during the first search as they were either too faint to pass the cuts or because they exhibited FWHM > 30 d. The remaining six, however, passed the cuts but they were not identified due to the large number of transients in the visual inspection. With the addition the final RETs sample discussed in this thesis stands at 106 events. The full sample and the updated search method have been presented in Wiseman et al. (2020a).

The small number of RETs discovered with the described enhanced selection criteria highlights the fact that the original search, despite its simplicity, was very efficient in discovering RETs in the first place, even if all inspected events were not identified in the first search. However, a parameter space quantifying the rise timescale and the colour during the rise is undoubtedly significantly better as can be seen based on the reduced number of events that passed the cuts visual inspection ($\sim$ 550 vs. $\sim$ 1600). Furthermore, such an approach is likely very useful during a live selection of transients for follow-up observations as it relies only observable properties during the rise.

3.3 Sample Overview

The two searches described above resulted in discovery of 106 RETs including 52 with known spectroscopic redshifts. The sample represents the largest collection of rapidly evolving extragalactic events to date and it provides an intriguing data-set to study. The analysis of RET properties form the bulk of this thesis and in next three Chapters I will present the observable properties of the sample of RETs, followed by an investigation of their host galaxies and a discussion on the implications of the findings on the physical interpretation. Here, however, I will provide a brief overview of the sample and discuss aspects such as redshift and absolute magnitude distribution of sample and the host galaxy association of the individual transients. All DES-SN light curves presented in this thesis in the context of scientific analysis have been corrected for Milky Way extinction using colour excesses from Schlafly & Finkbeiner (2011). Throughout the thesis I assume a flat ΛCDM cosmology with $\Omega_{\rm M} = 0.3$ and $\rm H_0 = 70$ km s^{-1} Mpc^{-1}.

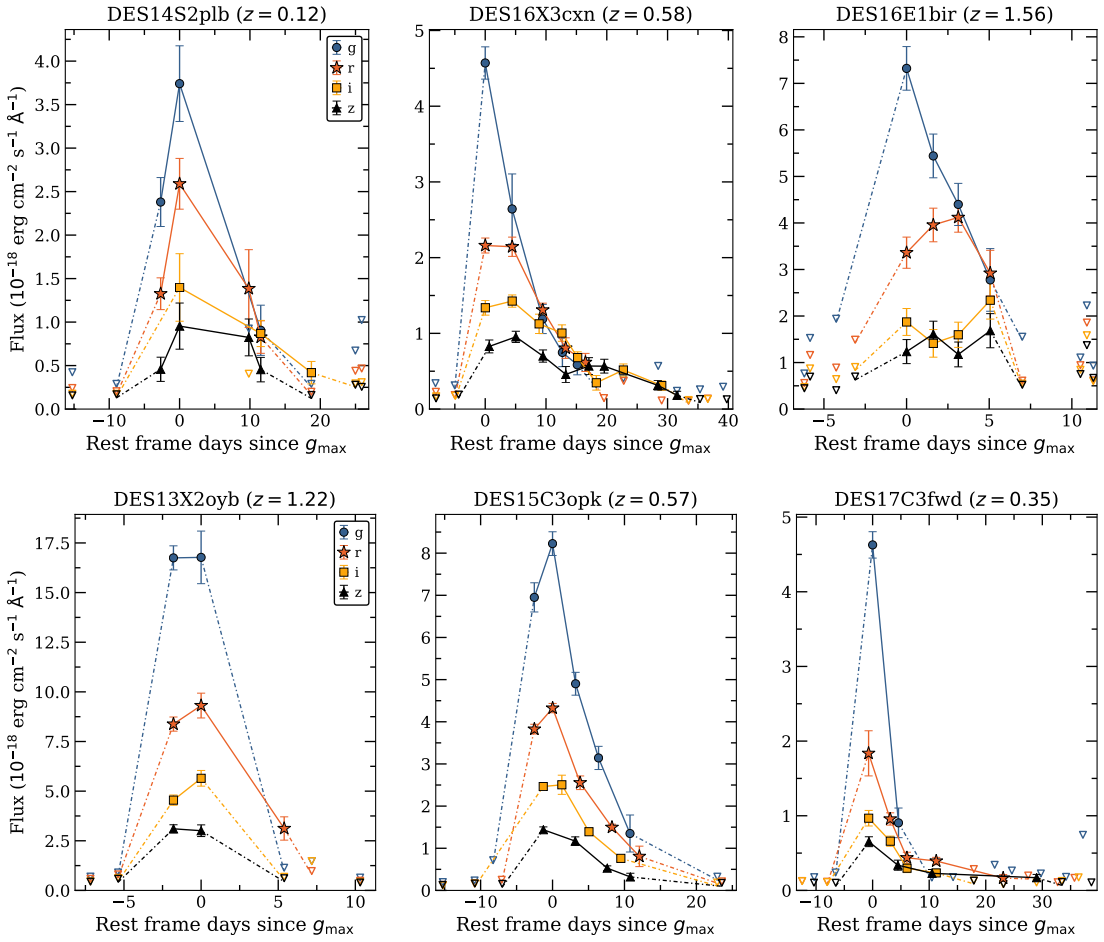

FIGURE 3.7: Example rest frame light curves for three gold sample (top) and silver (bottom) transients. Open triangles represent 1σ error of data points below 3σ detection. Time is measured from the observed peak in g band.

The basic information of the sample is presented in Tables B.1 – B.3, where the transients have been divided into gold, silver and bronze samples based on the quality of the available data. The spectroscopic redshifts of the gold and silver transients are known, but the gold ones have better photometric observations. They are required to have at least three 1.5 d epochs during which at least 3/4 bands have a detection. As a result, the silver sample RETs have either less than three epochs altogether or several 1.5 d intervals with detections but less than three with data in more than two bands. A significant portion of the silver sample transients are in the DES-SN deep fields and thus they have otherwise good quality photometric data but different bands are often observed on different nights. Multi-band observations during the same epoch are important for the blackbody fits performed in Chapter 4. In case a transient has several such epochs of data, the evolution of temperature and radius can be analysed. The gold sample consists of 27 RETs and the silver 25 bringing the number of RETs with known redshift to 52. A few example rest frame light curves of the gold and silver sample RETs are presented

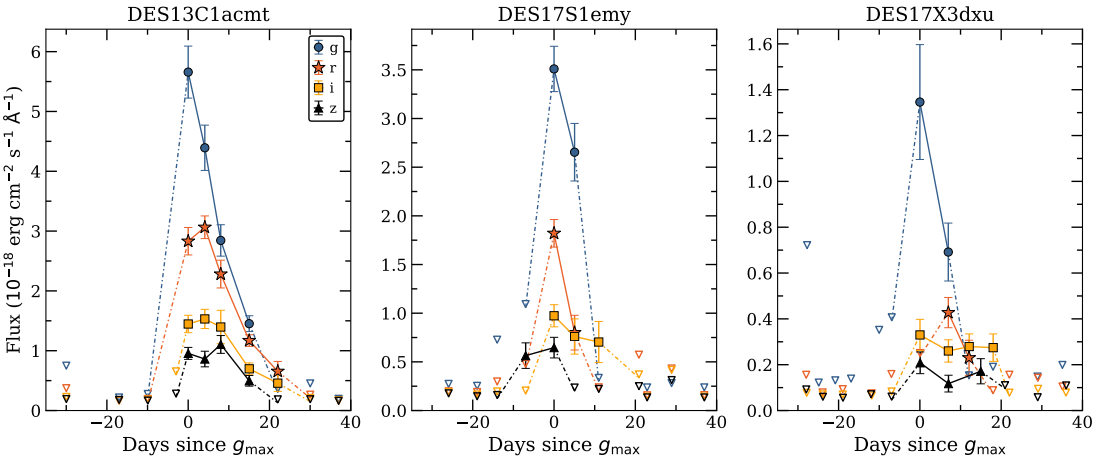

FIGURE 3.8: Example observer frame light curves for three bronze sample transients. Open triangles represent 1σ error of data points below 3σ detection.

in Figure 3.7 and all of the light curves in Figures C.1 and C.2 in Appendix C.

The remaining 54 bronze sample transients look photometrically similar to gold and silver ones in observer frame, but their spectroscopic redshifts are not known. Therefore, while several of them have good quality light curves, their true luminosities and timescales can not be assessed. The majority of the analysis presented in this thesis is performed on the gold and silver transients, but the bronze events are an important addition to the sample to demonstrate how common the rapid extragalactic phenomena truly are. A few example observe frame light curves of the bronze sample transient are presented in Figure 3.8 and all of them in Figure C.3 in Appendix C.

Using the 52 RETs with known redshift the distribution of the sample can be investigated. The RETs are found on a wide redshift range from 0.05 to 1.5 and the corresponding absolute magnitudes range from -15.8 of faint CCSNe to -22.6 equalling most of the SLSNe. The wide distribution is demonstrated in Figure 3.9 where the absolute magnitudes measured at the observed epoch closest to peak in g band is shown for all four bands against the redshift. A significant majority of the observed transients are found between redshifts 0.2 and 0.8 with only a few outside this range. Above redshift $z = 0.8$ most key emission features in host galaxy spectra used to determine the redshifts are shifted out of view for optical spectrographs and the remaining lines — such as [OII] λ3727 — are shifted into wavelength ranges heavily contaminated by night sky lines. As such OzDES had difficulties obtaining spectroscopic redshifts above $z = 0.8$ (Childress et al. 2017). The figure also presents the approximate k-corrected magnitudes estimated based on the blackbody fits at the peak epoch. Due to the high redshifts of the transients, many of them would have been several magnitudes fainter had they occurred in the local Universe.

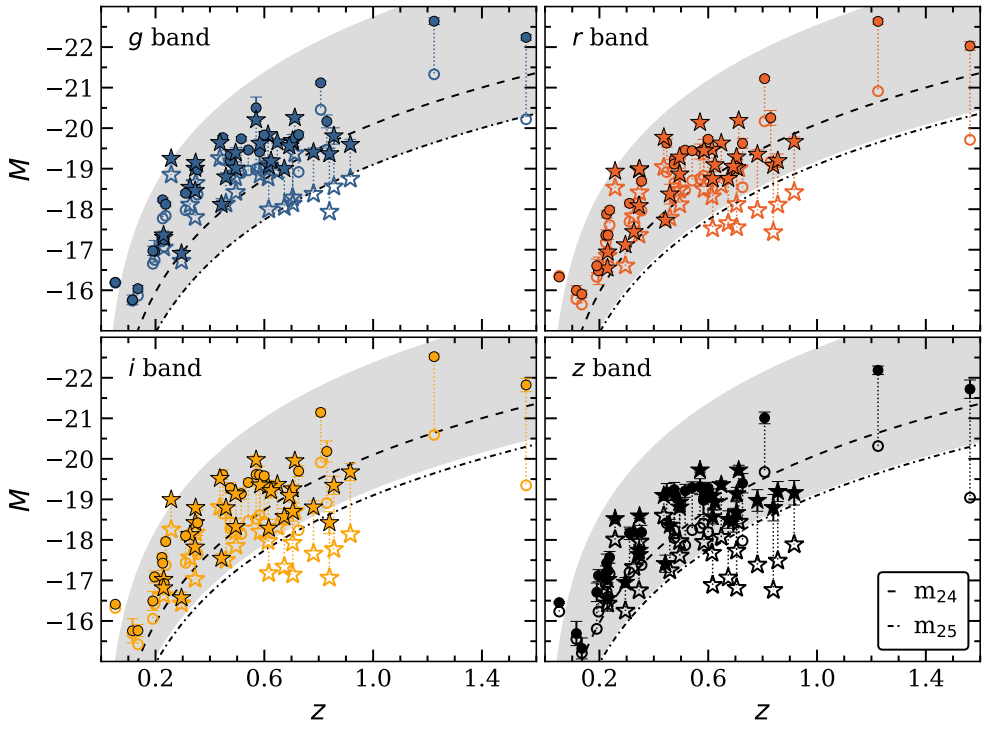

FIGURE 3.9: Peak absolute magnitudes of RETs against redshift. The peak was assumed to be the time of the brightest observed g band data point and the magnitudes are the ones taken closest to that. Objects found in DES-SN deep and shallow fields are marked with stars and circles, respectively. The open markers represent corresponding k-corrected magnitudes as estimated based on best blackbody fits at peak. The k-corrected values have not been plotted for those RETs whose blackbody fits at peak were based on two bands. Dashed and dot-dashed lines correspond to apparent magnitudes of 24 and 25, respectively. Grey band underneath represents the region where bronze sample RETs would be based on their apparent peak magnitudes.

All gold and silver sample RETs and the majority of the bronze sample RETs (41/54) have a reliable host galaxy identification and the information of the these hosts is presented in Tables B.4 – B.3. For gold and silver samples the spectroscopic redshifts, $z_{\rm Spec}$, of the host galaxies are known, but for the hosts of bronze sample events they could not be obtained. Instead for most of the bronze sample hosts photometric redshifts, $z_{\rm Phot}$, have been estimated based on the host galaxy Spectral Energy Distributions (SEDs; Bonnett et al. 2016). While $z_{\rm Phot}$ values are less reliable, and thus cannot be trusted to yield exact results in case of every transient, they can be used to compare the distributions of the spectroscopic and photometric samples. Note that the $z_{\rm Phot}$ were estimated using the DES-SN science verification data and thus eight fainter host galaxies discovered in the "deep-stack" images (Wiseman et al. 2020b) do not have $z_{\rm Phot}$ estimated by DES-SN yet. The deep stacks were created by coadding all good quality science exposures from the five years of DES-SN together and thus they are significantly deeper than the SV images.

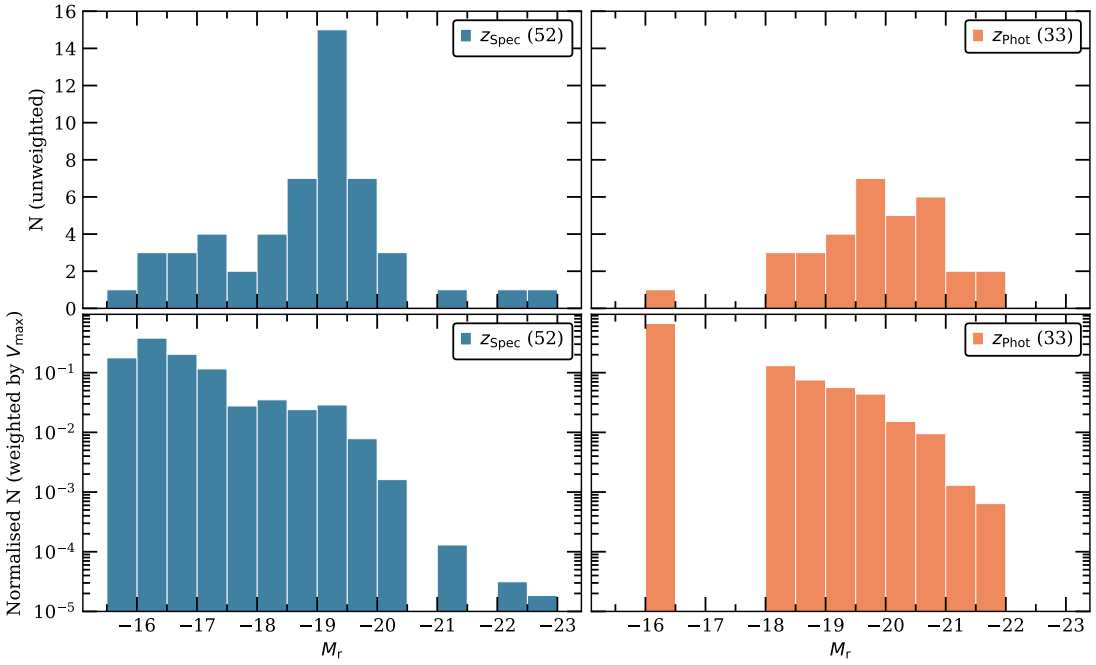

FIGURE 3.10: Absolute magnitude histograms of the RETs in the r band (top panel) and the corresponding normalised distributions weighted by the maximum observable volume, V_{max}, each event would have been seen in (bottom panel). The gold and silver events are shown in blue (left) and those bronze sample events with z_{Phot} estimate in red (right).

The absolute magnitude histograms for r band are shown in Figure 3.10 for both the 52 RETs with z_{Spec} and the 33 with z_{Phot} (top panel). Both distribution look visually similar and peak around $M_r \sim -19.5$. However, in the figure the same distributions are also shown after weighing each transient for the maximum volume, V_{max}, it could have been detected in. The threshold apparent magnitudes for the detection were assumed to be 24 mag in shallow fields and 25 mag in deep fields. The created $1/V_{max}$ distributions clearly show that in fact the fainter transients are more common, but they are only discovered in small numbers in the nearby Universe. The histograms also imply that brighter end of the distribution ($M_r \lesssim -20$) is significantly rarer than the faint end, but that it is also underrepresented in the gold and silver samples. Such a result is reasonable as rarer events are more likely discovered at high redshifts (i.e. larger volume) and thus spectroscopic redshifts to the hosts are less likely obtained due to the faintness of the hosts.

Using a similar technique to $1/V_{max}$ luminosity distribution above, it is possible to estimate a rough volumetric event rate based on the sample of 52 events with a spectroscopic redshifts. The recovery efficiency of every RET was assumed to be the ratio of the maximum volume it could be detected in and the volume at a cutoff redshift of $z = 1.56$ where the most distant RET was discovered. Note that efficiency could not be higher than 1. The found rate of $\gtrsim 10^{-6}$ events per Mpc^{-3} yr^{-1} is $\sim 1.5\%$ of the volumetric

CCSN rate (Li et al. 2011b). It important to emphasises that this is a lower limit of the rate, as it was estimated with the assumption of complete sample (down to the limiting magnitudes of the DES-SN search fields). As a result the rate is smaller but consistent with the rate of $4.8 - 8.0 \times 10^{-6}$ events per Mpc^{-3} yr^{-1} estimated by Drout et al. (2014) for the PS1-MDS sample and $\sim 4.0 \times 10^{-6}$ events per Mpc^{-3} estimated by Tampo et al. (2020) for HSC-SSP Transient Survey RETs.

Finally, it is worth noting that the redshifts of the sample of 72 events published in Pursiainen et al. (2018) have been updated in case of few events. New redshifts were obtained for the hosts of DES13X2oyb and DES16X3erw by OzDES and these events have been upgraded to join the silver sample. In case of DES13X2oyb the redshift was based one strong line present in the spectra. The line has been assumed to be [OII] λ3727, corresponding to redshift 1.22. Furthermore, OzDES also retracted redshift of host galaxy of DES13X3pby and the transient is now found in the bronze sample.

3.4 Summary

In this Chapter I presented the results of the two searches used to look for rapidly evolving transients in the DES-SN data. In the first search, the light curves of all DES-SN SSTs were characterised by using linear fits to estimate the background variation outside the nominal discovery season and Gaussian fits to roughly characterise the light curve duration. Using various cuts determined based on spectroscopically classified SNe and AGN from DES-SN a sample of $\sim 1600/21000$ transients were visually inspected in order to discovery truly rapidly evolving ones. The search was first performed on the first four years of DES-SN data and once year five had finished that data was queried as well. This part of the analysis resulted in discovery of 92 RETs from DES-SN.

However, as the first search was very simplistic it relied heavily on visual inspection of the available data and thus it is difficult to be certain how complete the discovered sample truly was. In order to verify the success of the first search, a more sophisticated one was designed based on the discovered sample of 92 RETs. The blue colours and fast rise times of RETs distinguish them well from known SNe classes. Therefore, the search was designed to use rise time in r band and $g - r$ colour at peak, as estimated based on GP light curves, to select candidates for further inspection. Various contaminants, such as AGN, type Ia SNe and slow declining transients, were excluded by implementing cuts using a CNN classifier, `PSNID` fits and light curve decline behaviour. As a result light curves of ~ 550 transients were visually inspected and a further 14 RETs were added to the sample. While more RETs were discovered with the new method, the result verifies that the original search was very good at discovering RETs despite its simplicity.

The discovered sample of 106 RETs is the largest single compilation of rapid extragalactic phenomena to date. The 52 RETs with $z_{\rm Spec}$ are found on a wide range from $z = 0.05$ to $z = 1.56$ and correspondingly they exhibit peak luminosities from faint CCSN of $M = -15.8$ to bright SLSN of $M = -22.6$. The significant majority of the RETs (93/106) are associated with a host galaxy and by using the host redshifts (both $z_{\rm Spec}$ and $z_{\rm Phot}$), the luminosity functions of the sample were determined. While the faintest RETs are small in numbers they appear to be the most likely ones in both spectroscopic and photometric samples. Furthermore, while the bright RETs ($M \lesssim -19.5$) appear to be significantly rarer compared to the fainter ones, they also seem to be under represented in the spectroscopic sample due to difficulties obtaining spectroscopic redshifts to their distant hosts. Finally, the estimated rate of $\gtrsim 10^{-6}$ events per Mpc^{-3} yr^{-1} is $\sim 1.5\%$ of the volumetric CCSN rate (Li et al. 2011b) is in good accordance with literature rates.

In the next three Chapter I will perform analysis of the discovered RETs. In Chapter 4 I will present the observable properties including both photometric and spectroscopic data and in Chapter 5 I will focus on analysing the host galaxy properties. Finally in Chapter 6 I will discuss the implications of the performed analysis on the physical interpretation of the RETs and compare properties of RETs with discovered fast literature transients.

Chapter 4

Rapidly Evolving Transients: the Observational Properties

In the previous chapter I introduced the sample of 106 rapidly evolving transients and discussed how I discovered them in DES-SN data-set. In this chapter I will carry on the analysis of the sample and will present the observable properties — both photometric and spectroscopic — they exhibit and compare them to literature transients. The work in the chapter is performed on the 52 gold and silver sample RETs alone, because the spectroscopic redshift is a crucial detail and thus the properties of the bronze sample events are not well enough constrained.

4.1 Photometric Properties

The most striking photometric properties of the RET sample are the fast evolution of the DES-SN light curves and the wide range of peak brightness found between absolute magnitudes -15.8 and -22.6. The features are similar to the previously discovered sample of 10 RETs from PS1-MDS (Drout et al. 2014). A comparison is shown in Figure 4.1 where example g and r band light curves of DES-SN RETs are shown with three representative events from Drout et al. (2014). However, while the light curves are visually similar, the DES-SN RETs are found in a significantly wider range of brightnesses (-17 to -20 mag for PS1-MDS sample). Thus the DES-SN provides a improved data-set to investigate the properties of the fast transients. Note that none of the light curves in the Figure 4.1 have been k-corrected and thus they can probe different rest frame wavelengths.

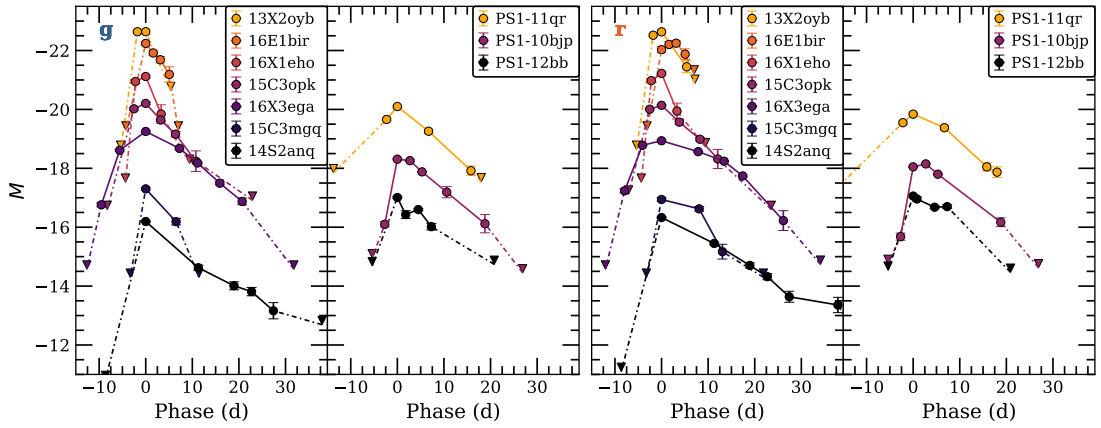

FIGURE 4.1: Light curves of selected DES-SN and PS1-MDS RETs in g (left) and r (right) bands. Note that light curves are not k-corrected and probe different rest frame wavelengths.

4.1.1 Rise and Decline Timescales

In this thesis I refer to the brightest observed data point in g band as the peak of the event, but the rise and decline times for a given band are calculated with respect to the date of observed brightest data point in that band. The rise time, $t_{\rm rise}$, is then defined to be the rest frame time between the observed peak and the last non-detection ($< 3\sigma$) before it in each band. While such a definition will not probe the real physical rise time of the transients, any other parametrisation of the rise would be difficult to estimate for the majority of the RETs. Due to their fast light curve evolution, the weekly cadence of DES-SN is too long to capture the majority of the RETs on the rise. As a result, the first detection is the observed peak for a significant portion of the sample and thus only the time of the non-detection can be used to uniformly constrain the rise time. Therefore, the resulting estimates of $t_{\rm rise}$ are not exact. Furthermore, based on the fact that RETs are typically rapidly declining from the peak (See Figures C.1 and C.2) the rise times are likely upper limits in case of many RETs.

In a similar manner, estimating the decline times also has its challenges. While there are more data points to characterise the decline than the rise, there are still only a handful per band. Thus, estimating a uniform parameter of the decline is difficult without an underlying assumption of a model. Here, I have assumed that the declines are exponential in nature as seems to be the case based on the fits presented in Figure 4.2. The fits were performed on every data point on the decline including the peak. Furthermore, when available the first two post-peak non-detections were also included to provide extra data points to constrain the fits. The non-detections are not shown in the figure. The peak was excluded from the fit if it was clear that the peak detection was not yet on the decline. While not every data point of every transient is well fitted by the model, the

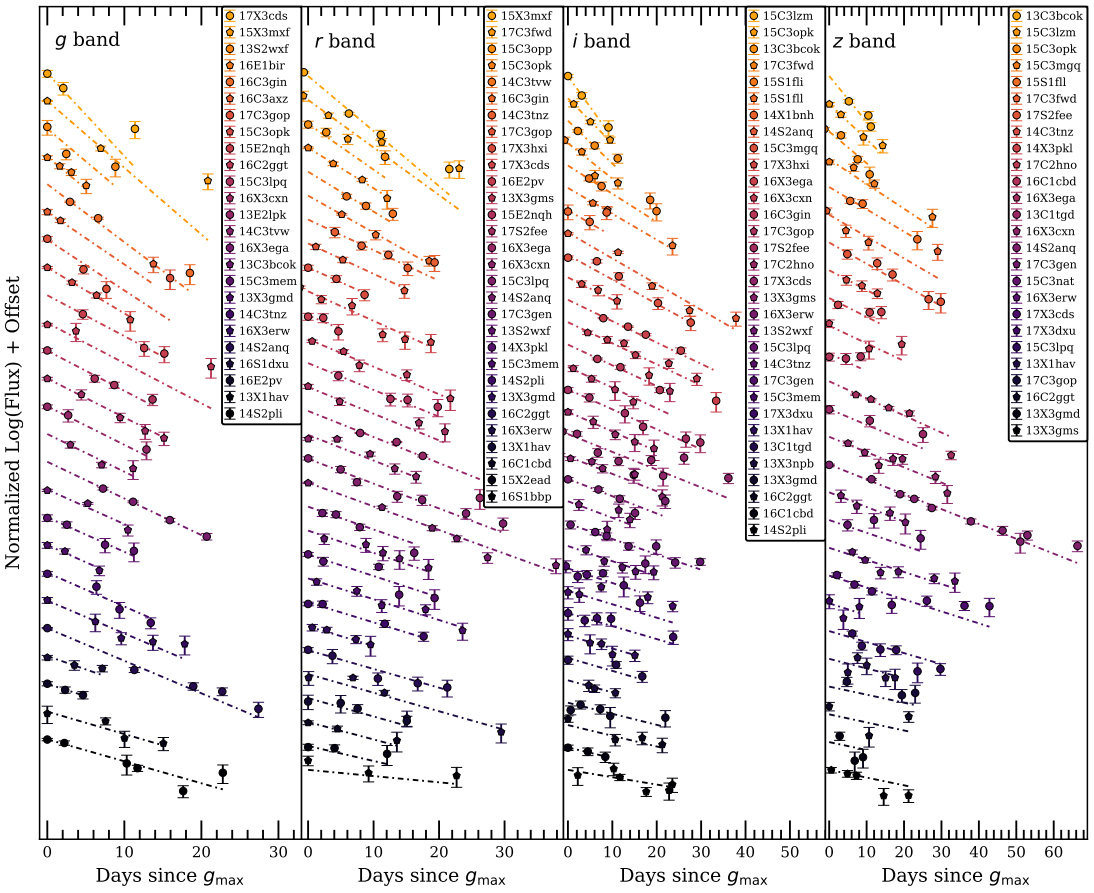

FIGURE 4.2: Exponential fits to RET post-peak light curves. Only events with more than two 3σ detections are shown. The best fits are plotted up until the last shown data point for each event.

grand majority are. Therefore, a simple exponential model appears to describe the light curve declines of the RETs.

I have defined the decline time, $t_{\rm decline}$, as the time the exponential fit takes to decline to 1/10 of the observed peak flux, but the decline can also be parametrised by an exponential decay timescale τ (see e.g. Arnett 1982). Time above half maximum brightness, $t_{1/2}$, was also estimated based on the rise time and the fits on the decline. Both rise and decline times are determined with respect to the observed maximum, and therefore they are subject to the weekly cadence in the observer frame. The uncertainties for decline times were estimated with a Monte Carlo approach with 1000 realisations of the light curves based on errors on the data. The errors are stated at 1σ confidence. The rise and decline times as well as the above half maximum brightness for all 52 RETs are given in Tables B.7 and B.8 in g band.

Even though the rise times estimates are likely upper limits, the majority of the transients still have $t_{\rm rise} \lesssim 10$ d. In fact, only three RETs in the gold and silver samples have longer rise times in g band. Out of these, DES13X3gms has a $\sim$ 10 d gap in the g band

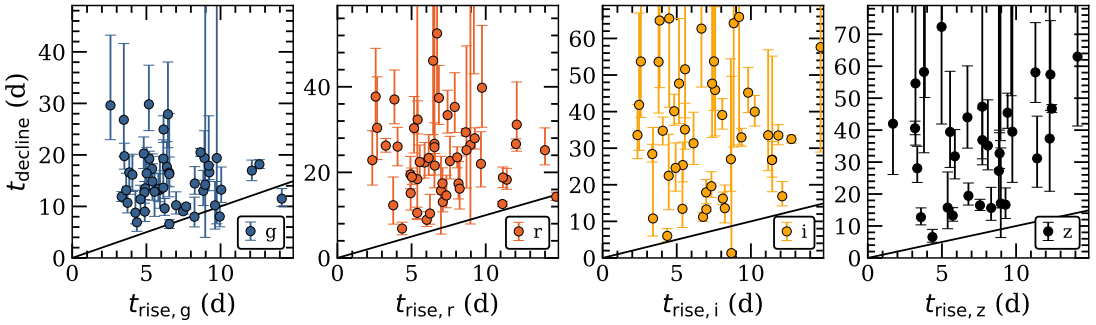

FIGURE 4.3: $t_{\rm decline}$ against $t_{\rm rise}$ for gold and silver samples transients in all four bands. The black solid line represents $t_{\rm decline} = t_{\rm rise}$.

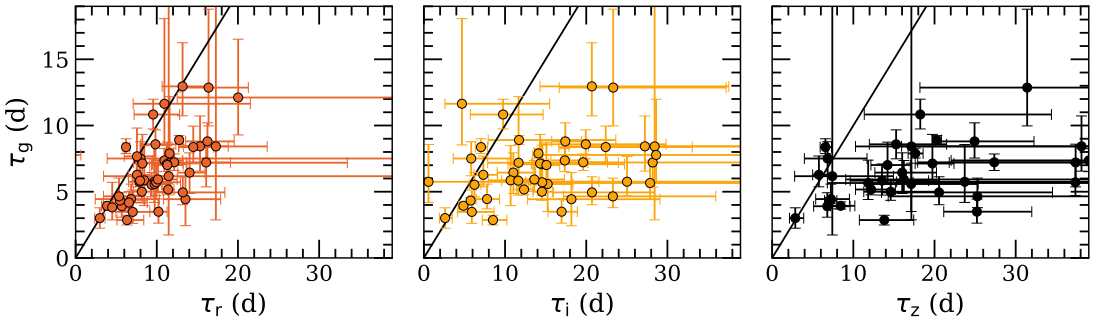

FIGURE 4.4: Decay timescale $\tau_{\rm g}$ of gold and silvers sample RETs plotted against $\tau_{\rm r}$, $\tau_{\rm i}$ and $\tau_{\rm z}$. Black solid line represents equal timescales.

observations before the peak, DES16C3gin has a detection on the rise and thus the first non-detection is more than 10 days before peak. However, in the case of DES16X3ega, the photometric data shows clear detections in g and i bands roughly 10 days before the peak and thus rise time is longer than that (see light curve in Figure C.2).

RETs are slower to decline than to rise, as can be seen in Figure 4.3 where the decline times are presented against rise times for each band. A similar finding was reported by Drout et al. (2014), but virtually all SNe exhibit the same behaviour. The exponential decline timescales also appear to be longer the redder the band in question is, as can be seen in Figure 4.4 where $\tau_{\rm r}$, $\tau_{\rm i}$ and $\tau_{\rm z}$ are shown against $\tau_{\rm g}$. Furthermore, the mean values of τ were found to be 6.7, 11.1, 14.9 and 17.6 days in the *griz* bands. While the trend seems reasonable, note that as the RETs are intrinsically fainter in the redder bands constraining the decline times for these bands is difficult and the values have large uncertainties.

The exponential fits were also used to estimate Δm_{15} (magnitudes an event declines in the first 15 days after the peak; Phillips 1993) value for all RETs. Thus, to further demonstrate the fast timescales of the discovered RETs, their peak magnitudes are shown as a function of Δm_{15} in Figure 4.5 in comparison to selected transient events from literature. The majority of the RETs are found at similar values of Δm_{15} and M as the

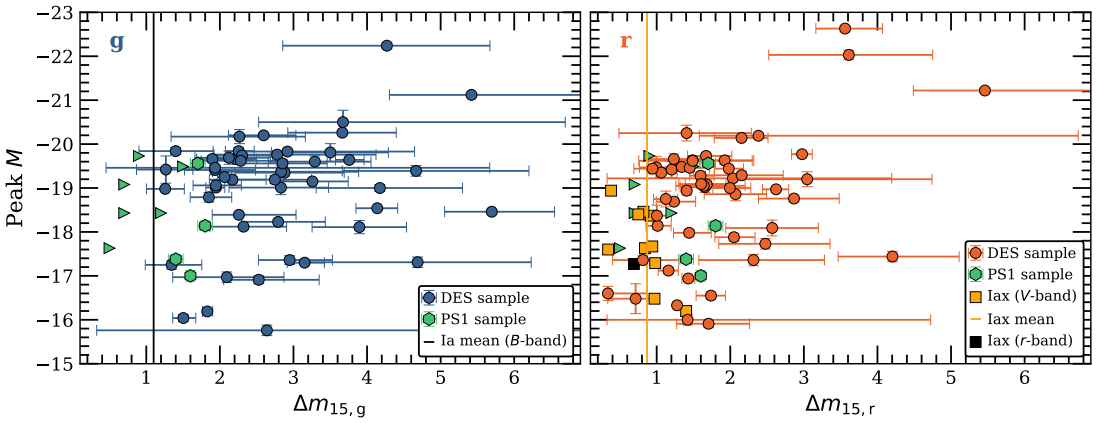

FIGURE 4.5: Δm_{15} distribution of gold and silver sample RETs in g (left) and r (right) bands in comparison with other transient types. Δm_{15} for the prototypical type Ia SN 2011fe (Pereira et al. 2013) in B band is considerably smaller than $\Delta m_{15,g}$ for all of our events. Δm_{15} for Iax SNe in V band (Foley et al. 2013) partly overlap with the slower end of our events in r band. However, as V band is bluer than r one would expect it to have a higher value in comparison. Additionally, Δm_{15} for Iax SN 2015H in r band (Magee et al. 2016) is smaller than most measured in V band. The values of Δm_{15} coincide well with the PAN-STARRS1 (PS1) events from Drout et al. (2014). Right pointing triangles refer to PS1 events that have only lower limit on Δm_{15}. Δm_{15} for our events has been estimated based on exponential fits.

PSI-MDS fast events, but the DES-SN distribution seems to extend towards faster and brighter regions of the Figure. Thus, as expected, the RETs also appear to be significantly faster when compared to type Ia and Iax SNe. Note that the estimating Δm_{15} is difficult for many of the RETs as the light curves are not necessarily observed that long. Thus, the values presented in Figure 4.5 are estimated based on the exponential fits on the post-peak light curves presented in Figure 4.2.

Finally, the gold and silver sample RETs are characterised by fast photometric evolution with time above half of the peak brightness $t_{1/2} \lesssim 12$ d in rest frame (see Tables B.7 and B.8). As discussed in Chapter 1, such a threshold distinguishes the fast transients from the grand majority of standard SNe types and it is a clear implication that the work presented in this thesis is probing similar transients as presented in Drout et al. (2014).

4.1.2 Blackbody Fits

The next part of the analysis was to investigate the distribution and evolution of temperature and radius of the RETs based on blackbody fits performed on their photometric data. According to the DES-SN observing strategy the four *griz* bands were not always observed during the same night. Due to this, the data points used for the blackbody fitting were not required to be taken on the same night, but the could be taken on consecutive night. As such the fits were performed on every interval of 1.5 rest frame days

that had a data point in at least two bands. The temperature T and radius R of the transient at a given epoch were found by fitting the observed fluxes of different bands, F_λ, with the following equations:

$$F_\lambda(T,R) = \frac{2\pi hc^2}{\lambda_{\rm eff}^5} \cdot \frac{1}{e^{\frac{hc}{\lambda_{\rm eff} kT}} - 1} \cdot \left(\frac{R}{D_{\rm l}}\right)^2, \tag{4.1}$$

$$\lambda_{\rm eff} = \frac{\int_{\lambda_{\rm l}}^{\lambda_{\rm h}} t(\lambda) \cdot B(\frac{\lambda}{1+z}, T) \cdot \lambda \cdot d\lambda}{\int_{\lambda_{\rm l}}^{\lambda_{\rm h}} t(\lambda) \cdot B(\frac{\lambda}{1+z}, T) \cdot d\lambda}, \tag{4.2}$$

$$B(\lambda,T) = \frac{2\pi hc^2}{\lambda^5} \cdot \frac{1}{e^{\frac{hc}{\lambda kT}} - 1}, \tag{4.3}$$

where $D_{\rm l}$ is the luminosity distance of the transient, $t(\lambda)$ the transmission function of the band in question and $\lambda_{\rm l}$ and $\lambda_{\rm h}$ the wavelength limits for that band. Note that, the blackbody fits were performed using the effective wavelength, $\lambda_{\rm eff}$, of each band. The effective wavelength depends not only on the redshift of the event, but also on the shape of blackbody SED. To estimate the shape, the corresponding blackbody has to be calculated in the rest frame ($\lambda/(1+z)$) and then shifted in to the observer frame.

The best fitting blackbody SEDs for every epoch of nine example RETs are shown in Figure 4.6. A blackbody model describes the data well around the peak brightness, but in some cases the model starts to diverge from the data after a few weeks. For instance, the data of DES14S2anq is fitted almost perfectly up to $t = 11.3$ d, but afterwards the blackbody seems provide a poor fit. Similarly the fits to DES15C3lpq and DES16X3cxn seem to be worse at the last few epochs than they were at the earlier ones around the peak brightness. Therefore, it is possible that the late phase emission of the rapid events is not well described by a blackbody in at least some cases. However, the majority of the RETs only have photometric data up to a few weeks and thus it is not possible to investigate if all of the events eventually diverge from a blackbody. The best fitting blackbody parameters at the epoch of peak brightness, including the corresponding pseudo-bolometric luminosities and number of bands fits performed on, are given in Tables B.9 and B.10 in Appendix B. The uncertainties are stated at 1σ and they were estimated with a Monte Carlo approach with 500 realisations assuming Gaussian uncertainties.

4.1.3 The Distribution of Peak Temperatures and Radii

The peak temperatures are found mostly between $\sim$ 8000 – 30000 K but higher values also exist such as 60820^{+39200}_{-22700} K for DES14C3tnz. While the uncertainties of the high temperatures are large, it is because the peak of the blackbody SED is now in the UV regime due to the high temperature and the fitting is done on the slope of the SED. As a result constraining the temperature is uncertain. However, for instance for DES14C3tnz

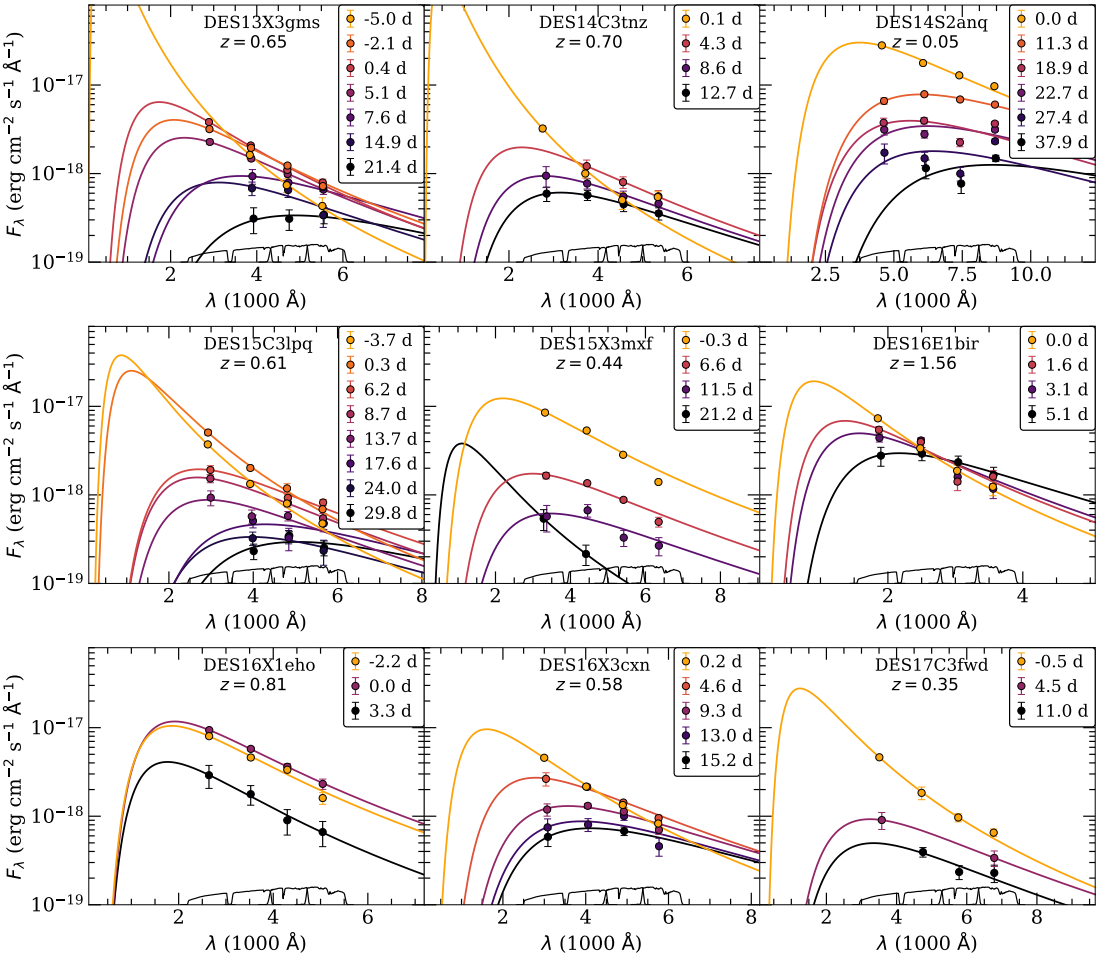

FIGURE 4.6: Example blackbody fits of nine RETs. Times of the individual fits are given as the mean of the used data points since the observed peak in g band in rest frame days.

it is clear that the g band emission is very strong in comparison riz bands (see Figure 4.6) and its safe to assume the temperature at peak is truly very hot in the first epoch.

Similarly to the temperatures, the peak radii are also found on a wide range of values between a few 10^{14} cm and a few tens of 10^{14} cm. The found distributions of both temperatures and radii are broadly consistent with the ones found in literature. Arcavi et al. (2016) and Whitesides et al. (2017) discussed temperature and radius evolution for bright objects ($M_g \sim -20$), finding these to be cooler (with temperatures around 10000 K) and mostly larger (with $R \gtrsim 10^{15}$ cm) than the DES-SN RETs with comparable absolute magnitudes. On the other hand, Drout et al. (2014) found the temperatures to be slightly higher when compared with objects of similar brightness in the DES-SN sample, and therefore the radii are several times smaller. Regardless of the slight differences, the estimated peak bolometric luminosities found in the range $\sim 10^{42} - 10^{44}$ erg/s are comparable with other fast transients.

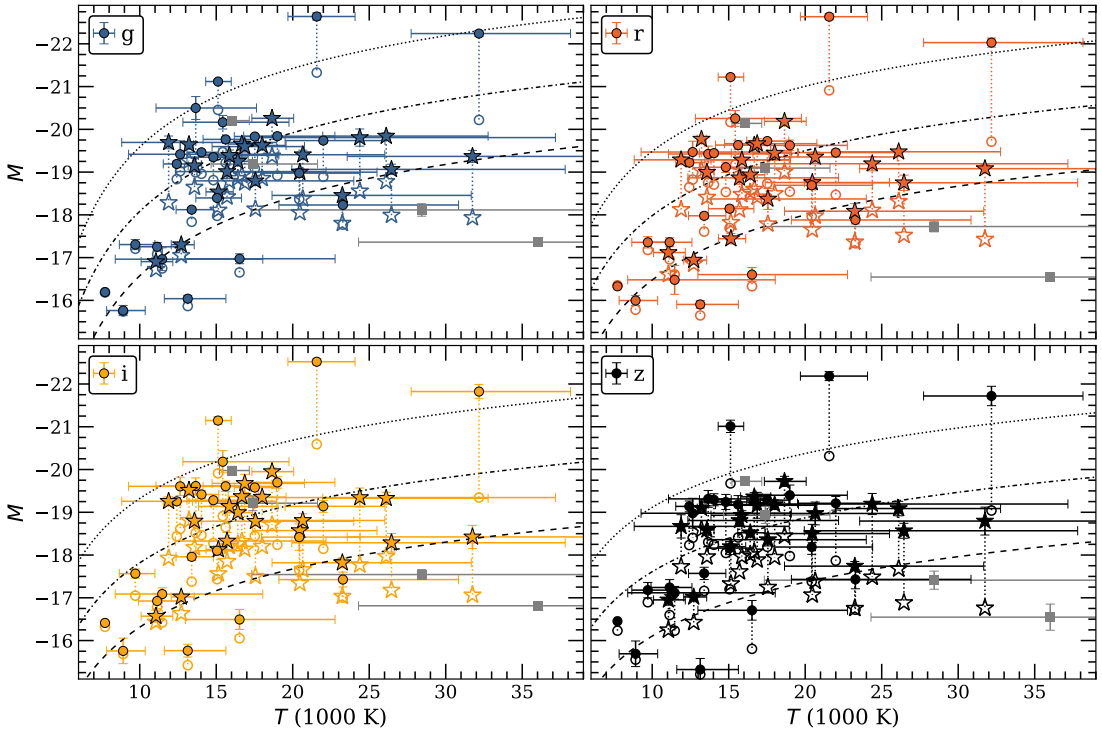

FIGURE 4.7: The peak absolute magnitude against best fitting blackbody temperature at the time of peak brightness. The magnitudes are taken from the data points closest to the peak in g band. RETs in deep and shallow fields are plotted with stars and circles, respectively. The open markers refer to magnitudes k-corrected with the peak blackbody fits. The k-corrected magnitudes have not been given for RETs whose peak fits were based on only two bands (grey squares). Note that the few RETs with peak temperature > 40000 K are excluded from the Figure. Errors for temperatures are quoted at 1σ confidence. The three dashed lines correspond to absolute magnitudes in the rest frame for constant radii of $R = 5 \cdot 10^{14}$ cm (bottom), $R = 10^{15}$ cm (middle) and $R = 2 \cdot 10^{15}$ cm (top).

The brightness of any blackbody is dependent on its temperature to the fourth power and radius to the second. Thus it is not surprising that the peak temperatures of RETs are clearly correlated with the absolute magnitudes as illustrated in figure 4.7. The majority of DES-SN RETs are clustered around ~ 15000 K, while the faintest objects have temperatures $\lesssim 10000$ K and the brightest are found at $\sim 20000 - 30000$ K. However, in the Figure it is also clear that the temperature alone does not define the peak brightness. To examine the impact of radius on the brightness of the RETs, curves of constant radius are also shown in the Figure for $R = 5 \cdot 10^{14}$ cm, $R = 10^{15}$ cm and $R = 2 \cdot 10^{15}$ cm. The curves are in rest frame and thus correspond to the magnitudes after the k-corrections shown with open markers. A trend similar to the peak temperatures is visible. The fainter RETs seem to be found with smaller values of radii while the brighter appear to be larger in size.

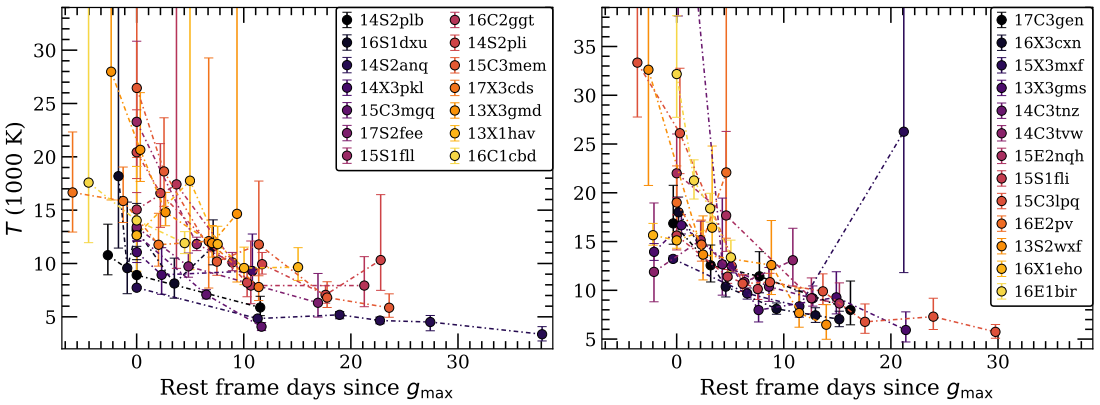

FIGURE 4.8: Temperature evolution of gold sample transients, with events fainter than $M_{\mathrm{g,peak}} = -19.5$ shown on the left and brighter on the right. Brighter events are plotted sequentially in brighter colours in both panels.

4.1.4 Temperature and Radius Evolution

The blackbody can also be used to investigate the evolution of temperature and radius of the RETs. The evolution of temperature based on the fits is shown in Figure 4.8 for the gold sample transients. The fainter half of shown RETs ($M_{\mathrm{g,peak}} > -19.5$) are presented on the left and the brighter half ($M_{\mathrm{g,peak}} < -19.5$) on the right. While the resolved temperatures have high uncertainties as the observed data points do not probe the peak of the blackbody SEDs, the trend clearly shows that the temperatures are decreasing rapidly in time. Virtually all of the presented RETs are found to have temperatures below 10000 K within a few weeks of the peak brightness, regardless of the peak temperature.

For most RETs the decrease of temperature is accompanied by an increase in radius, as shown in Figure 4.9 (left) for six gold sample RETs. The rate of increase based on these curves imply photospheric velocities from $v \sim 8000$ km/s for DES14S2plb up to $v \sim 35000$ km/s for DES16E1bir. The stated values are not the true ejecta velocities due to the decreasing opacity of the expanding material, but they can be used as a lower limit for the expansion rate. Such high velocities constrain the explosion time to be $\lesssim 5$ d before the first detection in several cases. For instance, the radius of DES14S2plb would recede to zero in ~ 3 d and the radius of DES16E1bir ~ 2 d, when assuming constant expansion rates.

The velocities are well in the midst of those observed in SNe. Type II SNe are found at $\lesssim 10000$ km/s 50 d after explosion (Gutiérrez et al. 2017b) and type Ia SNe at ~ 9000 – 14000 km/s (Benetti et al. 2005) matching with the lower velocities. On the other hand, the higher more extreme velocities have also been reported for SNe as for instance type Ic-BL SNe are found with velocities up to 30000 km/s (see e.g. Modjaz 2011)

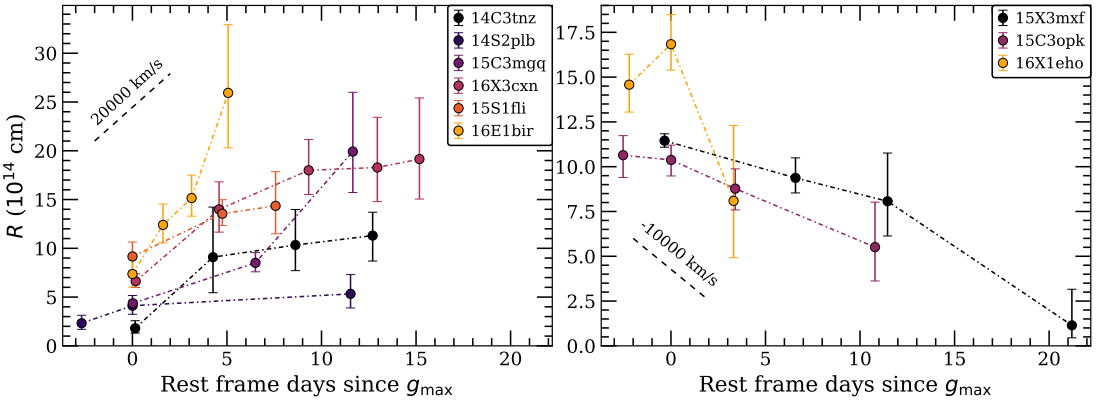

FIGURE 4.9: Radius evolution for six example gold sample transients with increasing radii are shown on left and the three transients with decreasing radii on right. Note that DES16C3opk is a silver sample RET. Reference velocities are plotted with dashed lines. Brighter events are plotted sequentially in brighter colours in both panels.

including one very rapidly evolving Ic-BL, iPTF16asu, that expanded at 34500 ± 5400 km/s (Whitesides et al. 2017).

However, the radius does not appear to increase for all RETs. In Figure 4.9 (right panel) three transients — DES15X3mxf, DES15C3opk and DES16X1eho — that seem to have receding photospheres are shown. While the errors of the estimated radii are large and thus the exact values of them are uncertain, it is clear that events are not expanding like the other RETs seem to. While DES15X3mxf and DES15C3opk show only a moderately shallow decrease in size, DES16X1eho has a photosphere that recedes from $R \sim 16{\cdot}10^{14}$ cm at peak to $R \sim 8{\cdot}10^{14}$ cm in just 3.4 d. The decreasing radii of these RETs are accompanied by temperatures that either stay roughly constant (DES15C3opk and DES16X1eho) or slightly decrease during their evolution (DES15X3mxf). Such a difference in their temporal evolution could mean that these three events are physically different from the majority of the RETs. One fast evolving bright transient in literature, AT2018cow, is known for having a receding photosphere and it is possible that the three DES-SN RETs could be similar in nature. The prospect is investigated in Chapter 6.

4.2 Spectroscopic Properties

Despite good photometric coverage on the sample of RETs, the number of spectra showing clear transient features is unfortunately small due to two main reasons. First, DES-SN primarily discovers transients at high redshifts and thus obtaining follow-up spectra is difficult and time consuming. Furthermore, the majority of the RETs were discovered in an archival search and thus the likelihood of those RETs being observed depended on whether they fulfilled the criteria for the existing follow-up programmes heavily focused

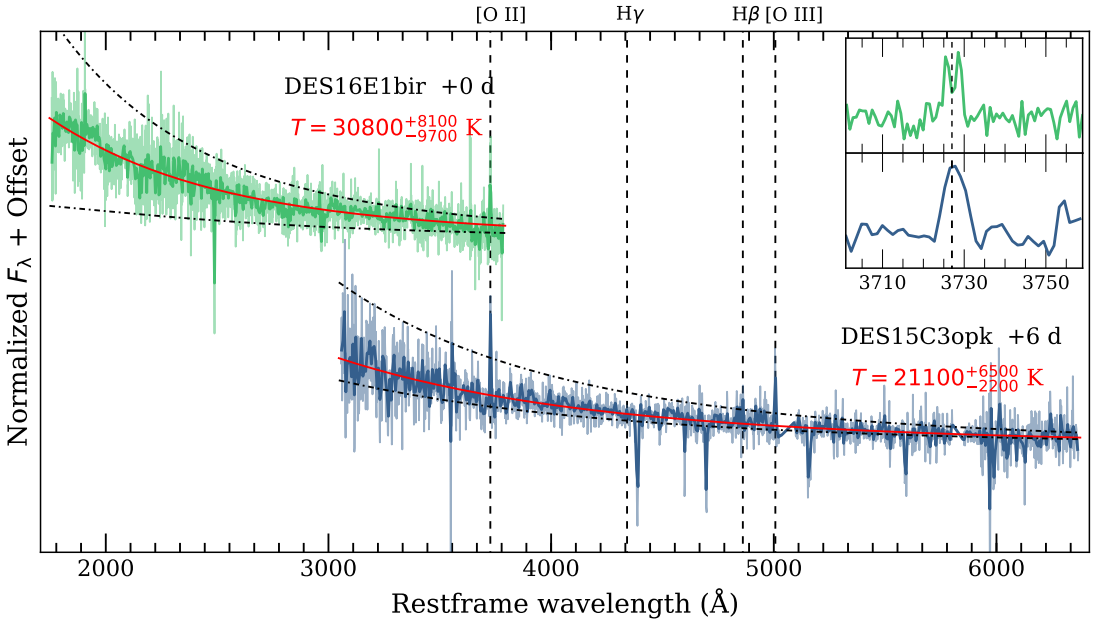

FIGURE 4.10: Spectra for DES15C3opk at $z = 0.57$ and DES16E1bir at $z = 1.56$ (lighter shade) and the corresponding spectra binned by factor of five (darker shade). The spectra for DES15C3opk and DES16E1bir have strong underlying blue continuum best fitted with shown blackbody SEDs (red lines). The uncertainties on temperature are quoted at 1σ and corresponding SEDs are shown with dashed lines. Inset: [OII] λ3727 doublet line for DES16E1bir and DES15C3opk.

on classifying probable type Ia SNe (see Section 2.5). As a result only two RETs in the gold and silver samples have spectra with transient signal in them. DES15C3opk was observed with LDSS3 on the Magellan Clay Telescope six rest frame days after the peak brightness and DES16E1bir at peak with X-shooter on VLT.

The resulting spectra are presented in Figure 4.10. Note that the shown X-shooter spectra is created based on the UVB and VIS arms. For both of the spectra, the most prominent feature is the underlying blue continuum corresponding to the high temperature blackbody emission coming from the transient itself. When fitted, the resulting blackbody temperatures are 30800^{+8100}_{-9700} K for DES16E1bir and 21100^{+6500}_{-2200} K for DES15C3opk. The value for DES16E1bir is consistent with the temperatures found based on the photometric data (32000^{+6000}_{-4400} K at peak), but for DES15C3opk the photometry results in slightly lower temperature of 15100^{+1700}_{-1100} K at +3.4 d. However, with such high temperatures the peak of the blackbody SED is not seen potentially causing further uncertainty in the values. No other transient features are present but the spectra also show a set of host galaxy emission lines. The visible lines in the spectrum of DES15C3opk are [OII] λ3727 doublet and [OIII] λ5007 lines with a trace of Hβ at $z = 0.57$. The redshift of DES15C3opk was first obtained from this spectrum until it was later confirmed by OzDES. The [OII] doublet line is also present in the spectrum of DES16E1bir, where this

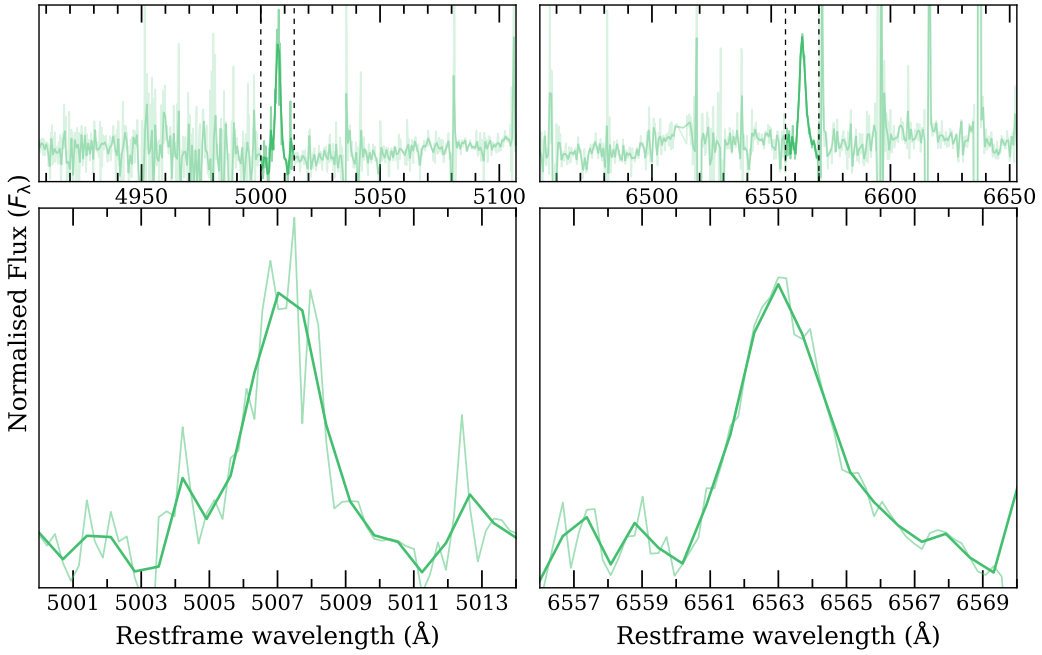

FIGURE 4.11: X-shooter NIR arm spectrum of DES16E1bir shown around Hα and [OIII] λ5007 (lighter shade) and the corresponding spectra binned by factor of five (darker shade).

line has been used to estimate the redshift $z = 1.56$. The line is presented more prominently in the inset of Figure 4.10. Note that both spectra have been flux calibrated using the DES-SN *griz* photometry of the transients at the date closest to the epoch of spectra. For DES16E1bir the observation were taken on the same night, but for DES15C3opk data from different night had to be used, potentially affecting the calibration.

The X-shooter NIR spectrum of DES16E1bir has not been presented in Figure 4.10 due to problematic sky subtraction. However, due to the identified [OII] λ3727 doublet suggesting $z = 1.56$, the spectrum was investigated for host galaxy line features aligning with the same redshift. Snippets of regions around Hα and [OIII] λ5007 are shown in Figure 4.11 demonstrating that such lines are indeed detected. Thus it is safe to conclude that redshift $z = 1.56$ is secure for the host of DES16E1bir.

A number of other RETs were also observed under DES-SN follow-up programmes, but they did not show clear transient features. DES14S2anq and DES16X3ega were observed by a OzDES few weeks after the peak brightness. However, DES14S2anq was too faint at the epoch in comparison to the host galaxy to result in any reasonable transient spectra and DES16X3ega was simply too faint to provide enough signal. Furthermore during DES-SN Y5, two bronze sample RETs, DES17X2cvk and DES17X2dqk, were observed by X-shooter on the VLT. Both of the spectra showed tentative noisy blue continua, but no other distinct features that could be used to characterise the events or estimate the redshifts. As such those spectra are excluded from this thesis.

The strong blue continuum is a typical feature in the spectra of previously discovered fast transients, at least around peak brightness (see e.g. Arcavi et al. 2016; Whitesides et al. 2017). Such a featureless continuum has also been observed in the near-peak spectra of CCSNe. Khazov et al. (2016) analysed early spectra ($\lesssim$ 10 d after explosion) of 84 type II SNe and found that 27 of them had blue featureless spectra and 12 had high ionisation lines with an underlying blue continuum. These lines included mostly Balmer and He II lines as typical for type II, but also OII and OIII lines on a few occasions. While its possible that such lines could be emitted from the RETs due to the strong ionising emission produced by high temperature ejecta, such lines are not clearly present in the spectra of DES16E1bir or DES15C3opk.

4.3 Summary

In this Chapter I presented the observable properties of the discovered rapidly evolving transients. Rise times were estimated as time between the observed peak and the last non-detection before it and decline times as the time exponential fits took to decline to 1/10 of the peak flux. Based on the estimated values, RETs appear to rise faster than decline as is typical for SNe in general. Furthermore, declines seem to be slower the redder the band in question is. Based on the estimated Δm_{15} and $t_{1/2}$ values the RETs exhibit similar light curve evolution as the PS1-MDS RETs, faster than is typically expected of standard classes of SNe.

The DES-SN *griz* SEDs are well matched with blackbody model around peak brightness, but for a few events the late time emission few week after the peak brightness diverges from the model. The blackbody fits show that the RETs exhibit high temperatures of $\sim$ 8000 – 30000 K and large photospheric radii $\sim 10^{14}$ – 10^{15} cm at the time of peak brightness. The majority of the RETs show evidence of expanding/cooling photospheres, with example expansion velocities estimated to be in range $\sim$ 10000 – 30000 km/s. However, three individual RETs did not behave in a similar manner. Instead they demonstrated shrinking photospheres with roughly constant temperatures, similar to the enigmatic AT2018cow.

Only two RETs in the sample have spectra with visible transient emission. For both DES16E1bir and DE15C3opk, the spectra showed underlying blue continuum best fitted with a blackbody model. The resulting temperatures are different, but broadly consistent with the values estimated based on the photometry. Other transient features were not clearly present in the spectra, but the redshifts of the two host galaxies were estimated based on the visible narrow emission lines.

Chapter 5

Rapidly Evolving Transients: Host Galaxy Properties

Now that the observational properties of the RET sample have been unveiled, it is time to turn our attention towards the host galaxies of the sample. The distribution of host galaxy properties provides important insight into which progenitors scenarios are realistic. For instance, virtually all CCSNe are found in star-forming galaxies (see e.g. Fruchter et al. 2006; Anderson et al. 2010; Graur et al. 2017; Wiseman et al. 2020b) strongly implying that the they are some how related to short-lived massive stars. On the other hand, type Ia SNe are spread amongst both passive and star-forming hosts and thus they require progenitors that are prominent in both. WDs — stellar remnants of stars that did not explode — fit the picture perfectly. Therefore, investigating the properties of RET hosts is crucial to the analysis as it can directly favour or disfavour certain physical mechanisms. Example host environments of DES-SN RETs are presented in Figure 5.1

As discussed earlier in the Chapter 3, all 52 gold and silver sample RETs and 41/54 bronze sample RETs have a reliable host galaxy identification. As a result, the DES-SN sample of RETs provides the first proper opportunity to investigate the host galaxy properties with a statistically significant sample of rapid transients. The sophisticated host galaxy analysis – including estimations of metallicities and star-formation rates (SFRs) – has been performed in Wiseman et al. (2020a). Therefore, I will not discuss the analysis of that study in great detail, but rather focus in providing an overview of the host galaxy properties as analysed by myself. At end of the Chapter I will compare the results to the conclusions of Wiseman et al. (2020a) and discuss the implications of the host galaxy properties on the RETs themselves.

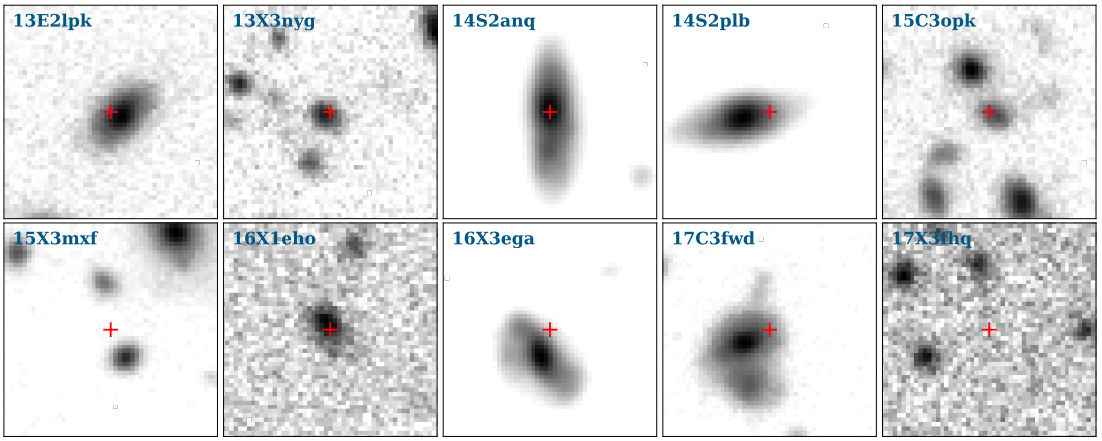

FIGURE 5.1: Host galaxy environments for ten example RETs. Transient sites are marked with red crosses. Each stamp is roughly 13.5″ on a side. Note that no host was detected for DES17X3fhq.

5.1 Host Galaxy Spectroscopy

The clearest observational evidence for galaxy types comes from spectroscopy. Approximately half of the RETs (49/106) have host galaxy spectra taken by OzDES or is otherwise publicly available. OzDES obtained 41 of the spectra and the remaining were collected from following surveys: three by Looking at the Distant Universe with the MeerKAT Array (LADUMA) survey[1], two by the Arizona CDFS Environment Survey (ACES; Cooper et al. 2012) and one each by the Australia telescope large area survey (Mao et al. 2012), the Galaxy and Mass Assembly survey (GAMA; Driver et al. 2009; Baldry et al. 2018) and SDSS. Furthermore, while DES16E1bir does not have a host galaxy spectrum, the presence of [OII] λ3727, [OIII] 5007 and Hα in the transient spectrum implies star-formation in the host (see Figures 4.10 and 4.11). Additionally, two host galaxy redshifts were obtained by the PRIsm MUlti-object Survey (PRIMUS; Coil et al. 2011; Cool et al. 2013), but the spectra themselves have been excluded from this part of the analysis as they were low resolution ($R \sim 40$). Representative spectra of the host galaxies have been presented in Figure 5.2.

Based on visual inspection of the available spectra, the host galaxies show some level of star-formation in their spectra as indicated by visible narrow lines. The most notable lines in the spectra are Hα λ6563, Hβ λ4861, [OII] λ3727, [OIII] $\lambda\lambda$4959, 5007, [NII] $\lambda\lambda$6548, 6583, and [SII] $\lambda\lambda$6717, 6731 and some of them have been indicated with dashed lines in Figure 5.2. Based on the existence of these lines it is possible to conclude that at least 50/106 RETs originate in star-forming galaxies. These lines were identified by OzDES following a procedure for determining a galaxy redshift. OzDES required that either several lines matching to the same redshift or a single strong line was seen in the

[1] http://www.laduma.uct.ac.za

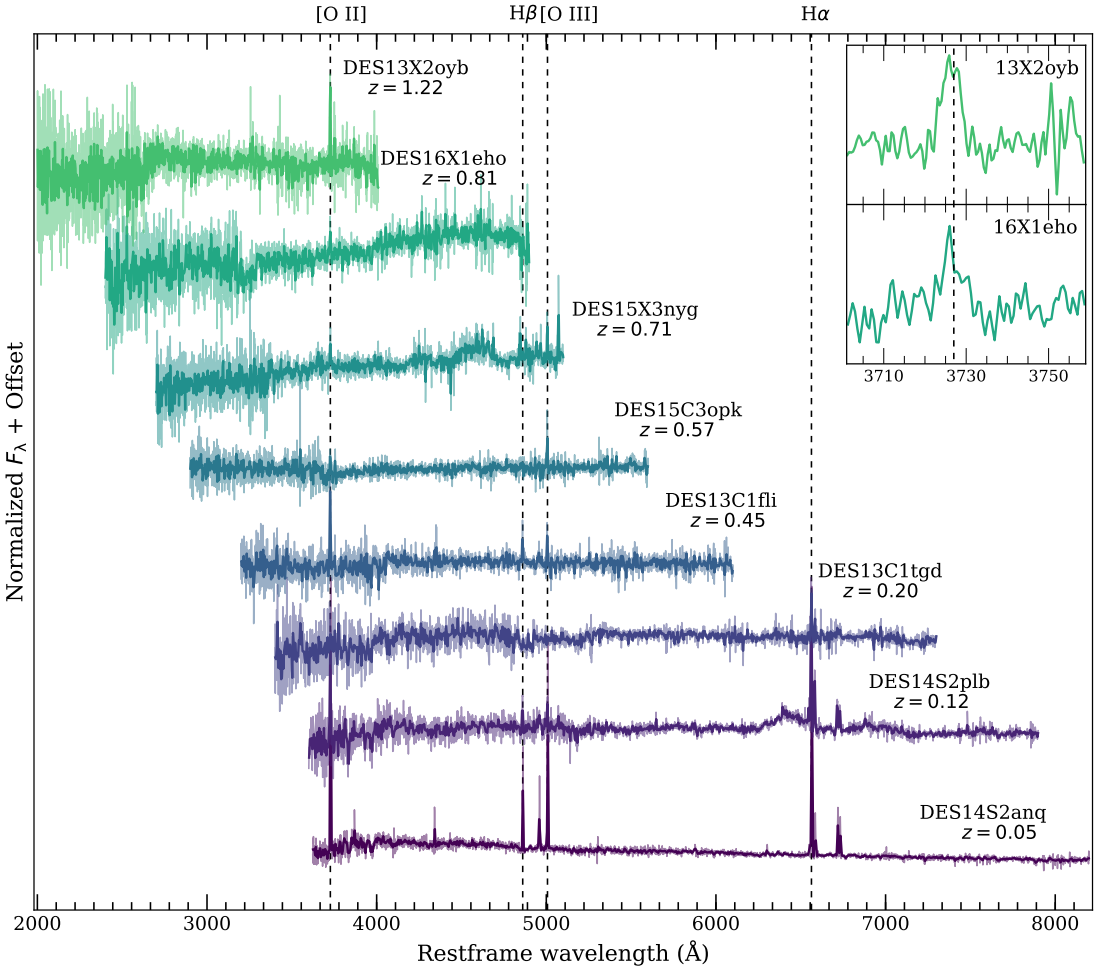

FIGURE 5.2: Host galaxy spectra for example host galaxies across the RET redshift range.

spectra. OzDES estimated that such procedure reached $> 95\%$ confidence that the lines were real and the obtained redshifts were secure (Lidman et al. 2020). However, while all 50 hosts with spectra appear to be star-forming, this still leaves 56 RETs for which the host type is not certain. While it is not realistic to assume that all of them are found in passive environments, a significant fraction could be. To investigate the possibility of passive host galaxies, a larger subsample of RET hosts has to be incorporated into the analysis.

5.2 Host Galaxy – Transient Separation

The next host galaxy feature that could give insight into what kind of hosts DES-SN RETs occurred in is the distribution of host – transient separations. As discussed in Chapter 2, DES-SN evaluated the unitless $d_{\rm DLR}$ value (Sullivan et al. 2006; Gupta et al. 2016; Sako et al. 2018) for the nearest galaxies of each new transient. The value provides

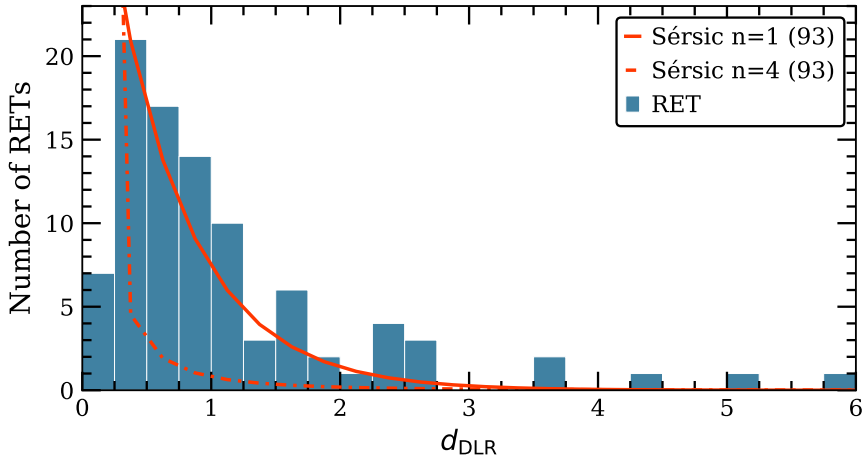

FIGURE 5.3: d_{DLR} histogram of the 93 RETs with host galaxies. A Sérsic profile for $n = 1$ typically used describe the distribution of light (i.e. stars) for spiral galaxies is shown in red line and profile for $n = 4$ used for elliptical galaxies is shown in red dashed line for comparison. The profiles were drawn to match the number of RETs.

the ratio of the transient separation from its host galaxy and the galaxy size to the direction of the transient, and thus its distribution should directly probe the RET host population. The resulting d_{DLR} histogram for all RETs with associated host galaxies is presented in Figure 5.3. The values are found on a range from 0 to 6 with the majority below $d_{\mathrm{DLR}} \sim 4$ referring to solid cases of host association. $d_{\mathrm{DLR}} = 4$ has also been applied as threshold for a "host" by DES-SN team in the automated data processing (see e.g. D'Andrea et al. 2018; Wiseman et al. 2020b). While only a small number of events are found at higher values, it is important to note that in these cases its possible that the real host has not been detected resulting in a wrong host association and thus higher value of d_{DLR} (see e.g. Gupta et al. 2016).

In the Figure 5.3 I also present a Sérsic profile for $n = 1$ typically used to describe the distribution of light (i.e. stars) in spiral galaxies and a profile for $n = 4$ used to describe elliptical galaxies (Sérsic 1963). The drawn profiles are normalised to the number of the shown RETs. The distribution of RETs is significantly better matched by the $n = 1$ model as the the light of elliptical galaxies is very strongly concentrated on the central regions of the galaxies causing the profile to give a poor match to the distribution.

The only interval where the $n = 1$ model diverges clearly from the data is at very small values of d_{DLR} (< 0.25). One possible way to explain the difference from the data is that the transients occurring in the nuclear regions of their host galaxies might be more difficult to detect due to strong host galaxy emission. As a result, some faint transients could potentially be missed (i.e. the classical "Shaw Effect", Shaw 1979). However, as bright elliptical galaxies would suffer from it as well, the reasoning does not provide any information on the host galaxy types.

The seen difference can also be related to the assumption that RETs originate in star-forming galaxies. The nuclear regions of the spiral galaxies are known to host older stellar populations than the surrounding galaxy structure (see e.g. González Delgado et al. 2015). Therefore, if the RETs require star-formation to occur, the small number of RETs discovered in the central regions of their galaxies could be explained by the lack of young massive stars in those regions. Given that the profile for spiral galaxies also describes data well in comparison to elliptical galaxies, the idea seems reasonable. However, even if one assumes that the reasoning is correct, it still does not verify that the RETs are exclusively found in star-forming galaxies as several RETs could still be found in passive environments without it having a noticeable effect on the distribution.

5.3 Host Galaxy Brightness and Colour

As discussed above, it does seems like at least 50 of the RETs are found in star-forming galaxies. However, not all of the RETs have been incorporated into the analysis so far and thus it is important to investigate if the host sets used above are representative of the whole sample of 106. Furthermore, even if the d_{DLR} distribution might imply that star-formation is important for the RETs, it is still possible that many of the RETs originated in bright, passive galaxies. The importance of such galaxies can be discussed by investigating the distribution of the host magnitudes and colours as the passive galaxies are typically brighter and redder than the star-forming ones. The used r band magnitudes and redshifts are given in in Tables B.4 – B.3.

In addition to the 52 hosts with a spectroscopic redshift, photometric redshifts have been estimated for hosts of 33 bronze sample events prior to the discovery of the sample. The resulting r band apparent and absolute magnitude – redshift distribution of these 85 host galaxies have been presented in Figure 5.4 with corresponding magnitude and redshift histograms. First, it is obvious that the majority of the presented bronze sample hosts do not have measured z_{Spec} as they are too faint. This is perfectly demonstrated by the fact that 20/33 are $m_{\mathrm{r}} > 24$, while only one spectroscopic redshift has been estimated in the same magnitude range and even that redshift was obtained based on the X-shooter spectrum of DES16E1bir presented in Figure 4.10 and 4.11. The redshift completeness of OzDES drops quickly after $m_{\mathrm{r}} \sim 23$ and its virtually zero at $m_{\mathrm{r}} \sim 24.5$ (Lidman et al. 2020), providing a natural explanation for the sharp cut off seen in the figure. As a result, the histograms of the 52 z_{Spec} hosts are emphasising the transients at lower redshifts ($z \lesssim 0.8$) — and thus in apparently brighter host galaxies ($m_{\mathrm{r}} \lesssim 23$) — while the 33 hosts with only z_{Phot} clearly indicate that the RETs are found continuously up to $z \sim 1.5$.

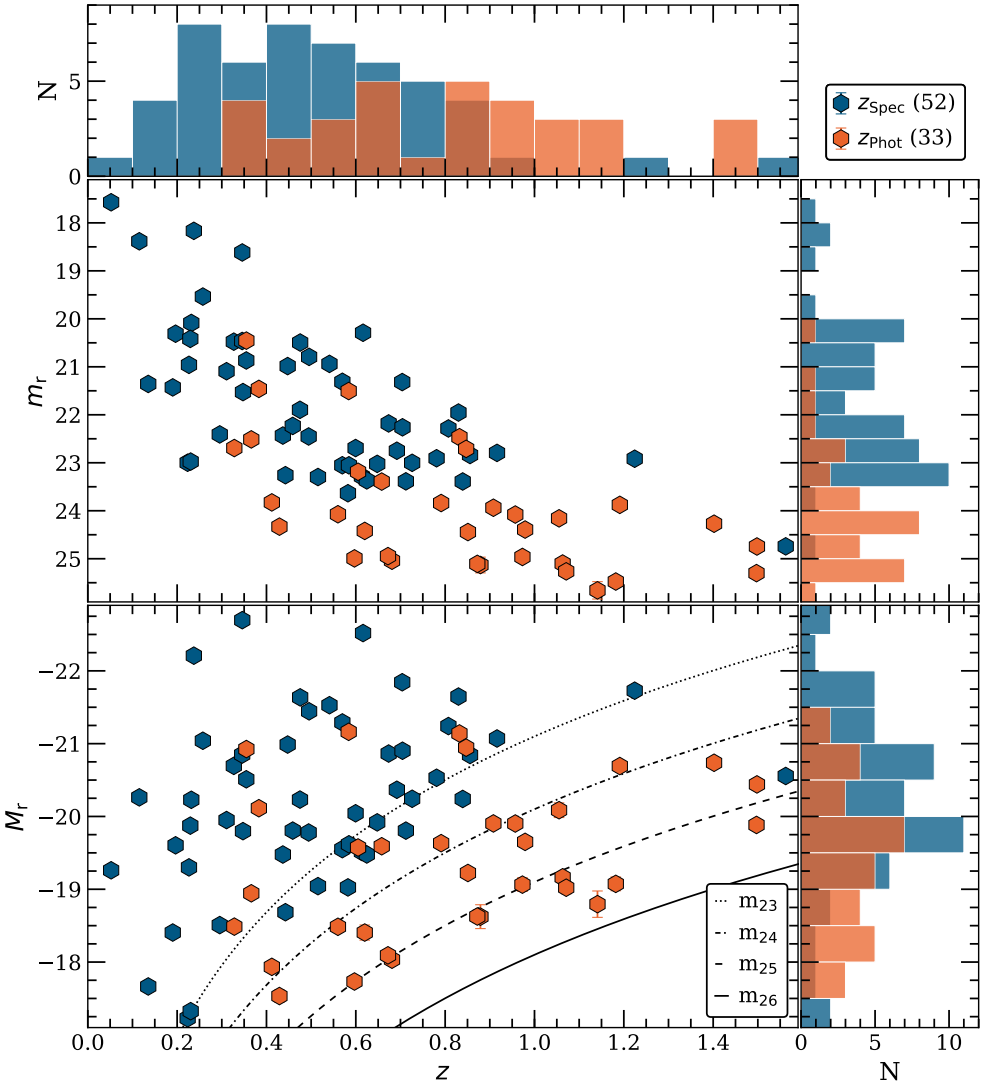

FIGURE 5.4: Apparent and absolute magnitude distributions of RET host galaxies against redshift. The hosts with $z_{\rm Spec}$ are shown in blue and the ones with only $z_{\rm Phot}$ in red.

Despite majority of the bronze sample hosts being too faint to have spectroscopic redshifts, some of hosts are actually fairly bright — 3/33 are $m_{\rm r} < 22$ and a further 4/33 $m_{\rm r} < 23$. This raises a question whether these brighter hosts could lack spectroscopic redshifts due to absence of clear narrow emission lines in their spectra and thus if they could in fact be passive galaxies. However, further investigation revealed that five of the seven hosts were not targeted by OzDES at all, and thus only in two case the host was observed but no redshift was obtained as the spectra were dominated by noise. For both DES16X1ddm and DES17E1gsx the hosts were fairly bright ($m_{\rm r} = 21.5$ and $m_{\rm r} = 22.7$, respectively) and they were exposed for ~ 11 h each. However, some apparently brighter RET hosts have required a similar amount of time to secure a redshift. For example the host of DES13C1tgd is $m_{\rm r} = 20.3$, but it was exposed for ~ 10 h before a redshift was

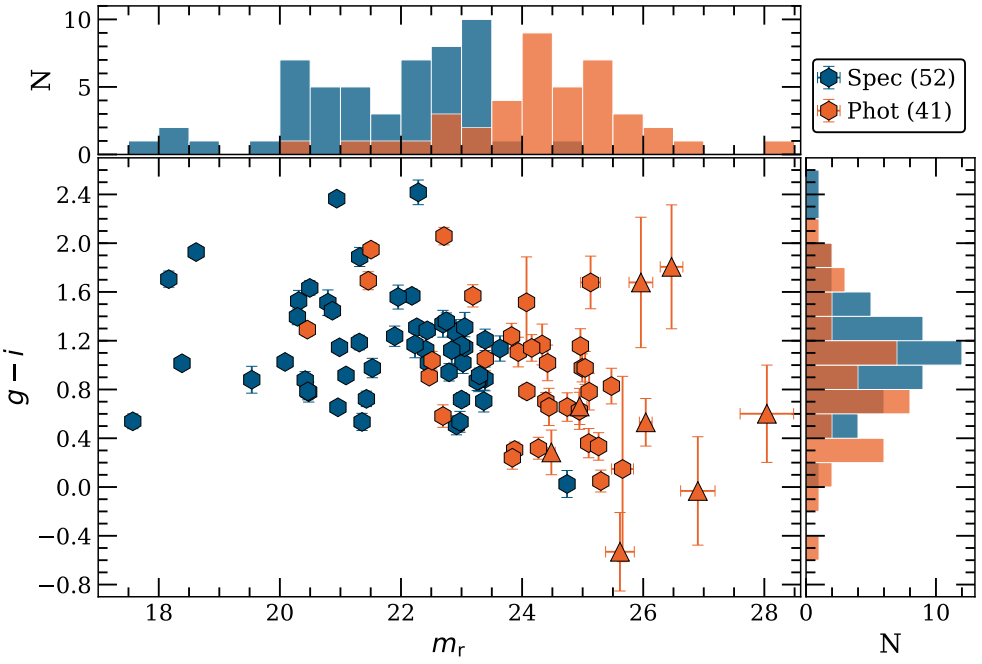

FIGURE 5.5: The host $g-i$ colour against the host apparent magnitude m_r. The eight host discovered in the deep stacks and thus not presented in Figure 5.4 are given with triangles, but they are included in the histograms. Note that the values have not been k-corrected.

obtained. Furthermore, as the two events are from the last two years of DES-SN, the amount of time OzDES could expose their hosts was limited. While the noisy spectra of these hosts cannot be used to determine if these hosts are star-forming there does not seem to be a reason to assume they are not.

Similarly one can investigate the absolute magnitude distribution as well. The host galaxies of the samples with spectroscopic and photometric redshifts are found on similar broad distributions of absolute magnitude. The only clear differences between the two are that the $z_{\rm Phot}$ sample increases the number of RETs found in fainter host galaxies in range -17.5 – -19, while the spectroscopic redshifts have been obtained for all transients in bright hosts ($M_r \lesssim -21.5$). Both of the features make perfect sense as obtaining $z_{\rm Spec}$ is harder the fainter the host in question is and thus brighter galaxies are favoured (i.e. the classical Malmquist bias; Malmquist et al. 1922, 1925). The similarity of the spectroscopic and photometric samples implies that they are drawn from a similar distribution of host galaxies, only affected by the observational bias against fainter targets.

As a whole the sample of 85 host galaxies spreads over a wide range of absolute magnitudes between -17 and -23 — typical for galaxies in general (see e.g. Blanton et al. 2001). While magnitudes exceeding $M_r \sim -22$ are rare for star-forming galaxies (i.e. spiral galaxies) they do occur in nature (see e.g. Nakamura et al. 2003) and due to their extreme brightness they are likely strongly over-represented in the sample as they are

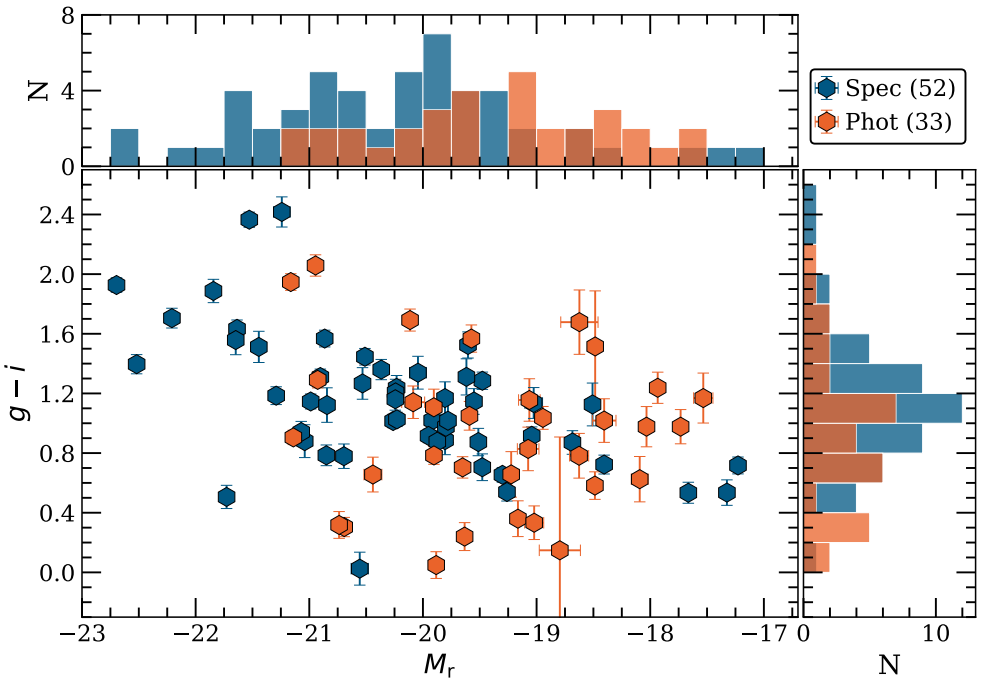

FIGURE 5.6: The host $g-i$ colour against the host absolute magnitude M_r. The eight host discovered in the deep stacks are not shown in the figure due to the unknown photometric redshifts. Note that the values have not been k-corrected.

more likely to have a $z_{\rm Spec}$ value, despite the high redshifts. Similarly, while very faint galaxies ($M_r \gtrsim -18$) are very common (Schechter 1976), they cannot be seen far and thus they are very likely under-represented in the sample.

In addition to the 85 RET hosts presented in Figure 5.4, there are 21 RETs whose hosts have not been discussed. Eight of them did not have visible hosts in the SV templates, but the very faint hosts were identified in the deep stacks of the DES-SN fields (Wiseman et al. 2020b). The deep stacks have limiting magnitudes of $m_r \lesssim 25.5$ in the shallow and $m_r \lesssim 26.5$ in the deep fields, thus providing additional depth in order of ~ 1 mag in shallow and ~ 2 mag in deep fields over the SV templates (Wiseman et al. 2020b). The hosts can be recognised in Table B.3 as they do not have $z_{\rm Phot}$ values estimated. Most of these hosts have a small $d_{\rm DLR}$ value, making the association fairly clearly, but a few have a large value (~ 5) and it is possible that the highly separated RETs occurred in even fainter galaxies unseen in the deep stacks. Due to the extreme faintness of these hosts it is unlikely that they would have a significant effect to the host galaxy distribution, other than increasing the importance of faint hosts.

The remaining 13 RETs are deemed to be "hostless" as either no host was seen in the deep stack images or because the host association was unclear. A perfect example of such a case is the explosion environment of DES17X3fhq presented in Figure 5.1. While there are several faint host candidates, none of them are particularly close ($d_{\rm DLR} \gtrsim 7$)

to the event itself, and thus it is likely that host is not detected. Furthermore, given that eight new hosts were discovered based on the deep stack images, it seem reasonable to assume that at least some of the remaining 13 hostless RETs occurred in hosts too faint to see even in the deep stacks. With the very faint apparent magnitude limits of the images even galaxies with $M_{\rm r} \sim -19$ could be missed if they were at high redshifts. However, such hosts would again only increase the emphasis on RETs in faint hosts.

The comparison of host $g-i$ colour between the spectroscopic and photometric samples is presented in Figure 5.5 against the host $m_{\rm r}$. Note that the shown photometric sample now includes the eight hosts discovered in the deep stacks. The distributions are found on a very similar range of values, but what is surprising is that the sample without $z_{\rm Spec}$ seems to be inherently bluer. Even if one ignores the eight extremely faint host discovered in the deep stacks (shown with triangles), the colour range is found to be the same as for the hosts with $z_{\rm Spec}$. Similarly, the distribution of $g-i$ colour against the host absolute magnitude $M_{\rm r}$ reveals a similar story. The host galaxies with only $z_{\rm Phot}$ estimates appear to be found on very similar range of values as the galaxies with spectroscopic redshifts. In fact, based on the shown histograms sample without $z_{\rm Spec}$ values seems to be both bluer and fainter — a contrary result to what would be expected if the galaxies of that sample were dominantly passive and/or at significantly higher redshift.

Based on the analysis presented above, the sample of 52 RETs with spectroscopic redshifts appear to be dominated by lower-redshift transients occurring in galaxies with above-average brightnesses. While the host galaxies with and without spectroscopic redshifts have differences in the distributions of $m_{\rm r}$, $M_{\rm r}$ and $g-i$ colour, it seems possible that those differences are a result of observational bias — i.e. redshifts are harder to obtain for fainter galaxies thus increasing the importance of transients in brighter and closer-by galaxies. However, while the analysis does not seem to provide a reason to assume that the RETs are found in passive environments, it is important to emphasise that the star-forming nature has been verified only for the 50 hosts with spectra and at least some of the remaining 56 hosts might be passive.

5.4 Comparison to analysis of Wiseman et al. (2020a)

The star-forming nature of DES-SN RET hosts is supported by the analysis of Wiseman et al. (2020a) performed on the same sample of events. However, in their work the host galaxy data was investigated more thoroughly allowing them to go further in their conclusion. They fitted the observed photometric data of each host for stellar mass and SFR in order to obtain the resulting specific SFR (sSFR) values. sSFR is normalised for stellar mass and thus it provides a better measurement of star-formation efficiency in

the galaxy than SFR itself. Furthermore, they also fitted the host spectra to resolve the metallicities of the hosts for a subset of the sample where enough narrow emission lines were present. For exact details on the fitting procedures see Wiseman et al. (2020a).

The resulting metallicites and sSFRs were then compared with literature samples of type II SNe, SESNe, SLSNe and Long duration Gamma-Ray Bursts (LGRBs). They discovered that while DES-SN RETs do require star-formation as do all comparison samples, there are also clear differences. The distribution of sSFR for RETs appears to be between the normal CCSN (type II and SESN) and more extreme LGRB and SLSN hosts. Similarly, the metallicities of RET hosts seem to be higher than for the hosts of LGRB and SLSNe, but significantly lower than for type II SNe hosts as well as the general population of field galaxies from SDSS. Furthermore, the RET host metallicities were found to be similar to those of SESN.

The results of Wiseman et al. (2020a) are intriguing as while they do seem to link RETs with CCSNe, the RETs appear to occur in environments that are more metal-poor and more star-forming than the host of CCSNe typically are. Even so the hosts are not as extreme as the hosts of SLSNe and LGRBs that are known of being very metal-poor and highly star-forming. Based on the analysis they concluded that RETs are likely associated with very massive stars as indicated by the high sSFR, and that the explosion mechanism of RETs could possibly be some kind of intermediate step between SLSNe/LGRBs and CCSNe.

5.5 Summary

In this Chapter I presented the host galaxy properties of the rapidly evolving transients. First, the host galaxy spectra of 49/106 RETs were visually inspected. All of the spectra show evidence of narrow emission lines indicative of recent star-formation in the respective host galaxies. Furthermore, the X-shooter transient spectrum of DES16E1bir also exhibited narrow galaxy emission line features. Thus, at least 50 RETs are found in star-forming hosts.

Next I investigated the distribution of the transient – host galaxy separations quantified with $d_{\rm DLR}$. The distribution of the 93 RETs with a detected host galaxy is well described with a Sérsic profile for $n = 1$ typically used to describe the distribution of light in spiral galaxies. On the other hand, a profile for $n = 4$ used for elliptical galaxies provided a poor match to the data as it was overly emphasising the importance of the central regions of the galaxies. The Sérsic profile for spiral galaxies diverged clearly from the data only at the central regions of the hosts where a significantly smaller number of

RETs are discovered when compared to the model. It is possible that the seen difference is caused by strong host emission hiding some of faint, nuclear RETs, but it might also indicate that star-formation is important for RETs. The central regions of spiral galaxies are known to host older stellar populations and thus less RETs should be discovered in such regions in case they require star-formation.

The analysis of the host galaxy $m_{\rm r}$ and $M_{\rm r}$ distributions revealed that the sample of 52 RETs with spectroscopic redshifts appear to be found in host galaxies with lower redshifts and higher brightnesses than in the bronze sample. The difference is likely caused by an observational bias as obtaining redshifts to fainter and more distant galaxies is more difficult. Furthermore, the bronze sample hosts appear to be slightly fainter and bluer in comparison to the hosts with $z_{\rm Spec}$, unlike would be expected if the hosts of the sample were mostly passive. While the analysis does not seem to suggest that the RETs are found in passive environments, the star-forming nature was confirmed only for the 50 hosts with spectra and thus at least some of the remaining 56 hosts might be passive.

The analysis performed by Wiseman et al. (2020a) on the same sample of RETs also seems to imply a star-forming origin. In their study they concluded that RETs are likely associated with very massive stars due to the high sSFRs of the RET hosts. As such RETs at least some of the RETs could in fact be similar to SESNe in origin. The results of this Chapter – including the conclusions provided by Wiseman et al. (2020a) – have strong implications to the physical scenarios that are applicable to the DES-SN RETs and they will be the focus of the next Chapter.

Chapter 6

Rapidly Evolving Transients: Physical Interpretation

In the last few Chapters I have presented the observable properties of the RETs themselves and discussed properties of their host galaxies as well. Now I will turn the focus on using the results of the analysis to discuss the potential physical scenarios to explain the rapid nature of RETs. Due to the photometric and spectroscopic features, as well as the verified explosion environments, it seems reasonable to assume that the population of RETs is somehow related to CCSNe. However, even if the presented analysis leans towards that conclusion, the lack of good quality spectroscopic data makes it impossible to thoroughly investigate the diversity of the sample in terms of classification and physical origin. Therefore, the aim of this chapter is not to provide a detailed scheme to explain any of the RETs physically, but rather to focus on comparing the DES-SN RETs with literature transients and discuss some models that have been applied to them. First, I will rule out the decay of radioactive nickel as the primary power source and then carry on discussing a shock-cooling scenario commonly used to explain pre-peak behaviour in CCSNe and SLSNe. Furthermore I will provide in-depth comparison to some of the most intriguing rapid transient discovered in the last few years – the well observed, bright and rapidly evolving AT2018cow and the KN AT2017gfo.

6.1 Nickel Decay

As discussed in Chapter 1, the ^{56}Ni decay chain is assumed to be the primary source of energy output in type Ia SNe and SESNe. Many of the literature RETs are classified as SESNe of some type (see Table 1.2), and additionally the host analysis of Wiseman et al. (2020a) implies that the DES-SN RETs are likely associated with massive stars

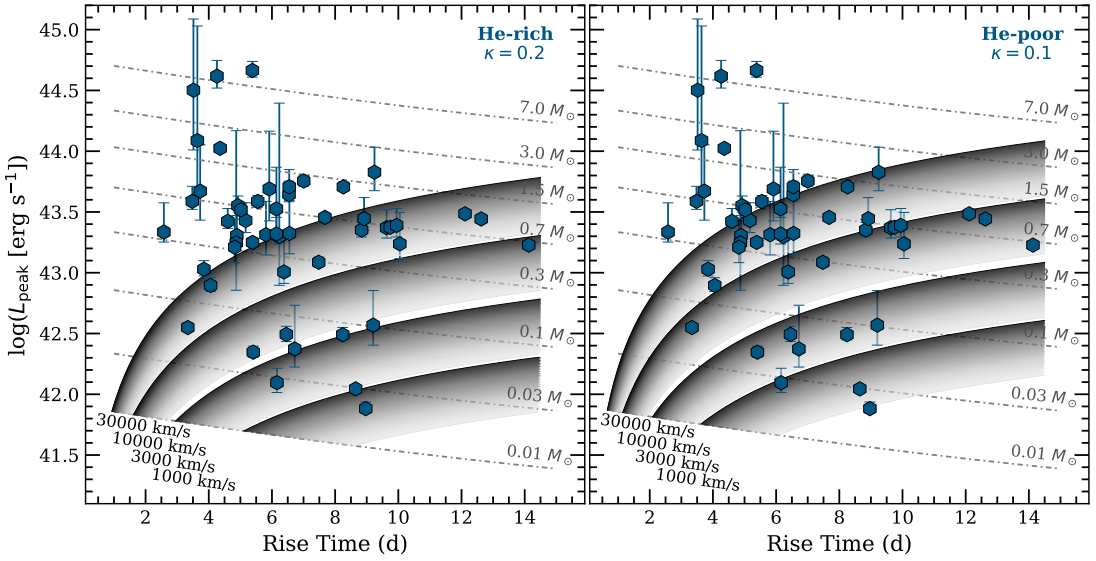

FIGURE 6.1: Pseudo-bolometric luminosity at peak based on the blackbody fits against the rise time in g band for all gold and silver sample RETs. The nearly horizontal grey lines correspond to required nickel mass for a given luminosity and rise time and the shaded regions to varying Nickel fractions of the ejecta for a given expansion velocity assuming hydrogen free ejecta with $\kappa = 0.2$ cm^2 g^{-1} (left) and hydrogen and helium free ejecta with $\kappa = 0.1$ cm^2 g^{-1} (right). Nickel fraction of the ejecta varies between one (dark shade) and half (light shade). All RETs above and/or left of a given region are unrealistic for the corresponding velocity. The reference lines have been drawn assuming spherical symmetry, optically thick ejecta and a constant density profile of the ejecta.

thought to be the progenitors of SESNe. Therefore, it does seems reasonable to assume that a significant fraction of the DES-SN RETs are in fact SESNe, but due to the lack of spectroscopic follow-up data they could not be classified. This applies especially to the RETs found at similar peak magnitudes as literature SESNe ($M \gtrsim -20$; Richardson et al. 2014). As such the radioactive nickel might in fact be the power source of the emission and it is important to investigate if the peak luminosities of RETs can be produced primarily by the ^{56}Ni decay chain.

According to Arnett's Rule (Arnett 1982), the peak bolometric luminosity is equal to the amount of energy released by ^{56}Ni and ^{56}Co decay at that epoch. Thus, in order to have a brighter transient more ^{56}Ni has to be created. In SESNe the nickel mass is typically $M_{\rm Ni} \lesssim 0.5\ M_\odot$ (see e.g. Lyman et al. 2016; Prentice et al. 2016) — less than in brighter type Ia SNe ($\sim 0.4 - 1.2\ M_\odot$; Childress et al. 2015). Furthermore, only up to a few tens of percent of the ejecta has been found to be ^{56}Ni in SESNe (see e.g. Lyman et al. 2016). Thus, increasing the nickel mass also quickly increases the ejecta mass leading to a higher opacity and diffusion timescale in the ejecta. As a result brighter SNe have longer rise times if they are powered primarily by the radioactive energy of ^{56}Ni.

Using the models from Arnett (1982) and Stritzinger & Leibundgut (2005), the peak

pseudo-bolometric luminosities and the rise times of RETs can be compared to a grid of values possible for ^{56}Ni decay as demonstrated in Figure 6.1 in two possible cases. The plot on the left assumes H-poor, He-rich ejecta with opacity of $\kappa = 0.2$ cm^2 g^{-1} and the plot on the right H-poor, He-poor ejecta with opacity of $\kappa = 0.1$ cm^2 g^{-1}. The pseudo-bolometric luminosities shown in the figure were estimated based on the blackbody fits at the peak epoch (see Tables B.9 and B.10). The corresponding rise times are those measured in g band (see Tables B.7 and B.8), which was selected to be most representative band to describe the bolometric rise due the very hot, rapidly cooling ejecta at early times (see Figure 4.8). While the used values are the best estimates to be analysed, it is likely that peak luminosities are underestimated and rise times overestimated. Due to the rapidly declining temperatures of RETs, the bolometric peak luminosities likely occurred earlier than the peak in g band as a result of the very strong UV emission created by the hot blackbody at the very early times. Similarly, the hot temperatures in the beginning would also cause the light curve rise to the bolometric peak to be quicker than in g band.

Based on the Figure 6.1, it is clear that in both of the cases the nickel mass needed to explain the peak luminosities are uncharacteristically high for SESNe ($M_{\mathrm{Ni}} \gtrsim 0.5\ M_{\odot}$) for about a half of the shown RETs with the brightest ones needing more than $M_{\mathrm{Ni}} \sim 7\ M_{\odot}$. However, whether the peak luminosity of a transient is realistic depends also on the rise time, which itself depends on the conditions in the ejecta, namely on the opacity and the ejecta velocity. Curved regions for four constant velocities are shown in the figure with shading between ejecta fully composed of ^{56}Ni and ejecta that consists of half of ^{56}Ni. As a result any event above and/or left of a given region would require more nickel than ejecta in mass and thus the transient would be unrealistic for the given line. Assuming a moderate expansion velocity of 10000 km/s, only roughly the eight faintest RETs could realistically be explained by ^{56}Ni decay in either case. Thus, the nickel could be the primary power source for the faintest events, requiring only $M_{\mathrm{Ni}} \sim 0.05\ M_{\odot}$ of nickel, but it cannot be used to explain the significant majority of the RETs in the sample.

While ^{56}Ni decay does not seem to be a probable candidate for the primary power source, it is still likely that if the RETs are related to SESNe, they do synthesise some amount of nickel but not in quantities that could explain the bright peak luminosities. Some hybrid scenarios involving ^{56}Ni decay have been suggested to describe literature RETs. For example, Clark et al. (2020) suggested that the peculiar properties of rapidly evolving SESN LSQ13ddu could be explained with a model of CSM interaction and ^{56}Ni decay. Interaction during the early phases would explain the quick rise peak brightness as well as narrow emission features in early spectra, but later evolution would be described by ^{56}Ni decay. Such hybrid scenarios could very well explain the observable properties of majority of the RETs presented in this thesis but in lack of spectroscopic evidence

the prospect is difficult to investigate. Furthermore, due to the diversity of both the literature RET classifications and the DES-SN RETs properties, it is likely that several different physical scenarios can produce the apparently similar light curves of the sample. For simplicity, in the following I focus on light curve comparisons to literature transients and only perform light curve fits with one easily describable model, the shock-cooling.

6.2 Shock-cooling

As scenario relying solely on radioactive nickel has been ruled out alternative scenarios have to be considered. One possible scenario is related to so called "shock-cooling", where the shock of the SN explosion heats some extended material (e.g. wind or extended envelope) surrounding the exploding star. The shock-heated matter then quickly expands and cools, providing a short duration hot "flash" seen in both blue and red bands (Nakar & Piro 2014). At least some small amount of emission arising from the heated material should be present in all SNe (Nakar & Sari 2010), but the timescale and total emitted luminosity depend strongly on the progenitor structure. While the peak luminosity is dictated by the size and temperature of the event, the duration depends most strongly on the mass of cooling matter (see e.g. Nakar & Sari 2010; Rabinak & Waxman 2011).

6.2.1 Comparison to CCSNe and SLSNe Light Curves

The shock-cooling scenario gives a natural explanation for the very early light curves of several double-peaked SESNe such as the type IIb SN1993J (Podsiadlowski et al. 1993; Wheeler et al. 1993, see e.g.) and SN2016gkg (Arcavi et al. 2017b; Tartaglia et al. 2017), type Ic SNe iPTF14gqr (De et al. 2018) and iPTF15dtg (Taddia et al. 2016). However, the scenario has also been deemed applicable to several SLSNe such as SN2006oz (Leloudas et al. 2012), LSQ14bdq (Nicholl et al. 2015b) and DES14X3taz (Smith et al. 2016a). All of these SNe exhibit very fast evolving pre-peaks ($\lesssim$ 10 d) followed by a typical SN light curve rising to the main peak. The pre-peaks are found on variety of brightnesses: for SESNe they can equal the luminosities of the main peaks ($-17 \gtrsim M \gtrsim -18$), while in SLSNe they always seem to be fainter in comparison to the main peak but still very bright ($-18 \gtrsim M \gtrsim -21$, see e.g. Angus et al. 2019). For example the pre-peak of type IIb SN1993J was $M_{\rm V} \sim -17.5$ and lasted for $\sim$ 5 d while the pre-peak of SLSN SN2006oz was $M_{\rm V} \sim -19.5$ and lasted for $\sim$ 10 d. It is generally accepted that these pre-peaks are created by shock-cooling in extended, low-mass material, with radius of $\sim 10^{13}$ cm and mass of $\sim 0.01 - 0.5\ M_{\odot}$ (see e.g. Woosley et al. 1994; Bernstein et al. 2012; Nakar & Piro 2014; Piro 2015).

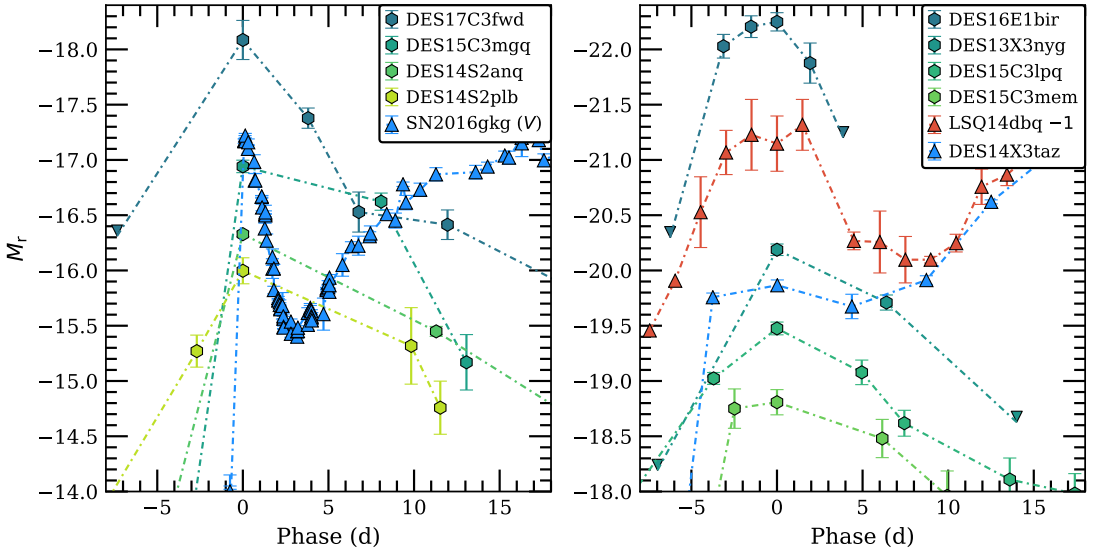

FIGURE 6.2: Light curve comparison of RETs and pre-peaks of a SESN (left) and SLSNe (right). Light curves are given in r band unless otherwise stated. Light curves of SN2016gkg and LSQ14bdq have been collected from Open Supernova Catalog (Guillochon et al. 2016) and they were first presented in Arcavi et al. (2017a) and (Bersten et al. 2018) (SN2016gkg) and Nicholl et al. (2015b) (LSQ14bdq). The light curve of DES14X3taz has been presented in Smith et al. (2016a). An offset of absolute magnitude has been applied to the light curve of LSQ14bdq for visual clarity. Note that the presented light curve have not been k-corrected.

Given the rapidly evolving nature of the pre-peaks, it is reasonable to investigate their similarity with DES-SN RETs. In Figure 6.2 light curves of representative RETs have been presented in comparison to pre-peaks of type IIb SN2016gkg and SLSNe LSQ14dbq and DES14X3taz. The pre-peak feature is typically very short duration in SESNe as demonstrated by the light curve of SN2016gkg. In comparison the presented faint RETs are clearly not evolving as fast. In fact, the pre-peak of SN2016gkg could have been completely missed with the weekly cadence of DES-SN due to its fast timescale of $\lesssim 5$ d. Furthermore, other CCSNe also seem to show evolution on similar timescales: the pre-peaks of type IIb SN1993J and type Ic SN iPTF15dtg had $M_{\mathrm{V/r}} \sim -17.5$ and lasted for ~ 5 d (Wheeler et al. 1993; Taddia et al. 2016), while the pre-peak of type Ic SN iPTF14gqr occurred in ~ 1 d with peak brightness of $M_{\mathrm{r}} \sim -17$. To conclude, the relatively faint pre-peaks seen in SESNe appear to be different from the DES-SN RETs and it is not likely that the fainter RETs are similar to them in nature.

On the other hand, the pre-peaks of the SLSNe presented in Figure 6.2 appear to be very similar to some of the brighter RETs as they share comparable luminosities and timescales. The similarity of the light curves can be taken as clear indication that the shock-cooling scenario is capable of producing evolution similar to that of RETs and in this light it does seem possible that some of the RETs could in fact be the shock-cooling emission originating from some kind of a stellar explosion. Thus, in the

following I investigate the possibility by comparing the *griz* light curves of RETs with an analytical shock-cooling model from Piro (2015). The same model was used to fit the data of LSQ14bdq suggesting that its pre-peak originated from low-mass extended material around the progenitor (~ 0.3 – $0.5\ M_{\odot}$; Piro 2015).

6.2.2 Shock-Cooling Modelling

The shock-cooling model of Piro (2015) is essentially aiming to connect the shock created by the explosion of a stellar core of mass $M_{\rm c}$ to the shock-cooling emission in the extended material of mass $M_{\rm e}$ and radius $R_{\rm e}$, using the following equations:

$$L\left(t\right) = \frac{t_e E_e}{t_p^2}\ \exp\left[-\frac{t\left(t+2t_e\right)}{t_p^2}\right] \text{ erg s}^{-1}, \tag{6.1}$$

$$t_e = R_e/v_e \text{ s}, \tag{6.2}$$

$$v_e \sim 2\cdot 10^9\ E_{51}^{0.5}\left(\frac{M_c}{M_{\odot}}\right)^{-0.7}\ \left(\frac{M_e}{0.01\ M_{\odot}}\right)^{0.7} \text{cm s}^{-1}, \tag{6.3}$$

$$E_e \sim 4\cdot 10^{49}\ E_{51}\left(\frac{M_c}{M_{\odot}}\right)^{-0.35}\left(\frac{M_e}{0.01\ M_{\odot}}\right)^{-0.15} \text{erg}, \tag{6.4}$$

$$t_p \sim 0.9\ \kappa_{0.34}^{0.5}\ E_{51}^{-0.25}\left(\frac{M_c}{M_{\odot}}\right)^{0.17}\left(\frac{M_e}{0.01\ M_{\odot}}\right)^{0.57} \text{d}, \tag{6.5}$$

where L is the bolometric luminosity, t_e the expansion timescale, v_e the velocity of the extended material, E_e the total energy passed to the extended material, $E_{51} = E_{\rm SN}/(10^{51}$ erg) the total explosion energy, and t_p the time of the bolometric peak. Note that the core mass, $M_{\rm c}$, only includes the ejected core mass and not the mass of a possible remnant. Piro (2015) also describe the evolution of radius as

$$R\left(t\right) = R_e + v_e t \text{ cm}. \tag{6.6}$$

In order to fit the model to the observed DES-SN *griz* light curves, the modelled bolometric luminosity had to be converted into fluxes of the four bands. Assuming the RETs are described by blackbody throughout their light curve evolution, Equations 6.1 and 6.6 can be used to solve the evolution of effective temperature $T_{\rm eff}$, which can then be used with Equation 6.6 to find the modelled *griz* flux values at the time of each observation. As the exact time of the bolometric peak is not known for any of the RETs, the *griz* light curves were allowed to be shifted in time to find the best fit.

Note that the core mass M_c and the explosion energy E_{SN} are degenerate with each other in the model as $E'_{SN} = (M'_c/M_c)^{0.7} E_{SN}$ so one of the values had to be fixed. Following Piro (2015) I decided to use values $M_c = 5, 20\ M_\odot$ chosen to be between the ones Piro (2015) used for SN1993J ($M_c = 2.5\ M_\odot$) and for LSQ14bdq ($M_c = 30\ M_\odot$). However, it is important to note that because of the unknown values of M_c and E_{SN} and the degeneracy between them, the used M_c values are only used to demonstrate the effect of M_c on the model. The best-fitting parameters for all 52 gold and silver sample RETs are presented in Tables B.11 and B.12 in Appendix B.

In Figure 6.3, I provide example fits for both M_c values for two example RETs at $z \lesssim 0.7$. For these RETs the fits are driven by the exponential declines, the most prominent in the redder bands due to the rapidly fading emission in the bluer bands. As a result the model underestimates the peak luminosities in the bluer bands, but also the tails of the light curves in the redder bands. As such these RETs clearly cannot be explained by the shock-cooling model alone. Similar conclusion was for instance made by Whitesides et al. (2017) who argued that the light curve of rapidly evolving type Ic-BL iPTF16asu at $z = 0.19$ can not be explained solely by the described-shock cooling model due to the relatively long decline.

While there are a few cases where the fits to RETs at low redshifts look visually good and provide $\chi^2_\nu \sim 1$ (see Tables B.11 and B.12), it is not actually reasonable to assume that these RETs can be explained by shock-cooling. The shock-cooling scenario requires an exploding CCSN (or SLSN) to create the pre-peak, but the SN would also produce the main light curve powered by ^{56}Ni decay that would have to be detected. All of the low redshift RETs exhibit smooth exponential declines without clear signatures of two separate power sources (see e.g. light curves of DES14S2anq and DES16X3ega in Appendix C) like would be expected under the shock-cooling scenario. While some SESNe are discovered with peak luminosities as low as $M \sim -15$ (Richardson et al. 2014) even those would be seen by DES-SN up to $z \sim 0.2$. However, even if one assumes that such faint SESNe could explain some of the RETs, they would have to produce very prominent pre-peaks several magnitudes brighter than the main light curve in optical bands but such strong pre-peaks have not reported. Therefore, it does not seem likely that the low redshift RETs could be explained by a shock-cooling model alone.

On the other hand, at higher redshift the situation is different as can be seen based on the fits presented in Figure 6.4 for two example RETs at $z \gtrsim 0.7$. The fits look visually convincing and their χ^2_ν values are smaller than for the fits presented in Figure 6.3. At these redshifts it is also possible that the main light curve of a SESN would be below the detection limit of DES-SN. A typical SESN has a peak brightness of $M_B \gtrsim -18$ (see e.g. Richardson et al. 2014) and such a SN would be seen up to $z \sim 0.6$ by DES-SN assuming

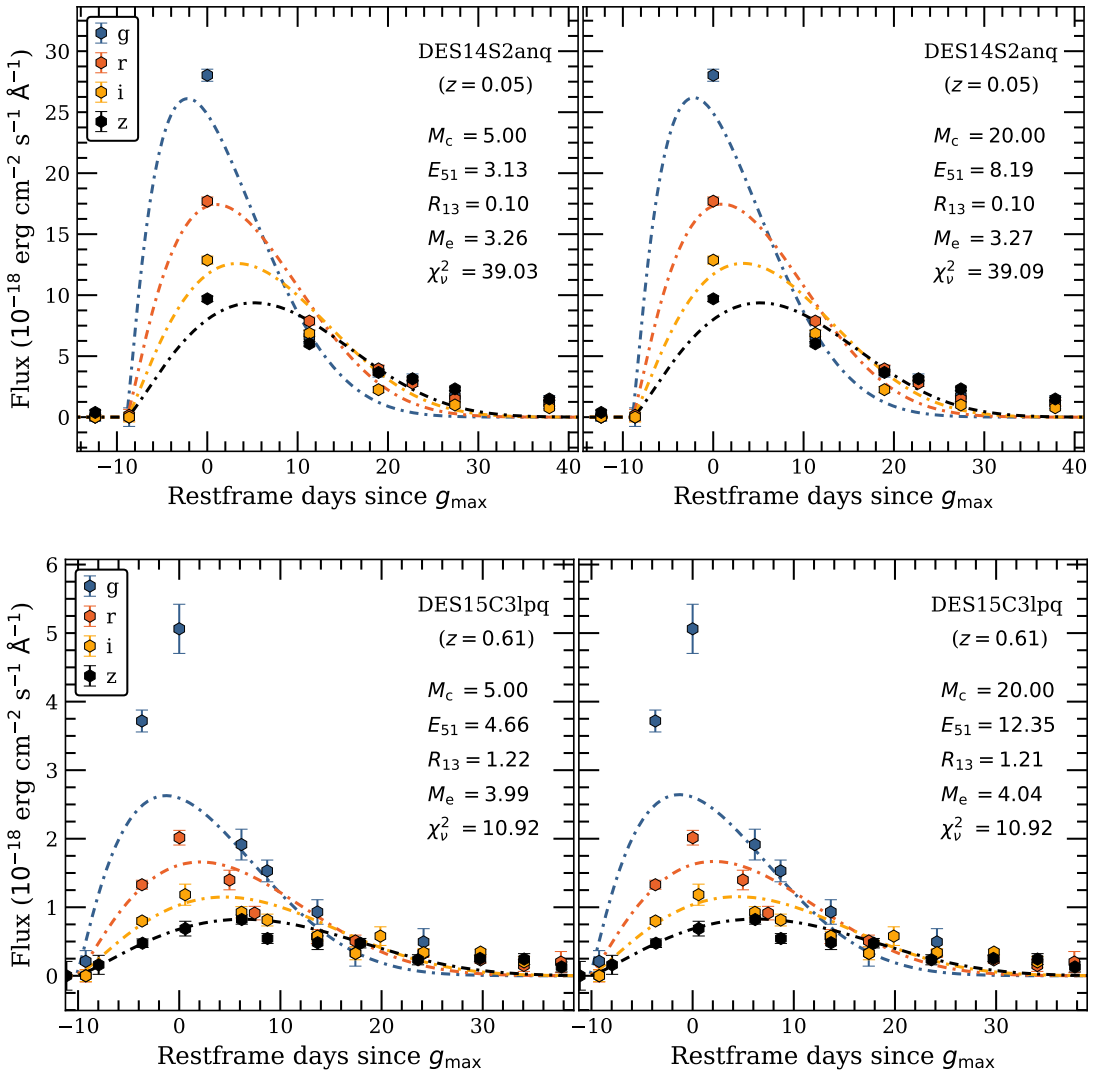

FIGURE 6.3: Shock-cooling fits to *griz* light curves of two example RETs at $z \lesssim 0.7$, DES14S2anq is shown in top panel and DES15C3lpq in the bottom panel. Fits using $M_c = 5\ M_\odot$ are given on left and $M_c = 20\ M_\odot$ on right. Note that $R_{13} = R_e/10^{13}$ cm.

limiting magnitude of 24.5, but not significantly further. Therefore, it is hypothetically possible that at least some of the high redshift RETs could actually be explained by the shock-cooling model, but the pre-peaks would have to be significantly brighter than the main light curve of the SESNe.

In the bluer bands (e.g. *gr*) it is possible to explain the brightness difference between the two peaks with the high temperatures associated with the shock-cooling scenario. For instance, the pre-peak of iPTF14gqr was measured to be arising from hot material of $T \sim 30000$ producing an SED that peaks in the NUV (De et al. 2018). At $z = 0.7$, the central wavelength of g band is at $\lambda \sim 2840$ Å and r band at $\lambda \sim 3785$ Å and thus the bands are in the NUV. As a result, the shock-cooling emission observed in *gr* bands at such redshift would be brighter than it would be in the rest frame. On the other

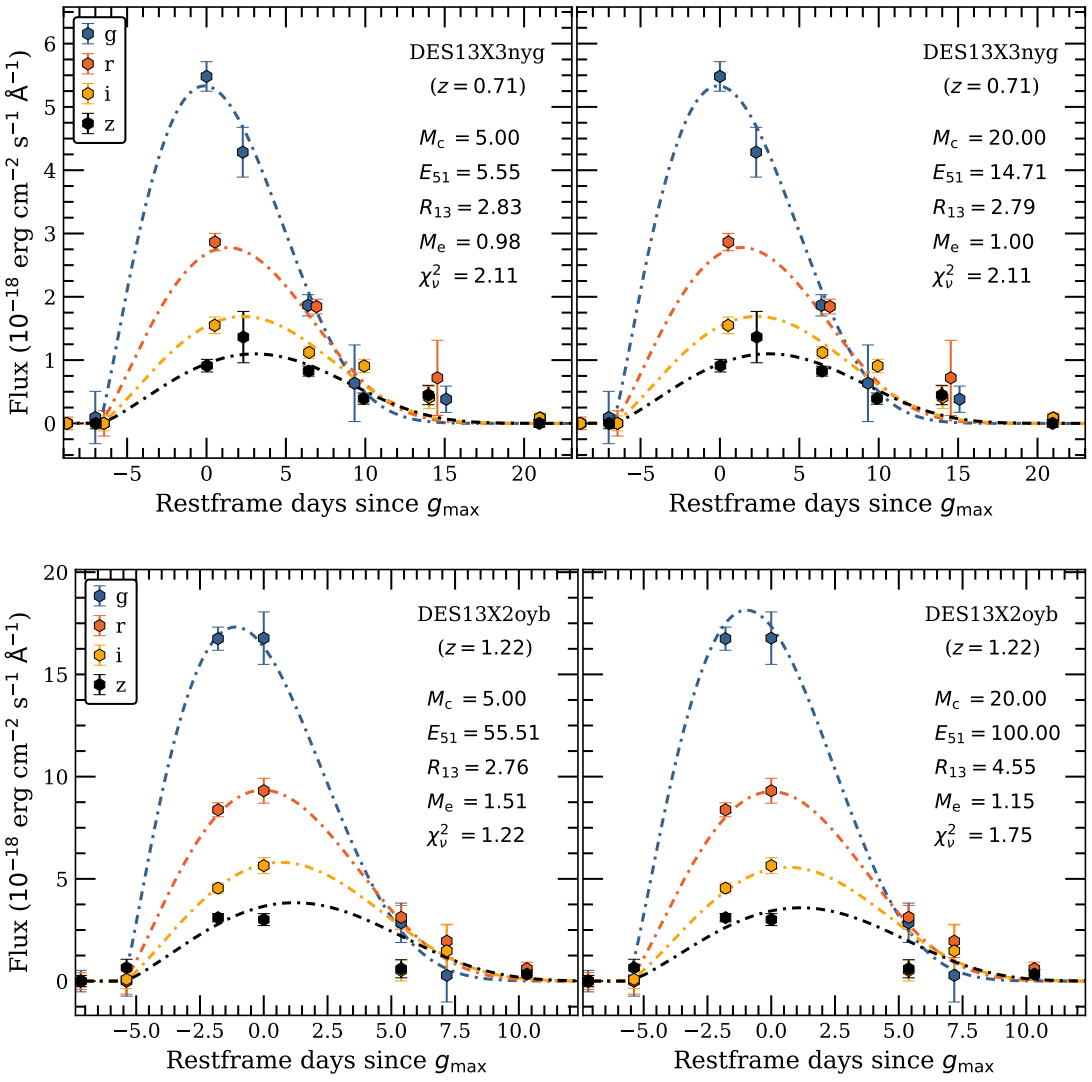

FIGURE 6.4: Shock-cooling fits to *griz* light curves of two example RETs at $z \gtrsim 0.7$. DES13X3nyg is shown in top panel and DES13X2oyb in the bottom panel. Fits using $M_c = 5\ M_\odot$ are given on left and $M_c = 20\ M_\odot$ on right. Note that $R_{13} = R_e/10^{13}$ cm.

hand, SESNe are typically significantly fainter in the NUV than in the optical (~ 2 mag; Pritchard et al. 2014). With these two effects the pre-peaks could be observed to be brighter than the main peaks in the *gr* bands, even if they were the same brightness in the rest frame.

However, under such scenario the redder bands (e.g. *iz*) would be probing similar wavelength ranges as the rest frame *gr* bands — at $z = 0.7$, the central wavelength of *i* band would be at $\lambda \sim 4605$ Å and *z* band at $\lambda \sim 5398$ Å, while the rest frame wavelengths of *gr* bands are $\lambda \sim 4830$ Å and $\lambda \sim 6430$ Å, respectively. SESNe are bright in these wavelengths and thus, unless the shock-cooling pre-peak is fundamentally brighter than the main SESN light curve in rest frame, the main light curve would have to be seen. Only at about $z = 1.5$ even the *z* band would be probing the NUV wavelengths ($\lambda \sim 3670$ Å) and

the situation could be different. As a result, one can conclude that for the shock-cooling to be a viable scenario to explain the RETs the pre-peaks would have to be brighter than the main light curves the SESNe even in the optical wavelengths.

6.2.3 Caveats of the Shock-cooling Scenario

The reasoning on how shock-cooling scenario could explain some high redshift RETs does seem believable, but there are several caveats to consider. For one, no shock-cooling pre-peak of a SESN has been observed to be comparable to those of SLSNe in brightness or duration and whether such a configuration is physically feasible remains unknown. While SLSNe and SESNe share characteristics, such as similarity of post-peak spectra of SLSNe and peak spectra of SESNe (e.g. Pastorello et al. 2010; Nicholl et al. 2015a), the differences between them in physical terms are not well understood. The reason why SLSNe are brighter and last longer than SESNe is not known, nor is the fact whether that physical mechanism can explain the differences in the brightness and duration of the pre-peaks as well.

Furthermore, if one assumes that SLSN-like pre-peaks similar to RETs can be created by SESNe, the resulting double-peaked events should also exist at lower redshifts and thus they should have been discovered by DES-SN. The original search for RETs I performed aimed to estimate the light curve duration roughly prior to a visual inspection so it is possible that the double-peaked transients would have been missed in that search. However, the updated search relied only on rise time and peak colour (for details see Chapter 3) and thus any transient with a rapidly rising double-peaked light curve with blue colours at peak should have been discovered. The only restriction is that the pre-peak likely had to be brighter than the main peak in order to have an acceptable rise time. However, due to DES-SN strategy emphasising depth over survey area the transients are likely found in high enough redshifts to fulfil the condition.

The search resulted in discovery of four transients that possibly showed evidence of two peaks in at least some of the bands, but only three of them have a spectroscopic redshift. The light curves of these three events are presented in Figure 6.5. DES13X1atuq and DE17C3cpg are low redshift transients ($z = 0.08$ and $z = 0.19$, respectively) where the pre-peak and the main peak are roughly the same brightness around $M \sim -16$ regardless of the band. For the two events the pre-peak also occurs on a timescale of ~ 5 d. Thus, these two events are similar to the discussed SESNe with pre-peaks and do not appear to have significant resemblance to the RETs.

The third transient shown in Figure 6.5 is more interesting in the discussed context. DES16C3did is a slightly brighter event with $M \sim -18.5$ pre-peak. The main peak,

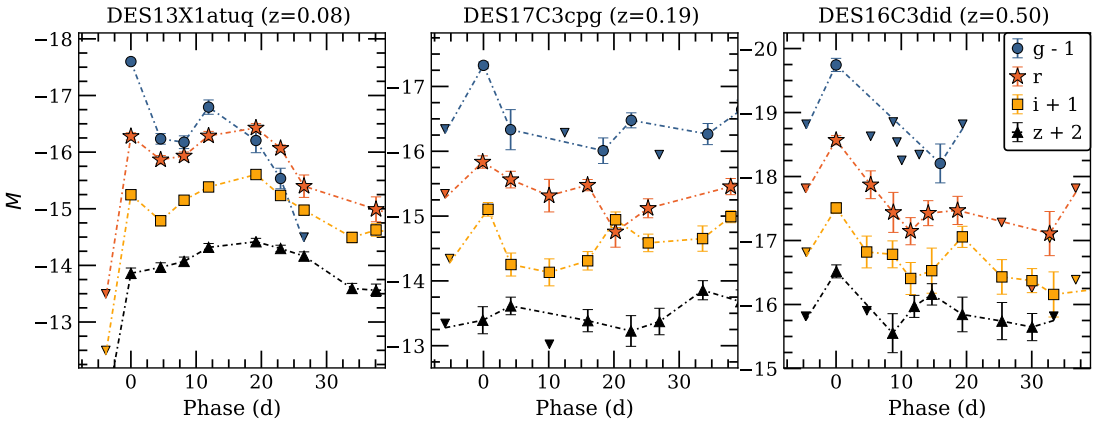

FIGURE 6.5: The *griz* rest frame light curves of the three DES-SN transients with spectroscopic redshift that showed evidence of double-peaked behaviour in at least some of the bands. Note that the bands have been offset for clarity

however, is barely seen in g and r bands due to the relatively high redshift ($z = 0.5$) and even in the iz bands the pre-peak appears to be slightly brighter than the main peak. Furthermore, the pre-peak timescale of DES16C3did is $\sim$ 10 d and thus similar to the RETs. However, even in this case the g band emission of the pre-peak drops very quickly and the first non-detection occurs only $\sim$ 5 days after the peak with a drop of at least 1.2 mag. Such evolution in the g band is fast even in for the sample of RETs and thus the event does not appear to be similar to the discussed high redshift events. Additionally the two peaks appear to have very similar peak magnitudes in i and z bands, unlike the discovered RETs. The fourth double-peaked DES-SN transient that was discovered shares a similar light curve evolution to DES16C3did in the observer frame, but as it does not have a spectroscopic redshift the luminosities and timescale cannot be discussed. To conclude, the lack of discovered double-peaked DES-SN transients where the first peak would resemble the RETs disfavours the shock-cooling scenario.

However, before the scenario can be ruled out one has to investigate if the observing cadence could affect the detection of such double peaked-transients. Due to the relatively high weekly cadence it is possible that the shock-cooling peak would be observed at one epoch, but by the time the field was targeted again, the pre-peak would have faded and the main light curve would be close to peak brightness. The resulting light curve would not show evidence for double-peaked behaviour and thus such a transient could potentially appear to be rapidly evolving single-peaked one. For instance, type Ic iPTF14gqr experienced a fast shock-cooling pre-peak in the beginning of the light curve, but the main peak of still rose to peak brightness in $\sim$ 7 from the explosion (De et al. 2018). Such an event could possibly be observed as a single-peaked transient in DES-SN. Furthermore, the light curve of one bronze sample RET, DES14E2bfx, shows a potential

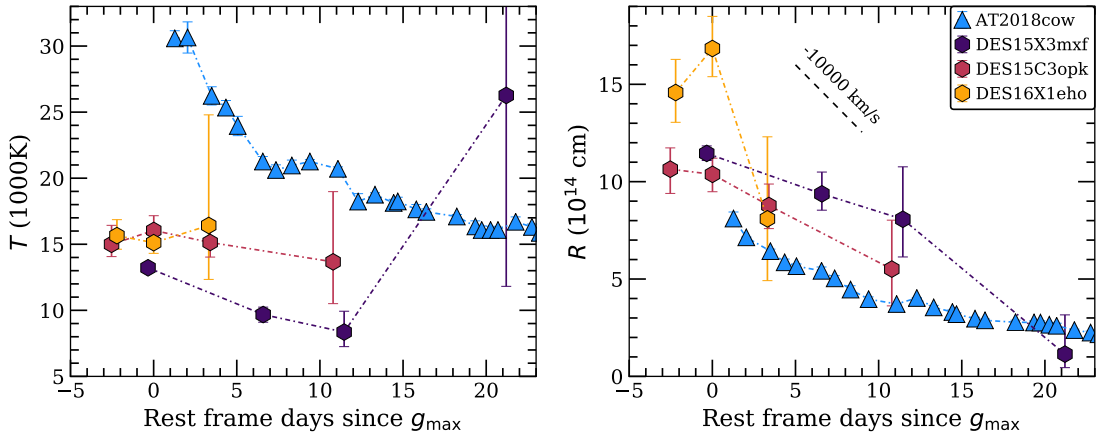

FIGURE 6.6: Comparison of temperature and radius evolution of AT2018cow and DES15X3mxf, DES15C3opk and DES16X1eho. The presented best-fitting temperatures and radii for AT2018cow are from Perley et al. (2019).

case where a shorter than average 5 day cadence actually reveals a double-peaked behaviour. The g band light curve of DES14E2bfx declines quickly from the first detection, but rises shallowly (0.1 mag) between second and third while r and z bands show shallow plateauing at the same time. Unfortunately the redshift of the RET is not known and the luminosities and timescales cannot be assessed, but even so the event is rapid even in the observer frame — the r band declined ~ 2 mag in 15 days.

However, observing a typical SESN pre-peak that lasts $\lesssim 5$ d (see Figure 6.2) near peak brightness so it appears brighter than the main peak is unlikely to occur. Furthermore, the main peak of the light curve would also have to be very rapidly evolving for the light curve evolution to appear smooth. This is especially true as the redshift increases and shorter and shorter timescales are probed. Such a main peak would likely be fast enough to qualify the event to be a RETs, even without a coincidental pre-peak detection. As a result it is entirely possible that the cadence could hide double-peaked behaviour and thus provide an explanation to individual RETs in the sample, but it is unlikely that such a scenario can be applied to a significant fraction of the events.

6.3 Comparison to AT2018cow

As discussed in the Chapter 1, one of the best observed rapid, blue transients in literature is AT2018cow at $z = 0.014$ and due to its rapidly evolving well observed light curve, it is an intriguing event to compare against the DES-SN RETs. However, AT2018cow exhibits one distinct photometric feature different from the bulk population of RETs: the evolution of photometric radius. The blackbody fits performed on the photometric data clearly show that the photospheric radius of AT2018cow was not increasing in time

— as is typical for the majority of the DES-SN RETs — but was in fact decreasing together with the high temperature (Prentice et al. 2018; Perley et al. 2019; Kuin et al. 2019). As discussed in Chapter 4, three out of the 52 gold and silver sample RETs show evidence of similar behaviour: DES15X3mxf at $z = 0.44$, DES15C3opk at $z = 0.57$ and DES16X1eho at $z = 0.81$ and this will focus on comparing these three events to AT2018cow.

The comparison of the temperature and radius evolution of AT2018cow and the three DES-SN RETs is presented in Figure 6.6. The presented values for AT2018cow are the best-fitting parameters of Perley et al. (2019) who fitted the UV-optical-NIR photometric data with a combined blackbody+synchrotron model, while for the DES-SN transients the fitting procedure is described in Section 4.1.2. Based on the figure its clear that the corresponding temperatures and radii are different — AT2018cow is both hotter and smaller than the three DES-SN RETs. Furthermore, the temperature of AT2018cow also evolves significantly faster in the early light curve evolution, while the temperatures of RETs stay roughly constant or decrease only slightly. The evolution of radius for AT2018cow and DES15X3mxf and DES16C3opk show relatively similar rate of decrease despite slightly different values but for DES16X1eho it is clearly different. Not only is it the only one that shows a signature of increasing radius in the early light curve, but it also recedes significantly faster than the others.

Despite the differences of temperature and radius evolution, it is important to compare the light curves as well. Due to the vast redshift differences between the RETs and AT2018cow ($z = 0.014$), direct light curve comparison is difficult to perform. However, using the presented best-fitting temperatures and radii from Perley et al. (2019) the light curve of AT2018cow can be recreated to match the DES *griz* filters at the observed redshifts of the three RETs. While Perley et al. (2019) also modelled synchrotron emission with the blackbody SED, it has a strong effect only in the NIR near the peak brightness and thus, in the observed, rest frame wavelength ranges of the three DES-SN RETs ($\lambda \lesssim 6400$ Å) the emission of AT2018cow is described solely by the blackbody part of the model. The resulting light curves are shown in Figure 6.7 in comparison with the three RETs. The light curves of DES-SN transients are shown since maximum observed brightness in g band, but AT2018cow has been shifted in time to match the light curves better. Note that the light curve of AT2018cow starts from the last non-detection at MJD 58284.13, 3.0 rest frame days before the peak detection as reported by Prentice et al. (2018), but as the blackbody fits require data in multiple bands, the fits start at MJD 58288.44, 1.3 d after the peak. Here the peak is assumed to be the observed maximum brightness in g' at MJD 58287.15 as presented by Prentice et al. (2018).

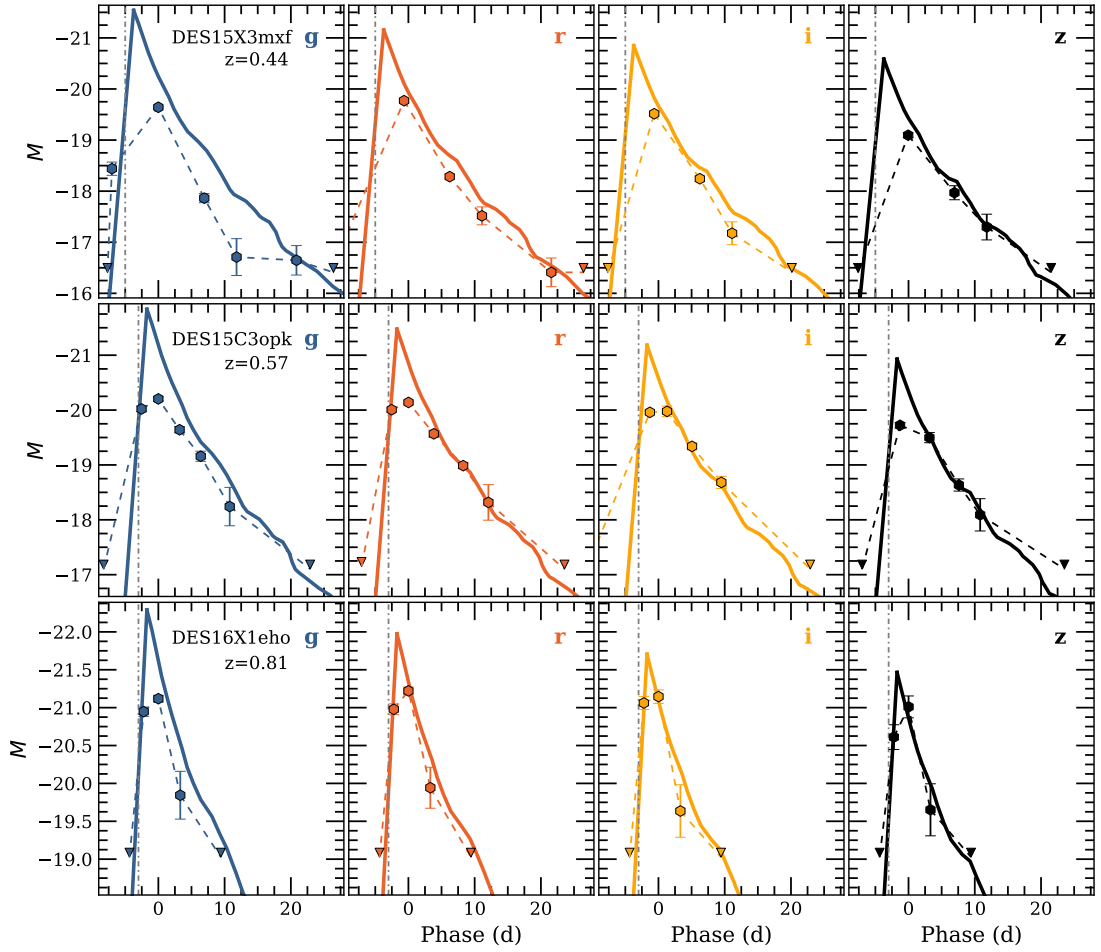

FIGURE 6.7: *griz* light curve comparison of AT2018cow shown with solid lines and DES15X3mxf, DES15C3opk and DES16X1eho shown with hexagons. The AT2018cow light curves have been created based on blackbody SED fits of Perley et al. (2019) to match with observed redshift. The RET light curves are presented since the observed peak in g band, but AT2018cow light curves has been shifted to match better with the DES photometric data. The shift is 5 days when compared with DES15X3mxf and 3 days when compared with DE15C3opk and DES16X1eho. The vertical dot-dashed line refers to the time of peak detection of AT2018cow as reported by Prentice et al. (2018). Note that the light curve of AT2018cow starts from the last non-detection 3.0 rest frame days before the peak detection as reported by Prentice et al. (2018) but, as the blackbody fits require data in multiple bands, the fits start 1.3 d after the peak.

The comparison shows that all three DES-SN RETs share very similar fast evolving light curves with the AT2018cow in all four bands, but there are also some minor differences. The first observations of DES15C3opk and DES16X1eho in the g and r bands seems to coincide well with the peak detection of AT2018cow, but the DES transients rise further. Furthermore, AT2018cow also appears to be significantly brighter than the two RETs in these bands. In the other two bands the light curve seem to match better. The differences seen in the two DES transients can be explained by the evolution of temperature. While AT2018cow starts at a high temperature of $\sim$ 30000 K and declines quickly to $\sim$ 20000 K, the DES-SN RETs do not exhibit temperatures above $\sim$ 15000 K.

The third RET, DES15X3mxf, has poorer constraints on the exact time of the peak, but it has an exceptionally well constrained explosion time with a non-detection in g, i and z ~ 0.65 d before the first detection in the g band. Unfortunately after this detection the field was observed next time ~ 6 rest frame days later and the peak of the transient was missed in all bands. The g band light curve of DES15X3mxf seems to decline faster than AT2018cow apart from the last detection, potentially indicating some kind of plateauing. However, the detection was accompanied by an r band observation at a similar epoch that clearly shows decline similar to the earlier light curve. Furthermore, the temperature estimated based on the g and r band observations of the epoch is wildly inconsistent with the previous values (see Figure 6.6). Thus, it seems likely that the measured g band flux is higher than in reality. In the remaining r, i and z bands the light curves are nearly perfectly aligned with AT2018cow.

Due the similarities of the light curves and the fact that all four transients show receding photospheres, it seems reasonable to assume that the three RETs could in fact be similar to AT2018cow in origin. However, because of the differences discussed above, the progenitor models would also have to allow a level of flexibility to match with the diversity of the observables. Regardless, if one assumes that the three RETs are indeed similar to AT2018cow in nature, it would strongly constrain the event rate of such transients. In literature the DES-SN sample of RETs has been commonly grouped with the AT2018cow, due to the apparent similarity of the light curves. However, if only 3/52 RETs are "cow-like" their event rate would be $0.23 - 0.4\%$ of the CCSNe rate when using the volumetric RET rate estimated by Drout et al. (2014). The rate is thus consistent with both $\sim 0.6\%$ estimated by Ho et al. (2020) and $\lesssim 0.25\%$ estimated by Coppejans et al. (2020) for "cow-like" transients. While the rate estimated here is only a very rough one, the comparison to literature values makes the similarity of the three DES-SN transients and AT2018cow even more believable.

6.4 Comparison to the Kilonova AT2017gfo

In the light of the recent discovery of the NS-NS merger GW170817 and its electromagnetic counterpart KN AT2017gfo (see e.g. Alexander et al. 2017; Andreoni et al. 2017; Arcavi et al. 2017b; Blanchard et al. 2017; Chornock et al. 2017; Coulter et al. 2017; Cowperthwaite et al. 2017; Drout et al. 2017; Fong et al. 2017; Kasliwal et al. 2017; Kilpatrick et al. 2017; Margutti et al. 2017; Nicholl et al. 2017; Siebert et al. 2017; Smartt et al. 2017; Soares-Santos et al. 2017), it is interesting to compare its optical properties with the sample of RETs. The KN rose to peak brightness almost immediately and had a very rapidly declining light curve with the last detections in g band roughly a week

after the merger event (Cowperthwaite et al. 2017; Drout et al. 2017; Soares-Santos et al. 2017). Such a fast light curve would definitely have qualified AT2017gfo as a RET if it had been observed by DES-SN.

AT2017gfo was a fairly faint transient with an absolute peak magnitude of $M \sim -15.5$ in the optical bands. Its SED is well described by a blackbody for the first few days with a temperature $T \sim 11000$ K and radius $R \sim 3 \cdot 10^{14}$ cm at 0.5 days (Kasliwal et al. 2017), $T \sim 8300$ K and $R \sim 4.5 \cdot 10^{14}$ cm at 0.6 days (Cowperthwaite et al. 2017) and $T = 5500 \pm 150$ K and $R \sim 7 \cdot 10^{14}$ cm at 1.5 days after the merger (Nicholl et al. 2017). Furthermore, Drout et al. (2017) presented temperatures of ~ 2500 K from 5.5 to 8.5 days after the merger, consistent with values given by Smartt et al. (2017) who found that AT2017gfo cooled down from $T = 7600 \pm 2000$ K at 0.6 days to $T = 1900 \pm 500$ K at 13.3 days.

In the gold and silver samples there are only two RETs with comparable peak luminosities: DES14S2anq ($M_{\rm g} = -16.2$) and DES14S2plb ($M_{\rm g} = -15.8$). The two RETs also exhibited similar peak temperatures and radii as the KN: $T = 7700$ K and $R = 6.6 \cdot 10^{14}$ cm for DES14S2anq and $T = 8900$ K and $R = 4.1 \cdot 10^{14}$ cm for DES14S2plb. However, while the KN had already declined ~ 4.5 mags in g and ~ 3.5 mags in r band in 5 days after the merger (see e.g. Drout et al. 2017), the DES events decline only 1.2 – 1.5 mags in g and 0.7 – 0.9 mags in r in roughly 10 days after the peak brightness. Due to the significantly slower decline rate, it is unlikely that these events are associated with a NS-NS merger. A similar conclusion was reported by Siebert et al. (2017) who compared the light curve of GW170817 to other optical transients, including several rapidly evolving events from Drout et al. (2014), and found that the KN evolved much faster in comparison.

It is also unlikely that any of the bronze sample RETs are similar to AT2017gfo either. These RETs lack spectroscopic redshifts as their host galaxies are mostly fainter than $m_{\rm r} \sim 24$ (see Chapter 5). In order for DES-SN to detect a KN with a peak magnitude $M \sim -15.5$, it would have to be at very low redshift ($z \lesssim 0.2$). However, it is unlikely that these host galaxies would be so local without having their spectroscopic redshift obtained by OzDES. At $z = 0.2$ a faint galaxy of $M \sim -18$ would have an apparent magnitude of $m \sim 22$ for which OzDES efficiency of obtaining a secure redshift was $\sim 90\%$ (Lidman et al. 2020).

While all suggested KNe do no exhibit similar "blue" light curves as AT2017gfo, the theorised "red" KNe evolve otherwise on similar timescales but they are significantly redder in comparison. The best example of such a red KN is the optical counterpart of GRB130603B that was observe to be most prominent in NIR (Tanvir et al. 2013; Berger et al. 2013). Prior to discovery of AT2017gfo, Doctor et al. (2017) searched for such red KNe in the first two years of DES-SN data and found no transients consistent with their

model predictions. Furthermore, Scolnic et al. (2017) used the observed AT2017gfo light curves to estimate that DES-SN should have found only 0.26 similar KNe during the five observing seasons. Due to the reasons discussed above it is unlikely that any of the DES-SN RETs are KNe.

6.5 Summary

In this Chapter I have presented discussion on possible physical scenarios to explain the light curves of the rapidly evolving transients. It seems reasonable to assume that the DES-SN RETs are drawn from a similar population of events as the literature ones, and thus it is likely that a significant fraction of them are SESNe of some kind. Furthermore, the host galaxy properties presented in Chapter 5 imply a similar conclusion. However, the decay of radioactive nickel, typically assumed to power the light curves of SESNe, does not seem to be able to explain the peak luminosities of the majority of the RETs due to the short rise times to peak brightness. Therefore, while ^{56}Ni is likely created in the RETs, it cannot be the main power source for the majority of the events.

As the nickel decay is ruled out as a possible power source, alternative scenarios related to SESNe have to be considered. In this Chapter I focused on a scenario of shock-cooling emission that is known to explain rapidly evolving pre-peak features seen in many SESNe and SLSNe. At low redshifts the model is problematic as the resulting fits provide poor matches to the observed data. Furthermore, the main light curve of any SESN that would create a prominent pre-peak feature would also have to be detected by DES-SN and thus the scenario does not seem applicable at low redshifts. While the model might seem more believable at higher redshifts it is difficult to explain why SLSN-like pre-peak would be created by a SESN when such phenomenon has not been reported in the literature.

The comparison of light curve and radius evolution revealed that three RETs could in fact be similar to the mysterious AT2018cow. All four events share receding photosphere and extremely bright rapidly evolving light curves. While the transients exhibit some differences, namely in the values of temperature and radius, it seems likely that at least some of three RETs are in fact similar to AT2018cow in origin. The conclusion is further supported by a event rate of cow-like transients estimated based on the three DES-SN RETs. The found value of 0.23 – 0.4% of the CCSNe rate is consistent with values presented in literature. Finally, the comparison of RETs with AT2017gfo revealed that the KN occurred on much faster timescales than the RETs and thus it is unlikely that any of the RETs could be a caused by a NS-NS merger.

While the nature of the RETs could not be determined, the observed diversity of the sample likely implies that rapid light curve evolution can be created by several progenitor channels. Possible scenarios discussed in the literature include for instance explosion of a stripped massive star (e.g. Drout et al. 2013; Tauris et al. 2013; Kleiser & Kasen 2014; Kleiser et al. 2018), shock breakout either in CSM (Ofek et al. 2010; Rest et al. 2018; Ho et al. 2019a) and CSM interaction (Arcavi et al. 2016). Many of the suggested mechanisms could explain the peculiar light curves and at this stage it is too early to definitely say which scenarios are the most prominent. More rapidly evolving events need be discovered early in the evolution to distinguish what power sources can be responsible for these peculiar transients.

Chapter 7

Photometric Twins DES17X1boj and DES16E2bjy

The Dark Energy Survey Supernova Programme has proven to be an excellent laboratory for discovering unusual types of extragalactic transients. Its deep ($\sim$ 24 mag per visit) multi-colour *griz* photometry provided the large sample of RETs presented earlier in this thesis, but the data-set has also been used to, for example, probe the diversity of type I SLSNe (Angus et al. 2019). In this Chapter I will carry on with theme of investigating peculiar optical transients found in DES-SN data and present two additional events, DES17X1boj and DES16E2bjy, characterised by highly atypical double-peaked light curves nearly identical to each other.

Light curves exhibiting several phases of rebrightening are not uncommon amongst extragalactic transients. Type Ia SNe have characteristic secondary peaks in the redder bands due to Fe III recombination (Kasen 2006), but also a fraction of CCSNe and SLSNe show double-peaked behaviour. As discussed in the Chapter 6, several type IIb SNe (e.g. SN1993J; Wheeler et al. 1993), type Ic iPTF14gqr (De et al. 2018) and several SLSNe (e.g. SN2006oz; Leloudas et al. 2012) all have short precursory bumps attributed to shock-cooling in extended material surrounding the SN. Even some normal type II SNe show rebrightening as several type IIP SNe been observed exhibiting a shallow rise during their plateau phase (e.g. SN2009N; Takáts et al. 2014). However, none of these SNe have visibly similar light curves with the two DES-SN transients.

While DES17X1boj and DES16E2bjy share a nearly identical light curve evolution, several other observable features are clearly different. The transients differ by nearly three magnitudes in brightness with DES17X1boj peaking at $M_{\rm r} = -15.4$ and DES16E2bjy reaching $M_{\rm r} = -17.9$. Furthermore, they are also found in different host environments: DES17X1boj's position is consistent with the nucleus of a star-forming spiral galaxy,

while DES16E2bjy appeared on the outskirts of a passive galaxy. The only common factor is thus a presence of old stellar populations in both environments. While the potential high-velocity ($v \sim 9400$ km/s) CaII absorption feature in the spectrum of DES17X1boj and the photospheric expansion velocity of DES16E2bjy ($v \sim 4800$ km/s) strongly indicate an explosive or eruptive origin for these transients, the exact physical scenario remains unknown. Due to the several different observed features it is also entirely possible that the transients do not share a similar origin, despite nearly identical light curve evolution.

7.1 Observations

DES17X1boj was first detected by DES-SN at a signal-to-noise > 5 in DECam *griz* images taken on 9th of October 2017 at R.A. $= 02^{\rm h}19^{\rm m}53.80^{\rm s}$, Decl. $= -04°57'10.4''$ (J2000) with a previous non-detection on the 29th of September. The transient reached a maximum brightness of $m_{\rm r} = 20.52$ ($M_{\rm r} = -15.35$) on the 17th of October and was detected for the last time on 13th of December the same year. In the beginning of the light curve, DES17X1boj was identified as a potential RET candidate in a live selection of targets during year five of DES-SN, where all new transients with relatively blue colours ($g - r < 0.2$) were visually inspected. However, promptly after the discovery it was identified to be another type of peculiar object due to the double-peaked light curve.

DES17X1boj was observed spectroscopically for 2400 s on the 22nd of October as part of the OzDES programme and the resulting data was reduced by the OzDES team with the pipeline described in Yuan et al. (2015). As the underlying galaxy is $1.0-1.5$ magnitudes brighter than DES17X1boj at peak brightness in all bands, the spectrum is dominated by host galaxy features. Prior to the transient event, the host of DES17X1boj was observed for 7200 s in November 2010 with AAT by the GAMA programme (Driver et al. 2009; Baldry et al. 2018).

DES16E2bjy was recovered with an archival search for transients that exhibited similar light curve evolution to DES17X1boj. The search was performed after the end of DES-SN observing operations (see Section 7.2). The transient was first detected by DES-SN on the 21st of September 2016 at R.A. $= 00^{\rm h}33^{\rm m}19.34^{\rm s}$, Decl. $= -44°20'19.6''$ (J2000), with a previous non-detection on the 13th of September. The transient reached maximum brightness of $m_{\rm r} = 20.99$ ($M_{\rm r} = -17.94$) on the 4th of October and was detected for the last time on the 17th of December the same year.

DES16E2bjy was spectroscopically observed for 2400 s on the 5th of October by OzDES, and for 2800 s on the 7th of October 2016 with the RSS on 10 meter-class SALT as it was

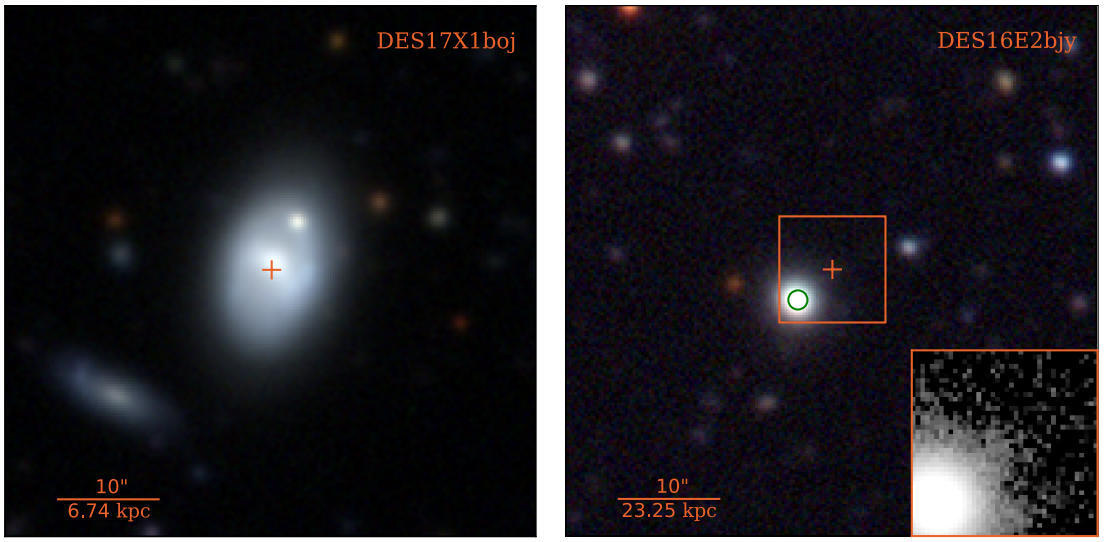

FIGURE 7.1: Host environments of DES17X1boj and DES16E2bjy. Transient locations are marked with red crosses and the assumed host of DES16E2bjy is shown with a green circle. The host of DES17X1boj is at $z = 0.0338$ and DES16E2bjy at $z = 0.1305$. For DES16E2bjy a zoom-in of the transient location in r band is shown in the bottom-right corner, revealing the presence of light presumably from the host galaxy at the location.

a high probability candidate for a type Ia SN. The SALT spectrum has a resolution of $R \sim 350$ and it was reduced using the `PySALT`[1] pipeline (Crawford et al. 2010). The same slit spectrum was used to reduce the host galaxy spectrum presented in this Chapter.

The transient environments are presented in Figure 7.1 with stamps created using the optimised DES-SN deep stacks (Wiseman et al. 2020b). The location of DES17X1boj is consistent with the nucleus of a spiral galaxy (LEDA 1051269, Brouty et al. 2003) at $z = 0.0338$, while DES16E2bjy appears to be associated with a red elliptical galaxy at $z = 0.1305$ with a separation of $\sim 5''$ (11.6 kpc). The host galaxy redshifts were obtained by the OzDES programme and all presented absolute magnitudes have been estimated based on them.

7.2 Sample Selection

After the double-peaked behaviour of DES17X1boj was first noticed, an archival search was performed on the full five years of DES-SN data to search for transients with a similar light curve evolution. For this purpose I used the generated GP light curves to estimate the peak times and brightnesses of every named DES-SN transient to easily query events fulfilling the used search criteria. For information of the created GP light curves see Section 2.6.

[1] `http://pysalt.salt.ac.za/`

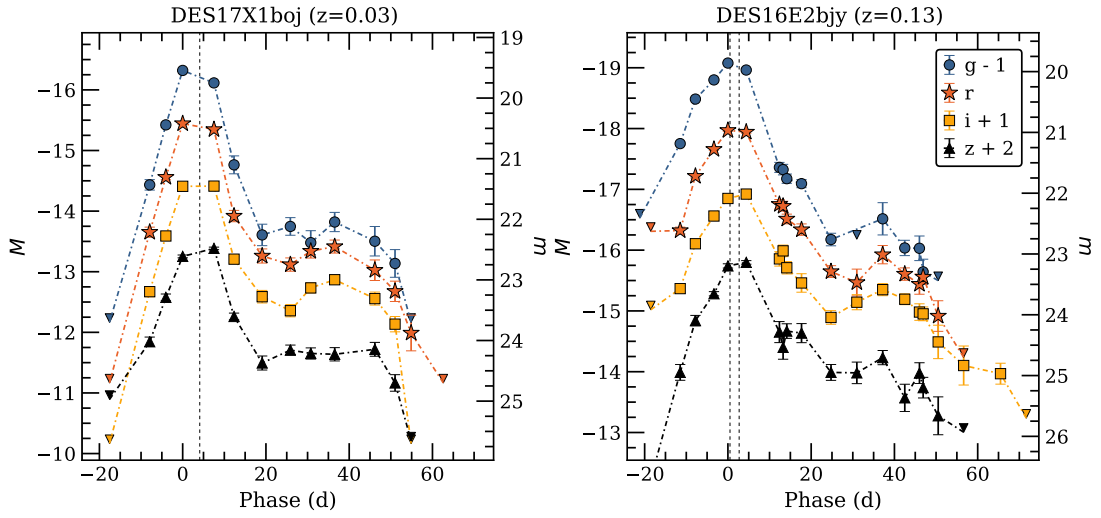

FIGURE 7.2: Rest frame DES-SN *griz* light curves of DES17X1boj and DES16E2bjy, with respect to maximum observed brightness in g band. Photometric bands are offset for clarity. Downward-facing triangles represent the upper limits of non-detections. The phases of spectroscopic observations have been marked with dashed vertical lines.

I searched for all unclassified DES-SN transients for which a secondary peak of a "boj-like" transient would have been seen to a limiting magnitude of 24 mags. This requirement corresponds to brightness of the primary peak of at least 22 mags. However, I also constrained the total observable volume by requiring the transient or its associated host galaxy to have a redshift of $z \leq 0.2$. At the limiting redshift, the peak brightness of a transient observed at 22 mag would correspond to $M = -18$. With the given criteria, DES17X1boj ($M_r = -15.4$) could have been recovered only up to $z = 0.07$. However, the search was designed to maximise the chance of discovering "boj-like" transients while also allowing them to be brighter than DES17X1boj.

In total 225 DES-SN transients passed the criteria. Light curves of these transients were visually inspected and only DES16E2bjy was found to have a similar double-peaked light curve evolution as DES17X1boj. Most of the other inspected transients had light curves similar to the traditional SN types and the few remaining transients were found to be spurious detections.

7.3 Photometric Properties

As shown in Figure 7.2, DES17X1boj and DES16E2bjy share a very similar light curve evolution. Both rise to maximum brightness, as measured from photometry in g band, in $15 - 20$ d and decline rapidly by $2 - 3$ mags in ~ 20 d before plateauing. In g and z bands the light curve exhibit a plateau with a possible tentative rise but the second peak-like feature is clear in both r and i bands for both of the transients showing a rise of

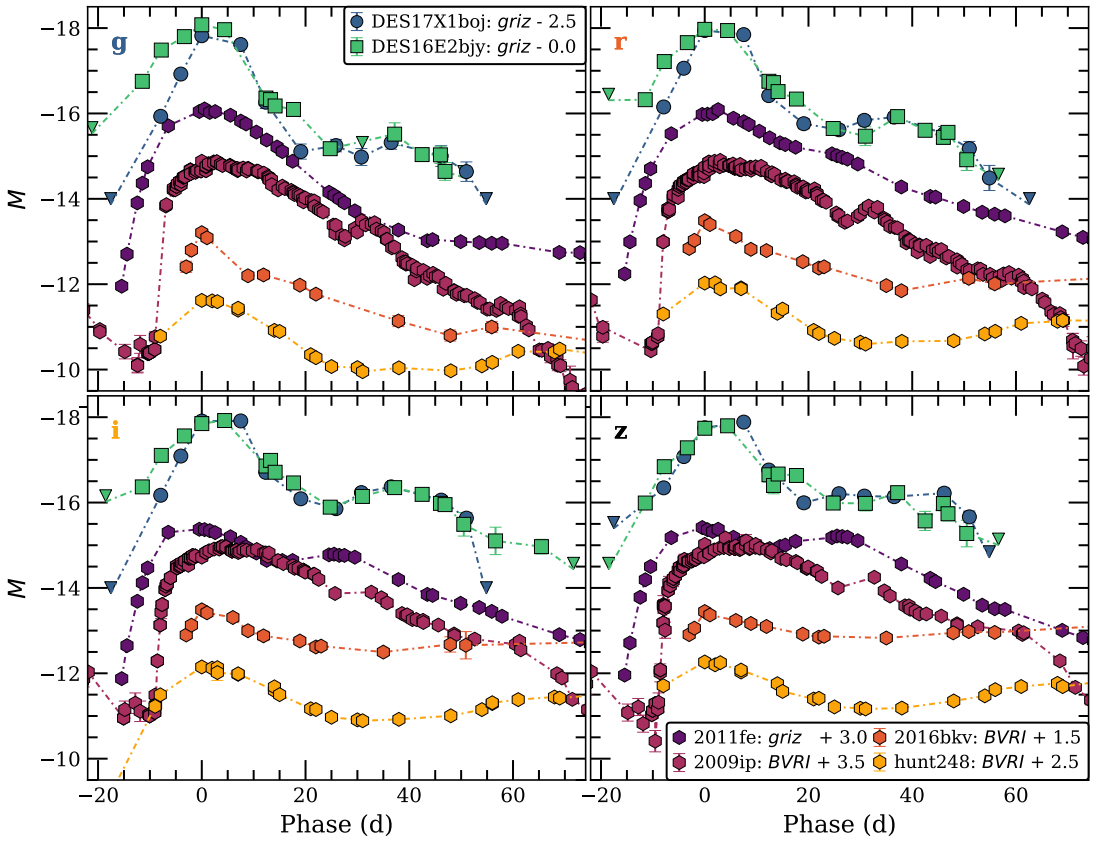

FIGURE 7.3: Light curves of DES16E2bjy and DES17X1boj, with respect to peak in g band. light curves of DES17X1boj have been scaled by 2.5 magnitudes. Type Ia SN2011fe (Richmond & Smith 2012; Munari et al. 2013; Tsvetkov et al. 2013), SN impostor SN2009ip (during the event in 2012; Fraser et al. 2013; Mauerhan et al. 2013; Pastorello et al. 2013; Brown et al. 2014), low-luminosity type IIP SN2016bkv (Hosseinzadeh et al. 2018; Nakaoka et al. 2018) and triple-peaked transient event SNhunt248 (Kankare et al. 2015; Mauerhan et al. 2015), proposed to be a LRN (Mauerhan et al. 2018), have been plotted for comparison. The light curves of literature events were collected from The Open Supernova Catalog (Guillochon et al. 2016), apart from SN2011fe for which the light curve was created based on BVRI light curves from the above sources which were k-corrected (Nugent et al. 2002) using a spectrophotometric templates from Hsiao et al. (2007). Note that offsets have been added to literature events for visual clarity.

~ 0.5 mags. After the peak/plateau both of transients fade quickly below the detection limit in all bands. While the light curves show some level of scatter, the secondary peaks seen in r and i are more significant than the slight variations. Furthermore, while the tentative rise seen in g and z bands is debatable due to the scatter, it is clear that these bands are at least plateauing at the same time as r and i exhibit the secondary peaks. Therefore, in this thesis I refer to that feature as the secondary peak and call these two events double-peaked.

Despite the similar light curves, the peak luminosities are very different: while DES17X1boj is $M_{\rm r} = -15.4$ at observed maximum brightness, DES16E2bjy reaches $M_{\rm r} = -17.9$. Note

that despite the events are found on different redshifts, the presented light curves have not been k-corrected due to unknown SEDs during the secondary peak. However, the significance of k-correction at maximum brightness can be estimated based on blackbody fits to the photometry (see Appendix D). The resulting correction for DES17X1boj is less than 0.1 mag and for DES16E2bjy 0.2 to 0.3 mag so that every band becomes fainter.

The similarity of the light curves is further emphasised in Figure 7.3, where a scaling of 2.5 mags (factor of ten in brightness) has been added to DES17X1boj to align the peak luminosities. The scaled light curves are nearly identical and the only significant difference between the two transients is the rise to maximum brightness which appears to be longer for DES16E2bjy especially in the bluer bands. The rise of DE16E2bjy also appears to have two phases; a faster rise until $\sim$ 10 d before peak and a slightly shallower, nearly linear rise to maximum brightness.

In Figure 7.3 I also present light curves of both normal and peculiar transients from the literature to demonstrate that the light curve evolution of DES17X1boj and DES16E2bjy is highly atypical. The transients have been selected as they evolve in similar timescales as the DES transients and show phases of rebrightening at similar epochs in at least some of the bands. Type Ia SNe (here illustrated with SN2011fe) typically exhibit rebrightening but it is prominent only in the redder bands (e.g. iz), while the secondary peaks seen of DES17X1boj and DES16E2bjy are visible in all four optical bands. Additionally the shape of the secondary peaks seen in i and z bands is very different from the DES-SN transients. Some type IIP SNe, such as SN2016bkv, show shallow rising during their plateau phase, but on much longer timescales and without significant changes in brightness. Even other peculiar transients with several phases of rebrightening, such as impostor SN2009ip (during the event in 2012) and LRN SNhunt248, do not show as extreme variation as seen in the light curves of DES17X1boj and DES16E2bjy.

In order to evaluate the evolution of temperature and radius for the events, blackbody fits were performed on every epoch of the four-band photometry using the description given in Section 4.1.2. The photometric data of both transients is well described with a blackbody model at least until $\sim$ 10 d after the initial peak. At later times the blackbody fits are less constrained due to fading targets. The fits are presented in Figures D.1 and D.2 in Appendix D. Note that the *griz* data points do not cover the peak of the blackbody SEDs at least in the early epochs of the light curves. Due to this, the presented uncertainties are likely underestimated and the fits are likely less constrained.

The blackbody temperature and radial evolution are shown in Figure 7.4 with the observed $g - r$ colour evolution. DES16E2bjy is clearly bluer and therefore hotter in the beginning of the light curve, but after $\sim$ +10 d the transients share similar colour and temperature evolution. However, while DES162E2bjy starts with a high temperature

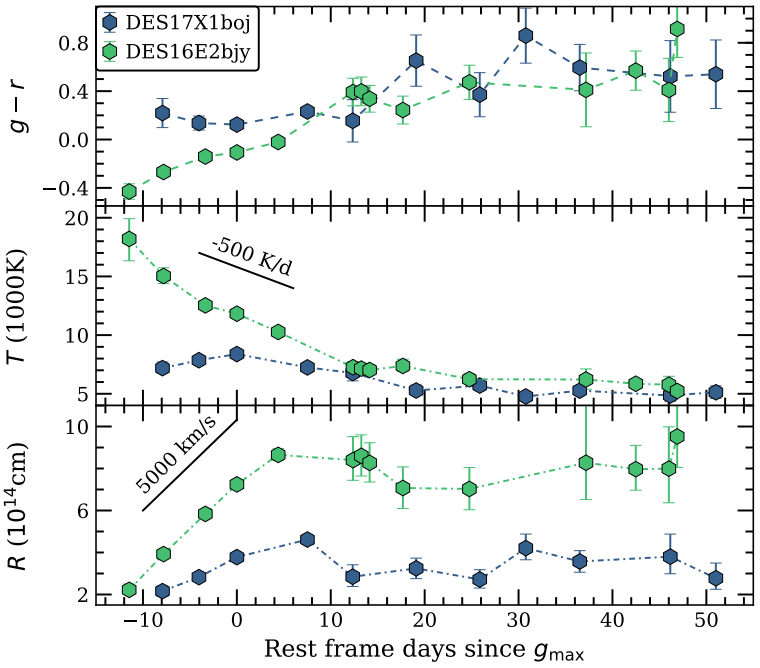

FIGURE 7.4: Observed $g-r$ colour (top) with temperature (middle) and radius evolution (bottom) based on blackbody fits to photometry. Errors for temperature and radius are given in 1σ confidence. Reference curves for velocity and change of temperature have been added for clarity.

of $T \sim 18000$ K and quickly cools down, the temperature of DES17X1boj appears to increase slightly until the peak brightness, reaching a temperature of ~ 8000 K. Afterwards the temperature gradually decreases. On the other hand, the radii of the transients evolve similarly to each other. First the radius increases nearly linearly until $\sim +10$ d, after which the radii either stay constant or decreases slightly. The mean photospheric expansion velocities based on the blackbody fits up to +10 d, as estimated by simple linear fits, are $v \sim 1800$ km/s for DES17X1boj and $v \sim 4800$ km/s for DES16E2bjy. Based on the sharp transition in the evolution of radii at roughly +10 d, it is likely that SEDs are not described by blackbody emission alone after this epoch (see Appendix D).

Finally, in Figure 7.5 I present the evolution of the pseudo-bolometric luminosity of DES17X1boj and DES16E2bjy, constructed using the blackbody fits (see Appendix D). The double-peaked shape of both light curves is clearly visible in the bolometric light curves. Furthermore, the two-phased rise of the initial peak of DES16E2bjy seen in the *griz* light curves (see Figure 7.2) appears to be slightly more pronounced in the bolometric light curve.

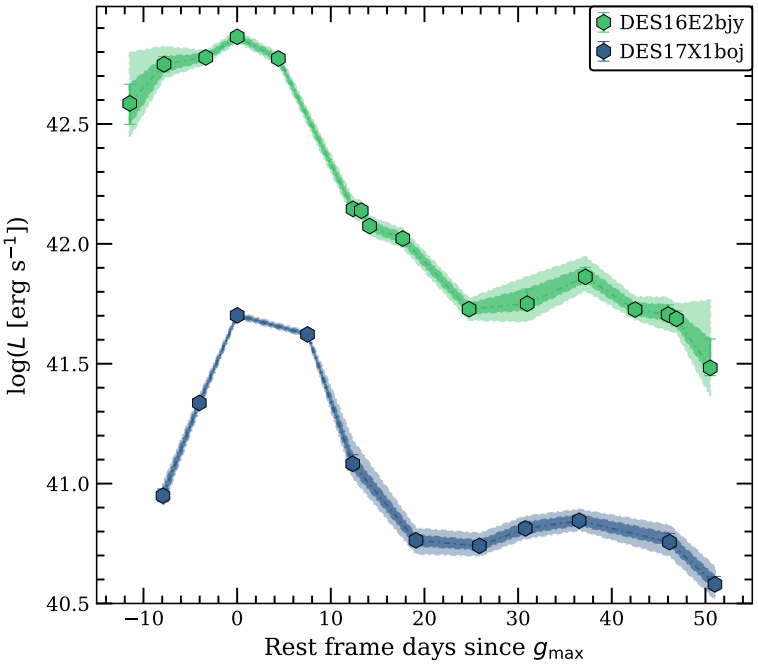

FIGURE 7.5: Pseudo-bolometric light curves of DES17X1boj and DES16E2bjy. Light curves are constructed using the blackbody fits and the shaded regions refer to 1σ (darker) and 2σ (lighter) confidence levels.

7.4 Spectroscopic Properties

The AAT spectrum of DES17X1boj is presented in Figure 7.6 with the host galaxy spectrum and resulting host galaxy subtraction. The spectrum was obtained four days after the observed maximum brightness, but even at this epoch the host galaxy was 1.0 – 1.5 mag brighter than the transient in all bands and thus the spectrum is dominated by host galaxy features. After the host galaxy subtraction, the spectrum shows a blue continuum best fit with a blackbody of $T = 9800^{+1000}_{-700}$ K which is slightly higher than the temperature based on the photometry ($T \sim 8000$ K, see Figure 7.4). The only significant line feature clearly visible in the subtraction is a relatively broad absorption at $\lambda \sim 3830$ Å. The feature resembles blueshifted calcium H&K absorption often seen in various types of SNe (see e.g. type Ia SN2011fe, type IIb SN2011dh and CaST SN2005E; Silverman et al. 2015, Arcavi et al. 2011 and Perets et al. 2010).

Assuming the feature is the blueshifted Ca absorption, the corresponding ejecta velocity would be $v \sim 9400$ km/s based on the wavelength at the middle of the feature. The feature has been plotted in Figure 7.7, where the best-fitting Gaussian absorption lines are also shown. The fitted Gaussian profiles were forced to be at 3813 Å and 3846 Å, corresponding to ejecta velocity of $v = 9400$ km/s, and they were required to have the same width. The best-fitting width was found to be $v_{\mathrm{FWHM}} = 2500^{+1600}_{-600}$ km/s, which is significantly higher than the resolution of the instrument $\Delta\lambda \sim 250$ km/s at Hα. All

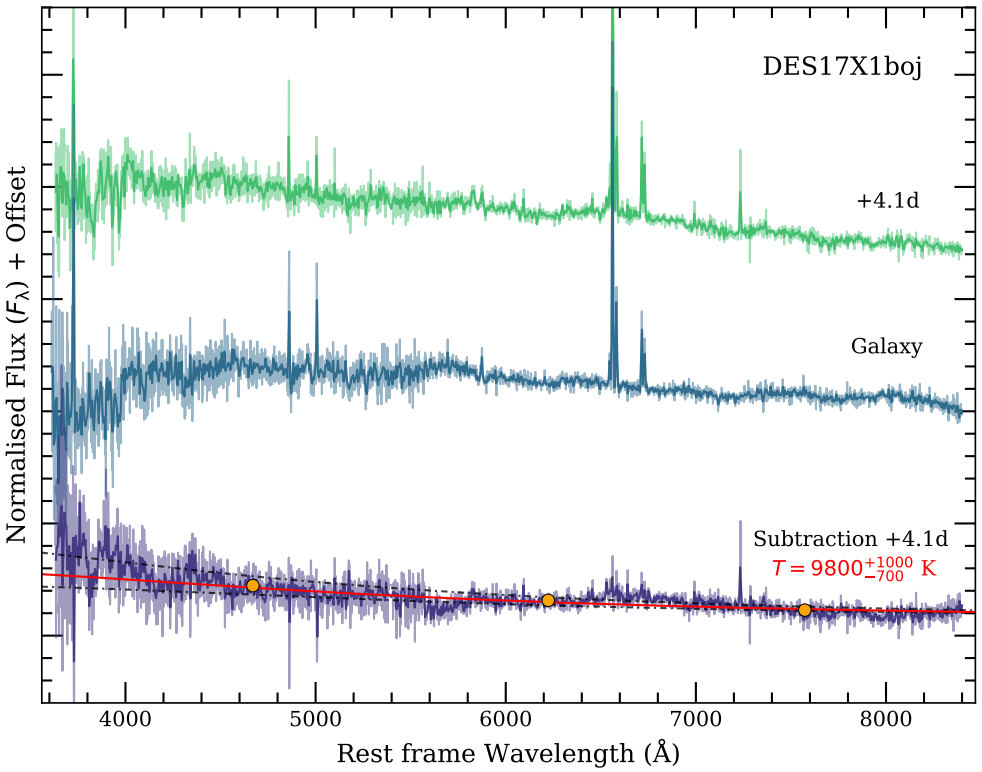

FIGURE 7.6: AAT spectrum of DES17X1boj, the host galaxy spectrum and the resulting host galaxy subtraction (lighter shade) and the corresponding spectra binned by factor of five (darker shade). The transient spectrum is taken a few days after the observed peak brightness and holds a considerable amount of transient light. The subtraction shows a blue continuum with blue-shifted CaII absorption feature at 3830 Å. The jump at 5600Å in the subtraction is caused by a dichroic issue in the galaxy spectrum. The red line is the best-fitting blackbody to the subtraction with black dashed lines corresponding to the given 1σ errors on the temperature. The orange circles are photometric *gri* data taken within a few days of the spectrum.

given errors were estimated using a Monte Carlo approach with 500 realisations and are shown in 1σ confidence.

The high velocity of this blueshifted CaII absorption is in good agreement with what is seen in SNe and thus it could suggest that DES17X1boj is a SN of some type. For instance, in the spectra of type IIb SN2011dh the feature occurs at higher velocity during the rise but it is found at $v \sim 10000$ km/s at the time of peak brightness (Sahu et al. 2013). On the other hand, the mean photospheric expansion velocity of this SN is $v \sim 3000$ km/s estimated based on the evolution of the blackbody radius presented in Ergon et al. (2014). While the value is higher than what was found for DES17X1boj, it demonstrates that a large velocity difference between the photosphere and the absorbing material can occur and has already been observed. Ergon et al. (2014) also estimated photospheric temperature evolution with a peak temperature of $T \approx 8000 - 9000$ K, similar to what is seen in DES17X1boj. Despite the discussed similarities, the light curve evolution of

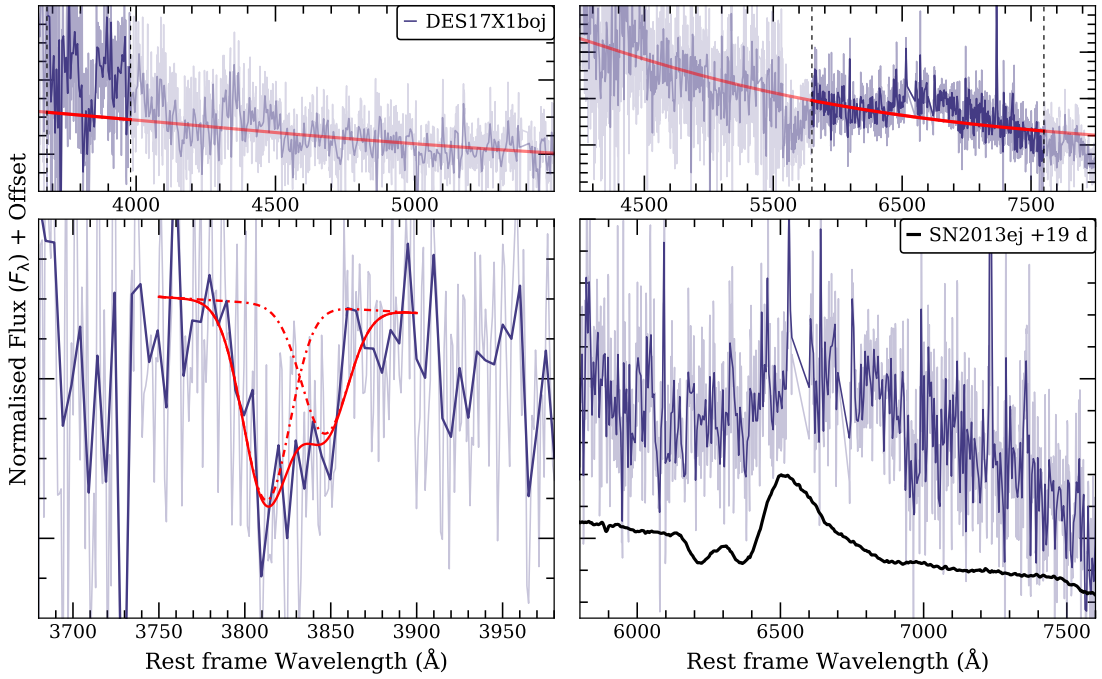

FIGURE 7.7: (left) Spectrum of DES17X1boj highlighting the blueshifted H and K absorption is shown in the top panel and the absorption feature with best-fitting Gaussian profiles given in red in the bottom panel. Lines were fixed to be at 3813 Å and 3846 Å (corresponding to ejecta velocity of $v = 9400$ km/s). Width of the lines was found to be $v_{\rm FWHM} = 2500^{+1600}_{-600}$ km/s. (right) Spectrum of DES17X1boj highlighting the excess emission around the Hα line is shown in the top panel and the the Hα region of DES17X1boj in comparison with type II SN2013ej around peak brightness, 19 days after the explosion (Dhungana et al. 2016) in the bottom panel. Note that residuals of narrow lines left from the host galaxy subtraction have been masked out. The solid red line in the top panels is the best-fitting blackbody presented in Figure 7.6. Note that the lighter shade refers to the subtracted spectrum and the darker shade represents the binned data as per Figure 7.6.

SN2011dh is smoother and slower than seen in DES17X1boj apart from the very short duration shock-cooling pre-peak often seen in type IIb SNe (Arcavi et al. 2011).

Furthermore, in Figure 7.6 there seems to be small amount of excess emission above the plotted blackbody fit around rest frame Hα at $\sim$ 6600 Å. To investigate the feature in detail, I show the spectrum of DES17X1boj around the Hα line in Figure 7.7 in comparison with type II SN2013ej 19 d after explosion (Dhungana et al. 2016, see also e.g. Valenti et al. 2014, Bose et al. 2015 and Huang et al. 2015). This SN was selected as it has a similar rise time to DES17X1boj in the r band and the spectrum was taken at comparable epoch around the peak brightness. DES17X1boj appears to exhibit excess emission that slightly resembles a broad Hα profile, potentially indicating that DES17X1boj is a type II SN. However, while the visual similarity appears to be reasonable, the high level of noise in the spectrum makes it difficult to say anything definite about the feature.

The AAT and SALT spectra of DES16E2bjy, taken shortly after peak brightness, are

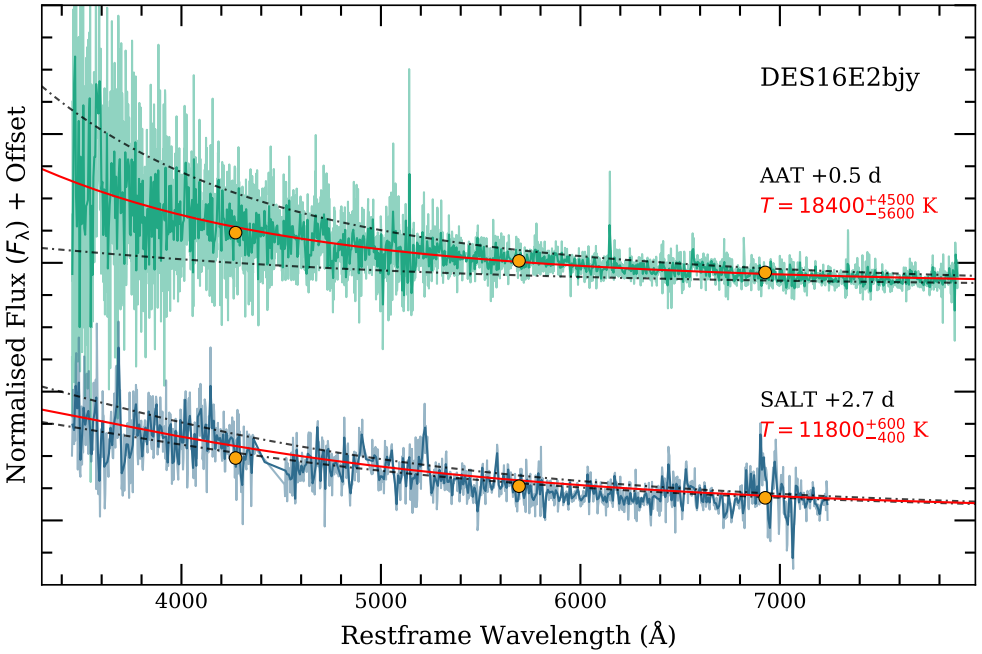

FIGURE 7.8: AAT and SALT spectra of DES16E2bjy close to peak brightness. The red lines are the best-fitting blackbody models to the spectra with the black dashed lines corresponding to the given 1σ errors on the temperature. The orange circles are the photometric data points taken within few days of the corresponding spectrum. Note that some strong residuals from sky subtraction have been removed for visual clarity and that there is a chip gap in the SALT spectrum around 4400 Å.

presented in Figure 7.8. Neither of the spectra show other features than underlying blue continuum which is best characterised with a blackbody. A blackbody fit to the AAT spectrum taken at +0.5 d after peak brightness in g band results in a temperature of $T = 18400^{+4500}_{-5600}$ K, which is higher than that based on the blackbody fits to photometry ($T \sim 12500$ K, see Figure 7.4) due to the high level of noise in the blue part. The SALT spectrum at +2.7 d shows a blackbody with $T = 11800^{+600}_{-400}$ K, consistent with the value based on photometry.

All spectra presented in this Section have been flux calibrated using the DES-SN *griz* photometry of the transients at the date closest to the epoch of spectra (the maximum difference being 3 days). For DES17X1boj the aperture photometry of the host from the DES-SN SV data was also applied. In the case of DES16E2bjy, the host galaxy brightness was estimated to be $m \sim 24.8 - 26.0$ depending on the band in the $2''$ aperture. This is significantly fainter than the transient at peak brightness ($m \sim 21$) when both of the spectra were taken and thus the contribution of the host galaxy is assumed to be negligible.

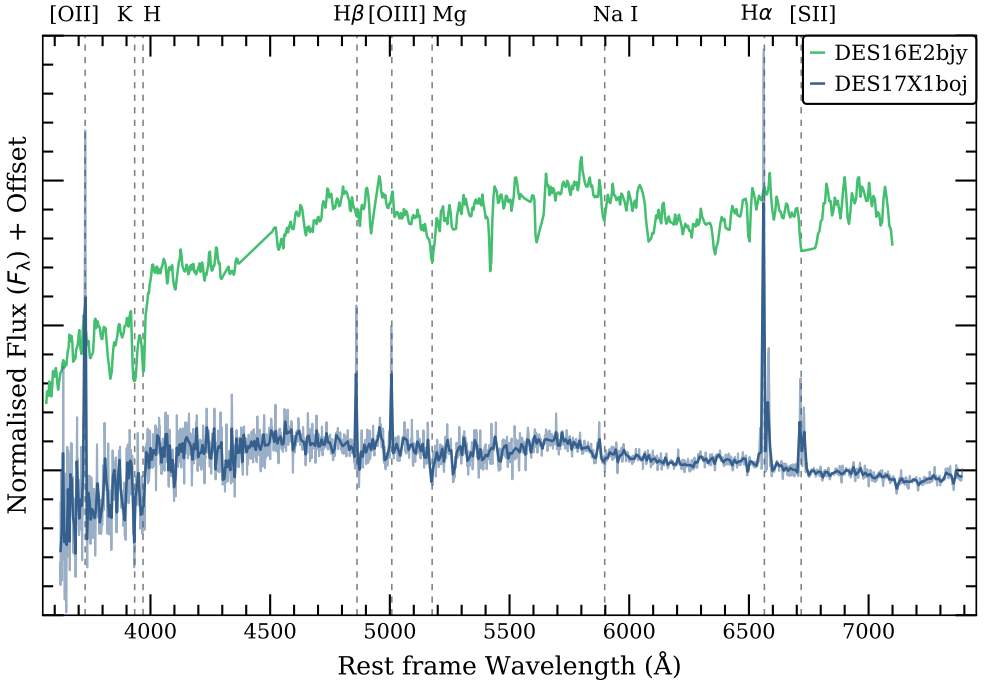

FIGURE 7.9: Host spectra of DES17X1boj and DES16E2bjy (lighter shade) and the corresponding spectra binned by a factor of five (darker shade). Some common absorption and emission lines have been marked with dashed lines.

7.5 Host Galaxy Properties

As mentioned earlier, DES17X1boj and DES16E2bjy seem to have occurred in different host environments (see Figure 7.1), and the conclusion is further supported by the host galaxy spectra presented in Figure 7.9. It is clear that the hosts of these two transients are different: DES17X1boj occurred in a star-forming galaxy characterised by numerous strong nebular emission lines, while the host of DES16E2bjy is a passive galaxy with no obvious signatures of recent star formation in the optical spectrum (e.g. Hα, [OIII], [NII]). The host of DES17X1boj was observed with the AAT under the GAMA programme with a 2″ fibre positioned at the centre of the host galaxy where the transient also occurred. As DES16E2bjy was separated by 5″ from its host, the host spectrum was obtained from the long-slit transient spectrum observed with SALT.

To estimate the star-formation history (SFH) of the hosts, the spectra was fitted using the `pPXF` spectral fitting code (Cappellari & Emsellem 2004; Cappellari 2012, 2017), based on the stellar templates provided by the MILES empirical stellar library (Vazdekis et al. 2010). `pPXF` simultaneously fits the continuum, stellar absorption features as well as ionised gas emission lines, providing a more robust measure of the emission-line fluxes than a continuum subtraction with a simple flat continuum. The resulting SFHs are presented in Figure 7.10. While the host of DES17X1boj consists of younger stellar

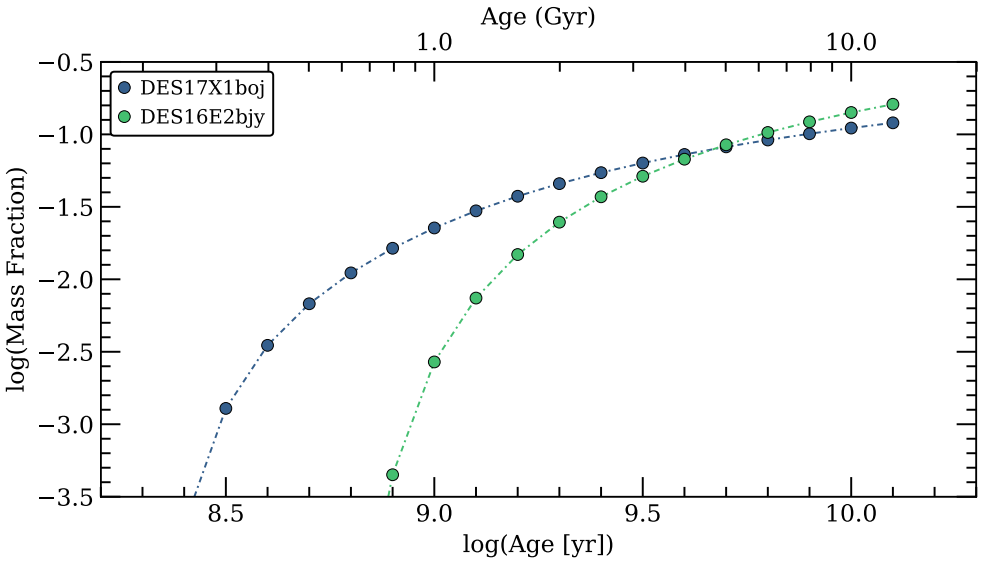

FIGURE 7.10: Star-formation history of the best-fitting models for the two transient hosts. The host of DES16E2bjy is clearly older with an average age of the stellar population of 7.6 Gyr and no significant population younger than 1 Gyr. The average age in DES17X1boj is 5.4 Gyr.

populations than the host of DES16E2bjy, it still has a dominant population of older, smaller stars which is the only clear similarity between the two hosts. The resulting average age of the continuum stellar population based on the `pPXF` fit is 5.4 Gyr for the host of DES17X1boj, while for the host of DES16E2bjy it is 7.6 Gyr with no significant population younger than 1 Gyr.

The presence of old populations in the host of DES17X1boj can also be clearly seen in the spectrum itself as the spectrum is reasonably red despite the strong, ionised lines that require a young population of stars (see Figure 7.9). The age of the young population can be estimated with the equivalent width of Hα and the found value, $W(\mathrm{H}\alpha) = 19$ Å, indicates that the average age of that population is $\sim$ 10 Myr or older (see e.g. Kuncarayakti et al. 2016; Xiao et al. 2019).

Next, the *griz* SEDs of the hosts were fitted with the `CIGALE` code (Boquien et al. 2019) to determine the host galaxy masses. The Bruzual and Charlot stellar population models (Bruzual & Charlot 2003) with a Salpeter initial mass function (Salpeter 1955) were used for the fitting and SFH was modelled as a delayed one with an optional exponential burst. The host mass of DES17X1boj was found to be $\log(\mathrm{M}/\mathrm{M}_\odot) = 9.76 \pm 0.16$ while for DES16E2bjy it is significantly higher with $\log(\mathrm{M}/\mathrm{M}_\odot) = 10.46 \pm 0.06$.

For the host of DES17X1boj, the flux measurements from the Hα, [SII], and [NII] lines were used to calculate the gas-phase metallicity (Dopita et al. 2016), which results in a slightly subsolar value of $12 + \log(\mathrm{O}/\mathrm{H}) = 8.51 \pm 0.03$. The gas-phase metallicity of

the DES16E2bjy host galaxy can not be estimated due to lack of host galaxy emission lines. The SFR of DES17X1boj host galaxy was then estimated to be $2.00 \pm 0.03 \cdot 10^{-2}$ $M_\odot$ yr^{-1} based on the observed Hα flux within the $2''$ aperture using the formula of Kennicutt (1998). Extrapolating the value over the whole galaxy results in SFR ~ 3 $M_\odot$ yr^{-1}, corresponding to sSFR log(sSFR) $= -9.3$. While the resulting sSFR is likely underestimated due to the central location of the aperture, it demonstrates that the host is definitely star-forming.

Apart from the DES-SN optical photometry, the host galaxy of DES16E2bjy has also been detected in the ultraviolet (UV) regime by the Galaxy Evolution Explorer (GALEX; Martin et al. 2005) in both far UV (FUV, 1350 – 1750 Å in observer frame) and near UV (NUV, and 1750 – 2750 Å). The UV magnitudes (FUV $= 22.75 \pm 0.07$ and NUV $= 22.56 \pm 0.05$) correspond to colors FUV $- r = 3.99$ and NUV $- r = 3.79$ indicating that the host is rather bright in UV for a such passive galaxy in the optical (see e.g. Petty et al. 2013). Assuming that all the UV emission of the galaxy comes from some residual star-formation still occurring in the galaxy, the resulting SFR is 0.14 $M_\odot$ yr^{-1} (using the formula from Kennicutt 1998) and the corresponding sSFR is log(sSFR) $= -11.3$. While these values demonstrate that some star-formation could still be happening in the host, its level is fairly low.

As the location of DES17X1boj is consistent with the nucleus of its host galaxy, it is essential to verify if the host harbours an AGN. In Figure 7.11 (top), I show that the 5-year DES-SN light curve of the transient shows no significant variation that would be expected for an AGN. In the same figure I also present the location of emission line flux ratios for the host galaxy on the Baldwin-Phillips-Terlevich (BPT) diagram (Baldwin et al. 1981), compared to data from SDSS (Tremonti et al. 2004) and theoretical lines from Kewley et al. (2001) and Kauffmann et al. (2003). BPT diagrams use line ratios (in this case $[NII]_{\lambda 5007}/H\alpha$ and $[OIII]_{\lambda 6584}/H\beta$) to distinguish if the line emitting region has been excited by star-formation or an AGN. Based on the diagram, the host of DES17X1boj is found below both of the theoretical lines, indicating that the host does not appear to have an AGN and thus the transient is unlikely to be an AGN flare. In Figure 7.11 (bottom) I also show that the 5-year light curve of DES16E2bjy does not exhibit significant variation either.

Due to the reasonably large separation of the DES16E2bjy and the centre of its assumed host galaxy ($5''$), it is possible that there is a small satellite galaxy in the vicinity of the passive galaxy that is actually the host. However, while something faint is present at the location of the transient in the DES-SN deep stacks (see Figure 7.1), its measured colours are consistent with the passive galaxy and thus it is likely associated with the putative host due to its similar stellar population.

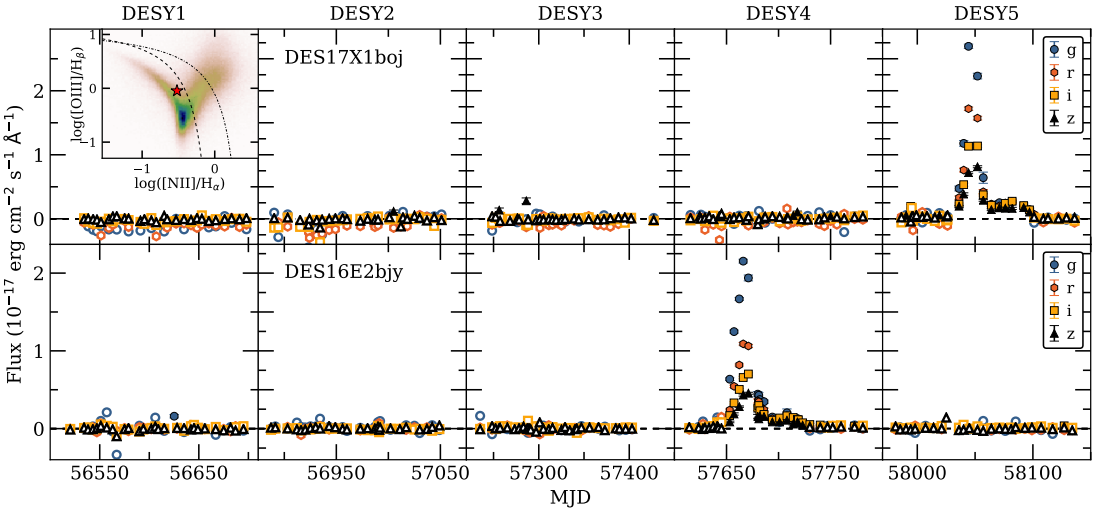

FIGURE 7.11: 5-year flux light curves of DES17X1boj (top) and DES16E2bjy (bottom). Neither of the transients show significant variation outside the events themselves. A BPT diagram (Baldwin et al. 1981) created with SDSS data (Tremonti et al. 2004) has been plotted for DES17X1boj. The host galaxy, plotted with red star, is located below the theoretical lines from Kewley et al. (2001) and Kauffmann et al. (2003) and thus it is unlikely that the host harbours an AGN. Note that 3σ detections are plotted with filled markers and non-detections with open markers and that errors are shown only for the detections.

7.6 Discussion

In the sections above, I have presented the analysis of the two peculiar DES-SN transients, DES17X1boj and DES16E2bjy, and their host galaxies. Based on the relatively fast mean photospheric expansion velocities ($v \sim 1800$ km/s for DES17X1boj and $v \sim 4800$ km/s for DES16E2bjy) the transients are likely either explosive or eruptive in origin. Additionally, the blueshifted CaII absorption feature identified in the near-peak spectrum of DES17X1boj may imply that it is a SN. As the light curves of the transients evolve very similarly, it is natural to assume that DES17X1boj and DES16E2bjy are products of a similar evolutionary channel. However, the large difference in the peak luminosities and photospheric expansion velocities are difficult to describe under any single scenario. Thus, while in the following I discuss scenarios that could explain the peculiar observational features of both of them, it is important to emphasise that whether the two transients originate in similar progenitors is still unclear.

The most striking photometric feature of DES17X1boj and DES16E2bjy is their peculiar double-peaked light curve evolution. As discussed in Chapter 6, several CCSNe and SLSNe have been observed to have precursory bumps often credited to a short-lived shock-cooling phase early in the light curve evolution and in many of these cases the pre-bumps have actually been as bright or slightly brighter than the main peak of the SN (see e.g. SN1993J and iPTF14gqr; Wheeler et al. 1993; De et al. 2018). However,

these pre-bump features typically last for only $\lesssim 10$ d due to rapidly cooling/expanding material (see e.g. DES14X3taz; Smith et al. 2016a).

In contrast, the first peaks of the two DES-SN events last for roughly 20 days during which the photospheric radii are clearly increasing. If one assumes that these peaks are powered by shock-cooling in extended material, their long-lasting light curves have to be explained. One possibility could be linked to the photospheric expansion velocities that are not particularly high ($v \approx 1800$ km/s for DES17X1boj and $v \approx 4800$ km/s for DES16E2bjy) and it is possible that extended material could stay optically thick for long enough to produce the peaks of the light curves. The secondary peaks would then occur after the extended material has dissipated and an underlying slow-rising CCSN would finally emerge. However, while the secondary peak of DES16E2bjy at $M_{\rm r} \approx -16$ is reasonable for a CCSN, $M_{\rm r} \approx -13.5$ of DES17X1boj is very faint for any kind of a SN. The faintest known CCSN to date is the type II SN1999br at $M = -13.77$ (Pastorello et al. 2004; Anderson et al. 2014), and this scenario DES17X1boj would have to be even fainter. Additionally, a shock-cooling pre-peak that is 2 – 3 mags fainter than the main SN in optical would be very peculiar. Unfortunately both of the transients were too faint at the time of the second peak for spectroscopic follow-up and thus no definite conclusion can be made of the nature of the second peak.

The data also poses an additional challenge to the shock-cooling scenario. While the temperature evolution of DES16E2bjy is rapidly declining from the first detection (as expected for rapidly heated, expanding material, see e.g. iPTF14gqr; De et al. 2018), the temperature of DES17X1boj increases slightly up to the peak brightness. Such an evolution can be explained with shock-cooling only if the temperature gradient in the shock heated material is steep enough so that the decreasing opacity would reveal deeper layers of the ejecta which are still hotter than the outer layer of the photosphere was at the beginning of the light curve, despite adiabatic expansion. Whether such a configuration is physically feasible is unclear.

As the spectrum of DES17X1boj shows some broad excess emission around Hα line (see Figure 7.7), it is natural to compare the DES transients with type II SNe, especially given that there are some photometric similarities as well. For instance, the peak brightnesses fit well within the distribution of type II SNe ($-14 \gtrsim M \gtrsim -19$, see e.g. Anderson et al. 2014; Richardson et al. 2014), the majority of type II SNe have plateaus after peak that in some cases show shallow rising (see e.g. SN2009N; Takáts et al. 2014), and both photometry and spectroscopy are well described with a blackbody in the beginning of the light curve. Under this scenario one would have to assume that the secondary peaks of the DES events would then be plateaus seen in SNe II. However, the assumption is problematic due to the following reasons. The DES-SN light curves drop 2 mags in 15 –

20 days in r band (see Figure 7.2) before the start of the secondary peak. Such a decline rate is significantly faster than detected for type II SNe (0.9 - 8.2 mag/100 d in V band; Anderson et al. 2014; Gutiérrez et al. 2017a). The "plateaus", lasting for $\sim$ 20 d, would also be on the short side of what is expected of type IIs (25 - 72 d in V band; Anderson et al. 2014). Additionally, the duration of SN II plateaus appear to be correlated with peak brightness so that a shorter plateau is associated with a brighter peak magnitude (Anderson et al. 2014; Galbany et al. 2016). Thus a short plateau would be unusual for faint a transient such as DES17X1boj. Even if the spectrum of DES17X1boj shows some broad excess around Hα, some of the discussed photometric properties of the DES-SN transients do not cohere with observed type II SNe. Therefore, if they actually were type II SNe they would have to be peculiar, and given their apparent similarity to each other they might be first examples of a strange kind of type II SNe.

Another interesting type of transient to compare DES17X1boj and DES16E2bjy with are the SN impostors. As shown in Figure 7.3, SN2009ip has a short phase of re-brightening around the same phase as the secondary peak of the DES-SN transients, and its peak brightness ($M_{\rm V} = -17.7$; see e.g. Fraser et al. 2013) is similar to DES16E2bjy. However, several other features distinguish the double-peaked DES-SN transients from the SN impostors. While SN2009ip does show rebrightening, its light curve evolution is clearly different from the DES transients. Additionally, other impostor candidates such as SN2015bh (see e.g. Elias-Rosa et al. 2016) and SN2016bdu (Pastorello et al. 2018) have very similar light curves with SN2009ip, but do not exhibit rebrightening. Furthermore, the DES-SN photometric data also constrains the long term variability of DES17X1boj to a level below what was seen in SN2009ip (Pastorello et al. 2013) and SN2016bdu (Pastorello et al. 2018) in the years before the brightest event ($M_{\rm V}$ in range -13 to -14). For the more distant event DES16E2bjy, such outbursts would have been below the detection threshold.

Regarding to spectroscopic data, the impostors exhibit strong, narrow hydrogen and helium lines around peak brightness (see e.g. Fraser et al. 2013; Mauerhan et al. 2013; Pastorello et al. 2013). No such features are seen in either of the DES-SN transients (see Figures 7.6 and 7.8), but it is possible that the lines are hidden in the noise. To investigate this the limiting equivalent widths (EWs) of a Gaussian-shaped narrow Hα line with $v_{\rm FWHM} = 500$ km/s were estimated in the spectra. Hydrogen lines with similar widths are often seen in both SN impostors (Smith et al. 2011) and in type IIn SNe (Taddia et al. 2013) where $v_{\rm FWHM} \sim 100 - 1000$ km/s are typically measured. For the given configuration I found limits of EW $\lesssim 5$ Å for DES17X1boj and EW $\lesssim 14$ Å for DES16E2bjy. In the case of of type IIn SNe the line strengths are typically measured in several tens to hundreds of Ångstroms (EW$\gtrsim 40$ Å; Smith et al. 2014), and thus it is unlikely that narrow Hα lines are hiding in the spectra. Due to both photometric and

spectroscopic differences it is unlikely that DES17X1boj and DES16E2bjy are events similar to SN impostors.

LRNe exhibit long-term light curve evolution often with several peaks like is the case for SNhunt248 (e.g. Kankare et al. 2015) shown in Figure 7.3. LRNe are also photometrically very inhomogeneous class of transients and reach luminosities of $M_{\rm V} \gtrsim -15$ (e.g. Pastorello et al. 2019) and therefore at least DES17X1boj could be a member of this class. However, the light curve evolution of LRNe is typically significantly slower than what is seen in the DES transients and DES16E2bjy is approximately three magnitudes brighter than any classified LRN. In regards to spectra, many LRNe exhibit strong, narrow lines in their spectra throughout their light curves (see e.g. Pastorello et al. 2019), but not all of them. For instance, for V838 Mon narrow H_α emission was present 5 days after peak brightness (Smith et al. 2011), but the line was not visible in the decline phase 30 to 60 days post-peak (Smith et al. 2016b). Thus, while the absence of narrow emission lines in the spectra of the DES transients (see Figures 7.6 and 7.8) cannot be used to rule out the LRNe as a possible scenario, different light curve evolution timescales and high peak brightness of DES16E2bjy makes it unlikely.

One topic that could give insight on the origin of the DES-SN transients is where they occurred in their host galaxies. The event location is one of the most constraining observational features about DES16E2bjy: it is found in the outskirts of a passive galaxy. If this galaxy is truly the host of DES16E2bjy it would disfavour scenarios related to progenitors with massive stars as only few CCSNe have been associated with passive galaxies (see e.g. type II SNe Abell399_11_19_0 and SN2016hil and Ibn SN PS1-12sk; Graham et al. 2012, Irani et al. 2019 and Hosseinzadeh et al. 2019). This is almost contradictory to the fact that the photometric and spectroscopic data appears to be well described with a blackbody, which typically requires a significant amount of material that can be shock-heated and thus it is a feature often seen in CCSNe. Therefore, one of the following must be true: either there has been a small amount of recent star-formation in the host galaxy leading to this peculiar transient, or this is a new type of transient that originates in an environment with old stellar populations. As discussed in Section 7.5, the UV $-$ r colors are higher than expected from early type galaxies, potentially suggesting that residual star-formation is still occurring in the galaxy (see e.g. Petty et al. 2013). Therefore, it is not possible to conclusively determine if DES16E2bjy is a product of an old stellar population. DES17X1boj, on the other hand, is associated with a star-forming galaxy with a non-negligible old stellar population, so the transient could originate from either young or old populations.

As DES16E2bjy appears to be associated with a passive galaxy, one also has to consider

a thermonuclear origin for it. However, as seen in Figure 7.3, its light curve shape is completely different when compared with prototypical type Ia SN2011fe, even if its absolute magnitude is loosely within the Ia distribution ($-18 \gtrsim M \gtrsim -20$, see e.g. Richardson et al. 2014). Comparison with type Iax SNe, the largest class of peculiar thermonuclear SNe also known as SN2002cx-like (Li et al. 2003; Jha et al. 2006; Foley et al. 2013), yields a similar result. While their peak magnitudes are lower than for "normal" type Ia SNe ($-13 \gtrsim M \gtrsim -19$, see e.g. Jha 2017), they have no stronger secondary peaks powered by FeIII recombination seen in type Ia SNe and therefore they are clearly different than DES16E2bjy. Additionally, the color of SNe Iax is significantly redder than for DES16E2bjy in the beginning of the light curve ($B-V \gtrsim 0.0$; Foley et al. 2013). Due to the different light curve shapes and inconsistent colours, it is unlikely that thermonuclear SN alone can be responsible for DES16E2bjy and even less for DES17X1boj due to its lower peak magnitude.

It is possible that the DES-SN transients are thermonuclear with addition of some other power source, for instance interaction with CSM. Under this scenario the thermonuclear explosion cannot be a standard type Ia SN as they are too bright, so it would have to be a peculiar one such as type Iax. However, as these appear to be too red in the beginning of the light curve, the interaction would have to be such that it causes the beginning of the light curve to be bluer and still produces the secondary peak. While no narrow emission lines are present in the peak spectra of the DES transients, the EW of narrow Hα emission in the interacting type Ia SNe (Ia-CSM) is not statistically different than for IIn SNe (Silverman et al. 2013). Thus based on the limits estimated of the emission, it is unlikely that there is a significant amount of interaction at the time of peak brightness. The presence of interaction cannot be ruled out during the secondary peaks, as there was no spectral coverage during these epochs. However, due to the needed strong effect of interaction on the light curves of the DES transients, this particular scenario of thermonuclear SNe with CSM interaction sounds contrived. Therefore, it is unlikely but it is possible that some other power source in addition to peculiar thermonuclear SNe could produce these transients.

As DES17X1boj occurred near the nucleus of its host galaxy, it is possible that at least some of the brightness difference between the two transients could be explained by host galaxy extinction. However, the blue bands (especially g) are bright and persistent throughout the light curve evolution (see Figure 7.2) and the blackbody fits are very good in the beginning of the light curve (see Figure D.1). Neither of these features would be expected in case of strong extinction. Thus, while it is likely that there is some extinction in the host galaxy, meaning DES17X1boj is intrinsically bluer and brighter, it does not seem probable that the difference in brightness between the two transients is caused by that.

As both DES-SN events were found at relatively low redshifts and as DES16E2bjy is reasonably bright at peak, it is interesting that no transients with similar light curve evolution have been identified in the literature, especially if one wants to assume that they are powered by same physical mechanism. However, as the main characterising feature is the faint, secondary peak seen in all four *griz* bands some of these transients may have gone by unrecognised. The argument can be put in context with the example of CaSTs described by absolute magnitudes of -15 to -16.5. Even though the first such event was published nearly a decade ago (SN2005E; Perets et al. 2010) their total number has stayed low (~ 10). However, even so their volumetric rate in the local universe has been estimated to be a significant fraction of the type Ia SNe rate ($\gtrsim 10\%$; Perets et al. 2010; Frohmaier et al. 2018). This demonstrates that even if transients such as DES17X1boj or DES16E2bjy were relatively common, the faintness of the secondary peak might make them difficult to distinguish from the general SN population.

7.7 Summary

In this Chapter I presented an analysis of two peculiar DES-SN transients, DES17X1boj and DES16E2bjy. While their peak magnitudes differ by 2.5 mags ($M_{\rm r} = -15.4$ for DES17X1boj and $M_{\rm r} = -17.9$ for DES16E2bjy), they share nearly identical double-peaked light curves. The evolution is characterised by a relatively normal rise to peak brightness in ~ 20 d, followed by a combination of first dropping 2 – 3 mag from the first peak in ~ 20 d and quickly rising to ~ 2 mag fainter secondary peak. Afterwards the transients faded quickly below the detection limit. The presented light curves are highly atypical and no transients exhibiting similar evolution have presented in literature.

The blackbody fits to photometry revealed moderately expanding photospheres with $v \sim 1800$ km/s for DES17X1boj and $v \sim 4800$ km/s for DES16E2bjy until ~ 10 d after the peak brightness. The increasing radius is accompanied by decreasing temperature for DES16E2bjy, but for DES17X1boj the temperature rose shallowly until the peak brightness before it started to decrease slowly. At later epochs, the *griz* SEDs still appear to be well fit by a blackbody model but due to faintness of the targets at these epochs the fits are poorly constrained. However, based on drastic change in the evolution of radii at ~ 10 d after peak, it is entirely possible that a blackbody is not enough to explain the late-phase emission of the transients.

The spectra of the events revealed noisy blue continuum best fitted with a blackbody. However, in case of DES17X1boj some other features may also be present. First, a broad absorption feature at $\lambda \sim 3830$ Å was identified as blueshifted Ca H&K absorption often seen in various types of SNe. The resulting ejecta velocity of $v \sim 9400$ km/s is higher

than the expansion velocity of the photosphere, but such a difference has been observed in literature SNe as well. Furthermore, the spectrum also shows some broad excess emission around Hα. While the feature looks visually similar to type II SNe, the low signal-to-noise makes it impossible to draw any certain conclusions.

While the observed blue continua are more typical for CCSNe than for thermonuclear ones, the host galaxy environments of the two transients imply a different story. DES17X1boj is found in a central region of a star-forming spiral galaxy while DES16E2bjy occurred at the outskirts of a passive galaxy, and the only apparent similarity between the two environments is the presence of dominant old population of stars. While some CCSNe have been discovered in passive environments, it would be difficult to explain how such a peculiar CCSN would originate in such an atypical environment. Thus, it is possible that these peculiar transients are thermonuclear in origin, but a comparison of observable properties against type Ia and type Iax SNe clearly indicate they are different. However, comparison to known double-peaked transients originating from massive stars, such as type IIb SNe and LRNe, resulted in a similar conclusion.

Based on the presented analysis it is not possible to verify what these peculiar transients are physically and thus their origin remains unknown. Furthermore, it is possible that despite the nearly identical light curve evolution and the fact that no similar transients are found in the literature, the events are not physically similar to each other and are in fact produced via different progenitor channels. Thus, more transients with similar light curves need to be discovered before stronger conclusion can be made.

Chapter 8

Summary and Future Perspectives

8.1 Summary

In this thesis I have performed an analysis of peculiar optical transients I discovered in the Dark Energy Survey Supernova Programme (DES-SN) data-set. The main focus of the thesis was on the sample of 106 enigmatic Rapidly Evolving Transients (RETs) that exhibited faster evolution timescales than is typically expected of standard classes of SNe, but I have also analysed the properties of two peculiar double-peaked transients, DES17X1boj and DES16E2bjy. In this final chapter, I summarise my results.

8.1.1 Discovery of Rapidly Evolving Transients in DES-SN

The sample of RETs was discovered in the DES-SN archival data with two dedicated searches to identify transients with rapidly evolving light curves. In the first search, the durations and peak brightnesses of every Single-Season Transient (SST) in DES-SN were estimated using Gaussian fits to the *griz* light curves. Furthermore, linear fits to light curves outside the events season were used to exclude transients that exhibited multi-season variability. Using the cuts provided in Chapter 3, the mean full width at half maximum (FWHM) brightness of the Gaussian fits was used to select candidate transients. Approximately 1600 events were visually inspected, resulting in a sample of 92 RETs.

The second search was created to investigate how successful the first simplistic search was. It was build based on the observed characteristics of the discovered sample of 92 RETs by finding a parameter space that distinguished the RETs from other known classes of extragalactic transients. The chosen parameters, rise time, $t_{\rm rise}$ in r band and peak $g-r$ colour, performed well especially when the interpolated Gaussian Process

(GP) light curves were used. The parameters were estimated for all unclassified DES-SN SSTs resulting in ~ 1200 candidates that based the search criteria. Additional cuts were employed to exclude contaminating Active Galactic Nuclei (AGN), type Ia supernovae (SNe) and fast rising but slowly declining events, finally resulting in ~ 550 candidates for further inspection. Only 14 of them were deemed rapidly evolving clearly indicating that the first search was successful at identifying rapid evolution, but due to the rudimentary approach not all RETs were discovered.

The final sample of RETs consisted of 106 transient events, 52 of which had a spectroscopic redshift used to evaluate the true luminosities and timescales. The sample was discovered at redshifts 0.05 – 1.56, corresponding to a wide range of peak magnitudes from relatively faint core-collapse SNe (CCSNe) at $M \sim -15.6$ to brightnesses of superluminous SNe (SLSNe) at $M \sim -22.6$. Based on the luminosity distributions of spectroscopic and photometric samples, the fainter end of RETs seemed to be significantly more common than the brighter end, but their numbers were small in the sample due to the restricted volume they could be detected in. Furthermore, the very brightest end of RET ($M \lesssim -20$) seemed to be underrepresented in the spectroscopic sample because of difficulties obtaining the redshifts to distant host galaxies. Finally, the estimated volumetric rate of $\gtrsim 1.5\%$ of CCSN was smaller but consistent with estimates presented in literature.

8.1.2 Observable Properties of Rapidly Evolving Transients

In Chapter 4, I investigated the observable properties of the gold and silver sample RETs. The RETs were characterised by fast light curve evolution with $t_{\rm rise} \lesssim 10$ d and consecutive exponential decline with $\Delta m_{15} \gtrsim 1.5$ in g band. The resulting time above half-maximum values were found to be $t_{1/2} \lesssim 12$ d, clearly separating them from standard SNe. Furthermore, the rise times were shorter than the decline times, and the bluer bands were found to evolve faster than the redder ones.

The photometric *griz* Spectral Energy Distributions (SEDs) were well described with a blackbody model until at least a few weeks after the peak brightness. The resulting peak temperatures were found in a range $T \sim 8000$ — 30000 K, although significantly higher values, such as $T \sim 61000$ K for DES14C3tnz were also seen. The corresponding photospheric radii were found in range from a few 10^{14} cm to a few 10^{15} cm. The resulting evolution of temperatures and radii revealed that the majority of the RETs appeared to expand and cool in time. Rough photospheric expansion velocities were found between ~ 8000 km/s and ~ 35000 km/s, well within the values seen in SNe. However, three RETs in the sample were to found to be evolving differently. They

exhibit receding photosphere with roughly constant temperature — behaviour that is tentatively similarly to the peculiar rapidly evolving AT2018cow.

Finally, two of the RETs, DES15C3opk and DES16E1bir, had spectra with visible transient light. Both of the spectra showed noisy blue continuum, well fitted with a blackbody, but no other transient features. The found temperatures were slightly different than the values found based on the photometry but broadly consistent. Furthermore, the spectra also exhibited a number of narrow galaxy lines that were used to determine the host redshifts.

8.1.3 Host Galaxy Properties of Rapidly Evolving Transients

In Chapter 5 I focused on the host galaxy properties of the sample. Host galaxies were identified for 93/106 RETs and the remaining 13 RETs were deemed to be "hostless" as no galaxy was detected in their vicinity or the host galaxy association was unclear. 52 of the host galaxies have a known spectroscopic redshift and in this thesis I visually inspected the spectra of 49 of them. All of these galaxies exhibited clear narrow emission lines, indicating at least some level of star-formation in the hosts. The transients spectrum of DES16E1bir also showed evidence of the same narrow emission lines leading to same conclusion. Furthermore, the transients – host galaxy separations of the 93 RETs were well described by a Sérsic profile for spiral galaxies, further implying that star-formation is important for the RETs.

The distributions of the host galaxy $m_{\rm r}$, $M_{\rm r}$ and $g-i$ colour were also investigated to verify that all of the hosts were drawn from a similar distribution of galaxies. First, the bronze sample hosts seemed lack the spectroscopic redshifts because were too faint for the redshifts to be obtained, unlike would be expected if the hosts were passive in nature. Furthermore, the distributions of $M_{\rm r}$ and $g-i$ colour were similar between the hosts with and without spectroscopic redshifts. Therefore, the hosts of gold and silver sample RETs were verified to be representative of the whole sample and it was concluded with a reasonable certainty that the RETs require star-formation to occur. The conclusion was also supported by the analysis of Wiseman et al. (2020a) performed on the same sample of RETs. However, their study also implied that the RETs were found in more extreme environments than Stripped Envelope SNe (SESNe), but not in as extreme as SLSNe.

8.1.4 Physical Interpretation of Rapidly Evolving Transients

In Chapter 6 I discussed the physical interpretation of RETs. As significant portion of literature RETs are classified as SESNe of some kind and as the host analysis of

Wiseman et al. (2020a) implied that DES-SN RETs are found in strongly star-forming environments, it seems reasonable to assume that a significant portion of the DES-SN RETs are SESNe, but in lack of good quality spectroscopic they could not be classified as such. However, the ^{56}Ni decay scenario typically assumed to explain the emission in standard SESNe is not able to realistically describe the peak luminosities of the RETs given the short rise times. In case RETs truly are SESNe, some ^{56}Ni is undoubtedly synthesised but not in the needed quantities.

Similarly, the shock-cooling scenario used to describe short-lived pre-peak features often seen in SESNe and SLSNe, had issues as well. While several bright RETs appear to be similar to the pre-peak of the SLSNe and shock-cooling fits to these RETs look visually convincing, the pre-peaks of SESNe are significantly faster and fainter. Thus, for the shock-cooling to be a viable physical scenario, a SLSN-like pre-peak would have to be created by a fainter SESN or otherwise the main ^{56}Ni decay powered light curve would be seen despite the high redshift. However, the search for such double-peaked transient phenomena did not result in any reasonable matches, unlike would be expected if such a combination of features was truly prominent.

The comparison of photometric properties of the RETs with the enigmatic AT2018cow revealed that three DES-SN events may in fact be similar in origin. These RETs exhibit receding photospheres similarly to AT2018cow, but also show very similar bright and blue light curve evolution. While there are differences in the properties, such as the photospheric temperatures, it is likely that the events are physically similar to each other due to the observed similarities. The conclusion is further supported by the volumetric rate estimated based on the three DES-SN RETs ($0.23 - 0.4\%$ of the CCSN rate) found to be consistent with literature values. Finally, the comparison of RETs with the kilonova (KN) AT2017gfo revealed that the KN occurred on much faster timescales than the RETs and thus it is unlikely that any of the RETs could be a caused by a NS-NS merger.

While the exact nature of the sample of RETs could not be determined, their observed diversity seems to imply that rapid light curve evolution can be produced via different progenitor channels. As several different physical mechanisms could be able to power these peculiar transients, more RETs need to be discovered to distinguish what physical scenarios are viable.

8.1.5 Analysis of the Photometric Twins DES17X1boj and DE16E2bjy

In Chapter 7 I focused on the analysis of the peculiar double-peaked DES-SN transients DES17X1boj and DES16E2bjy discovered as a part of the search for the rapidly evolving transients. While their peak magnitudes are significantly different ($M_{\rm r} = -15.4$ for

DES17X1boj and $M_{\rm r} = -17.9$ for DES16E2bjy), they exhibit nearly identical light curves evolution in all four DES-SN bands. Even more remarkably their light curve evolution is highly atypical and no similar transients are found in the literature.

The *griz* photometry of both transients was well fitted with a blackbody at least until ~ 10 d after the peak brightness. The fits revealed moderately expanding photospheres with $v \sim 1800$ km/s for DES17X1boj and $v \sim 4800$ km/s for DES16E2bjy and the increase in radius was found to be accompanied by rapidly decreasing temperature for DES16E2bjy. For DES17X1boj the temperature increased slightly until the epoch of peak brightness, before starting a shallow decline.

While both of the events have near-peak spectroscopy, the must prominent feature was the underlying blue continuum best described with a blackbody. However, for DES17X1boj some other features were also seen. Blueshifted calcium H&K absorption lines were identified at ejecta velocity $v \sim 9400$ km/s. While the velocity was higher than for the photosphere, similar differences have been reported in literature. Additionally, potential broad excess emission around Hα was seen, possibly implying that DES17X1boj was a hydrogen-rich type II SN.

The analysis of the transient properties seemed to imply an origin somehow related to massive stars. However, the investigation of host galaxy properties revealed that while DES17X1boj occurred in a very central region of its star-forming host galaxy, DES16E2bjy was found on the outskirts of a passive galaxy. Thus, the only apparent similarity between the hosts is the presence of dominant old stellar populations. Some CCSNe in the literature have been discovered in passive environments, but it would be hard to explain why such an atypical CCSN would be occur there.

Based on the host environments it is possible that these events are some kind thermonuclear explosions, but their observed properties do not resemble type Ia or type Iax SNe. However, as comparison to known double-peaked transients originating from massive stars, such as type IIb SNe and LRNe, resulted in a similar conclusion, the origin of the two DES-SN transients remains unknown. It is even possible that the events are only apparently similar and do not originate from the same progenitors.

8.2 Future Perspectives

The work presented in this thesis has focused on two observational classes of extragalactic transients discovered in the DES-SN data, the rapidly evolving ones and the double-peaked transients similar to DES17X1boj. As the physical diversity of either class is poorly understood, the discovered samples have direct implication to the future studies.

8.2.1 Rapidly Evolving Transients

The most obvious implication of the discovered RET sample is based on its sheer size as the sample of 106 discovered RETs clearly demonstrates that the rapidly evolving extragalactic transients are truly very common. While similar conclusion have been presented in literature before, as for instance Drout et al. (2014) stated a rather large volumetric event rate of 4 – 7% of CCSNe rate based on the PAN-STARRS Medium Deep Survey (PS1-MDS) sample, the number of RETs in DES-SN makes their existence very apparent. Therefore, it is probable that a significant number of such events will be discovered by current and future short-cadence surveys such as Zwicky Transient Facility (ZTF; Bellm et al. 2019), BlackGEM (Bloemen et al. 2015) and Legacy Survey of Space and Time (LSST; Ivezić et al. 2019).

Transients occurring on short timescales have become an interest for the scientific community. This in part due to the discovery of several peculiar individual events over the last decade, most notably AT2018cow, but also due to the interest raised by the discovered PS1-MDS and DES-SN samples. The interest is well-founded. As discussed in this thesis many of the literature RETs are classified as SESNe of some type. In case all of the DES-SN RETs are SESNe, their volumetric rate would imply that 20 – 30% of SESNe have been excluded in the studies as the fast-evolving end of the SESN distribution has been missed. Regardless, even if they are not SESNe, the question what physical mechanism can produce such fast evolving and common events remains.

While DES-SN is an extremely good photometric transient survey, its deep imagining results in difficulties in obtaining spectroscopic follow-up observations. As a result, the physical origin of discovered DES-SN transients is difficult to assess and it could not be determined for the sample of RETs presented in this thesis. Thus, for understanding the explosion mechanism than can lead to fast evolving light curves, it is more important that individual fast transients are identified early in the light curve evolution to perform extensive spectroscopic follow-up. Only in this way can the true physical aspects be investigated.

In order to identify fast transients early in their evolution, one has to rely on single epoch detections. While the most important parameter is the rise rate (i.e. how much the transient brightened in time), additional, potentially crucial information can be extracted from the colour. Based on the sample RETs presented in this thesis the fast light curve evolution is accompanied by high temperature especially in the early light curve evolution, thus resulting in very blue optical colours. While the DES-SN $g-r$ vs. $t_{\rm rise}$ parametrisation presented in this thesis might not be directly transferable to other

survey due to the effects of the adopted observing strategy, similar parameters can be used as triggering criteria for follow-up observations.

Once a large number of classified rapidly evolving events are discovered, their study as a sample can produce very exciting results. Using the SESNe as an example, it would be interesting to know how the rapidly evolving light curves fit in their scheme. For instance, is the rapid evolution a feature seen only in certain subtypes of SESNe or is it seen in all of them are important questions when the physical scenarios explaining the rapid evolution are discussed. Even without classifications or good quality spectroscopy, a sample of events can provide important implications. For example, the study performed by Wiseman et al. (2020a) on the sample of DES-SN RETs, discovered that the RETs occurred in more extreme star-forming environments than typical SESNe, implying that they originate in very massive stars. Therefore, studying a sample of RETs with spectroscopic follow-up data will likely provide further insight into these peculiar transients and thus collecting such a sample is important for understanding their nature and physical diversity.

8.2.2 DES17X1boj-like Transients

As DES17X1boj and DES16E2bjy share a nearly identical peculiar double-peaked optical light curves, one has to consider the possibility that they are also physically similar, despite the differences in the peak luminosities and the host environments. Under such a hypothesis it is only a matter of time that more transients exhibiting similar light curves are discovered and hopefully, with the example of the two transients, they are followed-up extensively. In case several such transients are found and they all exhibit similar observables, one can conclude that it is likely that DES17X1boj and DES16E2bjy are members of the newly founded class.

Even if one assumes that the DES-SN events are physically different, the fact that two transients with nearly identical peculiar light curves were discovered in DES-SN promotes the idea that more apparently similar transients will be discovered by other surveys. As the nature of these events is still unknown, spectroscopic follow-up of the discovered new transients should provide insight into what powering mechanisms can produce such peculiar double-peaked light curves and thus their relation to other classes of extragalactic transients can be investigated.

Appendix A

CNN architecture for the SN – AGN Binary Classification

One of the largest contaminants for the updated selection of RETs in DES-SN, discussed in Section 3.2, are AGN and thus removing at least a significant portion of them is an important step in the analysis. The most prominent difference that distinguishes the light curves of SN-like transients and AGN from each other is related to their multi-year variability. Significant portion of AGN exhibit continuous variation of brightness over several years while SNe discovered by DES-SN vary only within one or possibly two. Furthermore, the variation of AGN often includes several phases of re-brightening, while SNe are mostly described by a single rise and decline. The described differences should be clearly visible in the 5-year DES-SN light curves and thus applying machine learning should yield great results when trying to cut down the number of AGN in the selection.

To distinguish the AGN from SN-like transients I used a one dimensional Convolutional Neural Network (CNN). CNN was selected as it can use the GP light curves directly instead of using some model parameters and thus it does not implement any additional biases. Furthermore, CNN selects the features the classification is based on automatically, while being "trained" by a representative sample. In 1D CNN features are searched for only in dimension (i.e. in time) but those features can be found in several dimension (i.e in four optical bands) along that. The CNN classification was performed with `python` using package `Keras`, with the following architecture:

- 1D CNN layer
  - Filters: 4
  - Size: 5

- Dropout layer
- 1D Max pooling layer
- 1D CNN layer
  - Filters: 8
  - Size: 41
- Dropout layer
- Softmax layer.

Each CNN layer has two parameters: "filter" defines the number of individual features the algorithm looks for and the "size" defines the number of data points those features are found in. Thus, the first CNN layer searched for four individual features (such as the change of flux or colour) that happened in 2 d intervals in the GP light curves. The features were searched for in consecutive interval by moving the search range forward one data point (0.5 d) at a time. At this stage the CNN layer produced feature maps for each filter quantifying the importance of the features in each interval.

After the first CNN layer, additional layers were added to increase the speed and quality of the classifier. First, a commonly used dropout layer was applied to prevent the algorithm from overfitting. The layer ignores or "drops out" certain "neurons", individual values in the created feature maps. The neurons were chosen randomly so that 40% were dropped at each iteration and thus the classifier was forced to learn on different sets of neurons preventing it from overfitting. Next, a max pooling layer for was added to increase the speed of the classifier. The layer took in pairs of consecutive values in each feature map (i.e. from intervals 0.0–2.0 and 0.5–2.5) and passed on only the more significant value of each pair. The feature maps were reduced to half of the original size and now they refer to 2.5 d intervals with 1.0 d shift between consecutive values (i.e. 0.0–2.5 and 1.0–3.5).

After the max pooling layer, a second CNN layer was introduced now taking in the feature maps passed on by the max pooling layer. The CNN layer searches for eight features in intervals of 41 consecutive values. Due to the downsizing introduced by the max-pooling layer, 41 values in the feature maps were drawn from 43.5 d interval in the original GP light curves. In essence, the second CNN layer was probing how the features found during the first CNN layer evolve over significantly longer timescales. Finally, the softmax layer was used to produce the classification probabilities i.e. what is the probability for the individual transient to be an AGN or SN-like transient. The CNN classifier was run until the accuracy of the classifier was no longer increasing.

TABLE A.1: Number of transients used for training of the CCN classifier. Total number of transients in each class have been split into training sample, test sample and sample that did not meet the requirements to be used as neither.

Type	**SN Ia**	**SN II**	**SN Ibc**	**SLSN**	**RET**	**AGN**
Total	406	68	16	18	92	306
Train	124	19	4	5	30	182
Test	264	42	10	12	62	79
Fail	18	7	2	1	0	45

The sizes of the CNN layers were chosen so that "SN-like" transients would be identified in comparison to AGN. For this probing the evolution of the light curve features occurring on both very short timescales of few days and longer ones of several weeks to more than a month seemed to be crucial. Several different combinations of values were tested prior deciding to use the shown architecture, but no significant difference were found with the set ups. Thus, it is important to note that the exact combination of the timescale and the number of filters seem to have only a small effect on the classifier and slightly different values would likely produce equally good results.

Training and testing of the classifier was performed using the sample of 92 RETs, spectroscopically classified samples of SNe and AGN from DES-SN, but also AGN monitored by OzDES. The resulting number of SN-like transients was 600 and AGN 306. However, due to variations of data quality from object to object the duration of GP light curves could be significantly different in given band or year. Thus, in order to have uniform sample of light curves, the duration in each band and year had to be more than 50 days reducing the samples to 572 for SN-like and 261 for AGN.

Being the class with small numbers, the 261 AGN were divided into training and testing samples by a 70/30 split resulting in 182 AGN in training sample and 79 in test sample. In case the same 70/30 split was applied to SN-like transients, the resulting training sample would be 400 in size — twice the size of the AGN set. If uneven training samples were used the classifier would emphasise the SN-like transients over AGN thus skewing the results. To avoid the issue of imbalanced training sets, the training sample of the SN-like transients was designed to be the same size as the AGN one. The sample was compiled so that the same percentages of each class of SNe and RETs was selected. The corresponding test set was 390 in size. I chose to use this setup as it seemed like the only reasonable way of producing balanced training samples while still having a significant number of AGN in the test sample to investigate the performance of the classifier. The other option would have been to use simulated or augmented light curves as the basis of training and testing. However, due to the risk of creating a biased library of light curves and thus skewing the classifier, the observed data was used as the basis of the GP

light curves. The total numbers of SNe, RETs and AGN, their fractions distributed to training and test samples and the number of events not included in the classification are given in Table A.1.

The classifier finished at 0.992 accuracy with the test sample, with 4/79 ($\sim$ 5%) AGN misclassified as SN-like and no SN or RET classified as AGN. As the total number of SN-like transients in the test set was 390 the result is very good, especially as the purpose of the classifier was to remove large fraction of AGN without removing any SN-like transients.

Appendix B

Tables for RETs

In this appendix chapter I provide the tables that characterise the main features of the DES-SN rapidly evolving transient sample.

TABLE B.1: Basic information of the 27 gold sample rapidly evolving transients. Given redshifts are from the the host galaxies. The presented Milky way colour excesses are taken from Schlafly & Finkbeiner (2011).

Name (DES)	**R.A. (J2000)**	**Decl. (J2000)**	$z_{\mathbf{spec}}$	$E_{\mathbf{B-V}}$
Gold Sample				
DES13S2wxf[a]	02:46:27.02	-00:01:35.13	0.57	0.0274
DES13X1hav	02:20:07.80	-05:06:36.53	0.58	0.0185
DES13X3gmd[a]	02:26:01.02	-04:13:09.83	0.78	0.0228
DES13X3gms	02:23:12.27	-04:29:38.35	0.65	0.0246
DES14C3tnz[a]	03:31:26.95	-28:30:47.09	0.70	0.0066
DES14C3tvw	03:33:17.61	-27:54:23.92	0.70	0.0058
DES14S2anq	02:45:06.67	-00:44:42.77	0.05	0.0294
DES14S2plb	02:47:25.62	-01:37:06.91	0.12	0.0369
DES14S2pli	02:44:54.76	-01:05:52.74	0.35	0.0256
DES14X3pkl	02:28:50.64	-04:48:26.44	0.30	0.0332
DES15C3lpq	03:30:50.89	-28:36:47.08	0.61	0.0078
DES15C3mem[a]	03:28:34.14	-29:03:29.50	0.62	0.0061
DES15C3mgq	03:31:04.56	-28:12:31.74	0.23	0.0080
DES15E2nqh	00:38:55.59	-43:05:13.14	0.52	0.0076
DES15S1fli	02:52:45.15	-00:53:10.21	0.45	0.0675
DES15S1fll	02:51:09.36	-00:11:48.71	0.23	0.0611
DES15X3mxf	02:26:57.72	-05:14:22.81	0.44	0.0237
DES16C1cbd	03:39:25.97	-27:40:20.37	0.54	0.0100
DES16C2ggt	03:35:33.88	-29:13:29.36	0.31	0.0089
DES16E1bir	00:30:58.64	-42:58:37.18	1.56	0.0064
DES16E2pv	00:36:50.19	-43:31:40.16	0.73	0.0059
DES16S1dxu	02:50:43.53	-00:42:33.29	0.14	0.0486
DES16X1eho	02:21:22.87	-04:31:32.64	0.81	0.0229
DES16X3cxn	02:27:19.32	-04:57:04.27	0.58	0.0234
DES17C3gen[a]	03:31:44.08	-29:00:39.47	0.92	0.0086
DES17S2fee	02:45:37.97	-01:20:00.37	0.24	0.0337
DES17X3cds	02:25:06.57	-03:47:56.19	0.49	0.0235

[a] Discovered with enhanced search described in Section 3.2.

TABLE B.2: Basic information of the 25 silver sample rapidly evolving transients. Columns are described in Table B.1.

Name (DES)	**R.A. (J2000)**	**Decl. (J2000)**	$z_{\mathbf{spec}}$	$E_{\mathbf{B-V}}$
		Silver Sample		
DES13C1tgd	03:36:15.42	-27:38:19.07	0.20	0.0105
DES13C3bcok	03:32:06.47	-28:37:29.70	0.35	0.0081
DES13C3uig	03:31:46.55	-27:35:07.96	0.67	0.0073
DES13E2lpk	00:40:23.80	-43:32:19.74	0.48	0.0058
DES13X2oyb	02:21:14.55	-05:40:44.03	1.22	0.0212
DES13X2wvv[a]	02:19:27.66	-06:42:58.05	0.47	0.0213
DES13X3npb	02:26:34.11	-04:08:01.96	0.50	0.0242
DES13X3nyg	02:27:58.17	-03:54:48.05	0.71	0.0233
DES14X1bnh	02:14:59.79	-04:47:33.32	0.83	0.0173
DES15C2eal	03:36:14.68	-29:13:49.32	0.22	0.0086
DES15C3lzm	03:28:41.86	-28:13:54.96	0.33	0.0063
DES15C3nat	03:31:32.44	-28:43:25.06	0.84	0.0086
DES15C3opk	03:26:38.76	-28:20:50.12	0.57	0.0119
DES15C3opp	03:26:57.53	-28:06:53.61	0.44	0.0084
DES15X2ead	02:25:57.38	-06:27:04.78	0.23	0.0289
DES16C3axz	03:31:14.15	-28:40:00.26	0.23	0.0082
DES16C3gin	03:31:03.06	-28:17:30.98	0.35	0.0082
DES16S1bbp[a]	02:53:03.40	00:22:18.21	0.19	0.0734
DES16X3ega	02:28:23.71	-04:46:36.18	0.26	0.0308
DES16X3erw	02:24:49.31	-04:30:51.45	0.46	0.0205
DES17C2hno	03:34:54.38	-29:11:51.71	0.60	0.0101
DES17C3fwd	03:31:37.17	-27:28:12.84	0.35	0.0098
DES17C3gop[a]	03:34:08.53	-28:24:00.03	0.69	0.0075
DES17X3dxu	02:26:14.20	-03:50:39.57	0.86	0.0271
DES17X3hxi	02:23:11.09	-04:31:01.70	0.62	0.0284

[a] Discovered with the second search described in Section 3.2.

TABLE B.3: Basic information of the 54 Bronze sample rapidly evolving transients. Columns are described in Table B.1.

Name (DES)	R.A. (J2000)	Decl. (J2000)	E_{B-V}	Name (DES)	R.A. (J2000)	Decl. (J2000)	E_{B-V}
Bronze Sample							
DES13C1acmt	03:37:18.99	-26:50:00.99	0.0101	DES16C1bde	03:37:12.34	-26:45:29.93	0.0105
DES13C3abtt	03:30:28.91	-28:09:42.12	0.0065	DES16C2grk	03:40:16.36	-29:17:20.18	0.0112
DES13C3asvu	03:31:20.82	-27:21:38.89	0.0086	DES16C3auv	03:27:36.51	-27:35:27.33	0.0077
DES13C3avkj	03:27:52.97	-27:31:40.86	0.0078	DES16C3axz[a]	03:29:55.76	-28:02:33.13	0.0065
DES13C3nxi	03:27:51.22	-28:21:26.21	0.0071	DES16C3cdd	03:29:42.53	-27:08:35.49	0.0081
DES13C3smn	03:27:53.08	-28:05:00.93	0.0080	DES16S2fqu	02:47:05.94	-00:20:50.40	0.0313
DES13X3aakf	02:22:50.84	-04:41:57.01	0.0217	DES16X1ddm	02:15:18.88	-04:21:52.07	0.0183
DES13X3afjd	02:28:00.31	-04:34:59.39	0.0248	DES16X2bke	02:24:02.30	-07:16:17.87	0.0256
DES13X3alnb	02:28:44.39	-05:08:32.47	0.0249	DES16X3ddi	02:21:45.39	-04:41:08.95	0.0215
DES13X3kgm	02:26:00.92	-04:51:59.29	0.0231	DES16X3wt	02:24:56.98	-05:32:42.19	0.0224
DES13X3pby	02:25:19.98	-05:18:50.58	0.0223	DES17C1fes	03:36:56.09	-27:34:12.11	0.0116
DES14C1jnd	03:37:24.36	-27:29:35.03	0.0095	DES17C2end[a]	03:36:46.39	-28:48:02.25	0.0096
DES14C3gzj[a]	03:30:17.19	-28:08:24.67	0.0061	DES17C3fjt	03:25:52.26	-28:08:27.95	0.0154
DES14C3htq	03:30:17.34	-27:41:46.61	0.0071	DES17C3gof	03:32:53.53	-27:37:53.79	0.0080
DES14E1aqi[a]	00:34:57.44	-43:24:05.24	0.0086	DES17C3icf	03:26:55.36	-27:57:24.45	0.0105
DES14E2bfx	00:42:40.58	-44:25:05.62	0.0057	DES17E1gsx	00:32:27.81	-42:46:05.78	0.0079
DES14E2xsm	00:38:42.27	-43:35:14.11	0.0067	DES17S1emy	02:53:27.05	00:25:02.49	0.0751
DES14X1qzg	02:19:43.65	-05:26:30.87	0.0197	DES17S1hih	02:50:18.31	-00:45:42.83	0.0602
DES14X3pko	02:27:37.95	-03:41:44.27	0.0268	DES17X1dge	02:19:14.14	-05:24:13.04	0.0216
DES15C3edw	03:30:12.59	-27:42:34.93	0.0071	DES17X1hjj	02:16:57.68	-04:12:42.78	0.0216
DES15C3mfu	03:28:36.08	-28:44:20.00	0.0085	DES17X1hjk	02:20:38.22	-05:29:50.28	0.0254
DES15C3pbi	03:28:56.68	-28:00:07.98	0.0073	DES17X2cvk	02:23:44.54	-07:19:19.59	0.0293
DES15E2lmq	00:38:28.82	-43:59:14.04	0.0055	DES17X2dqk	02:21:52.59	-07:06:29.73	0.0284
DES15X3atd	02:23:21.64	-04:17:28.95	0.0230	DES17X3bvf	02:24:55.38	-05:29:08.09	0.0263
DES15X3kyt	02:25:05.98	-05:24:39.65	0.0229	DES17X3cdp[a]	02:29:07.85	-04:18:15.80	0.0237
DES15X3nlv	02:24:10.70	-05:01:38.47	0.0237	DES17X3fhq	02:23:44.57	-03:58:37.52	0.0300
DES15X3oma	02:26:59.07	-05:06:37.70	0.0239	DES17X3gmp[a]	02:29:36.46	-04:39:01.95	0.0233

[a] Discovered with the second search described in Section 3.2.

TABLE B.4: Host galaxy information of the gold sample rapidly evolving transients. For DES16E1bir the spectroscopic redshift was obtained with VLT X-SHOOTER spectroscopy of the transient.

Name	Survey[a]	Offset ($''$)	Offset (kpc)	d_{DLR}[b]	z_{spec}	z_{phot}	m_{r} (AB)
Gold Sample							
DES13S2wxf	OzDES	0.43	2.83	0.56	0.57	0.42	21.31 ± 0.03
DES13X1hav	OzDES	0.35	2.33	0.53	0.58	0.64	23.63 ± 0.08
DES13X3gmd	OzDES	0.71	5.30	0.86	0.78	0.78	22.91 ± 0.05
DES13X3gms	OzDES	0.81	5.62	0.88	0.65	0.64	23.02 ± 0.06
DES14C3tnz	OzDES	0.69	4.98	0.52	0.70	0.71	22.26 ± 0.03
DES14C3tvw	ACES	3.75	26.88	3.53	0.70	0.65	21.32 ± 0.03
DES14S2anq	SDSS	0.29	0.30	0.23	0.05	0.08	17.57 ± 0.04
DES14S2plb	OzDES	1.75	3.65	0.90	0.12	0.12	18.38 ± 0.03
DES14S2pli	OzDES	1.40	6.97	1.61	0.35	0.39	20.87 ± 0.03
DES14X3pkl	OzDES	0.27	1.21	0.44	0.30	0.43	22.41 ± 0.06
DES15C3lpq	OzDES	0.40	2.67	0.53	0.61	0.62	23.29 ± 0.04
DES15C3mem	PRIMUS	1.16	7.84	1.02	0.62	0.36	20.29 ± 0.05
DES15C3mgq	OzDES	0.08	0.29	0.12	0.23	0.26	22.97 ± 0.03
DES15E2nqh	OzDES	0.49	3.02	0.77	0.52	0.46	23.30 ± 0.04
DES15S1fli	OzDES	0.77	4.40	0.80	0.45	0.46	20.99 ± 0.03
DES15S1ffl	OzDES	2.90	10.55	2.07	0.23	0.21	20.96 ± 0.04
DES15X3mxf	OzDES	1.69	9.56	2.35	0.44	0.43	22.43 ± 0.05
DES16C1cbd	OzDES	0.81	5.16	0.72	0.54	0.54	20.94 ± 0.03
DES16C2ggt	OzDES	1.32	6.00	1.45	0.31	0.35	21.09 ± 0.03
DES16E1bir	-	0.34	2.84	0.92	1.56	0.53	24.74 ± 0.08
DES16E2pv	OzDES	0.93	6.73	1.23	0.73	0.82	23.00 ± 0.05
DES16S1dxu	OzDES	4.11	9.86	3.67	0.14	0.13	21.36 ± 0.03
DES16X1eho	OzDES	0.37	2.79	0.42	0.81	0.82	22.29 ± 0.07
DES16X3cxn	OzDES	0.70	4.62	0.85	0.58	0.64	23.05 ± 0.04
DES17C3gen	PRIMUS	1.00	7.87	1.48	0.92	0.86	22.79 ± 0.04
DES17S2fee	OzDES	5.26	19.79	1.75	0.24	0.26	18.17 ± 0.05
DES17X3cds	OzDES	0.13	0.78	0.21	0.49	0.41	22.45 ± 0.06

[a] The survey that provided the spectroscopic redshift.
[b] The ratio of the host–transient separation and the host radius (see Section 2.4.2).

TABLE B.5: Host galaxy information of the silver sample rapidly evolving transients.

Name	Survey[a]	Offset ($''$)	Offset (kpc)	d_{DLR}[b]	z_{spec}	z_{phot}	m_{r} (AB)
Silver Sample							
DES13C1tgd	OzDES	0.38	1.23	0.38	0.20	0.32	20.31 ± 0.06
DES13C3bcok	LADUMA	0.76	3.73	0.35	0.35	0.30	18.62 ± 0.03
DES13C3uig	ACES	0.76	5.33	0.90	0.67	0.66	22.18 ± 0.03
DES13E2lpk	OzDES	0.76	4.53	0.77	0.48	0.38	20.49 ± 0.04
DES13X2oyb	OzDES	0.28	2.33	0.43	1.22	1.27	22.92 ± 0.06
DES13X2wvv	OzDES	0.33	1.96	0.52	0.47	0.47	21.90 ± 0.03
DES13X3npb	OzDES	0.31	1.87	0.21	0.50	0.37	20.79 ± 0.05
DES13X3nyg	OzDES	0.43	3.13	0.64	0.71	0.68	23.39 ± 0.06
DES14X1bnh	OzDES	0.43	3.27	0.55	0.83	0.80	21.95 ± 0.04
DES15C2eal	OzDES	2.43	8.75	4.33	0.22	0.26	23.00 ± 0.03
DES15C3lzm	ATLAS[c]	0.59	2.78	0.68	0.33	0.30	20.48 ± 0.03
DES15C3nat	OzDES	0.50	3.84	0.85	0.84	0.81	23.39 ± 0.03
DES15C3opk	OzDES	0.41	2.67	0.49	0.57	0.59	23.05 ± 0.03
DES15C3opp	OzDES	0.41	2.33	0.61	0.44	0.37	23.26 ± 0.04
DES15X2ead	OzDES	0.55	2.03	0.61	0.23	0.25	20.09 ± 0.03
DES16C3axz	LADUMA	0.28	1.01	0.32	0.23	0.23	20.42 ± 0.04
DES16C3gin	OzDES	1.77	8.70	1.81	0.35	0.41	21.53 ± 0.04
DES16S1bbp	OzDES	1.33	4.23	1.19	0.19	0.23	21.43 ± 0.05
DES16X3ega	GAMA	2.36	9.42	1.97	0.26	0.19	19.54 ± 0.05
DES16X3erw	OzDES	0.33	1.92	0.46	0.46	0.41	22.23 ± 0.03
DES17C2hno	OzDES	1.42	9.51	1.75	0.60	0.56	22.69 ± 0.07
DES17C3fwd	LADUMA	1.77	8.69	1.21	0.35	0.33	20.46 ± 0.02
DES17C3gop	OzDES	1.06	7.56	0.89	0.69	0.72	22.75 ± 0.03
DES17X3dxu	OzDES	0.25	1.90	0.29	0.86	0.93	22.84 ± 0.04
DES17X3hxi	OzDES	0.10	0.69	0.17	0.62	0.41	23.37 ± 0.03

[a] The survey that provided the spectroscopic redshift.
[b] The ratio of the host–transient separation and the host radius (see Section 2.4.2).
[c] Here "ATLAS" refers to Australia Telescope Large Area Survey (Mao et al. 2012).

TABLE B.6: Host galaxy information of the bronze sample rapidly evolving transients.

Name	Offset ($''$)	d_{DLR}[a]	z_{phot}	m_{r} (AB)	Name	Offset ($''$)	d_{DLR}[a]	z_{phot}	m_{r} (AB)
Bronze Sample									
DES13C1acmt	0.57	0.84	0.60	23.19 ± 0.04	DES16C1bde	0.41	1.01	0.97	24.96 ± 0.09
DES13C3abtt[b]	2.09	2.53	0.58	21.51 ± 0.04	DES16C2grk	2.77	1.60	0.35	20.45 ± 0.04
DES13C3asvu[b]	0.37	0.50	0.83	22.47 ± 0.03	DES16C3auv	0.18	0.34	0.98	24.39 ± 0.05
DES13C3avkj	0.37	0.53	0.96	24.08 ± 0.05	DES16C3bor	0.10	0.18	0.79	23.84 ± 0.04
DES13C3nxi	0.61	1.02	0.60	24.99 ± 0.05	DES16C3cdd	0.29	0.48	1.40	24.27 ± 0.05
DES13C3smn	0.15	0.26	1.50	25.30 ± 0.06	DES16S2fqu	-	-	-	-
DES13X3aakf	0.80	1.13	1.18	25.47 ± 0.09	DES16X1ddm	1.66	2.52	0.38	21.46 ± 0.05
DES13X3afjd	-	-	-	-	DES16X2bke	1.60	2.36	0.88	25.13 ± 0.16
DES13X3alnb	0.14	0.29	0.68	25.04 ± 0.06	DES16X3ddi	1.15	1.50	0.91	23.94 ± 0.04
DES13X3kgm	0.40	1.65	-	26.47 ± 0.19	DES16X3wt	0.72	2.37	-	26.90 ± 0.28
DES13X3pby	0.19	0.35	0.41	23.83 ± 0.05	DES17C1fes	0.42	0.94	0.62	24.42 ± 0.10
DES14C1jnd	0.27	0.51	0.43	24.33 ± 0.09	DES17C2end	-	-	-	-
DES14C3gzj	0.23	0.71	-	26.04 ± 0.10	DES17C3fjt	0.33	1.38	-	28.04 ± 0.44
DES14C3htq	-	-	-	-	DES17C3gof	-	-	-	-
DES14E1aqi	1.60	5.96	-	25.62 ± 0.24	DES17C3icf	-	-	-	-
DES14E2bfx	-	-	-	-	DES17E1gsx	0.17	0.25	0.85	22.71 ± 0.05
DES14E2xsm	0.48	0.80	0.66	23.39 ± 0.04	DES17S1emy	1.22	1.12	0.37	22.51 ± 0.05
DES14X1qzg	-	-	-	-	DES17S1hih	0.17	0.36	-	24.95 ± 0.12
DES14X3pko	2.87	5.01	-	24.48 ± 0.06	DES17X1dge	0.33	0.38	1.05	24.16 ± 0.10
DES15C3edw	1.90	2.50	0.33	22.69 ± 0.03	DES17X1hjj	0.31	0.73	0.56	24.07 ± 0.06
DES15C3mfu	-	-	-	-	DES17X1hjk	-	-	-	-
DES15C3pbi[b]	0.13	0.31	1.06	25.10 ± 0.05	DES17X2cvk	-	-	-	-
DES15E2lmq	0.43	1.16	1.14	25.66 ± 0.18	DES17X2dqk	0.56	2.31	-	25.96 ± 0.20
DES15X3atd	0.29	0.41	1.19	23.88 ± 0.05	DES17X3bvf	-	-	-	-
DES15X3kyt	0.29	0.57	1.50	24.75 ± 0.08	DES17X3cdp	0.51	1.01	0.87	25.11 ± 0.08
DES15X3nlv	0.20	0.47	1.07	25.26 ± 0.08	DES17X3fhq	-	-	-	-
DES15X3oma	0.32	0.66	0.67	24.95 ± 0.07	DES17X3gmp	0.22	0.40	0.85	24.44 ± 0.07

[a] The ratio of the host–transient separation and the host radius (see Section 2.4.2).
[b] Host galaxy classified as "quasi-stellar" due to its apparent shape.

TABLE B.7: Light curve parameters of gold sample RETs in g band. Errors for $t_{\rm decline}$ are given in 1σ confidence, but no errors are given for $t_{\rm rise}$ or $t_{1/2}$ as the values are effectively upper limits.

Name	$t_{\rm peak}$[a] **(MJD)**	$M_{\rm peak}$	$t_{\rm rise}$[b] **(days)**	$t_{\rm decline}$[c] **(days)**	$t_{1/2}$[d] **(days)**
		Gold Sample			
DES13S2wxf	56631	-20.50±0.27	9.6	$10.21^{+4.63}_{-4.61}$	7.61
DES13X1hav	56551	-19.42±0.31	2.6	$29.62^{+13.63}_{-6.66}$	11.10
DES13X3gmd	56563	-19.41±0.11	8.9	$19.41^{+5.28}_{-4.32}$	10.36
DES13X3gms	56567	-19.66±0.04	12.1	$16.96^{+2.04}_{-1.95}$	11.22
DES14C3tnz	57018	-19.66±0.08	3.5	$19.76^{+2.51}_{-2.53}$	8.01
DES14C3tvw	57029	-19.69±0.15	6.4	$17.66^{+4.92}_{-3.70}$	8.56
DES14S2anq	56903	-16.19±0.02	8.6	$20.50^{+0.76}_{-0.79}$	10.44
DES14S2plb	56990	-15.76±0.12	9.0	$14.21^{+100.92}_{-10.22}$	11.54
DES14S2pli	56987	-18.98±0.04	5.2	$29.83^{+7.58}_{-5.11}$	11.84
DES14X3pkl	56987	-16.91±0.09	5.4	$14.84^{+3.44}_{-3.64}$	7.47
DES15C3lpq	57317	-19.84±0.08	9.2	$16.62^{+1.45}_{-1.42}$	9.54
DES15C3mem	57327	-19.06±0.12	6.1	$19.28^{+3.64}_{-2.92}$	9.07
DES15C3mgq	57331	-17.30±0.04	3.3	$11.90^{+0.97}_{-0.93}$	5.30
DES15E2nqh	57366	-19.74±0.06	6.5	$16.30^{+3.30}_{-2.49}$	11.57
DES15S1fli	57276	-19.76±0.06	4.9	$13.49^{+6.03}_{-4.40}$	9.59
DES15S1ffl	57276	-18.23±0.05	5.8	$13.43^{+2.91}_{-2.51}$	12.71
DES15X3mxf	57356	-19.64±0.02	7.7	$9.98^{+0.52}_{-0.51}$	6.84
DES16C1cbd	57660	-19.46±0.05	9.7	$19.39^{+63.57}_{-12.77}$	10.85
DES16C2ggt	57756	-18.39±0.05	3.8	$16.60^{+3.18}_{-4.24}$	7.32
DES16E1bir	57653	-22.24±0.07	4.3	$8.78^{+4.36}_{-2.17}$	5.45
DES16E2pv	57629	-19.84±0.08	3.5	$26.81^{+14.80}_{-7.16}$	9.76
DES16S1dxu	57717	-16.04±0.08	6.2	$24.94^{+2.66}_{-2.52}$	11.16
DES16X1eho	57722	-21.12±0.05	4.4	$6.92^{+1.79}_{-1.75}$	4.25
DES16X3cxn	57694	-19.62±0.05	5.0	$16.42^{+5.06}_{-2.98}$	7.82
DES17C3gen	58093	-19.60±0.13	4.6	$11.40^{+2.72}_{-2.14}$	5.92
DES17S2fee	58076	-18.12±0.05	4.1	$16.15^{+3.98}_{-3.25}$	7.01
DES17X3cds	58054	-19.39±0.12	9.9	$8.04^{+2.20}_{-1.99}$	7.44

[a] MJD of the observed maximum brightness in g band.
[b] Time measured between last the non-detection and the peak.
[c] Time for the exponential fit to decline 1/10 of the peak brightness.
[d] Time above half maximum brightness measured assuming linear rise and exponential decline.

TABLE B.8: Light curve parameters of Silver sample RETs in g band. Errors for $t_{\rm decline}$ are given in 1σ confidence, but no errors are given for $t_{\rm rise}$ or $t_{1/2}$ as the values are effectively upper limits.

Name	$t_{\rm peak}$[a] **(MJD)**	$M_{\rm peak}$	$t_{\rm rise}$[b] **(days)**	$t_{\rm decline}$[c] **(days)**	$t_{1/2}$[d] **(days)**
		Silver Sample			
DES13C1tgd	56615	-16.96±0.27	6.7	-	-
DES13C3bcok	56653	-19.01±0.04	5.2	$19.27^{+1.45}_{-1.13}$	8.64
DES13C3uig	56625	-19.00±0.08	4.9	$8.98^{+2.35}_{-1.90}$	5.18
DES13E2lpk	56575	-19.19±0.07	5.4	$17.29^{+2.92}_{-3.01}$	8.02
DES13X2oyb	56579	-22.64±0.08	5.4	-	-
DES13X2wvv	56628	-19.35±0.08	8.8	$13.03^{+3.97}_{-2.86}$	8.34
DES13X3npb	56676	-19.01±0.16	10.0	$13.25^{+4.39}_{-2.47}$	8.97
DES13X3nyg	56591	-20.26±0.05	7.0	$10.23^{+2.60}_{-1.71}$	7.79
DES14X1bnh	56915	-20.17±0.16	6.5	$16.55^{+11.49}_{-4.69}$	8.19
DES15C2eal	57276	-17.31±0.12	8.2	$8.00^{+3.80}_{-1.98}$	6.70
DES15C3lzm	57327	-18.54±0.04	7.5	$9.06^{+0.68}_{-0.57}$	6.51
DES15C3nat	57356	-19.37±0.14	5.9	$13.24^{+6.49}_{-3.59}$	6.98
DES15C3opk	57389	-20.20±0.03	8.3	$14.45^{+3.27}_{-2.09}$	8.51
DES15C3opp	57385	-18.11±0.15	6.2	$9.62^{+1.90}_{-1.36}$	6.31
DES15X2ead	57273	-17.25±0.10	6.5	$27.89^{+10.14}_{-6.50}$	12.63
DES16C3axz	57643	-17.36±0.10	4.9	$12.72^{+2.13}_{-2.09}$	6.24
DES16C3gin	57775	-19.15±0.03	14.1	$11.51^{+1.96}_{-1.49}$	12.96
DES16S1bbp	57626	-16.97±0.12	9.2	$17.90^{+9.69}_{-4.84}$	9.72
DES16X3ega	57730	-19.25±0.02	12.6	$18.17^{+0.91}_{-0.79}$	14.91
DES16X3erw	57730	-18.79±0.11	4.8	$20.26^{+3.23}_{-2.90}$	8.42
DES17C2hno	58108	-19.83±0.05	5.5	$12.85^{+3.62}_{-4.78}$	6.70
DES17C3fwd	58093	-18.46±0.04	6.6	$6.58^{+0.84}_{-0.86}$	5.26
DES17C3gop	58099	-19.56±0.08	3.6	$13.15^{+3.30}_{-2.31}$	5.58
DES17X3dxu	58064	-19.81±0.20	3.7	$10.71^{+3.17}_{-1.97}$	5.13
DES17X3hxi	58122	-19.19±0.09	6.1	$13.65^{+3.29}_{-2.09}$	7.22

[a] MJD of the observed maximum brightness in g band.
[b] Time measured between last the non-detection and the peak.
[c] Time for the exponential fit to decline 1/10 of the peak brightness.
[d] Time above half maximum brightness measured assuming linear rise and exponential decline.

TABLE B.9: The best-fitting blackbody parameters at the time of peak brightness for gold sample RETs. Uncertainties are given in 1σ confidence.

Name	$T_{\rm peak}$ (1000 K)	$r_{\rm peak}$ (10^{14} cm)	$L_{\rm peak}$ (10^{43} erg/s)	No.[a]
		Gold Sample		
DES13S2wxf	$13.66^{+3.97}_{-2.60}$	$9.72^{+3.99}_{-2.92}$	$2.35^{+0.96}_{-0.42}$	3
DES13X1hav	$12.64^{+6.45}_{-3.37}$	$10.89^{+7.37}_{-4.61}$	$2.16^{+1.60}_{-0.37}$	3
DES13X3gmd	$20.66^{+5.36}_{-2.96}$	$4.63^{+1.04}_{-1.08}$	$2.78^{+1.37}_{-0.56}$	4
DES13X3gms	$16.67^{+1.07}_{-0.89}$	$7.45^{+0.57}_{-0.59}$	$3.05^{+0.27}_{-0.23}$	4
DES14C3tnz	$60.82^{+39.18}_{-22.69}$	$1.80^{+0.77}_{-0.49}$	$31.73^{+90.62}_{-21.50}$	4
DES14C3tvw	$11.89^{+7.07}_{-3.07}$	$8.44^{+5.25}_{-3.74}$	$1.01^{+1.11}_{-0.20}$	3
DES14S2anq	$7.73^{+0.14}_{-0.14}$	$6.60^{+0.22}_{-0.19}$	$0.11^{+0.00}_{-0.00}$	4
DES14S2plb	$8.91^{+1.44}_{-1.08}$	$4.12^{+1.05}_{-0.88}$	$0.08^{+0.01}_{-0.01}$	4
DES14S2pli	$20.43^{+3.98}_{-2.46}$	$4.66^{+0.75}_{-0.77}$	$2.69^{+1.08}_{-0.55}$	3
DES14X3pkl	$11.06^{+1.10}_{-0.97}$	$4.56^{+0.72}_{-0.57}$	$0.22^{+0.03}_{-0.02}$	4
DES15C3lpq	$26.11^{+6.66}_{-4.14}$	$4.50^{+0.91}_{-0.86}$	$6.71^{+4.07}_{-1.98}$	4
DES15C3mem	$26.45^{+11.35}_{-6.51}$	$3.10^{+1.15}_{-0.86}$	$3.35^{+4.02}_{-1.36}$	3
DES15C3mgq	$12.71^{+0.85}_{-0.65}$	$4.36^{+0.32}_{-0.36}$	$0.35^{+0.03}_{-0.02}$	3
DES15E2nqh	$22.00^{+4.03}_{-2.50}$	$5.53^{+0.87}_{-0.89}$	$5.10^{+1.96}_{-0.93}$	4
DES15S1fli	$15.62^{+2.13}_{-1.48}$	$9.17^{+1.47}_{-1.47}$	$3.56^{+0.72}_{-0.40}$	4
DES15S1fll	$23.28^{+7.56}_{-4.18}$	$3.13^{+0.70}_{-0.71}$	$2.06^{+1.81}_{-0.65}$	4
DES15X3mxf	$13.22^{+0.31}_{-0.28}$	$11.45^{+0.39}_{-0.36}$	$2.85^{+0.08}_{-0.07}$	4
DES16C1cbd	$14.04^{+1.13}_{-0.95}$	$9.25^{+1.10}_{-1.06}$	$2.36^{+0.22}_{-0.15}$	4
DES16C2ggt	$15.06^{+1.59}_{-1.39}$	$5.40^{+0.78}_{-0.65}$	$1.07^{+0.19}_{-0.13}$	4
DES16E1bir	$32.17^{+5.98}_{-4.43}$	$7.36^{+1.50}_{-1.33}$	$41.41^{+14.44}_{-8.36}$	4
DES16E2pv	$18.99^{+3.76}_{-2.20}$	$6.46^{+1.14}_{-1.32}$	$3.87^{+1.27}_{-0.55}$	4
DES16S1dxu	$13.14^{+2.49}_{-1.53}$	$2.42^{+0.45}_{-0.46}$	$0.12^{+0.04}_{-0.02}$	4
DES16X1eho	$15.12^{+0.86}_{-0.81}$	$16.84^{+1.65}_{-1.45}$	$10.55^{+0.59}_{-0.49}$	4
DES16X3cxn	$18.00^{+1.56}_{-1.42}$	$6.63^{+0.77}_{-0.65}$	$3.29^{+0.46}_{-0.37}$	4
DES17C3gen	$16.86^{+3.90}_{-2.13}$	$6.78^{+1.71}_{-1.70}$	$2.65^{+0.73}_{-0.33}$	3
DES17S2fee	$13.40^{+1.42}_{-1.02}$	$5.85^{+0.65}_{-0.70}$	$0.79^{+0.12}_{-0.09}$	4
DES17X3cds	$15.86^{+3.18}_{-2.02}$	$7.38^{+1.32}_{-1.32}$	$2.45^{+0.92}_{-0.48}$	3

[a] Number of bands used for fitting.

TABLE B.10: The best-fitting blackbody parameters at the time of peak brightness for gold sample RETs. Uncertainties are given in 1σ confidence.

Name	$T_{\mathbf{peak}}$ **(1000 K)**	$r_{\mathbf{peak}}$ **(10^{14} cm)**	$L_{\mathbf{peak}}$ **(10^{43} erg/s)**	**No.**[a]
		Silver Sample		
DES13C1tgd	$11.47^{+6.57}_{-3.07}$	$4.38^{+2.49}_{-1.85}$	$0.24^{+0.30}_{-0.07}$	4
DES13C3bcok[b]	$100.00^{+0.00}_{-53.86}$	$1.31^{+0.92}_{-0.01}$	$122.37^{+2.68}_{-106.57}$	2
DES13C3uig	$20.46^{+5.05}_{-3.08}$	$4.03^{+1.02}_{-0.90}$	$2.02^{+0.93}_{-0.38}$	3
DES13E2lpk	$12.42^{+1.02}_{-0.88}$	$10.24^{+1.23}_{-1.15}$	$1.78^{+0.16}_{-0.13}$	4
DES13X2oyb	$21.57^{+2.50}_{-1.88}$	$17.30^{+2.41}_{-2.16}$	$46.14^{+8.64}_{-5.50}$	4
DES13X2wvv	$14.81^{+2.27}_{-1.73}$	$8.09^{+1.64}_{-1.42}$	$2.25^{+0.50}_{-0.28}$	4
DES13X3npb	$15.71^{+6.47}_{-3.38}$	$6.31^{+2.64}_{-2.06}$	$1.73^{+1.41}_{-0.42}$	3
DES13X3nyg	$18.65^{+1.42}_{-1.32}$	$8.12^{+0.85}_{-0.76}$	$5.69^{+0.66}_{-0.53}$	4
DES14X1bnh	$15.43^{+4.33}_{-2.61}$	$10.44^{+4.00}_{-3.31}$	$4.40^{+1.27}_{-0.56}$	3
DES15C2eal	$9.71^{+1.28}_{-1.05}$	$6.98^{+1.45}_{-1.22}$	$0.31^{+0.05}_{-0.03}$	4
DES15C3lzm	$15.14^{+0.97}_{-0.81}$	$5.71^{+0.41}_{-0.41}$	$1.22^{+0.13}_{-0.10}$	3
DES15C3nat	$31.75^{+19.04}_{-8.19}$	$2.60^{+0.89}_{-0.80}$	$4.89^{+9.72}_{-2.22}$	4
DES15C3opk	$16.04^{+1.12}_{-0.83}$	$10.38^{+0.83}_{-0.89}$	$5.08^{+0.50}_{-0.30}$	2
DES15C3opp	$28.43^{+49.53}_{-11.10}$	$2.07^{+1.42}_{-1.10}$	$1.99^{+22.87}_{-1.20}$	2
DES15X2ead	$11.14^{+1.46}_{-1.22}$	$5.32^{+1.02}_{-0.87}$	$0.31^{+0.05}_{-0.04}$	4
DES16C3axz	$36.01^{+45.85}_{-11.71}$	$1.21^{+0.50}_{-0.52}$	$1.76^{+12.98}_{-1.04}$	2
DES16C3gin	$13.58^{+0.46}_{-0.41}$	$8.35^{+0.35}_{-0.35}$	$1.69^{+0.09}_{-0.07}$	4
DES16S1bbp	$16.52^{+6.25}_{-3.54}$	$2.64^{+0.90}_{-0.74}$	$0.37^{+0.34}_{-0.12}$	4
DES16X3ega	$16.41^{+0.96}_{-0.82}$	$7.32^{+0.47}_{-0.46}$	$2.77^{+0.26}_{-0.22}$	3
DES16X3erw	$17.56^{+6.43}_{-3.96}$	$4.89^{+2.10}_{-1.51}$	$1.62^{+1.13}_{-0.41}$	3
DES17C2hno	$17.52^{+1.41}_{-1.34}$	$7.58^{+0.82}_{-0.70}$	$3.86^{+0.47}_{-0.39}$	4
DES17C3fwd	$23.24^{+8.43}_{-4.60}$	$3.18^{+0.91}_{-0.83}$	$2.11^{+1.82}_{-0.67}$	4
DES17C3gop	$41.85^{+58.15}_{-15.87}$	$2.37^{+1.46}_{-1.11}$	$12.23^{+94.91}_{-7.64}$	2
DES17X3dxu	$24.38^{+12.79}_{-6.74}$	$4.32^{+1.96}_{-1.44}$	$4.69^{+6.58}_{-1.98}$	3
DES17X3hxi	$17.40^{+4.22}_{-2.73}$	$5.65^{+1.59}_{-1.38}$	$2.08^{+0.77}_{-0.36}$	2

[a] Number of bands used for fitting.
[b] Temperature found at the upper fit boundary.

TABLE B.11: Best fitting parameters of Piro (2015) shock-cooling model using fixed core mass of $M_c = 5\ M_\odot$ for the 52 gold and silver sample RETs. The results are listed in order of increasing redshift

Name	z_{Spec}	No.[a]	E_{51} (10^{51} erg)	R_{13} (10^{13} cm)	M_e ($M_\odot$)	v_e (km/s)	χ^2_ν
DES14S2anq	0.05	26	3.13	0.10	3.26	8500	39.03
DES14S2plb	0.12	17	1.23	0.15	0.81	6500	0.88
DES16S1dxu	0.14	19	0.18	1.63	0.27	2900	1.26
DES16S1bbp	0.19	13	4.75	0.10	3.99	10100	2.48
DES13C1tgd	0.20	15	1.53	0.34	5.00	5500	2.61
DES15C2eal	0.22	12	2.07	0.56	0.45	9300	0.58
DES15S1fll	0.23	19	1.46	1.81	1.28	6600	2.22
DES16C3axz	0.23	15	0.67	0.70	1.37	4500	17.35
DES15C3mgq	0.23	18	7.03	0.10	1.07	15000	9.78
DES15X2ead	0.23	14	3.12	0.30	3.42	8400	1.62
DES17S2fee	0.24	22	15.70	0.10	4.28	18200	8.60
DES16X3ega	0.26	33	2.56	2.34	1.85	8300	69.55
DES14X3pkl	0.30	16	2.67	0.22	1.78	8600	2.83
DES16C2ggt	0.31	19	8.74	0.27	1.26	16300	8.69
DES15C3lzm	0.33	15	0.73	4.66	0.23	6100	34.52
DES17C3fwd	0.35	19	0.55	10.71	0.13	5700	11.15
DES13C3bcok	0.35	19	1.78	3.70	0.45	8600	14.68
DES16C3gin	0.35	23	3.10	1.79	1.02	10000	16.28
DES14S2pli	0.35	21	3.35	1.42	1.42	9900	4.78
DES15X3mxf	0.44	19	4.43	2.95	0.60	13000	16.00
DES15C3opp	0.44	11	0.49	3.63	0.37	4600	1.53
DES15S1fli	0.45	18	9.92	0.89	3.04	15200	2.89
DES16X3erw	0.46	27	11.37	0.24	4.35	15400	7.64
DES13X2wvv	0.47	11	5.27	1.25	0.98	13100	3.44
DES13E2lpk	0.48	13	6.74	0.92	0.79	15300	1.79
DES17X3cds	0.49	34	4.21	1.46	1.56	11000	10.09
DES13X3npb	0.50	11	3.41	1.43	0.56	11500	0.98
DES15E2nqh	0.52	18	2.40	4.95	1.11	8700	1.40
DES16C1cbd	0.54	17	8.67	0.80	1.67	15600	0.95
DES15C3opk	0.57	22	5.23	3.48	0.88	13300	12.34
DES13S2wxf	0.57	23	1.81	4.44	1.82	7000	1.17
DES13X1hav	0.58	22	5.66	1.05	2.44	11900	1.73
DES16X3cxn	0.58	30	12.54	0.51	3.63	16700	7.60
DES17C2hno	0.60	16	6.36	1.66	1.15	14100	3.47
DES15C3lpq	0.61	34	4.66	1.22	3.99	10000	10.92
DES15C3mem	0.62	25	2.20	1.39	2.87	7200	2.70
DES17X3hxi	0.62	16	4.71	0.91	1.13	12200	2.85
DES13X3gms	0.65	28	1.89	4.67	1.74	7200	3.17
DES13C3uig	0.67	13	3.20	1.03	0.59	11000	1.00
DES17C3gop	0.69	20	20.04	0.17	5.00	20100	9.57
DES14C3tvw	0.70	24	3.01	1.68	1.62	9200	2.68
DES14C3tnz	0.70	24	2.07	2.69	1.16	8000	3.84
DES13X3nyg	0.71	16	5.55	2.83	0.98	13500	2.11
DES16E2pv	0.73	16	1.63	7.67	0.69	7700	0.86
DES13X3gmd	0.78	23	0.92	7.82	0.73	5700	1.98
DES16X1eho	0.81	16	75.66	0.45	0.77	51600	3.62
DES14X1bnh	0.83	10	6.42	1.98	1.74	13300	3.14
DES15C3nat	0.84	15	2.67	1.44	2.47	8100	2.88
DES17X3dxu	0.86	16	1.70	3.23	0.70	7800	3.48
DES17C3gen	0.92	21	5.50	1.08	2.63	11600	1.44
DES13X2oyb	1.22	13	55.51	2.76	1.51	40000	1.22
DES16E1bir	1.56	20	15.24	5.19	1.12	21900	2.10

[a] Number of data pointed used for fitting, including last non-detection before rise in each band.

TABLE B.12: Same as Table B.11 with core mass of $M_c = 20\ M_\odot$.

Name	z_{Spec}	No.[a]	E_{51} (10^{51} erg)	R_{13} (10^{13} cm)	M_e ($M_\odot$)	v_e (km/s)	χ^2_ν
DES14S2anq	0.05	26	8.19	0.10	3.27	8400	39.09
DES14S2plb	0.12	17	3.25	0.15	0.82	6500	0.88
DES16S1dxu	0.14	19	0.49	1.61	0.27	3000	1.26
DES16S1bbp	0.19	13	12.42	0.10	4.13	10000	2.49
DES13C1tgd	0.20	15	3.98	0.34	5.00	5500	2.62
DES15C2eal	0.22	12	5.50	0.55	0.46	9300	0.58
DES15S1fll	0.23	19	3.87	1.79	1.30	6600	2.22
DES16C3axz	0.23	15	1.77	0.69	1.39	4400	17.35
DES15C3mgq	0.23	18	18.39	0.10	1.08	14900	9.79
DES15X2ead	0.23	14	8.27	0.30	3.47	8400	1.62
DES17S2fee	0.24	22	41.00	0.10	4.28	18100	8.62
DES16X3ega	0.26	33	6.79	2.31	1.88	8300	69.55
DES14X3pkl	0.30	16	7.07	0.22	1.80	8600	2.83
DES16C2ggt	0.31	19	23.16	0.26	1.27	16300	8.69
DES15C3lzm	0.33	15	1.93	4.59	0.24	6000	34.52
DES17C3fwd	0.35	19	1.46	10.59	0.13	5800	11.15
DES13C3bcok	0.35	19	4.71	3.65	0.46	8600	14.68
DES16C3gin	0.35	23	8.21	1.77	1.03	10000	16.28
DES14S2pli	0.35	21	8.89	1.40	1.44	9900	4.78
DES15X3mxf	0.44	19	11.73	2.91	0.61	13000	16.00
DES15C3opp	0.44	11	1.29	3.58	0.38	4600	1.53
DES15S1fli	0.45	18	26.29	0.88	3.09	15200	2.89
DES16X3erw	0.46	27	30.12	0.23	4.41	15400	7.64
DES13X2wvv	0.47	11	5.92	3.85	1.05	8500	0.96
DES13E2lpk	0.48	13	4.93	3.74	1.97	7000	1.19
DES17X3cds	0.49	34	11.16	1.44	1.58	11000	10.09
DES13X3npb	0.50	11	9.04	1.41	0.57	11500	0.98
DES15E2nqh	0.52	18	6.36	4.88	1.12	8700	1.40
DES16C1cbd	0.54	17	22.97	0.79	1.70	15500	0.95
DES15C3opk	0.57	22	13.87	3.43	0.89	13300	12.34
DES13S2wxf	0.57	23	4.81	4.38	1.85	7000	1.17
DES13X1hav	0.58	22	15.01	1.04	2.48	11900	1.73
DES16X3cxn	0.58	30	33.22	0.50	3.68	16700	7.60
DES17C2hno	0.60	16	16.87	1.64	1.17	14100	3.47
DES15C3lpq	0.61	34	12.35	1.21	4.04	10000	10.92
DES15C3mem	0.62	25	5.84	1.37	2.91	7200	2.70
DES17X3hxi	0.62	16	12.47	0.89	1.14	12200	2.85
DES13X3gms	0.65	28	5.01	4.61	1.76	7200	3.17
DES13C3uig	0.67	13	8.47	1.02	0.60	11000	1.00
DES17C3gop	0.69	20	52.13	0.17	5.00	19900	9.59
DES14C3tvw	0.70	24	7.97	1.66	1.64	9200	2.68
DES14C3tnz	0.70	24	5.49	2.66	1.18	8000	3.84
DES13X3nyg	0.71	16	14.71	2.79	1.00	13500	2.11
DES16E2pv	0.73	16	4.31	7.56	0.70	7700	0.86
DES13X3gmd	0.78	23	2.43	7.72	0.74	5700	1.98
DES16X1eho	0.81	16	100.00	1.01	0.59	38000	4.09
DES14X1bnh	0.83	10	17.01	1.95	1.77	13300	3.14
DES15C3nat	0.84	15	7.08	1.42	2.50	8100	2.88
DES17X3dxu	0.86	16	2.42	5.63	2.32	4800	2.28
DES17C3gen	0.92	21	14.57	1.07	2.66	11600	1.44
DES13X2oyb	1.22	13	100.00	4.55	1.15	34400	1.75
DES16E1bir	1.56	20	40.40	5.12	1.14	21900	2.10

[a] Number of data pointed used for the fit, including last non-detection before rise in each band.

Appendix C

Light Curves for RETs

In this appendix chapter I provide the flux light curves for all 106 rapidly evolving transients. For the gold and silver samples the light curves are provided in rest frame and for bronze sample in observer frame.

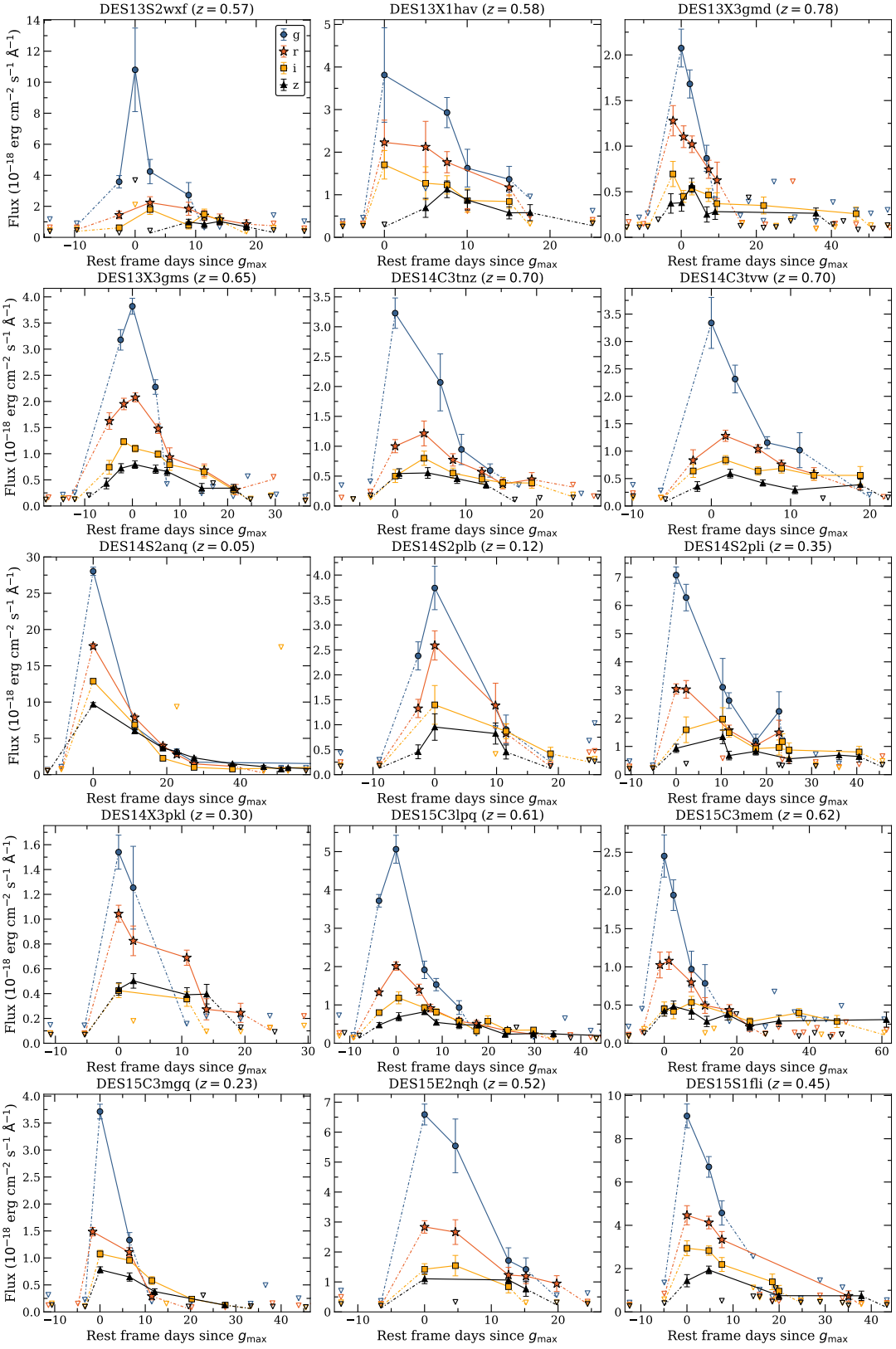

FIGURE C.1: Rest frame light curves of the 27 gold sample RETs. Open triangles represent 1σ error of data points below 3σ detection.

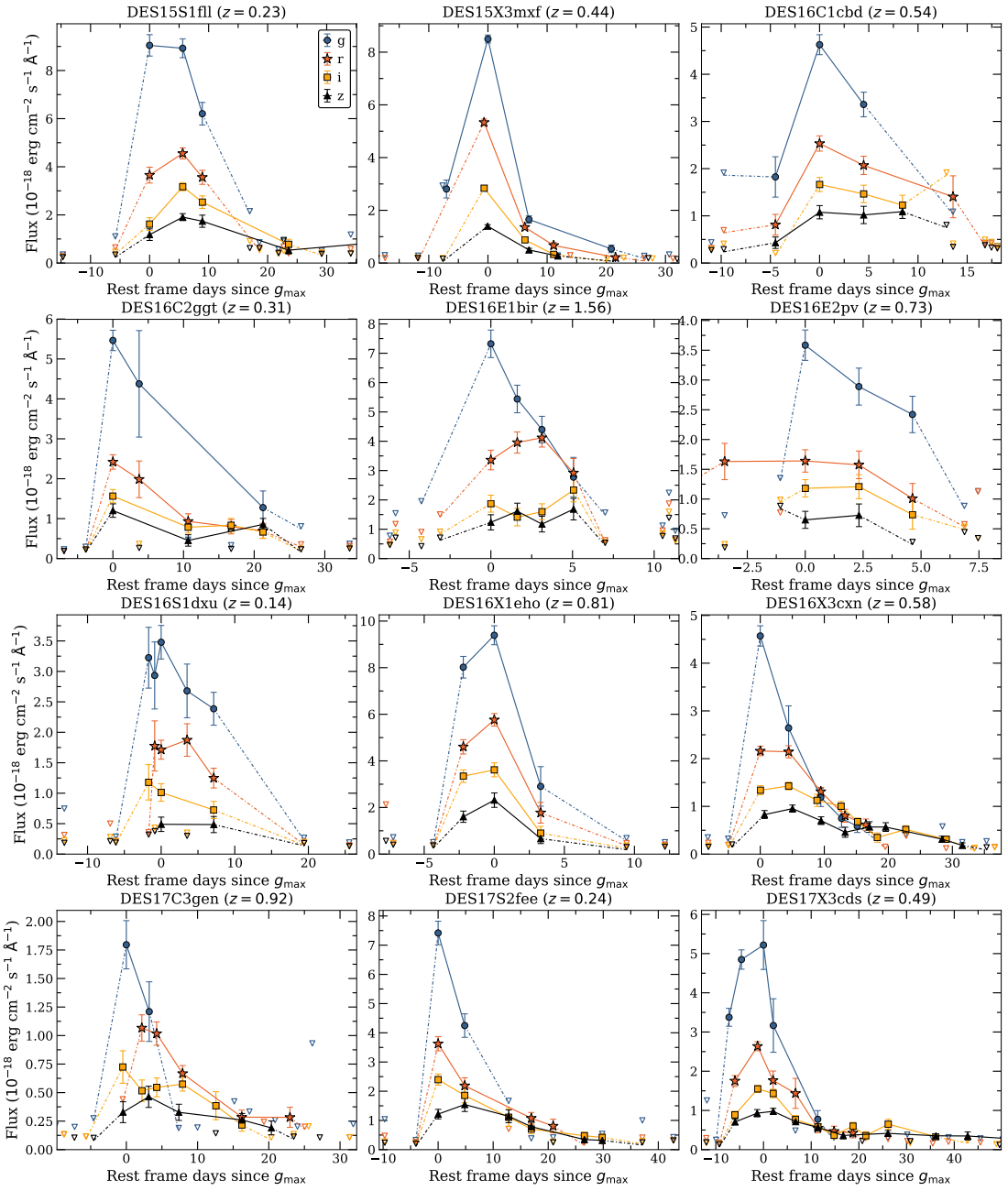

FIGURE C.1: Continued.

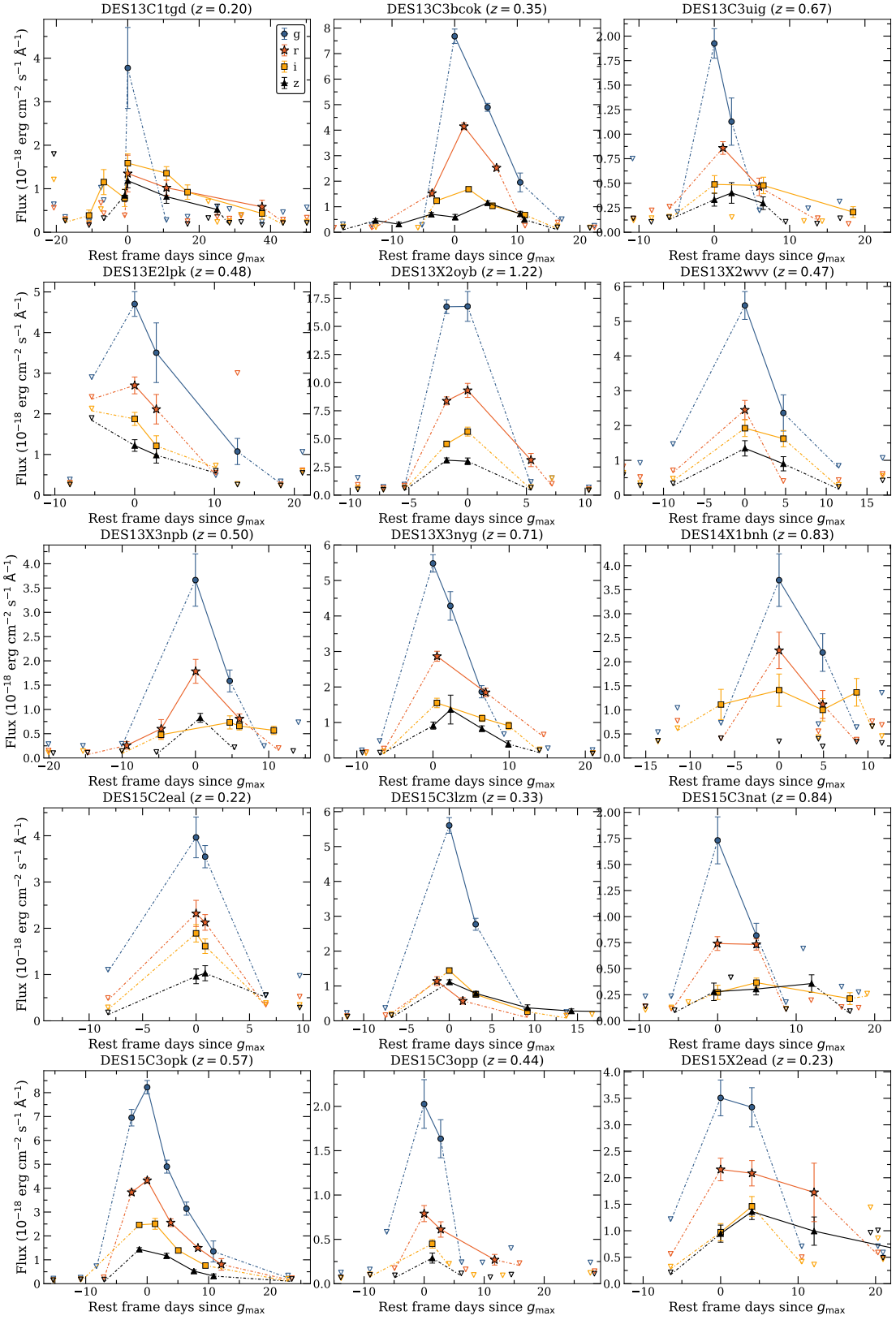

FIGURE C.2: Rest frame light curves of the 25 silver sample RETs. Open triangles represent 1σ error of data points below 3σ detection.

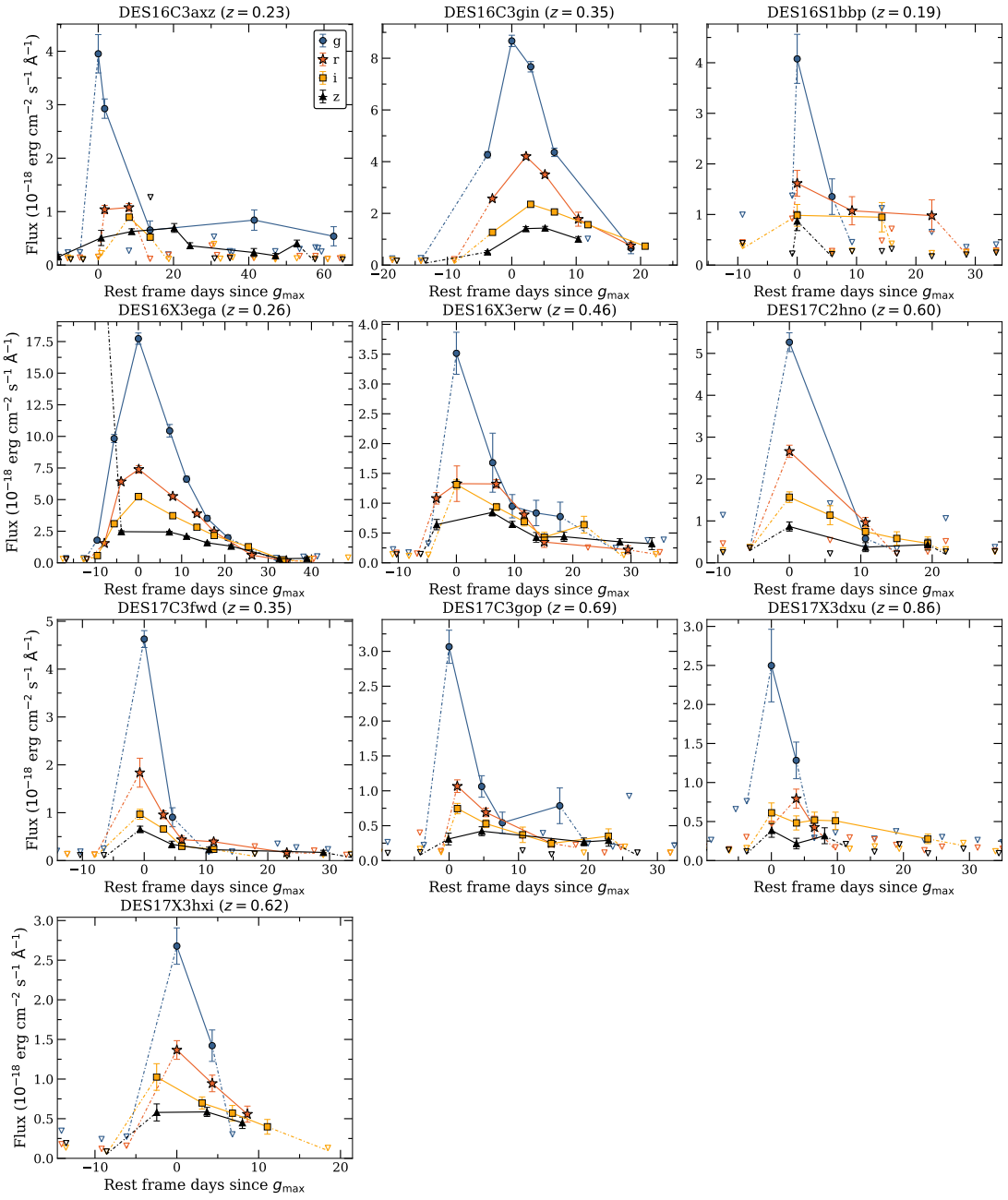

FIGURE C.2: Continued.

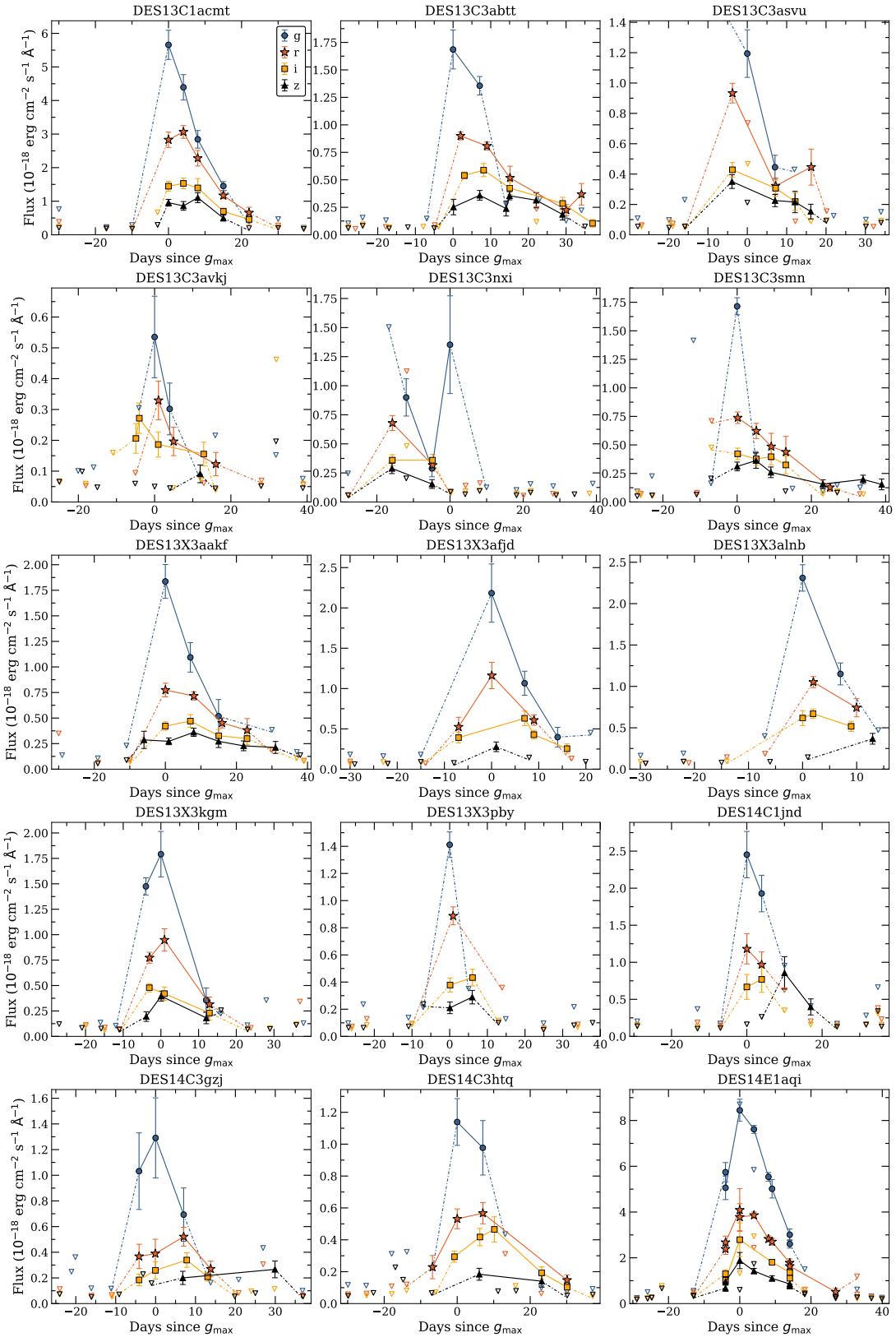

FIGURE C.3: Rest frame light curves of the 54 bronze sample RETs. Open triangles represent 1σ error of data points below 3σ detection.

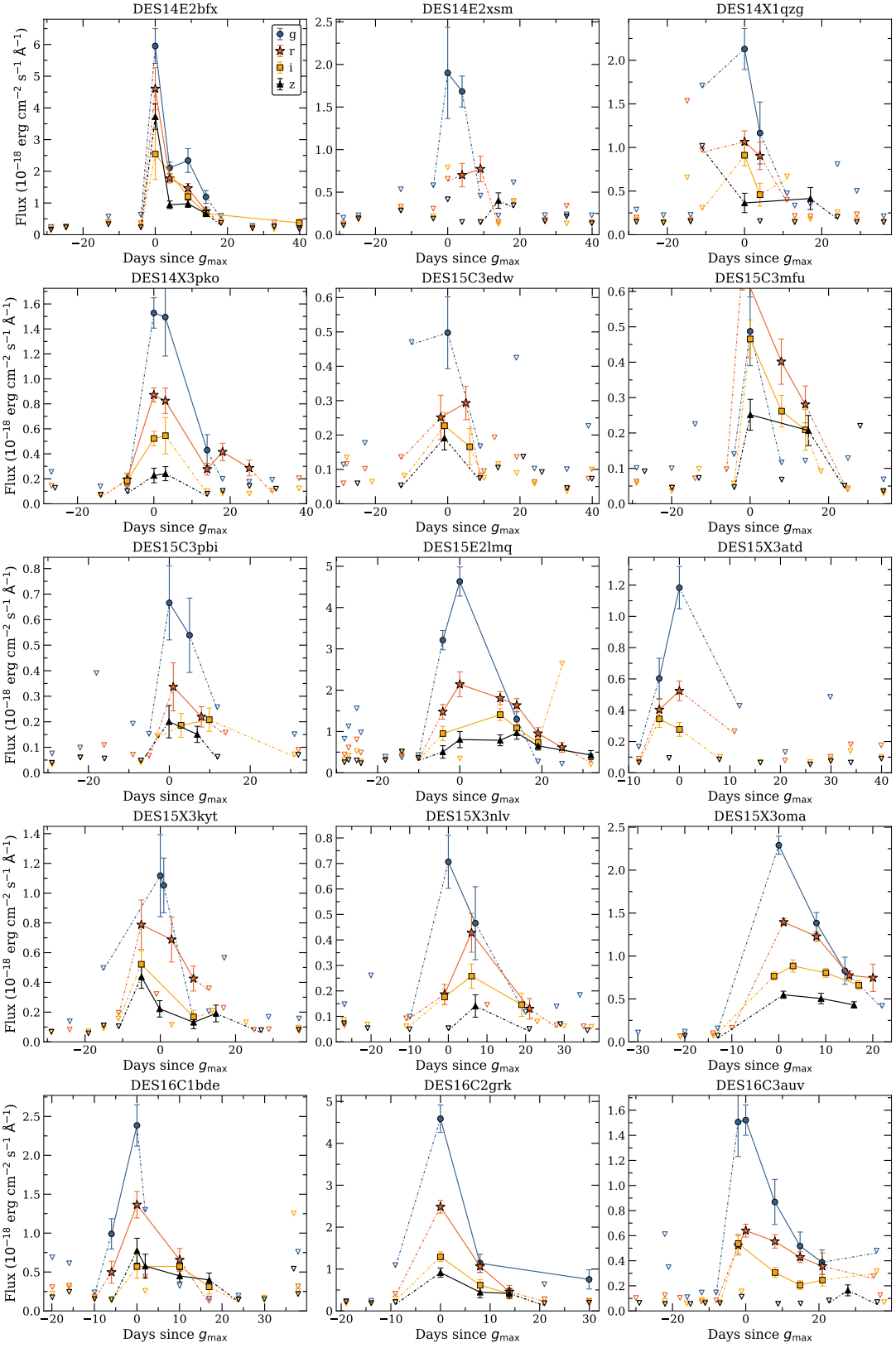

FIGURE C.3: Continued.

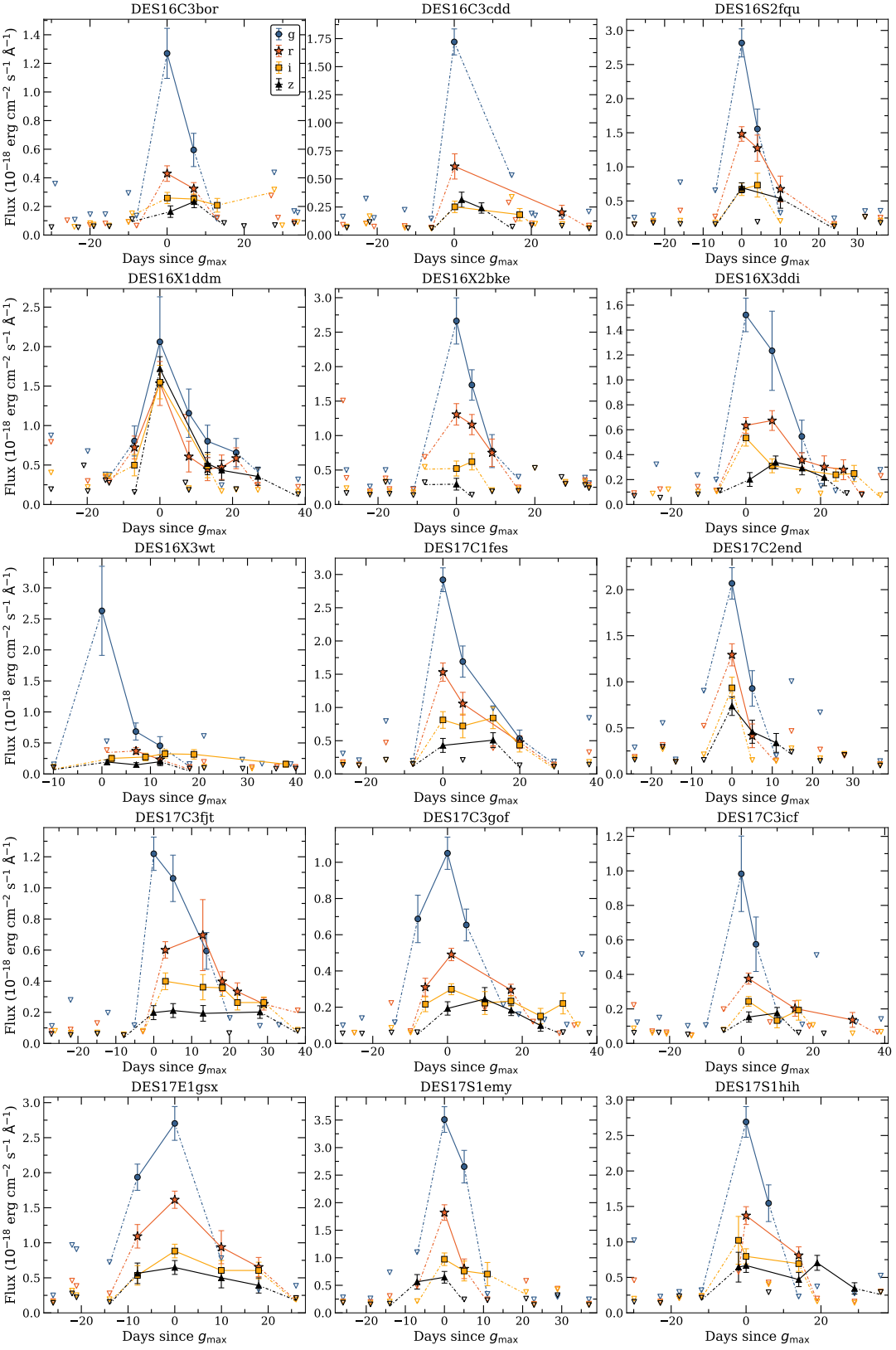

FIGURE C.3: Continued.

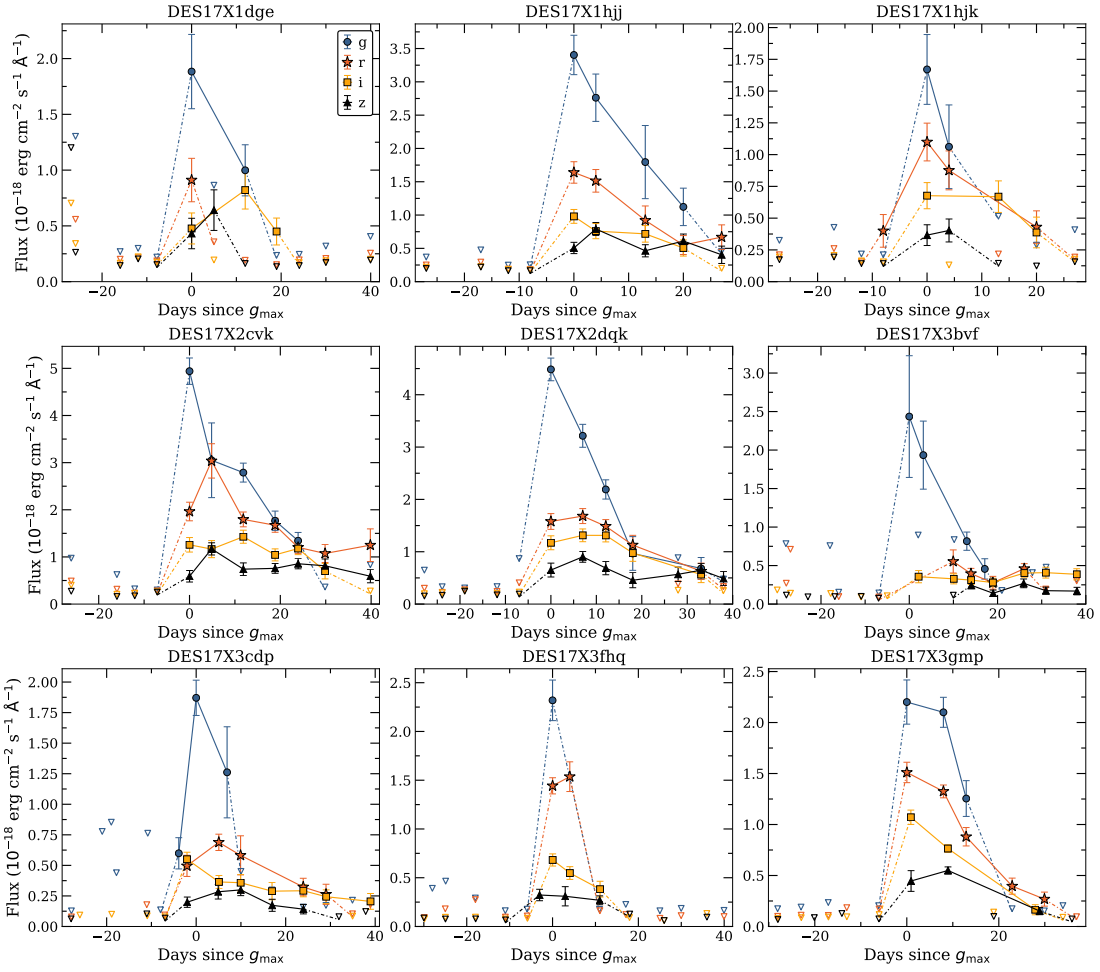

FIGURE C.3: Continued.

Appendix D

Blackbody Fits for DES17X1boj and DES16E2bjy

In this appendix chapter I provide the blackbody fits to every *griz* epoch for both DES17X1boj and DES16E2bjy.

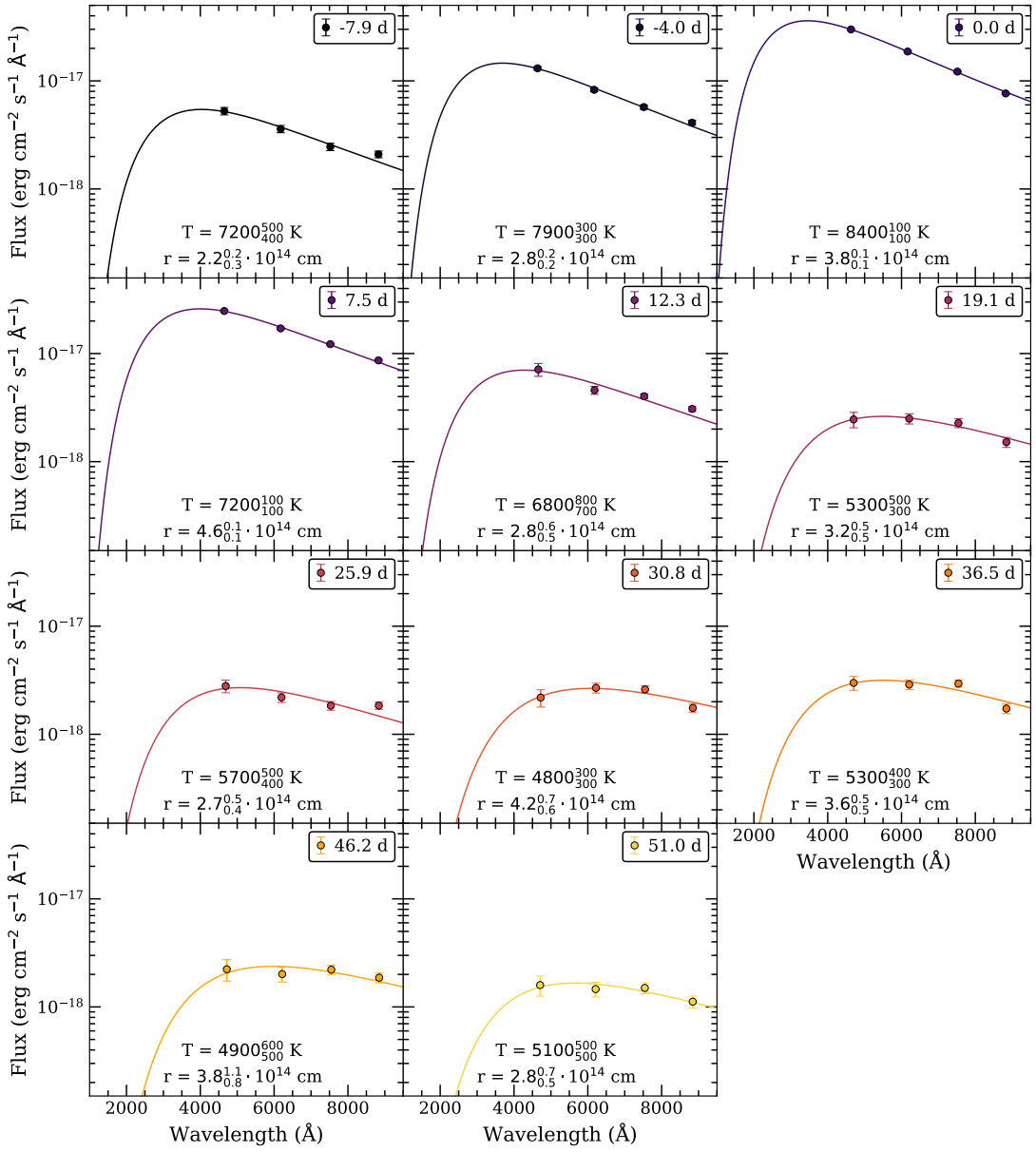

FIGURE D.1: Blackbody fits to photometry of DES17X1boj for every epoch with *griz* detections. Best-fitting temperatures and radii are given with 1σ uncertainties.

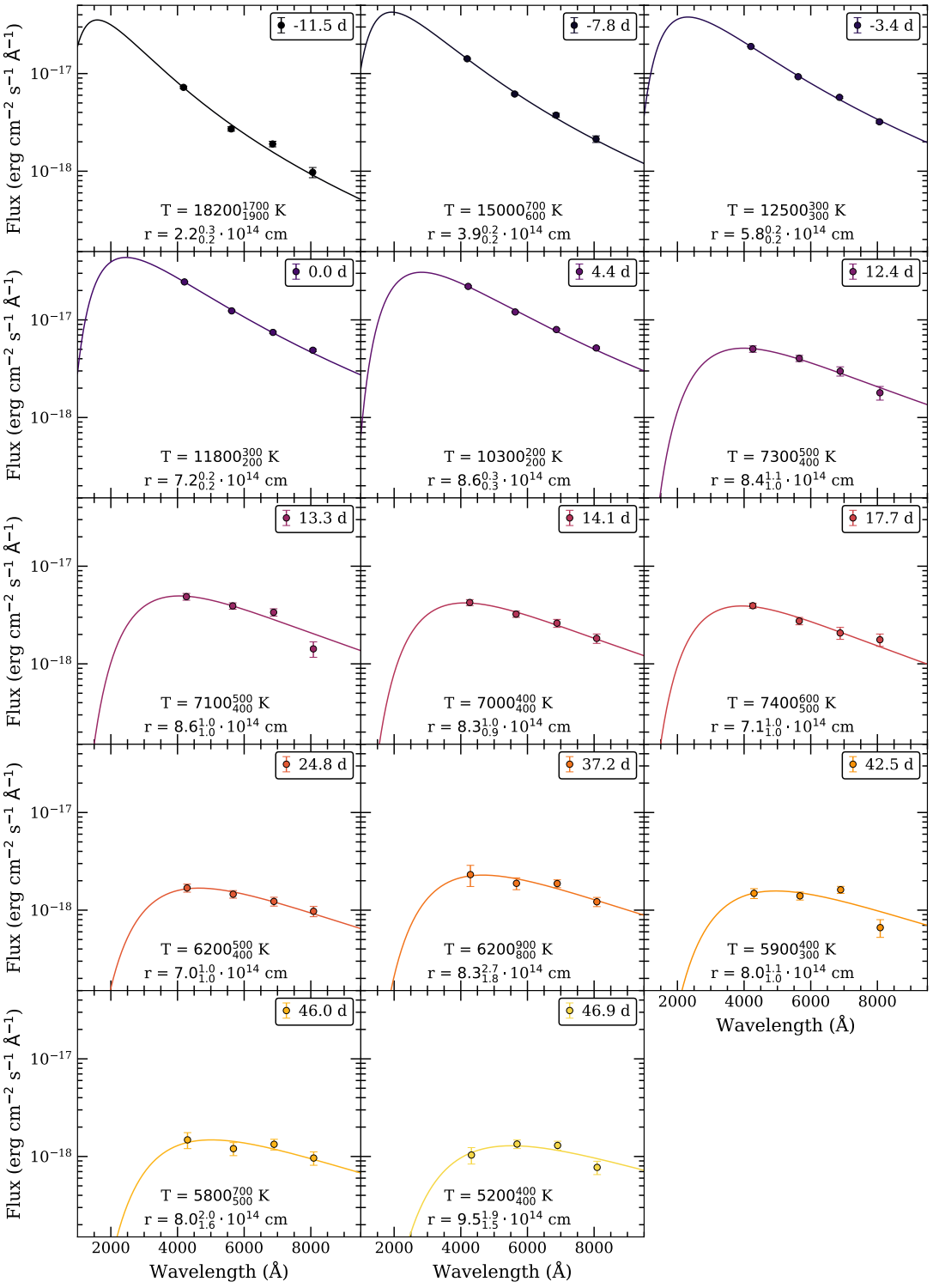

FIGURE D.2: Blackbody fits to photometry of DES16E2bjy for every epoch with *griz* detections. Best-fitting temperatures and radii are given with 1σ uncertainties.

Bibliography

Abbott, B. P., Abbott, R., Abbott, T. D., et al. 2017, Physical Review Letters, 119, 161101

Alekseev, E. N., Alekseeva, L. N., Krivosheina, I. V., & Volchenko, V. I. 1988, Soviet Astronomy Letters, 14, 41

Alexander, K. D., Berger, E., Fong, W., et al. 2017, The Astrophysical Journal, 848, L21

Ambikasaran, S., Foreman-Mackey, D., Greengard, L., Hogg, D. W., & O'Neil, M. 2016, IEEE Transactions on Pattern Analysis and Machine Intelligence, 38, 252

Anderson, J. P., Covarrubias, R. A., James, P. A., Hamuy, M., & Habergham, S. M. 2010, Monthly Notices of the Royal Astronomical Society, 407, 2660

Anderson, J. P., González-Gaitán, S., Hamuy, M., et al. 2014, The Astrophysical Journal, 786, 67

Andreoni, I., Ackley, K., Cooke, J., et al. 2017, Publications of the Astronomical Society of Australia, 34, e069

Andrews, J. E., Sugerman, B. E., Clayton, G. C., et al. 2011, Astrophysical Journal, 731

Angel, J. R. P., Hilliard, R. L., & Weymann, R. J. 1979, in The MMT and the Future of Ground-Based Astronomy, 87

Angus, C. R., Smith, M., Sullivan, M., et al. 2019, Monthly Notices of the Royal Astronomical Society

Arcavi, I. 2017, in Handbook of Supernovae (Springer International Publishing), 239–276

Arcavi, I., Gal-Yam, A., Cenko, S. B., et al. 2012, The Astrophysical Journal, 756, L30

Arcavi, I., Gal-Yam, A., Sullivan, M., et al. 2014, Astrophysical Journal, 793, 38

Arcavi, I., Gal-Yam, A., Yaron, O., et al. 2011, Astrophysical Journal Letters, 742, L18

Arcavi, I., Hosseinzadeh, G., Brown, P. J., et al. 2017a, The Astrophysical Journal, 837, L2

Arcavi, I., Hosseinzadeh, G., Howell, D. A., et al. 2017b, Nature, 551, 64

Arcavi, I., Wolf, W. M., Howell, D. A., et al. 2016, The Astrophysical Journal, 819, 35

Arnett, W. D. 1982, The Astrophysical Journal, 253, 785

Arnett, W. D., Bahcall, J. N., Kirshner, R. P., & Woosley, S. E. 1989, Annual Review of Astronomy and Astrophysics, 27, 629

Baade, W. 1938, The Astrophysical Journal, 88, 285

Baade, W. & Zwicky, F. 1934, Proceedings of the National Academy of Sciences, 20, 254

Baldry, I. K., Liske, J., Brown, M. J., et al. 2018, Monthly Notices of the Royal Astronomical Society, 474, 3875

Baldwin, J. A., Phillips, M. M., & Terlevich, R. 1981, Publications of the Astronomical Society of the Pacific, 93, 5

Barbary, K., Dawson, K. S., Tokita, K., et al. 2009, Astrophysical Journal, 690, 1358

Barbon, R., Cappellaro, E., & Turatto, M. 1989, Astronomy and Astrophysics, Suppl. Ser., 81, 421

Barbon, R., Ciatti, F., & Rosino, L. 1979, Astronomy and Astrophysics, 72, 287

Becker, A. 2015, Astrophysics Source Code Library, 04004B, ascl:1504.004

Begelman, M. C. & Sarazin, C. L. 1986, The Astrophysical Journal, 302, L59

Bellm, E. C., Kulkarni, S. R., Graham, M. J., et al. 2019, Publications of the Astronomical Society of the Pacific, 131

Benetti, S., Cappellaro, E., Mazzali, P. A., et al. 2005, The Astrophysical Journal, 623, 1011

Benetti, S., Nicholl, M., Cappellaro, E., et al. 2014, Monthly Notices of the Royal Astronomical Society, 441, 289

Berger, E., Fong, W., & Chornock, R. 2013, Astrophysical Journal Letters, 774, 23

Bernstein, J. P., Kessler, R., Kuhlmann, S., et al. 2012, The Astrophysical Journal, 753, 152

Bersten, M. C., Benvenuto, O. G., Folatelli, G., et al. 2014, The Astronomical Journal, 148, 68

Bersten, M. C., Benvenuto, O. G., Nomoto, K., et al. 2012, Astrophysical Journal, 757

Bersten, M. C., Folatelli, G., García, F., et al. 2018, Nature, 554, 497

Bertin, E. 2006, in Astronomical Data Analysis Software and Systems XV, ed. C. Gabriel, C. Arviset, D. Ponz, & E. Solano, 112

Bertin, E. 2011, in Astronomical Data Analysis Software and Systems XX, 435

Bertin, E. & Arnouts, S. 1996, Astronomy and Astrophysics Supplement Series, 117, 393

Bertin, E., Mellier, Y., Radovich, M., et al. 2002, in Astronomical Data Analysis Software and Systems XI, ed. D. A. Bohlender, D. Durand, & T. H. Handley, 228

Bethe, H. A. 1990, Reviews of Modern Physics, 62, 801

Bianco, F. B., Modjaz, M., Hicken, M., et al. 2014, Astrophysical Journal, Supplement Series, 213, 19

Bigelow, B. C., Dressler, A. M., Shectman, S. A., & Epps, H. W. 1998, in Optical Astronomical Instrumentation, Vol. 3355 (SPIE), 225–231

Bionta, R. M., Blewitt, G., Bratton, C. B., et al. 1987, Physical Review Letters, 58, 1494

Blagorodnova, N., Gezari, S., Hung, T., et al. 2017, The Astrophysical Journal, 844, 46

Blanchard, P. K., Berger, E., Fong, W., et al. 2017, The Astrophysical Journal, 848, L21

Blanton, M. R., Dalcanton, J., Eisenstein, D., et al. 2001, The Astronomical Journal, 121, 2358

Bloemen, S., Groot, P., Nelemans, G., & Klein-Wolt, M. 2015, Astronomical Society of the Pacific Conference Series, 496, 254

Blondin, S., Dessart, L., Hillier, D. J., & Khokhlov, A. M. 2013, Monthly Notices of the Royal Astronomical Society, 429, 2127

Bloom, J. S., Kasen, D., Shen, K. J., et al. 2012, Astrophysical Journal Letters, 744

Bonnett, C., Troxel, M. A., Hartley, W., et al. 2016, Physical Review D, 94, 042005

Boquien, M., Burgarella, D., Roehlly, Y., et al. 2019, Astronomy & Astrophysics, 622, A103

Bose, S., Sutaria, F., Kumar, B., et al. 2015, Astrophysical Journal, 806

Botticella, M. T., Pastorello, A., Smartt, S. J., et al. 2009, Monthly Notices of the Royal Astronomical Society, 398, 1041

Botticella, M. T., Riello, M., Cappellaro, E., et al. 2008, Astronomy and Astrophysics, 479, 49

Brouty, M., Dubois, P., Theureau, G., et al. 2003, Astronomy & Astrophysics, 412, 45

Brown, P. J., Breeveld, A. A., Holland, S., Kuin, P., & Pritchard, T. 2014, Astrophysics and Space Science, 354, 89

Bruzual, G. & Charlot, S. 2003, Monthly Notices of the Royal Astronomical Society, 344, 1000

Burbidge, E. M., Burbidge, G. R., Fowler, W. A., & Hoyle, F. 1957, Reviews of Modern Physics, 29, 547

Cameron, A. G. W. 1957, Publications of the Astronomical Society of the Pacific, 69, 201

Campana, S., Mangano, V., Blustin, A. J., et al. 2006, Nature, 442, 1008

Cano, Z. 2013, Monthly Notices of the Royal Astronomical Society, 434, 1098

Cao, Y., Kasliwal, M. M., Arcavi, I., et al. 2013, Astrophysical Journal Letters, 775

Cappellari, M. 2012, pPXF: Penalized Pixel-Fitting stellar kinematics extraction

—. 2017, Monthly Notices of the Royal Astronomical Society, 466, 798

Cappellari, M. & Emsellem, E. 2004, Publications of the Astronomical Society of the Pacific, 116, 138

Catchpole, R. M., Menzies, J. W., Monk, A. S., et al. 1987, Monthly Notices of the Royal Astronomical Society, 229, 15P

Catchpole, R. M., Whitelock, P. A., Feast, M. W., et al. 1988, Monthly Notices of the Royal Astronomical Society, 231, 75P

Cepa, J., Aguiar, M., Bland-Hawthorn, J., et al. 2003, in Revista Mexicana de Astronomia y Astrofisica: Serie de Conferencias, Vol. 16, 13–18

Chambers, K. C., Magnier, E. A., Metcalfe, N., et al. 2016, ArXiv e-prints

Chen, P., Dong, S., Stritzinger, M. D., et al. 2020, The Astrophysical Journal, 889, L6

Chevalier, R. A. 1976, The Astrophysical Journal, 207, 872

Chevalier, R. A. & Fransson, C. 1994, The Astrophysical Journal, 420, 268

Childress, M. J., Hillier, D. J., Seitenzahl, I., et al. 2015, Monthly Notices of the Royal Astronomical Society, 454, 3816

Childress, M. J., Lidman, C., Davis, T. M., et al. 2017, Monthly Notices of the Royal Astronomical Society, 472, 273

Chomiuk, L., Chornock, R., Soderberg, A. M., et al. 2011, Astrophysical Journal, 743

Chornock, R., Berger, E., Kasen, D., et al. 2017, The Astrophysical Journal, 848, L19

Chugai, N. N. & Danziger, I. J. 1994, Monthly Notices of the Royal Astronomical Society, 268, 173

Clark, P., Maguire, K., Inserra, C., et al. 2020, Monthly Notices of the Royal Astronomical Society, 492, 2208

Cobb, B. E., Bloom, J. S., Perley, D. A., et al. 2010, Astrophysical Journal Letters, 718, L150

Coil, A. L., Blanton, M. R., Burles, S. M., et al. 2011, The Astrophysical Journal, 741, 8

Colgate, S. A. 1974, The Astrophysical Journal, 187, 333

Colgate, S. A. & McKee, C. 1969, The Astrophysical Journal, 157, 623

Cool, R. J., Moustakas, J., Blanton, M. R., et al. 2013, Astrophysical Journal, 767, 118

Cooper, M. C., Yan, R., Dickinson, M., et al. 2012, Monthly Notices of the Royal Astronomical Society, 425, 2116

Coppejans, D. L., Margutti, R., Terreran, G., et al. 2020, ArXiv e-prints

Coulter, D. A., Foley, R. J., Kilpatrick, C. D., et al. 2017, Science, eaap9811

Cowan, J. J., Sneden, C., Lawler, J. E., et al. 2019, ArXiv e-prints

Cowperthwaite, P. S., Berger, E., Villar, V. A., et al. 2017, The Astrophysical Journal, 848, L17

Crawford, S. M., Still, M., Schellart, P., et al. 2010, SPIE Astronomical Instrumentation, 7737

D'Andrea, C. B., Smith, M., Sullivan, M., et al. 2018, ArXiv e-prints

Davidson, K., Dufour, R. J., Walborn, N. R., & Gull, T. R. 1986, The Astrophysical Journal, 305, 867

De, K., Kasliwal, M. M., Ofek, E. O., et al. 2018, Science, 362, 201

De Cia, A., Gal-Yam, A., Rubin, A., et al. 2018, The Astrophysical Journal, 860, 100

DES Collaboration, Abbott, T. M., Abdalla, F. B., et al. 2018a, Physical Review D, 98

—. 2019a, Monthly Notices of the Royal Astronomical Society, 483, 4866

DES Collaboration, Abbott, T. M. C., Abdalla, F. B., et al. 2018b, The Astrophysical Journal Supplement Series, 239, 18

DES Collaboration, Abbott, T. M. C., Allam, S., et al. 2019b, The Astrophysical Journal, 872, L30

Dessart, L., John Hillier, D., Woosley, S., et al. 2015, Monthly Notices of the Royal Astronomical Society, 453, 2189

—. 2016, Monthly Notices of the Royal Astronomical Society, 458, 1618

Dexter, J. & Kasen, D. 2013, Astrophysical Journal, 772, 30

Dhungana, G., Kehoe, R., Vinko, J., et al. 2016, The Astrophysical Journal, 822, 6

Díaz, M. C., Macri, L. M., Lambas, D. G., et al. 2017, The Astrophysical Journal, 848, L29

Djorgovski, S. G., Drake, A. J., Mahabal, A. A., et al. 2011, Proceedings of the International Astronomical Union, 7, 306

Doctor, Z., Kessler, R., Chen, H. Y., et al. 2017, The Astrophysical Journal, 837, 57

Dopita, M. A., Kewley, L. J., Sutherland, R. S., & Nicholls, D. C. 2016, Astrophysics and Space Science, 361, 61

Driver, S. P., Norberg, P., Baldry, I. K., et al. 2009, Astronomy and Geophysics, 50, 12

Drlica-Wagner, A., Sevilla-Noarbe, I., Rykoff, E. S., et al. 2018, The Astrophysical Journal Supplement Series, 235, 33

Drout, M. R., Chornock, R., Soderberg, A. M., et al. 2014, The Astrophysical Journal, 794, 23

Drout, M. R., Piro, A. L., Shappee, B. J., et al. 2017, Science, eaaq0049

Drout, M. R., Soderberg, A. M., Gal-Yam, A., et al. 2011, Astrophysical Journal, 741, 97

Drout, M. R., Soderberg, A. M., Mazzali, P. A., et al. 2013, The Astrophysical Journal, 774, 58

Eisenstein, D. J. 2005, Dark energy and cosmic sound

Elias, J. H., Matthews, K., Neugebauer, G., & Persson, S. E. 1985, The Astrophysical Journal, 296, 379

Elias-Rosa, N., Pastorello, A., Benetti, S., et al. 2016, Monthly Notices of the Royal Astronomical Society, 463, 3894

Ergon, M., Sollerman, J., Fraser, M., et al. 2014, Astronomy and Astrophysics, 562

Evans, P. A., Cenko, S. B., Kennea, J. A., et al. 2017, Science, 358, 1565

Faber, S. M., Phillips, A. C., Kibrick, R. I., et al. 2003, in Instrument Design and Performance for Optical/Infrared Ground-based Telescopes, Vol. 4841 (SPIE), 1657

Faran, T., Poznanski, D., Filippenko, A. V., et al. 2014, Monthly Notices of the Royal Astronomical Society, 445, 554

Filippenko, A. V. 1988, The Astronomical Journal, 96, 1941

Flaugher, B. 2005, International Journal of Modern Physics A, 20, 3121

Flaugher, B., Diehl, H. T., Honscheid, K., et al. 2015, The Astronomical Journal, 150, 150

Foley, R. J. 2015, Monthly Notices of the Royal Astronomical Society, 452, 2463

Foley, R. J., Berger, E., Fox, O., et al. 2011, Astrophysical Journal, 732

Foley, R. J., Blanchard, P. K., Challis, P., et al. 2015, The Astronomer's Telegram, 6877

Foley, R. J., Challis, P. J., Chornock, R., et al. 2013, The Astrophysical Journal, 767, 57

Foley, R. J., Papenkova, M. S., Swift, B. J., et al. 2003, Publications of the Astronomical Society of the Pacific, 115, 1220

Foley, R. J., Smith, N., Ganeshalingam, M., et al. 2007, The Astrophysical Journal, 657, L105

Fong, W., Berger, E., Blanchard, P. K., et al. 2017, The Astrophysical Journal, 848, L23

Frank, J. & Rees, M. J. 1976, Monthly Notices of the Royal Astronomical Society, 176, 633

Fransson, C., Chevalier, R. A., Filippenko, A. V., et al. 2002, The Astrophysical Journal, 572, 350

Fraser, M., Inserra, C., Jerkstrand, A., et al. 2013, Monthly Notices of the Royal Astronomical Society, 433, 1312

Freiburghaus, C., Rosswog, S., & Thielemann, F.-K. 1999, The Astrophysical Journal, 525, L121

Fremling, C., Sollerman, J., Taddia, F., et al. 2016, Astronomy and Astrophysics, 593

—. 2014, Astronomy and Astrophysics, 565

Frieman, J. A., Bassett, B., Becker, A., et al. 2008, Astronomical Journal, 135, 338

Frohmaier, C., Sullivan, M., Maguire, K., & Nugent, P. 2018, The Astrophysical Journal, 858, 50

Fruchter, A. S., Levan, A. J., Strolger, L., et al. 2006, Nature, 441, 463

Gal-Yam, A. 2012, Luminous supernovae

—. 2017, in Handbook of Supernovae, ed. A. Alsabti & P. Murdin (Springer), 195–237

—. 2019, Annual Review of Astronomy and Astrophysics, 57, 305

Gal-Yam, A., Ofek, E. O., & Shemmer, O. 2002, Monthly Notices of the Royal Astronomical Society, 332

Galama, T. J., Vreeswijk, P. M., Van Paradijs, J., et al. 1998, Nature, 395, 670

Galbany, L., Hamuy, M., Phillips, M. M., et al. 2016, The Astronomical Journal, 151, 33

Gall, E. E. E., Polshaw, J., Kotak, R., et al. 2015, Astronomy & Astrophysics, 582, A3

Gal-Yam, A., Leonard, D. C., Fox, D. B., et al. 2007, The Astrophysical Journal, 656, 372

García-Berro, E., Badenes, C., Aznar-Siguán, G., & Lorén-Aguilar, P. 2017, Monthly Notices of the Royal Astronomical Society, 468, 4815

Gaskell, C. M., Cappellaro, E., Dinerstein, H. L., et al. 1986, The Astrophysical Journal, 306, L77

Gezari, S., Chornock, R., Rest, A., et al. 2012, Nature, 485, 217

Gezari, S., Halpern, J. P., Grupe, D., et al. 2009, Astrophysical Journal, 690, 1313

Goldstein, D. A., D'Andrea, C. B., Fischer, J. A., et al. 2015, The Astronomical Journal, 150, 82

González Delgado, R. M., García-Benito, R., Pérez, E., et al. 2015, Astronomy and Astrophysics, 581

González-Gaitán, S., Tominaga, N., Molina, J., et al. 2015, Monthly Notices of the Royal Astronomical Society, 451, 2212

Graham, M. L., Sand, D. J., Bildfell, C. J., et al. 2012, Astrophysical Journal, 753, 68

Graur, O., Bianco, F. B., Modjaz, M., et al. 2017, The Astrophysical Journal, 837, 121

Groh, J. H., Georgy, C., & Ekström, S. 2013, Astronomy and Astrophysics, 558

Guillochon, J., Parrent, J., Kelley, L. Z., & Margutti, R. 2016, The Astrophysical Journal, 835, 64

Gupta, R. R., Kuhlmann, S., Kovacs, E., et al. 2016, The Astronomical Journal, 152, 154

Gutiérrez, C. P., Anderson, J. P., Hamuy, M., et al. 2017a, The Astrophysical Journal, 850, 90

—. 2017b, The Astrophysical Journal, 850, 89

Gutiérrez, C. P., Sullivan, M., Martinez, L., et al. 2020, ArXiv e-prints

Hamuy, M. 2003, The Astrophysical Journal, 582, 905

Harkness, R. P., Wheeler, J. C., Margon, B., et al. 1987, The Astrophysical Journal, 317, 355

Hartwig, E., Deichmüller, F., Oppenheim, H., et al. 1885, Astronomische Nachrichten, 112, 245

Hillebrandt, W. & Niemeyer, J. C. 2000, Annual Review of Astronomy and Astrophysics, 38, 191

Hills, J. G. 1975, Nature, 254, 295

Hirata, K., Kajita, T., Koshiba, M., et al. 1987, Physical Review Letters, 58, 1490

Ho, A. Y. Q., Goldstein, D. A., Schulze, S., et al. 2019a, The Astrophysical Journal, 887, 169

Ho, A. Y. Q., Perley, D. A., Kulkarni, S. R., et al. 2020, ArXiv e-prints

Ho, A. Y. Q., Phinney, E. S., Ravi, V., et al. 2019b, The Astrophysical Journal, 871, 73

Holland, S. E., Dawson, K. S., Palaio, N. P., et al. 2007, Nuclear Instruments and Methods in Physics Research, Section A: Accelerators, Spectrometers, Detectors and Associated Equipment, 579, 653

Holland, S. E., Groom, D. E., Palaio, N. P., Stover, R. J., & Wei, M. 2003, IEEE Transactions on Electron Devices, 50, 225

Holoien, T. W.-S., Auchettl, K., Tucker, M. A., et al. 2020, The Astrophysical Journal, 898, 161

Holoien, T. W.-S., Huber, M. E., Shappee, B. J., et al. 2019, The Astrophysical Journal, 880, 120

Hook, I. M., Jørgensen, I., Allington-Smith, J. R., et al. 2004, Publications of the Astronomical Society of the Pacific, 116, 425

Hoormann, J. K., Martini, P., Davis, T. M., et al. 2019, Monthly Notices of the Royal Astronomical Society, 453, 1701

Hosseinzadeh, G., Arcavi, I., Valenti, S., et al. 2017, The Astrophysical Journal, 836, 158

Hosseinzadeh, G., McCully, C., Zabludoff, A. I., et al. 2019, The Astrophysical Journal, 871, L9

Hosseinzadeh, G., Valenti, S., McCully, C., et al. 2018, The Astrophysical Journal, 861, 63

Howell, D. A. 2017, in Handbook of Supernovae, ed. A. Alsabti & P. Murdin (Springer), 431–458

Howell, D. A., Kasen, D., Lidman, C., et al. 2013, Astrophysical Journal, 779

Hoyle, F. & Fowler, W. A. 1960, The Astrophysical Journal, 132, 565

Hsiao, E. Y., Conley, A., Howell, D. A., et al. 2007, The Astrophysical Journal, 663, 1187

Hu, L., Wu, X., Andreoni, I., et al. 2017, Science Bulletin, 62, 1433

Huang, F., Wang, X., Zhang, J., et al. 2015, Astrophysical Journal, 807

Huang, K., Shimoda, J., Urata, Y., et al. 2019, The Astrophysical Journal, 878, L25

Inserra, C., Prajs, S., Gutierrez, C. P., et al. 2018a, The Astrophysical Journal, 854, 175

Inserra, C., Smartt, S. J., Gall, E. E., et al. 2018b, Monthly Notices of the Royal Astronomical Society, 475, 1046

Inserra, C., Smartt, S. J., Jerkstrand, A., et al. 2013, Astrophysical Journal, 770, 128

Irani, I., Schulze, S., Gal-Yam, A., et al. 2019, ArXiv e-prints

Ivezić, Ž., Kahn, S. M., Tyson, J. A., et al. 2019, The Astrophysical Journal, 873, 111

Janka, H.-T. 2017, in Handbook of Supernovae (Springer International Publishing), 1095–1150

Janka, H. T., Langanke, K., Marek, A., Martínez-Pinedo, G., & Müller, B. 2007, Theory of core-collapse supernovae

Jarvis, M. J., Bonfield, D. G., Bruce, V. A., et al. 2013, Monthly Notices of the Royal Astronomical Society, 428, 1281

Jha, S., Branch, D., Chornock, R., et al. 2006, The Astronomical Journal, 132, 189

Jha, S. W. 2017, in Handbook of Supernovae, ed. A. W. Alsabti & P. Murdin (Cham: Springer, Cham), 375–401

Kankare, E., Kotak, R., Pastorello, A., et al. 2015, Astronomy & Astrophysics, 581, L4

Kasen, D. 2006, The Astrophysical Journal, 649, 939

Kasen, D. & Bildsten, L. 2010, Astrophysical Journal, 717, 245

Kasliwal, M. M., Kulkarni, S. R., Gal-Yam, A., et al. 2012, The Astrophysical Journal, 755, 161

—. 2010, The Astrophysical Journal, 723, L98

Kasliwal, M. M., Nakar, E., Singer, L. P., et al. 2017, Science, eaap9455

Kauffmann, G., Heckman, T. M., Tremonti, C., et al. 2003, Monthly Notices of the Royal Astronomical Society, 346, 1055

Kennicutt, R. C. 1998, The Astrophysical Journal, 498, 541

Kessler, R., Bernstein, J. P., Cinabro, D., et al. 2009, Publications of the Astronomical Society of the Pacific, 121, 1028

Kessler, R., Marriner, J., Childress, M., et al. 2015, The Astronomical Journal, 150, 172

Kewley, L. J., Dopita, M. A., Sutherland, R. S., Heisler, C. A., & Trevena, J. 2001, The Astrophysical Journal, 556, 121

Khazov, D., Yaron, O., Gal-Yam, A., et al. 2016, The Astrophysical Journal, 818, 3

Kiewe, M., Gal-Yam, A., Arcavi, I., et al. 2012, Astrophysical Journal, 744

Kilpatrick, C. D., Foley, R. J., Kasen, D., et al. 2017, Science, eaaq0073

King, A. L., Martini, P., Davis, T. M., et al. 2015, Monthly Notices of the Royal Astronomical Society, 453, 1701

Klein, R. I. & Chevalier, R. A. 1978, The Astrophysical Journal, 223, L109

Kleiser, I., Kasen, D., & Duffell, P. 2018, Monthly Notices of the Royal Astronomical Society, 000, 0

Kleiser, I. K. W. & Kasen, D. 2014, Monthly Notices of the Royal Astronomical Society, 438, 318

Komossa, S. 2015, Tidal disruption of stars by supermassive black holes: Status of observations

Kuin, N. P. M., Wu, K., Oates, S., et al. 2019, Monthly Notices of the Royal Astronomical Society, 487, 2505

Kuncarayakti, H., Galbany, L., Anderson, J. P., Krühler, T., & Hamuy, M. 2016, Astronomy and Astrophysics, 593

Leloudas, G., Chatzopoulos, E., Dilday, B., et al. 2012, Astronomy & Astrophysics, 541, A129

Lewis, I. J., Cannon, R. D., Taylor, K., et al. 2002, Monthly Notices of the Royal Astronomical Society, 333, 279

Li, L.-X. & Paczyński, B. 1998, The Astrophysical Journal, 507, L59

Li, W., Bloom, J. S., Podsiadlowski, P., et al. 2011a, Nature, 480, 348

Li, W., Chornock, R., Leaman, J., et al. 2011b, Monthly Notices of the Royal Astronomical Society, 412, 1473

Li, W., Filippenko, A. V., Chornock, R., et al. 2003, Publications of the Astronomical Society of the Pacific, 115, 453

Li, W., Leaman, J., Chornock, R., et al. 2011c, Monthly Notices of the Royal Astronomical Society, 412, 1441

Lidman, C., Tucker, B. E., Davis, T. M., et al. 2020, Monthly Notices of the Royal Astronomical Society, 496, 19

Lidskii, V. & Ozernoi, L. 1979, Soviet Astronomy Letters, 5, 16

LIGO Scientific Collaboration, L. S., Virgo Collaboration, V., GBM, F., et al. 2017, The Astrophysical Journal, 848, L12

Lipunov, V. M., Gorbovskoy, E., Kornilov, V. G., et al. 2017, The Astrophysical Journal, 850, L1

Lonsdale, C. J., Smith, H. E., Rowan-Robinson, M., et al. 2003, Publications of the Astronomical Society of the Pacific, 115, 897

LSST Science Collaboration, L. S., Abell, P. A., Allison, J., et al. 2009, ArXiv e-prints

Lunnan, R., Chornock, R., Berger, E., et al. 2013, Astrophysical Journal, 771

Lunnan, R., Kasliwal, M. M., Cao, Y., et al. 2017, The Astrophysical Journal, 836, 60

Lyman, J. D., Bersier, D., James, P. A., et al. 2016, Monthly Notices of the Royal Astronomical Society, 457, 328

Lyutikov, M. & Toonen, S. 2019, Monthly Notices of the Royal Astronomical Society, 487, 5618

Maeda, K., Tanaka, M., Nomoto, K., et al. 2007, The Astrophysical Journal, 666, 1069

Maeder, A. & Conti, P. S. 1994, Annual Review of Astronomy and Astrophysics, 32, 227

Magee, M. R., Kotak, R., Sim, S. A., et al. 2016, Astronomy & Astrophysics, 589, A89

Malmquist, K. G., Malmquist, & G., K. 1922, On some relations in stellar statistics, Tech. rep.

—. 1925, A contribution to the problem of determining the distribution in space of the stars, Tech. rep.

Mao, M. Y., Sharp, R., Norris, R. P., et al. 2012, Monthly Notices of the Royal Astronomical Society, 426, 3334

Margutti, R., Berger, E., Fong, W., et al. 2017, The Astrophysical Journal, 848, L20

Margutti, R., Metzger, B. D., Chornock, R., et al. 2019, The Astrophysical Journal, 872, 18

Margutti, R., Milisavljevic, D., Soderberg, A. M., et al. 2014, Astrophysical Journal, 780

Martin, D. C., Fanson, J., Schiminovich, D., et al. 2005, The Astrophysical Journal, 619, L1

Matheson, T., Filippenko, A. V., Chornock, R., Leonard, D. C., & Li, W. 2000, The Astronomical Journal, 119, 2303

Mauerhan, J. C., Smith, N., Filippenko, A. V., et al. 2013, Monthly Notices of the Royal Astronomical Society, 430, 1801

Mauerhan, J. C., Van Dyk, S. D., Graham, M. L., et al. 2015, Monthly Notices of the Royal Astronomical Society, 447, 1922

Mauerhan, J. C., Van Dyk, S. D., Johansson, J., et al. 2018, Monthly Notices of the Royal Astronomical Society, 473, 3765

Maund, J. R., Smartt, S. J., Kudritzki, R. P., et al. 2006, Monthly Notices of the Royal Astronomical Society, 369, 390

Maund, J. R., Smartt, S. J., Kudritzki, R. P., Podsiadlowski, P., & Gilmore, G. F. 2004, Nature, 427, 129

Mazzali, P. A., Deng, J., Maeda, K., et al. 2002, The Astrophysical Journal, 572, L61

McBrien, O. R., Smartt, S. J., Chen, T.-W., et al. 2019, The Astrophysical Journal, 885, L23

McKenzie, E. H. & Schaefer, B. E. 1999, Publications of the Astronomical Society of the Pacific, 111, 964

Menzies, J. W., Catchpole, R. M., van Vuuren, G., et al. 1987, Monthly Notices of the Royal Astronomical Society, 227, 39P

Metzger, B. D., Martínez-Pinedo, G., Darbha, S., et al. 2010, Monthly Notices of the Royal Astronomical Society, 406, 2650

Miknaitis, G., Pignata, G., Rest, A., et al. 2007, The Astrophysical Journal, 666, 674

Miller, A. A., Chornock, R., Perley, D. A., et al. 2009, Astrophysical Journal, 690, 1303

Minkowski, R. 1941, Publications of the Astronomical Society of the Pacific, 53, 224

Modjaz, M. 2011, Astronomische Nachrichten, 332, 434

Modjaz, M., Li, W., Butler, N., et al. 2009, Astrophysical Journal, 702, 226

Mohan, P., An, T., & Yang, J. 2020, The Astrophysical Journal, 888, L24

Monet, D. G., Levine, S. E., Canzian, B., et al. 2003, The Astronomical Journal, 125, 984

Morganson, E., Gruendl, R. A., Menanteau, F., et al. 2018, Publications of the Astronomical Society of the Pacific, 130, 074501

Moriya, T. J., Tanaka, M., Yasuda, N., et al. 2019, The Astrophysical Journal Supplement Series, 241, 16

Müller, T., Prieto, J. L., Pejcha, O., & Clocchiatti, A. 2017, The Astrophysical Journal, 841, 127

Munari, U., Henden, A., Belligoli, R., et al. 2013, New Astronomy, 20, 30

Nadyozhin, D. K. 1994, The Astrophysical Journal Supplement Series, 92, 527

Nakamura, O., Fukugita, M., Yasuda, N., et al. 2003, The Astronomical Journal, 125, 1682

Nakaoka, T., Kawabata, K. S., Maeda, K., et al. 2018, The Astrophysical Journal, 859, 78

Nakar, E. & Piro, A. L. 2014, The Astrophysical Journal, 788, 193

Nakar, E. & Sari, R. 2010, The Astrophysical Journal, 725, 904

Neill, J. D., Sullivan, M., Gal-Yam, A., et al. 2011, Astrophysical Journal, 727, 15

Neilsen, E. & Annis, J. 2014, in Astronomical Data Analysis Software and Systems XXIII, ed. N. Manset & P. Forshay, 77

Newville, M., Ingargiola, A., Stensitzki, T., & Allen, D. B. 2014, Zenodo

Nicholl, M., Berger, E., Kasen, D., et al. 2017, The Astrophysical Journal, 848, L18

Nicholl, M., Smartt, S. J., Jerkstrand, A., et al. 2015a, Monthly Notices of the Royal Astronomical Society, 452, 3869

—. 2015b, The Astrophysical Journal Letters, 807, L18

Nomoto, K., Iwamoto, K., & Suzuki, T. 1995, Physics Reports, 256, 173

Nomoto, K., Suzuki, T., Shigeyama, T., et al. 1993, Nature, 364, 507

Nugent, P., Kim, A., & Perlmutter, S. 2002, Publications of the Astronomical Society of the Pacific, 114, 803

Nugent, P. E., Sullivan, M., Cenko, S. B., et al. 2011, Nature, 480, 344

Ofek, E. O., Cameron, P. B., Kasliwal, M. M., et al. 2007, The Astrophysical Journal, 659, L13

Ofek, E. O., Rabinak, I., Neill, J. D., et al. 2010, The Astrophysical Journal, 724, 1396

Oke, J. B., Cohen, J. G., Carr, M., et al. 1995, Publications of the Astronomical Society of the Pacific, 107, 375

Oke, J. B. & Searle, L. 1974, Annual Review of Astronomy and Astrophysics, 12, 315

Pan, Y. C., Foley, R. J., Smith, M., et al. 2017, Monthly Notices of the Royal Astronomical Society, 470, 4241

Papadopoulos, A., D'Andrea, C. B., Sullivan, M., et al. 2015, Monthly Notices of the Royal Astronomical Society, 449, 1215

Pastorello, A., Cappellaro, E., Inserra, C., et al. 2013, Astrophysical Journal, 767

Pastorello, A. & Fraser, M. 2019, Supernova impostors and other gap transients

Pastorello, A., Kochanek, C. S., Fraser, M., et al. 2018, Monthly Notices of the Royal Astronomical Society, 474, 197

Pastorello, A., Mason, E., Taubenberger, S., et al. 2019, Astronomy & Astrophysics, 630, A75

Pastorello, A., Mattila, S., Zampieri, L., et al. 2008, Monthly Notices of the Royal Astronomical Society, 389, 113

Pastorello, A., Smartt, S. J., Botticella, M. T., et al. 2010, Astrophysical Journal Letters, 724, L16

Pastorello, A., Smartt, S. J., Mattila, S., et al. 2007, Nature, 447, 829

Pastorello, A., Tartaglia, L., Elias-Rosa, N., et al. 2015, Monthly Notices of the Royal Astronomical Society, 454, 4293

Pastorello, A., Wang, X. F., Ciabattari, F., et al. 2016, Monthly Notices of the Royal Astronomical Society, 456, 853

Pastorello, A., Zampieri, L., Turatto, M., et al. 2004, Monthly Notices of the Royal Astronomical Society, 347, 74

Patat, F., Barbon, R., Cappellaro, E., & Turatto, M. 1994, Astronomy and Astrophysics, 282, 731

Patat, F., Cappellaro, E., Danziger, J., et al. 2001, The Astrophysical Journal, 555, 900

Pereira, R., Thomas, R. C., Aldering, G., et al. 2013, Astronomy & Astrophysics, 554, A27

Perets, H. B., Gal-Yam, A., Mazzali, P. A., et al. 2010, Nature, 465, 322

Perley, D. A., Mazzali, P. A., Yan, L., et al. 2019, Monthly Notices of the Royal Astronomical Society, 484, 1031

Perlmutter, S., Aldering, G., Goldhaber, G., et al. 1999, The Astrophysical Journal, 517, 565

Perryman, M. A. C., de Boer, K. S., Gilmore, G., et al. 2001, Astronomy & Astrophysics, 369, 339

Petty, S. M., Neill, J. D., Jarrett, T. H., et al. 2013, Astronomical Journal, 146

Phillips, M. M. 1993, The Astrophysical Journal, 413, L105

Phinney, E. S. 1989, in IAU Symposium, Vol. 136, 543

Pian, E., D'Avanzo, P., Benetti, S., et al. 2017, Nature, 551, 67

Piro, A. L. 2015, The Astrophysical Journal, 808, L51

Podsiadlowski, P., Hsu, J. J., Joss, P. C., & Ross, R. R. 1993, Nature, 364, 509

Podsiadlowski, P., Joss, P. C., & Hsu, J. J. L. 1992, The Astrophysical Journal, 391, 246

Pozanenko, A. S., Barkov, M. V., Minaev, P. Y., et al. 2018, The Astrophysical Journal, 852, L30

Poznanski, D., Chornock, R., Nugent, P. E., et al. 2010, Science, 327, 58

Prentice, S. J., Maguire, K., Flörs, A., et al. 2020, Astronomy and Astrophysics, 635

Prentice, S. J., Maguire, K., Smartt, S. J., et al. 2018, The Astrophysical Journal, 865, L3

Prentice, S. J., Mazzali, P. A., Pian, E., et al. 2016, Monthly Notices of the Royal Astronomical Society, 458, 2973

Pritchard, T. A., Roming, P. W., Brown, P. J., Bayless, A. J., & Frey, L. H. 2014, Astrophysical Journal, 787

Pritchet, C. & SNLS Collaboration. 2005, in Astronomical Society of the Pacific Conference Series, Vol. 339, Observing Dark Energy, ed. S. Wolff & T. Lauer, 60

Pursiainen, M., Childress, M., Smith, M., et al. 2018, Monthly Notices of the Royal Astronomical Society, 481, 894

Pursiainen, M., Gutiérrez, C. P., Wiseman, P., et al. 2020, Monthly Notices of the Royal Astronomical Society, 494, 5576

Quimby, R. M., Aldering, G., Wheeler, J. C., et al. 2007, The Astrophysical Journal, 668, L99

Quimby, R. M., Cia, A. D., Gal-Yam, A., et al. 2018, The Astrophysical Journal, 855, 2

Quimby, R. M., Kulkarni, S. R., Kasliwal, M. M., et al. 2011, Nature, 474, 487

Rabinak, I. & Waxman, E. 2011, The Astrophysical Journal, 728, 63

Rasmussen, C. E. & Williams, C. K. I. 2006, Gaussian Processes for Machine Learning

Rau, A., Kulkarni, S. R., Law, N. M., et al. 2009, Publications of the Astronomical Society of the Pacific, 121, 1334

Rees, M. J. 1988, Nature, 333, 523

Rest, A., Garnavich, P. M., Khatami, D., et al. 2018, Nature Astronomy 2018, 1

Richardson, D., Jenkins III, R. L., Wright, J., & Maddox, L. 2014, The Astronomical Journal, 147, 118

Richmond, M. W. & Smith, H. A. 2012, The Journal of the American Association of Variable Star Observers, vol. 40, no. 2, p. 872, 40, 872

Riess, A. G., Filippenko, A. V., Challis, P., et al. 1998, The Astronomical Journal, 116, 1009

Rykoff, E. S., Rozo, E., Hollowood, D., et al. 2016, The Astrophysical Journal Supplement Series, 224, 1

Sahu, D. K., Anupama, G. C., & Chakradhari, N. K. 2013, Monthly Notices of the Royal Astronomical Society, 433, 2

Sako, M., Bassett, B., Becker, A., et al. 2008, Astronomical Journal, 135, 348

Sako, M., Bassett, B., Becker, A. C., et al. 2018, Publications of the Astronomical Society of the Pacific, 130, 064002

Sako, M., Bassett, B., Connolly, B., et al. 2011, Astrophysical Journal, 738, 162

Salpeter, E. E. 1955, The Astrophysical Journal, 121, 161

Scalzo, R., Aldering, G., Antilogus, P., et al. 2012, Astrophysical Journal, 757

Schechter, P. 1976, The Astrophysical Journal, 203, 297

Schlafly, E. F. & Finkbeiner, D. P. 2011, The Astrophysical Journal, 737, 103

Schlegel, E. 1990, Monthly Notices of the Royal Astronomical Society, 244, 269

Scolnic, D., Kessler, R., Brout, D., et al. 2017, The Astrophysical Journal, 852, L3

Scolnic, D. M., Jones, D. O., Rest, A., et al. 2018, The Astrophysical Journal, 859, 101

Sérsic, J. L. 1963, Boletin de la Asociacion Argentina de Astronomia La Plata Argentina, 6, 41

Shappee, B. J., Simon, J. D., Drout, M. R., et al. 2017, Science, 358, 1574

Shappee, B. J. & Stanek, K. Z. 2011, Astrophysical Journal, 733

Shaw, R. L. 1979, Astronomy and Astrophysics, 76, 188

Shen, K. J., Kasen, D., Weinberg, N. N., Bildsten, L., & Scannapieco, E. 2010, Astrophysical Journal, 715, 767

Shen, K. J., Quataert, E., & Pakmor, R. 2019, The Astrophysical Journal, 887, 180

Shivvers, I., Filippenko, A. V., Silverman, J. M., et al. 2019, Monthly Notices of the Royal Astronomical Society, 482, 1545

Shivvers, I., Modjaz, M., Zheng, W., et al. 2017, Publications of the Astronomical Society of the Pacific, 129

Shivvers, I., Zheng, W. K., Mauerhan, J., et al. 2016, Monthly Notices of the Royal Astronomical Society, 461

Siebert, M. R., Foley, R. J., Drout, M. R., et al. 2017, The Astrophysical Journal, 848, L26

Silverman, J. M., Nugent, P. E., Gal-Yam, A., et al. 2013, Astrophysical Journal, Supplement Series, 207

Silverman, J. M., Vinkó, J., Marion, G. H., et al. 2015, Monthly Notices of the Royal Astronomical Society, 451, 1973

Smartt, S. J. 2009, Annual Review of Astronomy and Astrophysics, 47, 63

Smartt, S. J., Chen, T. W., Jerkstrand, A., et al. 2017, Nature, 551, 75

Smartt, S. J., Eldridge, J. J., Crockett, R. M., & Maund, J. R. 2009, Monthly Notices of the Royal Astronomical Society, 395, 1409

Smith, G. A., Saunders, W., Bridges, T., et al. 2004, in Ground-based Instrumentation for Astronomy, Vol. 5492 (SPIE), 410

Smith, M., Sullivan, M., D'Andrea, C. B., et al. 2016a, The Astrophysical Journal, 818, L8

Smith, M., Sullivan, M., Nichol, R. C., et al. 2018, The Astrophysical Journal, 854, 37

Smith, M. P., Nordsieck, K. H., Burgh, E. B., et al. 2006, in Ground-based and Airborne Instrumentation for Astronomy, Vol. 6269 (SPIE), 62692A

Smith, N. 2017, in Handbook of Supernovae (Springer International Publishing), 403–429

Smith, N., Andrews, J. E., Van Dyk, S. D., et al. 2016b, Monthly Notices of the Royal Astronomical Society, 458, 950

Smith, N., Li, W., Foley, R. J., et al. 2007, The Astrophysical Journal, 666, 1116

Smith, N., Li, W., Silverman, J. M., Ganeshalingam, M., & Filippenko, A. V. 2011, Monthly Notices of the Royal Astronomical Society, 415, 773

Smith, N., Mauerhan, J. C., & Prieto, J. L. 2014, Monthly Notices of the Royal Astronomical Society, 438, 1191

Smith, N., Miller, A., Li, W., et al. 2010, Astronomical Journal, 139, 1451

Soares-Santos, M., Holz, D. E., Annis, J., et al. 2017, The Astrophysical Journal, 848, L16

Soderberg, A. M., Berger, E., Page, K. L., et al. 2008, Nature, 453, 469

Soker, N., Grichener, A., & Gilkis, A. 2019, Monthly Notices of the Royal Astronomical Society, 484, 4972

Sollerman, J., Kozma, C., Fransson, C., et al. 2000, The Astrophysical Journal, 537, L127

Srivastav, S., Anupama, G. C., & Sahu, D. K. 2014, Monthly Notices of the Royal Astronomical Society, 445, 1932

Stritzinger, M. & Leibundgut, B. 2005, Astronomy & Astrophysics, 431, 423

Sullivan, M., Le Borgne, D., Pritchet, C. J., et al. 2006, The Astrophysical Journal, 648, 868

Suntzeff, N. B., Hamuy, M., Martin, G., Gomez, A., & Gonzalez, R. 1988, The Astronomical Journal, 96, 1864

Symbalisty, E. & Schramm, D. N. 1982, Astrophysical Letters, 22,, 143

Taddia, F., Fremling, C., Sollerman, J., et al. 2016, Astronomy and Astrophysics, 592

Taddia, F., Sollerman, J., Fremling, C., et al. 2019, Astronomy and Astrophysics, 621

Taddia, F., Sollerman, J., Leloudas, G., et al. 2015, Astronomy and Astrophysics, 574

Taddia, F., Stritzinger, M. D., Bersten, M., et al. 2018, Astronomy and Astrophysics, 609

Taddia, F., Stritzinger, M. D., Sollerman, J., et al. 2013, Astronomy & Astrophysics, 555, A10

Takáts, K., Pumo, M. L., Elias-Rosa, N., et al. 2014, Monthly Notices of the Royal Astronomical Society, 438, 368

Tampo, Y., Tanaka, M., Maeda, K., et al. 2020, The Astrophysical Journal, 894, 27

Tanaka, M., Utsumi, Y., Mazzali, P. A., et al. 2017, Publications of the Astronomical Society of Japan, 69, 102

Tanvir, N. R., Levan, A. J., Fruchter, A. S., et al. 2013, Nature, 500, 547

Tanvir, N. R., Levan, A. J., González-Fernández, C., et al. 2017, The Astrophysical Journal, 848, L27

Tartaglia, L., Fraser, M., Sand, D. J., et al. 2017, The Astrophysical Journal, 836, L12

Taubenberger, S. 2017, in Handbook of Supernovae (Springer International Publishing), 317–373

Taubenberger, S., Hachinger, S., Pignata, G., et al. 2008, Monthly Notices of the Royal Astronomical Society, 385, 75

Taubenberger, S., Pastorello, A., Mazzali, P. A., et al. 2006, Monthly Notices of the Royal Astronomical Society, 371, 1459

Tauris, T. M., Langer, N., Moriya, T. J., et al. 2013, The Astrophysical Journal, 778, L23

Tonry, J. L., Denneau, L., Heinze, A. N., et al. 2018, Publications of the Astronomical Society of the Pacific, 130

Tremonti, C. A., Heckman, T. M., Kauffmann, G., et al. 2004, The Astrophysical Journal, Volume 613, Issue 2, pp. 898-913., 613, 898

Troja, E., Piro, L., Van Eerten, H., et al. 2017, Nature, 551, 71

Tsvetkov, D. Y., Shugarov, S. Y., Volkov, I. M., et al. 2013, Contributions of the Astronomical Observatory Skalnate Pleso, 43, 94

—. 2018, Astronomy Letters, 44, 315

Tsvetkov, D. Y., Volkov, I. M., & Pavlyuk, N. N. 2015, Information Bulletin on Variable Stars, 1

Tucker, D. L., Annis, J. T., Lin, H., et al. 2007, in The Future of Photometric, Spectrophotometric and Polarimetric Standardization, 187

Turatto, M. 2003, in Supernovae an Gamma-Ray Bursters, ed. K. W. Weiler, 21–36

Tylenda, R., Hajduk, M., Kamiński, T., et al. 2011, Astronomy and Astrophysics, 528

Uno, K. & Maeda, K. 2020, ArXiv e-prints

Valenti, S., Elias-Rosa, N., Taubenberger, S., et al. 2008, The Astrophysical Journal, 673, L155

Valenti, S., Sand, D., Pastorello, A., et al. 2014, Monthly Notices of the Royal Astronomical Society: Letters, 438

Valenti, S., Sand, D., Stritzinger, M., et al. 2015, Monthly Notices of the Royal Astronomical Society, 448, 2608

Valenti, S., Sand, D. J., Yang, S., et al. 2017, The Astrophysical Journal, 848, L24

Valenti, S., Taubenberger, S., Pastorello, A., et al. 2012, Astrophysical Journal Letters, 749, L28

Van Dyk, S. D., Garnavich, P. M., Filippenko, A. V., et al. 2002, Publications of the Astronomical Society of the Pacific, 114, 1322

Van Dyk, S. D., Peng, C. Y., King, J. Y., et al. 2000, Publications of the Astronomical Society of the Pacific, 112, 1532

Vazdekis, A., Sánchez-Blázquez, P., Falcón-Barroso, J., et al. 2010, Monthly Notices of the Royal Astronomical Society, 404, 1639

Vernet, J., Dekker, H., D'Odorico, S., et al. 2011, Astronomy & Astrophysics, 536, A105

Villar, V. A., Guillochon, J., Berger, E., et al. 2017, The Astrophysical Journal, 851, L21

Walborn, N. R., Prevot, M. L., Prevot, L., et al. 1989, Astronomy and Astrophysics, 219, 229

Waldman, R., Sauer, D., Livne, E., et al. 2011, Astrophysical Journal, 738, 21

Watson, D., Hansen, C. J., Selsing, J., et al. 2019, Nature, 574, 497

Wheeler, J. C., Barker, E., Benjamin, R., et al. 1993, ApJ, 417, L71

Wheeler, J. C. & Harkness, R. P. 1990, Type I supernovae

Wheeler, J. C. & Levreault, R. 1985, The Astrophysical Journal, 294, L17

White, G. L. & Malin, D. F. 1987, Nature, 327, 36

Whitelock, P. A., Catchpole, R. M., Menzies, J. W., et al. 1988, Monthly Notices of the Royal Astronomical Society, 234, 5P

Whitesides, L., Lunnan, R., Kasliwal, M. M., et al. 2017, The Astrophysical Journal, 851, 107

Wiseman, P., Pursiainen, M., Childress, M., et al. 2020a, Monthly Notices of the Royal Astronomical Society, 498, 2575

Wiseman, P., Smith, M., Childress, M., et al. 2020b, Monthly Notices of the Royal Astronomical Society, 495, 4040

Woosley, S. E. 2010, Astrophysical Journal Letters, 719, L204

Woosley, S. E., Eastman, R. G., Weaver, T. A., & Pinto, P. A. 1994, The Astrophysical Journal, 429, 300

Woosley, S. E., Taam, R. E., & Weaver, T. A. 1986, The Astrophysical Journal, 301, 601

Woosley, S. E. & Weaver, T. A. 1986, Annual Review of Astronomy and Astrophysics, 24, 205

Xiao, L., Galbany, L., Eldridge, J. J., & Stanway, E. R. 2019, Monthly Notices of the Royal Astronomical Society, 482, 384

York, D. G., Adelman, J., Anderson, Jr., J. E., et al. 2000, The Astronomical Journal, 120, 1579

Yuan, F., Jerkstrand, A., Valenti, S., et al. 2016, Monthly Notices of the Royal Astronomical Society, 461, 2003

Yuan, F., Lidman, C., Davis, T. M., et al. 2015, Monthly Notices of the Royal Astronomical Society, 452, 3047

Zacharias, N., Finch, C. T., Girard, T. M., et al. 2013, Astronomical Journal, 145, 44

Zwicky, F. 1938, The Astrophysical Journal, 88, 529